

**Best
Available
Copy**

AD-775 228

CRYOGENIC SYSTEMS AND SUPERCONDUCTIVE
POWER

B. D. Hatch, et al

General Electric Company

Prepared for:

Advanced Research Projects Agency

1 October 1973

DISTRIBUTED BY:

NTIS

National Technical Information Service
U. S. DEPARTMENT OF COMMERCE
5285 Port Royal Road, Springfield Va. 22151

SECURITY CLASSIFICATION OF THIS PAGE (When Data Entered)

AD-775 228

REPORT DOCUMENTATION PAGE		READ INSTRUCTIONS BEFORE COMPLETING FORM	
1. REPORT NUMBER SRD-73-139	2. GOVT ACCESSION NO.	3. RECIPIENT'S CATALOG NUMBER	
4. TITLE (and Subtitle) CRYOGENIC SYSTEMS AND SUPERCONDUCTIVE POWER, Second Semiannual Technical Report		5. TYPE OF REPORT & PERIOD COVERED Semiannual, 12/1/72 to 9/30/73	
		6. PERFORMING ORG. REPORT NUMBER	
7. AUTHOR(s) B. D. Hatch, R. B. Fleming, D. W. Jones, D. L. Kerr, and S. H. Minnich		8. CONTRACT OR GRANT NUMBER(s) DAHC-15-72-C-0235	
9. PERFORMING ORGANIZATION NAME AND ADDRESS Research and Development Center General Electric Company Schenectady, New York 12301		10. PROGRAM ELEMENT, PROJECT, TASK AREA & WORK UNIT NUMBERS ARPA Order No. 2200	
11. CONTROLLING OFFICE NAME AND ADDRESS Department of Defense Advanced Research Projects Agency		12. REPORT DATE 1 October 1973	
		13. NUMBER OF PAGES 240	
14. MONITORING AGENCY NAME & ADDRESS (if different from Controlling Office)		15. SECURITY CLASS. (of this report) Unclassified	
		15a. DECLASSIFICATION/DOWNGRADING SCHEDULE	
16. DISTRIBUTION STATEMENT (of this Report) Approved for public release - distribution unlimited.			
17. DISTRIBUTION STATEMENT (of the abstract entered in Block 20, if different from Report)			
18. SUPPLEMENTARY NOTES Reproduced by NATIONAL TECHNICAL INFORMATION SERVICE U S Department of Commerce Springfield VA 22151			
19. KEY WORDS (Continue on reverse side if necessary and identify by block number) Cryogenic Liquid metal Refrigeration Propulsion Superconductive Electrical Turborefrigerator Machinery			
20. ABSTRACT (Continue on reverse side if necessary and identify by block number) Cryogenic refrigeration is a common requirement of all superconductivity applications. For this reason, dominant emphasis is being given to this portion of the program. Its specific application to an integrated superconductive ship propulsion system with the extreme environments involved will assure that particular attention is given to each factor affecting reliability, maintainability, safety, and availability of the cryogenic system components.			

Unclassified

SECURITY CLASSIFICATION OF THIS PAGE(When Data Entered)

20.

The specific objectives of this program are to:

- Conduct a limited but broad application survey of multiple applications in which the use of cryogenic and superconductive systems and components offer substantial advantages through improvements in the performance of propulsion, communication, detection, or weapons systems.
- Define, investigate, and experimentally evaluate the key elements of a representative cryogenic turborefrigerator subsystem suitable for providing reliable long-lived cryogenic refrigeration for a superconductive ship propulsion system.
- Provide a sound technical basis for subsequent applications of superconductive power in the area of ship propulsion. Other applications, and their requirements, will be reviewed and evaluated, in order to form a preliminary evaluation of those applications that might deserve more detailed study.
- Concentrate the experimental portions of this program on the identification of potential materials and process problem areas and the demonstration of potential resolution of such problems.

/a

Unclassified

SECURITY CLASSIFICATION OF THIS PAGE(When Data Entered)

Short Title of Work	CRYOGENIC SYSTEMS AND SUPERCONDUCTIVE POWER
Contract No.	DAHC-15-72-C-0235
ARPA Order No.	2200
Contractor	Cryogenics Branch Mechanical Engineering Laboratory Research and Development Center General Electric Company P. O. Box 43 Schenectady, New York 12301
Principal Investigator	B. D. Hatch
Project Scientists	R. B. Fleming D. W. Jones D. L. Kerr S. H. Minnich
Effective Date of Contract	1 June 1972
Contract Expiration Date	16 July 1974
Amount of Contract	\$705,997

FOREWORD

This second semiannual technical report was prepared by the Research and Development Center of the General Electric Company in Schenectady, New York, under Advanced Research Projects Agency Contract No. DAHC-15-72-C-0235, "Cryogenic Systems and Superconductive Power," ARPA Order No. 2200. This contract is administered by the General Electric Research and Development Center for the Department of Defense, Advanced Research Projects Agency, Washington, D. C.

The engineering development work reported covers the period from 1 December 1972 to 30 September 1973. This work is under the direction of Mr. B. D. Hatch, Principal Investigator.

ABSTRACT

Cryogenic refrigeration is a common requirement of all superconductivity applications. For this reason, dominant emphasis is being given to this portion of the program. Its specific application to an integrated superconductive ship propulsion system with the extreme environments involved will assure that particular attention is given to each factor affecting reliability, maintainability, safety, and availability of the cryogenic system components.

The specific objectives of this program are to:

- Conduct a limited but broad application survey of multiple applications in which the use of cryogenic and superconductive systems and components offer substantial advantages through improvements in the performance of propulsion, communication, detection, or weapons systems.
- Define, investigate, and experimentally evaluate the key elements of a representative cryogenic turborefrigerator subsystem suitable for providing reliable long-lived cryogenic refrigeration for a superconductive ship propulsion system.
- Provide a sound technical basis for subsequent applications of superconductive power in the area of ship propulsion. Other applications, and their requirements, will be reviewed and evaluated, in order to form a preliminary evaluation of those applications that might deserve more detailed study.
- Concentrate the experimental portions of this program on the identification of potential materials and process problem areas and the demonstration of potential resolution of such problems.

TABLE OF CONTENTS

<u>Section</u>		<u>Page</u>
1	SUMMARY	1
	Technical Problem	1
	Methodology	1
	Individual Tasks	3
	Cryogenic Turboalternators Development for Extreme Environments	3
	Refrigerator Transient Analysis	4
	Power Conditioner for Compressor Motors	4
	Liquid Metal Current Collector Technology	4
	Superconductive Coil Technology	5
2	CRYOGENIC TURBOALTERNATORS DEVELOPMENT FOR EXTREME ENVIRONMENTS	7
	Design for Performance	7
	Alternator Electromagnetic Design	20
	Cryosection Design	20
	Heat Exchanger Design	20
	Gas Bearing and Rotor Dynamics	22
	Bearing Design Requirements	22
	Bearing Selections	23
	Journal Bearing Design	26
	Procedure	26
	Performance	28
	Thrust Bearing Design	47
	Procedure	47
	Performance	48
	Turbine Wheel Thermal and Stress Analysis	66
	Impulse Wheel	66
	Reaction Wheel	72
	Alternator Design Basis	74
	Design for Open Cycle Tests	76
	Turboalternator Test Plans	78
	Test 80° K Turboalternator.	78
	Functional Tests	78
	Warm Performance	79
	Cold Performance	79
	Shock and Vibration	79
	Gas Bearing Materials Tests.	79
	Test 80° K Cryosection System	79
	Journal Bearing Material Evaluation Tests	80
	Contract Turboalternator Mechanical Design.	97
	Status of Turboalternator Parts	99

TABLE OF CONTENTS (Cont'd)

<u>Section</u>	<u>Page</u>
3 REFRIGERATOR TRANSIENT ANALYSIS	103
Transient Cooldown Results	104
Starting and Controlled Conditions	106
Transient Run	108
Discussion and Conclusions	113
Modeling Experience	113
Test Case Experience	114
Model Description	115
Heat Exchanger Model.	122
Equations for Balanced Flow, $M_1 = M_2$	125
Equations for Unbalanced Flow, $M_1 > M_2$	126
Equations for Unbalanced Flow, $M_2 > M_1$	127
Adjustment for Variable Specific Heat.	127
Decrements and Numerical Integration	128
Outline of Model Logic	129
Thermal Load Model	129
Equations for Type 0 -- Constant Q.	133
Equations for Type 1 -- Heat Leak	133
Equations for Type 2 -- Radiation	134
Liquid/Vapor Effects	135
Outline of Model Logic	136
Turboalternator Model	137
Model Equations	139
Optional Algebraic Solution	140
Outline of Model Logic	140
Joule-Thomson Liquefier Model	140
Outline of Model Logic	144
Alternative (Split) Configuration	146
Auxiliary Functions	146
Temperature-Enthalpy Relations	146
Miscellaneous Time Functions	150
Model Nomenclature	151
Detailed Model Nomenclature	154
Component Device Subroutines	158
Numerical Example	165
Component Device Time Constants	167
Temperature-Enthalpy Data	169
Sample Printout -- ARPA1.	170
Sample Printout -- ARPA2.	174
Program Listings.	174
ARPA1 Program	174
ARPA2 Program	174

TABLE OF CONTENTS (Cont'd)

<u>Section</u>		<u>Page</u>
4	POWER CONDITIONER FOR COMPRESSOR MOTORS. .	191
5	LIQUID METAL CURRENT COLLECTOR TECHNOLOGY	195
	Purpose	195
	Gallium Collector Tests	195
6	SUPERCONDUCTING COIL TECHNOLOGY	207
	Superconducting Coil Shock and Vibration Tests . .	207
	Model Description	207
	Shock Tests	215
	Requirements	215
	Shock Test Procedure	216
	Preliminary Tests	216
	Determination of Test Parameters	217
	Instrumentation Test Procedure	219
	Vibration Tests.	219
	Requirements	219
	Vibration Test Procedure	220
	Preliminary Tests	220
	Instrumentation Test Procedure	220
7	REFERENCES	221
<u>Appendix</u>		
I	SHOCK PARAMETERS	223
	Linear Impact	223
	Torsional Impact	224
II	VIBRATION CHARACTERISTICS	227

LIST OF ILLUSTRATIONS

<u>Figure</u>		<u>Page</u>
1	Program Work Schedule	2
2	Effect of Turboalternator Efficiency Improvement on Total Refrigerator Input Power, with Each Turboalternator's Efficiency Changed Separately	9
3	Effect of Simultaneous Turboalternator Efficiency Improvement in All Three Stages on Total Refrigerator Input Power.	10
4	Full Admission Radial Reaction Design Point Computer Printout	14
5	Partial Admission Radial Impulse Design Point Computer Printout	17
6	Schematic Diagram of Pivoted Pad Journal Bearing . . .	24
7	Cryogenic Turboalternator Tilting Pad Journal Bearing .	24
8	Gimbal-Mounted Spiral Groove Thrust Bearing	25
9	Schematic Diagram of Spiral Groove Thrust Bearing . .	25
10	Tilting Pad Journal Bearing	28
11	Design Specifications for Gas-Lubricated Journal Bearings	30
12	Turboalternator Journal Bearing (0-g Operation)	31
13	Turboalternator Journal Bearing (1-g Operation)	32
14	Turboalternator Journal Bearing (3-g Operation)	33
15	Journal Bearing Performance (0-g Operation)	34
16	Journal Bearing Performance (1-g Operation)	36
17	Journal Bearing Performance (3-g Operation)	38
18	Turboalternator Journal Bearing Performance as a Function of Pivot Circle Eccentricity (1-g Design Speed).	41
19	Turboalternator Journal Bearing Performance as a Function of Pivot Circle Eccentricity (1-g Maximum Speed)	42
20	Turboalternator Journal Bearing Performance as a Function of Pivot Circle Eccentricity (3-g Design Speed).	43

LIST OF ILLUSTRATIONS (Cont'd)

<u>Figure</u>		<u>Page</u>
21	Turboalternator Journal Bearing Performance as a Function of Pivot Circle Eccentricity (3-g Maximum Speed)	44
22	Helium-Lubricated Hydrodynamic Tilting Pad Journal Bearing Performance Characteristics for Load Between Fixed Pivots (Design Speed, Run 1)	45
23	Helium-Lubricated Hydrodynamic Tilting Pad Journal Bearing Performance Characteristics for Load Between Fixed Pivots (Maximum Speed, Run 1)	45
24	Helium-Lubricated Hydrodynamic Tilting Pad Journal Bearing Performance Characteristics for Load Between Fixed Pivots (Design Speed, Run 2)	46
25	Helium-Lubricated Hydrodynamic Tilting Pad Journal Bearing Performance Characteristics for Load Between Fixed Pivots (Maximum Speed, Run 2)	46
26	Typical Thrust Bearing Assembly	49
27	Geometry Showing Radial and Angular Coordinates for Drawing Logarithmic Spiral Grooves in Flat Thrust Face	50
28	Load Capability Versus One-Side Clearance	51
29	Power Versus One-Side Clearance	52
30	Helium-Lubricated Spiral Groove Thrust Bearing Parameters and Performance (Design Speed, One Side, Ratio of Outside Diameter to Inside Diameter = 2.06)	53
31	Helium-Lubricated Spiral Groove Thrust Bearing Parameters and Performance (Maximum Speed, One Side, Ratio of Outside Diameter to Inside Diameter = 2.06)	56
32	Helium-Lubricated Spiral Groove Thrust Bearing Performance (Design Speed, Two Sides, Ratio of Outside Diameter to Inside Diameter = 2.06)	62
33	Helium-Lubricated Spiral Groove Thrust Bearing Performance (Maximum Speed, Two Sides, Ratio of Outside Diameter to Inside Diameter = 2.06)	62
34	Spiral Groove Thrust Bearing Characteristics (Design Speed)	63

LIST OF ILLUSTRATIONS (Cont'd)

<u>Figure</u>		<u>Page</u>
35	Spiral Groove Thrust Bearing Characteristics (Maximum Speed)	64
36	Radial and Angular Coordinates for Drawing Logarithmic Spiral Grooves in Flat Thrust Face.	65
37	Impulse Wheel	66
38	Impulse Wheel Effective Stress Contours (0.5-Mil Fit on Radius, Condition C)	67
39	Impulse Wheel Displacement (0.5-Mil Fit on Radius, Condition C)	68
40	Impulse Wheel Effective Stress Contours (0.5-Mil Fit on Radius, Condition W).	69
41	Impulse Wheel Displacement (0.5-Mil Fit on Radius, Condition W).	69
42	Larson-Miller Parameter (φ) and Experimentally Obtained Creep-Rupture Curves	70
43	Minimum Contact Stress Versus Interference Fit (Condition C)	71
44	Maximum Effective Stress in Hub Versus Interference Fit (Condition W)	71
45	Reaction Wheel	72
46	Reaction Wheel Effective Stress Contours (0.5-Mil Fit on Radius, Condition C)	73
47	Reaction Wheel Displacements (0.5-Mil Fit on Radius, Condition C).	73
48	Reaction Wheel Effective Stress Contours (0.5-Mil Fit on Radius, Condition W).	74
49	Flow as a Function of Power	77
50	Tiny Tim Kentanium Tilting Pad Journal Bearing	82
51	Schematic Diagram of Open Cycle Turboalternator Test Station	83
52	Open Cycle Turboalternator Test Station	84
53	Two-Stage Turboalternator Assembly on Open Cycle Support Stand	85

LIST OF ILLUSTRATIONS (Cont'd)

<u>Figure</u>		<u>Page</u>
54	Shaft Orbits of Turboalternator Assembly with Kentanium Journal Bearing Operating at Room Temperature and 100,000 Rpm	87
55	Thrust Probe Signal of Turboalternator with Kentanium Journal Bearings Operating at Room Temperature and 100,000 Rpm	87
56	Schematic Diagram of Liquid Helium Open Cycle Turboalternator Test Station	89
57	Shaft Orbits of Turboalternator with Kentanium Journal Bearings Operating at No Load, Room Temperature, and 100,000 Rpm Before Liquid Helium Boil-Off Test	91
58	Shaft Axial Motion (upper trace) and Outer Thrust Bearing Motion (lower trace) of Turboalternator with Kentanium Journal Bearings Operating at No Load, Room Temperature, and 100,000 Rpm	91
59	Shaft Orbits of Turboalternator Operating at 95°K and 100,000 Rpm with 3.0-Watt Load Before Liquid Helium Boil-Off Test	92
60	Shaft Axial Motion (upper trace) and Outer Thrust Bearing Motion (lower trace) of Turboalternator Operating at 95°K and 100,000 Rpm with 3.0-Watt Load	92
61	Shaft Thrust End Orbit of Turboalternator Operating at 14°K and 100,000 Rpm with 13.4-Watt Load	94
62	Shaft Axial Motion (upper trace) and Outer Thrust Bearing Motion (lower trace) of Turboalternator Operating at 14°K and 100,000 Rpm with 13.4-Watt Load	94
63	Shaft Axial Motion (upper trace) and Outer Thrust Bearing Motion (lower trace) for Turboalternator Operating at 9.8°K and 100,000 Rpm with 142-Ohm Load	95
64	Second Liquid Helium Boil-Off Test: Shaft Axial Motion (upper trace) and Outer Thrust Bearing Motion (lower trace) with Turboalternator Operating at 16°K and 90,000 Rpm with 142-Ohm Load	95
65	Later Photograph of Second Liquid Helium Boil-Off Test: Shaft Axial Motion (upper trace) and Outer Thrust Bearing Motion (lower trace) with Turboalternator Op- erating at 16°K and 90,000 Rpm with 142-Ohm Load	96

LIST OF ILLUSTRATIONS (Cont'd)

<u>Figure</u>		<u>Page</u>
66	Liquid Helium Boil-Off Open Cycle Turboalternator Test Station	97
67	Single-Stage Big Bertha Cryogenic Turboalternator . .	98
68	Turboalternator Parts	100
69	Model for Transient Analysis	105
70	Turboalternator Startup	106
71	Input (Compressor/Intercooler) Startup	107
72	Controlled Joule-Thomson Valve and Bypass Flow Rate .	108
73	Heat Exchanger Temperatures	109
74	Heat Exchanger Response to Flow Switching	109
75	Thermal Load Performance	110
76	Thermal Load Response to Flow Switching	110
77	Turboalternator Performance	111
78	Heat Exchanger 1 Low-Temperature Performance . . .	111
79	Component Devices	117
80	Example of Interconnection	119
81	Computational Form	120
82	Flowchart of Basic Model Layout	123
83	Schematic Diagram of Heat Exchanger Model	124
84	Flowchart of Heat Exchanger Model (Logic and Calculation Sequence)	130
85	Schematic Diagram of Thermal Load Model	131
86	Flowchart of Thermal Load Model (Logic and Calculation Sequence)	137
87	Schematic Diagram of Turboalternator Model	138
88	Torque-Speed Relations for Turboalternator Model . .	138
89	Flowchart of Turboalternator Model (Logic and Calculation Sequence)	141
90	Conceptual Arrangement of Joule-Thomson Liquefier Model	142

LIST OF ILLUSTRATIONS (Cont'd)

<u>Figure</u>		<u>Page</u>
91	Flow Bypass Function Procedure	142
92	Flowchart of Joule-Thomson/Liquefier Model	145
93	Flowchart of Joule-Thomson Valve Model	147
94	Flowchart of Liquid Accumulator Model	148
95	General Form of True Function	149
96	Approximation Terminated by Linear Segment at Low-Temperature End	149
97	Basic Numbering Structure for Temperature and Enthalpy Functions	152
98	Basic Numbering Structure for Mass Flow Functions . .	153
99	Example of Model Nomenclature for Devices	155
100	Example of Model Nomenclature for M (J, I) (Mass Flow), E (J, I) (Enthalpy), L (J, I) (Torque), and W (J, I) (Speed)	156
101	Example of Model Nomenclature for T (J, I) (Temperature), Q (I) (Heat Flow), and P (I) (Power) . .	157
102	Flowchart of Heat Exchanger Subroutine	159
103	Flowchart of Thermal Load Subroutine	160
104	Flowchart of Turboalternator Subroutine	161
105	Flowchart of Joule-Thomson/Liquefier Subroutine . . .	162
106	Flowchart of Joule-Thomson Valve Subroutine	163
107	Flowchart of Liquid Accumulator Subroutine	164
108	System Configuration	165
109	Steady-State Design Point	166
110	Temperature-Enthalpy Sample Points	170
111	Heading Printout and Sample Data for ARPA1	171
112	Transient Cooldown Sample Data for ARPA2	175
113	Complete Listing of ARPA1 Program	178
114	Partial Listing of ARPA2 Program	188
115	Semiflooded Collector Test Rig	199

LIST OF ILLUSTRATIONS (Cont'd)

<u>Figure</u>		<u>Page</u>
116	Partially Assembled Test Rig Without Outer Collector .	203
117	Semifinished Outer Collectors	204
118	Model Setup for Linear Shock Test Applications	208
119	Model Setup for Torsional Shock Test Applications . . .	209
120	Shock Test Facility	210
121	Textolite Disks for Superconducting Coil Alignment and Cooling	211
122	Vibrator Arrangement for Linear Vibration Tests . . .	213
123	Vibrator Exciter	214
124	Vibrator Arrangement for Torsional Vibration Tests . .	215
125	Test Setup to Determine Yield Strength of Lead	216
126	Torsional Impact of Mass m_2 with Mass m_1	224

LIST OF TABLES

<u>Table</u>		
1	A-C Generator Refrigerator Turboalternator Design Summary	8
2	Comparison of Partial and Full Admission Turboalternators	11
3	Geometry and Design Conditions for Both Turbine Types	12
4	Turboalternator Design Summary.	13
5	Turboalternator Tilting Pad Journal Gas Bearing Design Summary	40
6	Turboalternator Spiral Groove Thrust Bearing Design Summary	61
7	Calculated Alternator Features and Performance. . . .	75
8	Turboalternator Data Obtained During Second Liquid Helium Boil-Off Test.	96
9	Inventory of Turboalternator Parts (Big Bertha Frame Size)	101

LIST OF TABLES (Cont'd)

<u>Table</u>		<u>Page</u>
10	End-of-Run Transient Data	112
11	Interconnection Specifications	120
12	First Subscript (J) Allocation Sequence.	151
13	Comparison of Power Conditioner Features or Characteristics	193
14	Specifications of Current Collector Test Rig	200
15	Results of Shock Tests to Determine Yield Strength of Lead	217
16	Mass and Polar Moment of Inertia of Superconducting Coils and their Support Structure	218

Section 1

SUMMARY

TECHNICAL PROBLEM

The specific objectives of this program are to:

- Conduct a limited but broad application survey of multiple applications in which the use of cryogenic and superconductive systems and components offer substantial advantages through improvements in the performance of propulsion, communication, detection, or weapons systems.
- Define, investigate, and experimentally evaluate the key elements of a representative cryogenic turborefrigerator subsystem suitable for providing reliable long-lived cryogenic refrigeration for a superconductive ship propulsion system.
- Provide a sound technical basis for subsequent applications of superconductive power in the area of ship propulsion. Other applications, and their requirements, will be reviewed and evaluated, in order to form a preliminary evaluation of those applications that might deserve more detailed study.
- Concentrate the experimental portions of this program on the identification of potential materials and process problem areas and the demonstration of potential resolution of such problems.

Cryogenic refrigeration is a common requirement of all superconductivity applications. For this reason, dominant emphasis was initially given to this portion of the program. Its specific application to an integrated superconductive ship propulsion system with the extreme environments involved will assure that particular attention is given to each factor affecting reliability, maintainability, safety, and availability of the cryogenic system components.

METHODOLOGY

The program presented provided that the work would be divided into three phases:

- Phase I -- Cryogenic Application Studies
- Phase II -- Systems Technology Evaluations
- Phase III -- Key Component Development

The work in each phase was divided into various major tasks and was scheduled as shown in Figure 1. Major milestones were established for the first two phases. All of the tasks necessary to fulfill the program were de-

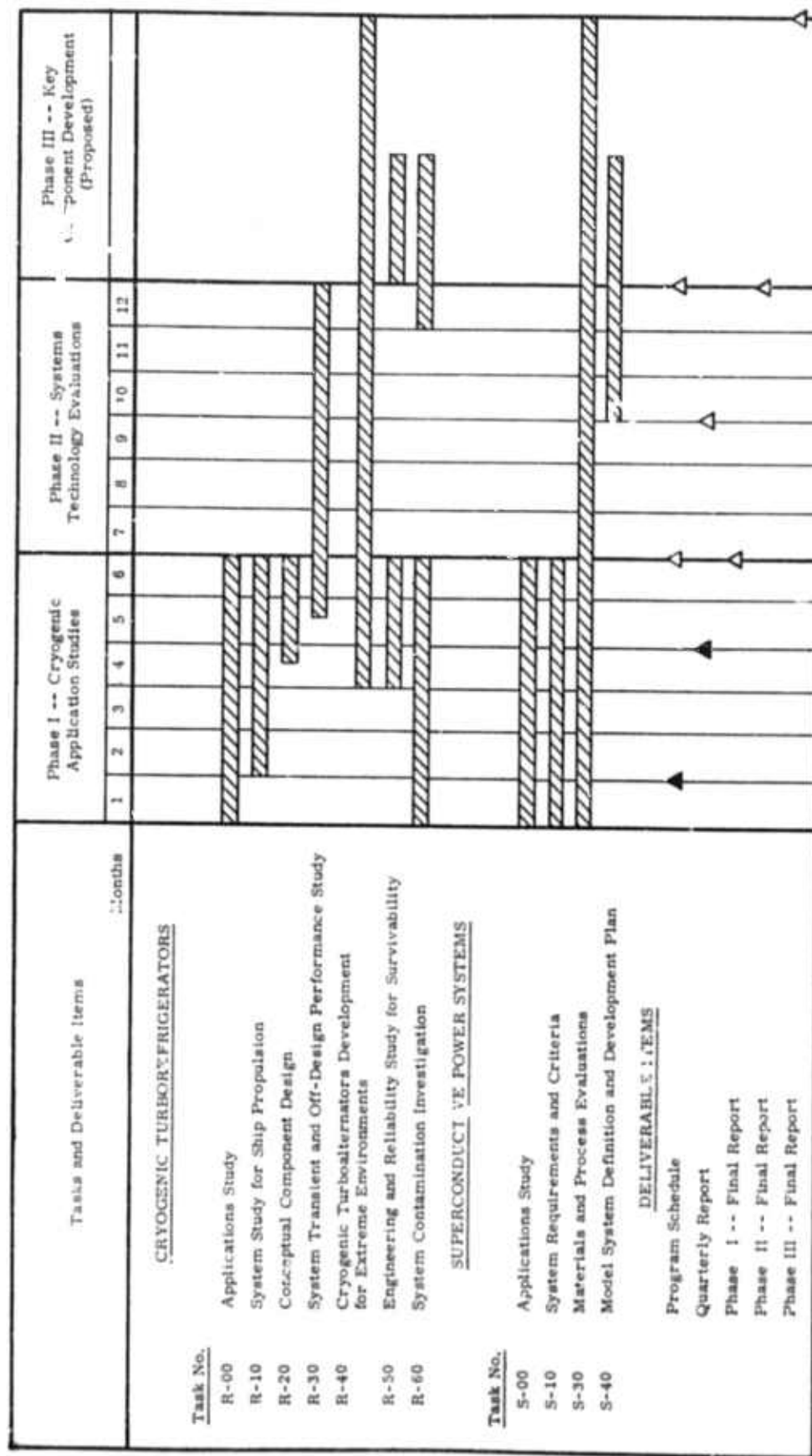


Figure 1. Program Work Schedule

scribed in the statement of work. To assure direction and clarity, these tasks were divided into two groups: cryogenic turborefrigerators and superconductive power systems.

The conduct of work under Phase II was modified by the Advanced Research Projects Agency as a result of the initiation of the Navy's program for the development of a superconducting propulsion system. These instructions terminated the work under Task R-40 and discontinued all cryogenic refrigerator work preparatory to Phase III, other than that necessary for the proper preparation of task effort suitable for the preparation of this report.

Continuing work in Phases II and III was directed to the identification of potential materials and process problems and the demonstration of a potential resolution of such problems in the area of Task S-30, "Materials and Process Evaluations."

This second semiannual technical report is therefore prepared to describe the accomplishments in the terminated areas of effort and to describe the preparation of materials and process evaluation preparations for the testing activities of Phase III. The continuing efforts fall into two areas:

- Liquid metal current collection technology
- Superconductive coil technology

Because no actual testing is to be conducted until Phase III, no effort is made here to centralize a report of these activities.

INDIVIDUAL TASKS

CRYOGENIC TURBOALTERNATORS DEVELOPMENT FOR EXTREME ENVIRONMENTS

The original intent of the contract was to construct, during Phase II, advanced turboalternators for the purpose of bearing materials development and shock and vibration testing. Before construction could be completed, all work related to the cryogenic refrigeration portion of the contract was terminated by the Government. This report therefore describes the accomplishments to the point of termination and the status of the refrigeration program at that time.

Parts for two turboalternator assemblies were started; one of these assemblies was to be used for bearing materials investigations and the other was to be used for testing under extreme environments, including shock and vibration. At the time of termination, these parts were about half completed.

In the area of bearing materials investigation, a significant result was produced. A key element of the turboalternator is the self-acting gas bearing system, and the material used in these bearings is critical. Using turbo-

alternator parts borrowed from another contract, a new bearing material (sintered titanium carbide) was experimentally evaluated for the first time at very low temperatures. Using helium gas boiled off from liquid, the turboalternator was operated to temperatures as low as 9.8°K. This is believed to be the lowest temperature at which self-acting gas bearings have operated. The significance is that the gas bearing operated well under conditions of very low gas viscosity existing at that very low temperature and that the temperature, and hence the viscosity, were lower than normal design levels. This test enhances the prospects for self-acting gas bearing turboalternators at very low temperatures.

REFRIGERATOR TRANSIENT ANALYSIS

The system transient and off-design analysis was completed. An analytical model of a Claude cycle refrigerator was developed, using modular component subroutines so that various arrangements of components could be analyzed. The cooldown of a two-expander Claude cycle machine, corresponding to a real system, was analyzed as a test of the digital computer program.

POWER CONDITIONER FOR COMPRESSOR MOTORS

A tentative conclusion from this work is that a dynamic power conditioner (a motor-generator set) has a number of advantages over a solid-state power conditioner for shipboard applications in the sizes needed.

LIQUID METAL CURRENT COLLECTOR TECHNOLOGY

The studies completed in this area during Phase I, as previously reported, led to the conclusion that only gallium (or gallium-indium) of the many liquid metals considered offered any promise of providing a better solution to the problems of liquid metal current collection than that obtainable using NaK as the liquid metal.

The advantages of gallium over NaK are confined primarily to the lower speeds of operation typical of motors where the higher conductivity and density result in lower overall machine losses as well as assisting in liquid metal retention in the conducting areas of the collector. Because gallium has no significant reaction with water and is nontoxic, it offers increased safety and maintenance ease, compared to NaK. However, it should be recognized that adequate maintenance of an oxygen (and/or moisture vapor) free cover gas over either liquid metal is equally important to the long life and trouble-free performance that are expected from these collectors.

The experimental demonstration of gallium performance in the selected collector configurations, when subjected to the high-intensity magnetic fields representative of operation in superconductive motors and generators, is the primary objective of this portion of the program. During Phase II, the prin-

ciple effort has been directed toward the design and fabrication of a collector configuration employing materials and processes that assure long-life compatibility with gallium (or gallium indium) and practical applicability to future use in superconductive propulsion systems.

The equipment has been completed and initial testing is ready to begin in Phase III. Upon completion of successful testing, these materials and processes will be more fully described.

SUPERCONDUCTIVE COIL TECHNOLOGY

Many areas of superconductive coil technology have been and are being worked on by other investigators in this country and in other countries. However, the availability of a satisfactorily stabilized superconductor (finely stranded niobium-titanium) and the availability of proven coil fabrication and potting methods (e.g., the Culham Laboratories technology) provide a sufficient and sound basis for proceeding with the design and development of superconductive machinery. It remains necessary to experimentally verify that these technological developments that have been proven satisfactory for coils in a stationary environment will also perform reliably in the dynamic environment of a shipboard propulsion system.

To assure materials and processes compatibility and to fabricate equipment and prepare testing facilities for this experimental verification of coil performance in a dynamic environment have been the principal objective of these Phase II activities.

Equipment has been completed and is ready for Phase II testing.

Section 2

CRYOGENIC TURBOALTERNATORS DEVELOPMENT FOR EXTREME ENVIRONMENTS

DESIGN FOR PERFORMANCE

A study was conducted to determine the most expedient approach to evaluate the performance of the Big Bertha turboalternator as applied to the subject cryogenic refrigeration systems. It was shown in the first semiannual technical report that there are operating areas where the performance of partial admission radial impulse turbines is probably the best choice. In addition, it was also shown that for one case the full admission radial reaction turbine will probably provide the most efficient turbine and hence improve the overall refrigeration cycle efficiency.

To illustrate this possible improved performance, a separate investigation was conducted. The effect of turboalternator performance on the type of refrigerator systems studies that were conducted during Phase I have been examined. The original base for turbine designs for the a-c generator refrigerator application is shown in Table 1.

For the a-c generator application of a cryogenic refrigerator system, additional cycle studies were conducted, with a variety of turboalternator efficiencies arbitrarily imposed to show the potential for improved turboalternator efficiencies. This work was only a demonstration of the potential effect on alternator efficiency at the various temperature stations of the cycle considered.

Results are shown in Figure 2, where the turboalternator efficiency at each of the three stations was arbitrarily increased by the amount shown. These results are based on influencing each turbine separately, leaving the other two turbines at the original cycle design point efficiency.

Then the results of improving all the turboalternator efficiencies simultaneously were examined (Figure 3). This study involved a refrigerator with three turbines. For systems with only two turbines, the improvement in turboalternator efficiency on reduced input power is even more pronounced (Ref. 1).

The comparison of two low-temperature, 12°K turboalternator designs is shown in Table 2. The full admission radial reaction shows a substantial efficiency advantage of more than 20 percent.

The turboalternator performance work that would have been conducted under this contract included the operation of a turboalternator for performance evaluation of the Big Bertha frame size, as was originally established in the proposed approach for this program.

Table 1
A-C GENERATOR REFRIGERATOR
TURBOALTERNATOR DESIGN SUMMARY*

Design Parameters	Model and Inlet Temperature		
	Big Bertha (12°K)	Big Bertha (35°K)	Grizzly Giant (120°K)
Total refrigeration power outputs (watts)	15.57	191.4	681.5
Design speed (rpm)	72,960	72,820	64,640
Maximum speed (rpm)	200,000	200,000	200,000
Refrigerator input power (kilowatts)			
<u>Principal Dimensions</u>			
Journal-bearing span (inches)	3.82	3.92	7.64
Journal and magnet diameter (inches)	0.5	0.5	1.0
Thrust-bearing outside diameter (inches)	0.84	0.84	1.68
Magnet length (inches)	0.705	0.705	1.410
<u>Performance Factors</u>			
Inlet temperature (°R)	21.6	63.0	216.0
Inlet temperature (°K)	12	35	120
Inlet pressure (psia)	41.35	41.77	42.19
Outlet pressure (psia)	17.08	16.83	16.58
Pressure ratio	2.422	2.482	2.545
Mass flow (pounds per hour)	67.14	53.44	57.92
Turbine run number	630601006	630602001	630603005
Wheel diameter (inches)	0.75	1.25	2.50
Electromagnetic efficiency (fraction)	0.998	0.985	0.952
Number of blades	37	50	77
Cycle required overall efficiency (fraction)	0.4725	0.5086	0.4674
Overall efficiency (fraction)	0.4809	0.5127	0.4804
Specific speed	23.57	15.95	10.79
Total friction losses (watts)	4.89	9.03	93.66
<u>Design Geometry</u>			
Admission (fraction)	0.3165	0.2216	0.1567
Cutter diameter (inches)	0.0278	0.0293	0.0470
Blade height (inches)	0.0935	0.1085	0.1534
Blade-height-to-diameter ratio	3.36	3.707	3.264
Blade angle (degrees)	60	60	60
Nozzle angle (degrees)	80	80	80

*Turbine type: partial-admission, radial impulse
 Load alternator type: permanent magnet
 Journal bearing type: self-acting tilting pad
 Thrust bearing type: inward pumping, spiral groove

CR-2314

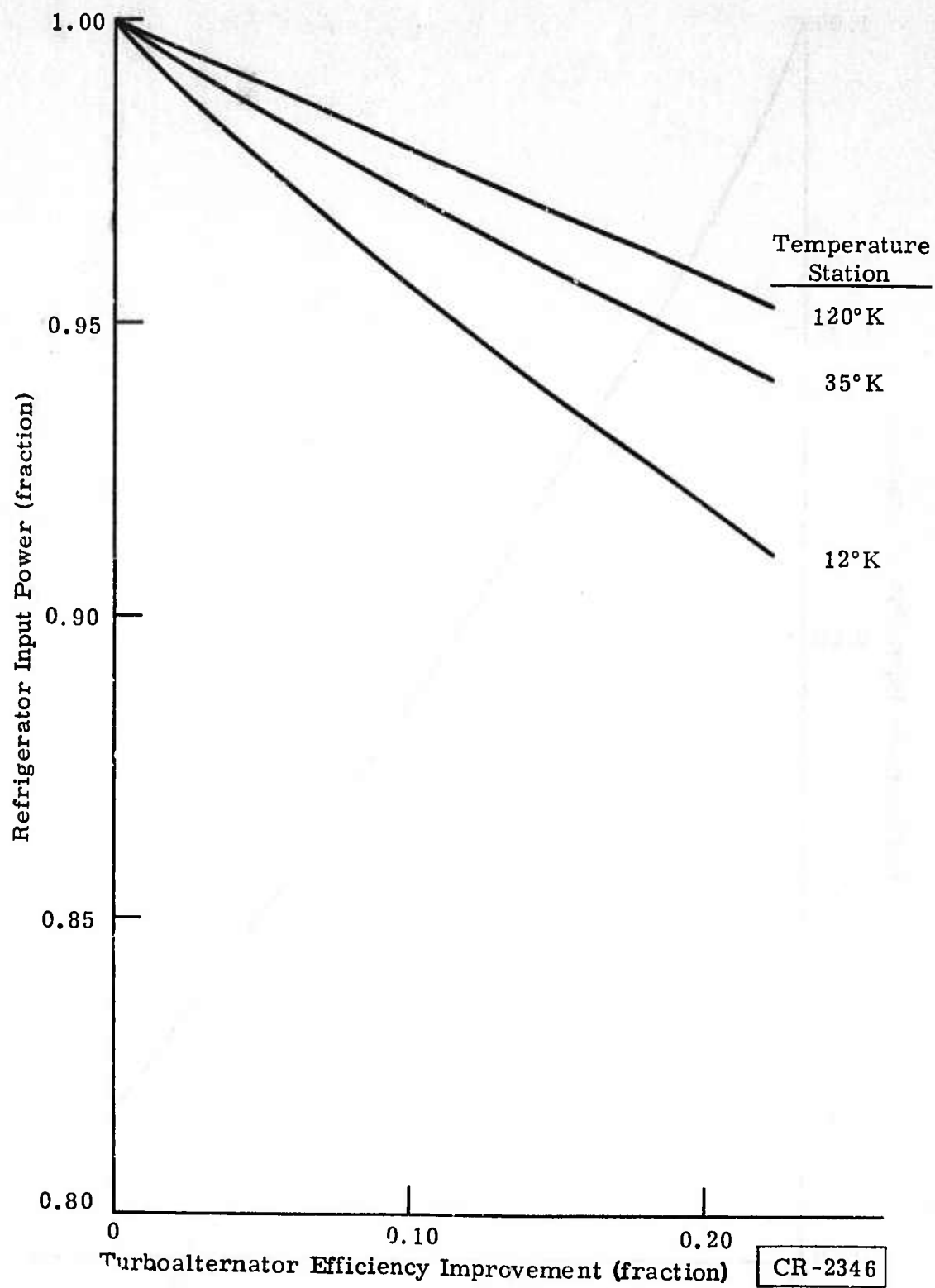


Figure 2. Effect of Turboalternator Efficiency Improvement on Total Refrigerator Input Power, with Each Turboalternator's Efficiency Changed Separately

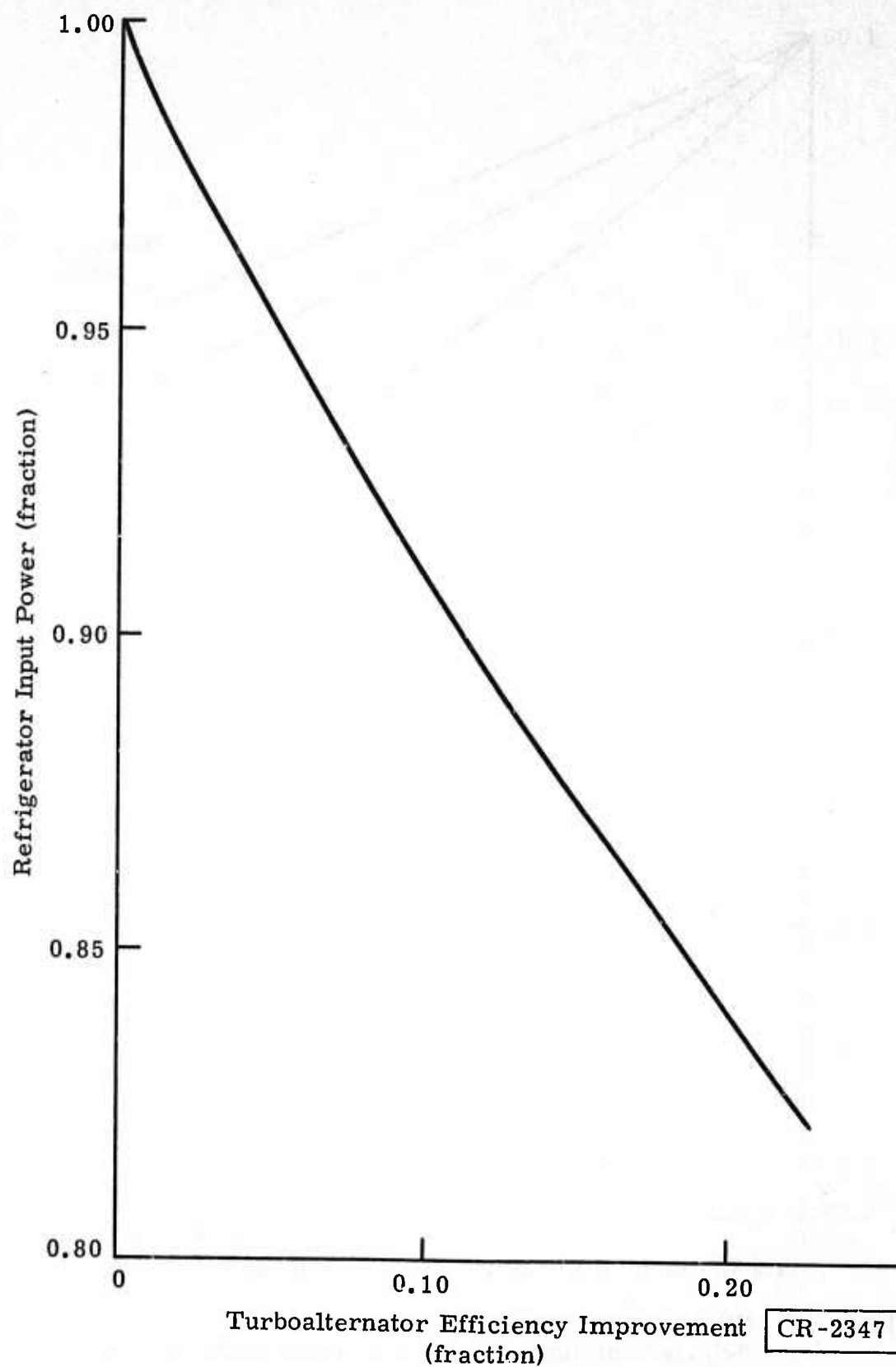


Figure 3. Effect of Simultaneous Turboalternator Efficiency Improvement in All Three Stages on Total Refrigerator Input Power

Table 2

COMPARISON OF PARTIAL AND FULL ADMISSION TURBOALTERNATORS*

Design Parameters	Turbine Type	
	Partial Admission, Radial Impulse (12°K)	Full Admission, Radial Reaction (12°K)
Total refrigeration power outputs (watts)	75.59	110.6
Design speed (rpm)	72,960	96,900
Maximum speed (rpm)	200,000	200,000
<u>Principal Dimensions</u>		
Journal bearing span (inches)	3.82	3.82
Journal and magnet diameter (inches)	0.5	0.5
Thrust bearing outside diameter (inches)	0.84	0.84
Magnet length (inches)	0.705	0.705
<u>Performance Factors</u>		
Inlet temperature (°R)	21.6	21.6
Inlet temperature (°K)	12	12
Inlet pressure (psia)	41.35	41.35
Outlet pressure (psia)	17.08	17.08
Pressure ratio	2.422	2.422
Mass flow (pounds per hour)	67.14	67.14
Turbine run number	630601006	630601007
Wheel diameter (inches)	0.75	0.80
Electromagnetic efficiency (fraction)	0.998	0.998
Number of blades	37	44
Overall efficiency (fraction)	0.481	0.704
Specific speed	23.57	30.50
Total friction losses (watts)	4.89	9.90
<u>Design Geometry</u>		
Admission (fraction)	0.3165	1.00
Cutter diameter (inches)	0.0278	NA
Blade height (inches)	0.0935	0.0222
Blade-height-to-diameter ratio	3.36	NA
Blade angle (degrees)	60	0
Nozzle angle (degrees)	80.0	81.9

*Model: Big Bertha

Load alternator type: permanent magnet

Journal bearing type: self-acting tilting pads

Thrust bearing type: inward pumping, spiral groove

CR-2313

The turbine performance would have been evaluated at the 80°K level, with a single heat exchanger in a cryogenic section. Pressure levels and flow rates available from the General Electric Research and Development Center compressor should have been considered in the design of such a turboalternator. The maximum flow available to the turboalternator is 32.7 grams per second, with an inlet pressure of 50.3 psia and an exit pressure of 18.7 psia for an overall pressure ratio of 2.7. These values are at the cryosection closed cycle test station valves leading to the turbine operating in the cryosection test station.

The turbine aerodynamic design would have been made for an operating condition in which the best of the two alternate versions could be established at a particular set of operating conditions. From the Phase I final report, it was shown that a probable cross-over point of efficiency of the partial admission turbine to the full admission turbine is at a specific speed of approximately 20.0. It is therefore desirable to design the different types of turbines at this same specific speed.

The principal geometry and design conditions chosen for both turbine types are shown in Table 3.

Table 3
GEOMETRY AND DESIGN CONDITIONS FOR BOTH TURBINE TYPES

Characteristic	Parameter
<u>Principal Dimensions</u>	
Journal bearing span	3.82 inches
Journal and magnet diameter	0.50 inches
Thrust bearing outside diameter	0.84 inches
Magnet length	0.705 inches
<u>Performance Factors</u>	
Inlet temperature	80.0°K
Inlet pressure	48.7 psia
Outlet pressure	19.5 psia
Pressure ratio	2.5
Specific speed	20.0

CR-2453

The outlet pressure from the turbine was established at slightly above the low-pressure return of the facility compressor, to allow for cryogenic exchanger, filter, and plumbing pressure losses. Then a pressure ratio of 2.5 was selected as a typical refrigeration cycle pressure ratio. This ratio

resulted in an inlet pressure of 48.7 psia, which can be easily accommodated by the facility compressor.

A series of full admission turbine computer design runs were carried out, and the results are shown as the first column of Table 4, resulting in a flow of 5.0 grams per second and a reasonably high power of 397.2 watts, obtaining a specific speed of 20.

The design speed of 150,000 rpm shown is reasonable. The maximum speed of 200,000 rpm was tentatively selected for fast cooldown but is subject to adjustment with the detailed gas bearing analysis and design.

The 56 blades represent a large number. This quantity would have been investigated further, and a trade-off would have been made, because a com-

Table 4
TURBOALTERNATOR DESIGN SUMMARY

Design Parameters	Full Admission, Radial reaction	Turbine Type				
		Partial Admission, Radial Impulse				
		Run 830601014	Run 630601017	Run 630601019	Run 630601021	Run 630601022
Total refrigeration power outputs (watts)	397.2	301.5	299.3	301.5	301.0	301.3
Design speed (rpm)	150,000	141,300	158,300	133,900	127,100	141,300
Maximum speed (rpm)	200,000	200,000	200,000	200,000	200,000	200,000
<u>Principal Dimensions</u>						
Journal bearing span (inches)	3.82	3.82	3.82	3.82	3.82	3.82
Journal and magnet diameter (inches)	0.5	0.5	0.5	0.5	0.5	0.5
Thrust bearing outside diameter (inches)	0.84	0.84	0.84	0.84	0.84	0.84
Magnet length (inches)	--	0.5489	0.4325	0.6114	0.6768	0.705
<u>Performance Factors</u>						
Inlet temperature (°R)	144	144	144	144	144	144
Inlet temperature (°K)	80	80	80	80	80	80
Inlet pressure (psia)	48.7	48.69	48.69	48.69	48.69	48.69
Outlet pressure (psia)	19.5	19.40	19.49	19.49	19.49	19.49
Pressure ratio	2.5	2.498	2.498	2.498	2.498	2.498
Mass flow (grams per second)	5	5	5	5	5	5
Wheel diameter (inches)	1.693	1.000	0.900	1.050	1.100	1.000
Electromagnetic efficiency (fraction)	0.980	0.975	0.975	0.975	0.975	0.9806
Number of blades	56.44	45.0	45.0	45.0	45.0	43.0
Overall efficiency (fraction)	0.6237	0.4734	0.4700	0.4734	0.4727	0.4732
Specific speed	20.97	15.97	22.38	18.94	18.00	19.97
Total friction losses (watts)	31.22	29.82	34.91	27.94	26.38	27.74
<u>Design Geometry</u>						
Admission (fraction)	1.00	0.2711	--	--	0.2461	0.2708
Cutter diameter (inches)	NA	0.03091	--	--	0.0344	0.03253
Blade height (inches)	0.0282	0.1069	0.1088	0.1069	0.1070	0.1070
Blade-height-to-diameter ratio	NA	3.458	3.898	3.275	3.111	3.289
Blade angle (degrees)	0	60	60	80	80	80
Nozzle angle (degrees)	83.85	80.00	80.00	80.00	80.00	80.00

CR-2348

promise was expected. The compromise would have been between: (1) decreased efficiency with increased slip and fewer blades and (2) the practical aspects of milling this turbine wheel. Other entries for the full admission turbine in Table 4 appear reasonable but are subject to adjustments during final design. The complete computer printout for this design case (630601014) is shown in Figure 4.

DESIGN CASE		630601014
GAS IS HELIUM		
OVERALL PERFORMANCE		
ELECTRICAL POWER OUTPUT (WATTS)	0.3972E+03	PTA
SPEED (RPM)	0.1500E+06	N
OVERALL EFFICIENCY (FRACTION)	0.6237E+00	ETATA
TEMPERATURES, PRESSURES, FLOW		
INLET TEMPERATURE (R)	0.1440E+03	TO
INLET TEMPERATURE (K)	0.8000E+02	TA
OVERALL TEMPERATURE DROP (R)	0.2742E+02	TEDR
OVERALL TEMPERATURE DROP (K)	0.1527E+02	TEDK
OUTLET TEMPERATURE EXIT (R)	0.1165E+03	T4P
OUTLET TEMPERATURE EXIT (K)	0.6473E+02	T4K
INLET PRESSURE (PSIA)	0.4869E+02	PO
INLET PRESSURE (ATM)	0.3313E+01	PA
NOZZLE EXIT PRESSURE (PSIA)	0.3164E+02	P2
OUTLET PRESSURE (PSIA)	0.1942E+02	P3
OUTLET PRESSURE (ATM)	0.1326E+01	PR
PRESSURE RATIO	0.2493E+01	PR
FLOW (LB/SEC)	0.1101E-01	W
FLOW (LB/HR)	0.3965E+02	WR
FLOW (G/SEC)	0.5000E+01	WA
PRIMARY DIMENSIONS		
WHEEL TIP DIAMETER (IN)	0.1693E+01	D
TIP BLADE HEIGHT (IN)	0.2820E-01	BH
EXDUCER TIP DIA. (IN)	0.4155E+00	ED
EXDUCER HUB DIA. (IN)	0.1662E+00	EHD
NUMBER OF BLADES	0.5644E+02	Z
THRUST BEARING		
LOAD(LBS.),	0.3549E+00	RTL
OUTSIDE DIAMETER(IN),	0.8400E+00	DT
DIAMETER RATIO	0.6543E+00	DR
CLEAR. TO DIA. RATIO	0.7000E-03	RDCR
LOAD COEFFICIENT	0.5752E-01	RTC
BEARING NUMBER	0.7543E+00	RTN
CLEARANCE, LOADSIDE(IN)	0.5880E-03	RLC
FRICTION POWER(WATTS)	0.1502E+01	BTPL

CR-2364-1

Figure 4. Full Admission Radial Reaction Design Point Computer Printout

JOURNAL BEARING		
LOAD(LBS.)	0.1774E+00	RJL
LOAD COEFFICIENT	0.7284E-01	RJC
BEARING NUMBER	0.1822E+01	BCN
CLEAR. TO DIA. RATIO	0.9081E-03	RCDR
MACHINED CLEARANCE (IN)	0.4541E-03	BMC
PIVOT FILM THICK(IN)	0.3006E-03	RJMF
FRICTION POWER(WATTS)	0.4577E+01	RJPL
GAS BEARINGS		
ROTATING ASSEMBLY WEIGHT (LBS)	0.3549E+00	PAW
ACCELERATION OF GRAVITY ("G")	0.1000E+01	ACG
TOT. BEARING FRICTION (WATTS)	0.1162E+02	PLR
PERFORMANCE TERMS		
ISENTROPIC HEAD (FT)	0.4261E+05	HS
PRODUCER LEAVING LOSS (FT)	0.7442E+03	HE
LEAVING LOSS FRACTION, ISEP. HEAD	0.1747E-01	HLF
ALTERNATOR GAP FLUX (KGAUSS)	0.1526E+02	AG
ALTERNATOR CORE LOSS COEFF.	0.1523E+01	KA
ALTERNATOR COPPER LOSS COEFF.	0.6595E+01	KR
NOZZLE EXIT GAS TEMP.(°)	0.1254E+03	T2
PRODUCER EXIT GAS TEMP.(°)	0.1144E+03	T3
EXHAUST DISC VOL. FLOW (CPS)	0.1721E+00	Q3
PERFORMANCE FACTORS		
TIP SPEED TO SPOUTING VEL. RATIO	0.6690E+00	SVR
TURB. PRESSURE REACT. RATIO	0.4163E+00	PRR
SPECIFIC SPEED	0.2097E+02	NS
SPECIFIC DIAMETER	0.4889E+01	DS
FLOW FACTOR	0.4798E+01	ASTP
WHEEL EFFICIENCY (FRACTION)	0.6723E+00	ETAW
HYDRAULIC EFFICIENCY (FRACTION)	0.6903E+00	ETA
ELECTROMAGNET EFF. (FRACTION)	0.9750E+00	ETEM
ISENTROPIC POWER (WATTS)	0.5363E+03	PTAS
WHEEL POWER OUTPUT (WATTS)	0.4284E+03	PTRW
SHAFT POWER OUTPUT (WATTS)	0.4076E+03	PTR
PARASITIC LOSSES (WATTS)		
ALTERNATOR TOTAL E-M	0.1045E+02	PLEL
JOURNAL DIA SHAFT FRICTION	0.8560E+01	PLSF
ALTERNATOR GAP FRICTION	0.5795E+00	PLGF
BEARING FRICTION	0.1162E+02	PLR
SUM ALL PARASITIC LOSSES	0.3122E+02	PLTP

CR-2364-2

**Figure 4. Full Admission Radial Reaction Design Point Computer Printout
(Continued)**

GEOMETRY

WHEEL TIP CLEARANCE (IN)	0.3386E-02	S
EXDUCER TIP CLEARANCE (IN)	0.1039E-02	SE
NOZZLE ANGLE (DEGREES)	0.8365E+02	ALP2
BLADE ANGLE (DEGREES)	0.	BP2
BLADE INCIDENCE ANGLE (DEG.)	-0.1826E+02	I
EXDUCER TIP BLADE ANGLE (DEG)	0.5116E+02	B3
TOTAL MACHINE SHAFT LENGTH (IN)	0.5050E+01	SL
JOURNAL SHAFT DIAMETER (IN)	0.5000E+00	UJ
JOURNAL FREE SHAFT LENGTH (IN)	0.3236E+01	US4
ALTERNATOR DIAMETER (IN)	0.5000E+00	DO
ALTERNATOR MAGNET LENGTH (IN)	0.6416E+00	DI
ALTERNATOR PERIF. SPEED(F.P.S.)	0.3272E+03	APS
ALTERNATOR RADIAL GAP (IN)	0.2875E-01	G
STATOR OVERHANG (IN)	0.8625E-01	OA
STATOR LAMINATION DIA. (IN)	0.1845E+01	DL
EMPIR. ALTERNATOR DIA.(IN)	0.4308E+00	DO-

VELOCITIES

SPOUTING VELOCITY (FPS)	0.1657E+04	CO
WHEEL TIP SPEED(FPS)	0.1103E+04	U
NOZZLE DISCHARGE VELOCITY (FPS)	0.1076E+04	C2
BLADE INLET RELATIVE VELOCITY(FPS)	0.1253E+03	W2
BLADE INLET RADIAL VELOCITY (FPS)	0.1190E+03	V2
BLADE INLET RELATIVE MACH NUMBER	0.7785E-01	W2
SLIP FACTOR	0.1074E+00	SLIP
EXDUCER AXIAL VELOCITY (FPS)	0.2130E+03	V3
EXDUCER TIP REL. VELOCITY (FPS)	0.3491E+03	W3
EXDUCER TIP REL. MACH NUMBER	0.2271E+00	W3

REYNOLDS NUMBERS

TURBINE DISC REYNOLDS NO.	0.1013E+07	WDO
JOURNAL DIAMETER REYNOLDS NO.	0.3560E+05	WDEJ
ALTERNATOR GAP REYNOLDS NO.	0.4027E+05	WDO

DRAG COEFFICIENTS

WHEEL REYNOLDS NUMBER CORRECTION	0.9720E+00	WDC
JOURNAL DIAMETER DRAG COEFF.	0.0197E-02	CDS
ALTERNATOR GAP MOMENT COEFF.	0.1764E-02	CDS

100 80.0 3.313 1.326 5.0
 200 .975 .48
 300 0.0 5.05 .500 .500
 400 .84 1.0 .0015 .0007
 500 150000. 200000. 300.
 600 630601014 2

CR-2364-3

Figure 4. Full Admission Radial Reaction Design Point Computer Printout
(Continued)

A series of partial admission turbine design runs were then made, to result in a counterpart design at the same flow rate of 5 grams per second, the same pressure, and an 80°K inlet temperature. Results of these runs are shown in the remaining columns of Table 4.

The design in the right-hand column would have been the selected partial admission design, subject to final detail design considerations. The complete computer printout for this design case (630601023) is shown in Figure 5.

DESIGN CASE		630601023
GAS IS HELIUM		
REFRIGERATION PWR OUT (WATTS)	0.3013E+03	PTHL
ELECTRICAL POWER OUTPUT (WATTS)	0.3013E+03	PTA
SPEED (RPM)	0.1413E+06	N
OVERALL EFFICIENCY (FRACTION)	0.4732E+00	ETATA
TEMPERATURES, PRESSURES, FLOW		
INLET TEMPERATURE (R)	0.1440E+03	TO
INLET TEMPERATURE (K)	0.8000E+02	TA
OVERALL TEMPERATURE DROP (R)	0.2086E+02	TEDR
OVERALL TEMPERATURE DROP (K)	0.1159E+02	TEOK
OUTLET TEMPERATURE EXIT (R)	0.1231E+03	T4R
OUTLET TEMPERATURE EXIT (K)	0.6841E+02	T4K
INLET PRESSURE (PSIA)	0.4869E+02	PO
INLET PRESSURE (ATM)	0.3313E+01	PA
OUTLET PRESSURE (PSIA)	0.1949E+02	P3
OUTLET PRESSURE (ATM)	0.1326E+01	PR
PRESSURE RATIO	0.2498E+01	PR
FLOW (LB/SEC)	0.1101E-01	W
FLOW (LB/HR)	0.3965E+02	WB
FLOW (G/SEC)	0.5000E+01	WA
PRIMARY DIMENSIONS		
WHEEL TIP DIAMETER (IN)	0.1000E+01	D
NUMBER OF BLADES	0.4300E+02	Z
BLADE HEIGHT (IN)	0.1070E+00	BH
BLADE HI. CUT. DIA. RATIO	0.3289E+01	BHCD
THRUST BEARING		
LOAD (LBS.),	0.3507E+00	RTL
OUTSIDE DIAMETER (IN),	0.8400E+00	DT
DIAMETER RATIO	0.6548E+00	DR
CLEAR. TO DIA. RATIO	0.7000E-03	BDCK
LOAD COEFFICIENT	0.5685E-01	RTC
BEARING NUMBER	0.7383E+00	RTN
CLEARANCE, LOADSIDE (IN)	0.5880E-03	ELC
FRICTION POWER (WATTS)	0.1384E+01	BTPL

CR-2363-1

Figure 5. Partial Admission Radial Impulse Design Point Computer Printout

JOURNAL BEARING		
LOAD(LBS.)	0.1754E+00	BJL
LOAD COEFFICIENT	0.7199E-01	BJC
BEARING NUMBER	0.1780E+01	BCN
CLEAR. TO DIA. RATIO	0.8917E-03	BCD
MACHINED CLEARANCE (IN)	0.4459E-03	BMC
PIV. FILM THICK(IN)	0.3006E-03	BJMF
FRICTION POWER(WATTS)	0.4080E+01	BJPL
TWO STAGE PERFORMANCE		
OTHER STAGE IN TEMP (K)	0.	TOA
TOTAL HEAT LEAK (WATTS)	0.	PHL
EXIT TEMPERATURE (K)	0.6841E+02	T4KH
SHAFT HEAT LEAK (WATTS)	0.	PHLS
HOUSG HEAT LEAK (WATTS)	0.	PHLH
GAS BEARINGS		
ROTATING ASSEMBLY WEIGHT (LBS)	0.3507E+00	RAW
ACCELERATION OF GRAVITY ("G")	0.1000E+01	ACG
TOT. BEARING FRICTION (WATTS)	0.1044E+02	PLB
PERFORMANCE TERMS		
ISENTROPIC HEAD (FT)	0.4261E+05	HS
HYDRAULIC EFF., FIRST TERM	0.6862E+00	ETAH1
HYDRAULIC EFF., SECOND TERM	0.1223E+00	ETAH2
HYDRAULIC EFF., THIRD TERM	0.5975E-04	ETAH3
TIP CLEARANCE EFF. CORRECTION	0.9847E+00	LC
TRAIL EDGE EFF. CORRECTION	0.9430E+00	LE
BLADE RE. NO. EFF. CORR.	0.9869E+00	LR
ALTERNATOR GAP FLUX (KGAUSS)		
ALTERNATOR CORE LOSS COEFF.	0.1407E+02	AR
ALTERNATOR COPPER LOSS COEFF.	0.1528E+01	KA
	0.6596E+01	KR
TEMPERATURE WHEEL EXIT GAS (R)		
TURBINE BLADE DISC VOL. FLOW (CFS)	0.1212E+03	T3
	0.1835E+00	Q3
PERFORMANCE FACTORS		
TIP SPEED TO SPOUTING VEL.RATIO	0.3725E+00	SVR
NOZZLE COEFFICIENT	0.9000E+00	PSIN
SPECIFIC SPEED	0.1997E+02	NS
SPECIFIC DIAMETER	0.2795E+01	DS
FLOW FACTOR	0.4798E+01	WSTP
WHEEL EFFICIENCY (FRACTION)		
HYDRAULIC EFFICIENCY (FRACTION)	0.5168E+00	ETAW
ELECTROMAGNET EFF. (FRACTION)	0.5639E+00	ETAH
	0.9806E+00	ETEM
ISENTROPIC POWER (WATTS)		
WHEEL POWER OUTPUT (WATTS)	0.6368E+03	PTAS
SHAFT POWER OUTPUT (WATTS)	0.3291E+03	PTRW
	0.3074E+03	PTR

CR-2363-2

Figure 5. Partial Admission Radial Impulse Design Point Computer Printout (Continued)

PARASITIC LOSSES (WATTS)		
ALTERNATOR TOTAL EM	0.6082E+01	PLEL
TURBINE DISC FRICTION	0.3809E+01	PLDF
JOURNAL DIAM SHAFT FRICTION	0.6884E+01	PLSF
ALTERNATOR GAP FRICTION	0.5243E+00	PLGF
BEARING FRICTION	0.1044E+02	PLB
SUM ALL PARASITIC LOSSES	0.2774E+02	PLTP
GEOMETRY		
WHEEL TIP CLEARANCE (IN)	0.2000E-02	S
BLADE PASSAGE CUTTER DIAMETER (IN)	0.3253E-01	R
BLADE TRAILING EDGE THICKNESS (IN)	0.4000E-02	E
ADMISSION ARC (FRACTION)	0.2708E+00	ARC
ADMISSION ARC (DEGREES)	0.9748E+02	ARCD
NOZZLE ANGLE (DEGREES)	0.8000E+02	ALP2
BLADE ANGLE (DEGREES)	0.6000E+02	BP2
BLADE INCIDENCE ANGLE (DEG)	0.1308E+02	I
BLADE CHORD (IN)	0.1123E+00	C
WHEEL INSIDE DIAMETER (IN)	0.7753E+00	D3
BLADE PRESSURE SURFACE RADIUS (IN)	0.6485E-01	Y
BLADE SUCTION SURFACE RADIUS (IN)	0.3232E-01	X
TOTAL MACHINE SHAFT LENGTH (IN)		
JOURNAL SHAFT DIAMETER (IN)	0.5000E+00	DJ
JOURNAL FREE SHAFT LENGTH (IN)	0.3175E+01	DSH
ALTERNATOR DIAMETER (IN)	0.5000E+00	DG
ALTERNATOR MAGNET LENGTH (IN)	0.7028E+00	DM
ALTERNATOR PERIF. SPEED(F.P.S.)	0.3085E+03	APS
ALTERNATOR RADIAL GAP (IN)	0.2875E-01	G
STATOR OVERHANG (IN)	0.8625E-01	DA
STATOR LAMINATION DIA. (IN)	0.1845E+01	DL
EMPIR. ALTERNATOR DIA.(IN)	0.4042E+00	DGE
WHEEL BACK SIDE OPTIMUM GAP (IN)	0.1544E-01	GD
VELOCITIES		
SPOUTING VELOCITY (FPS)	0.1656E+04	C0
WHEEL TIP SPEED(FPS)	0.6170E+03	U
NOZZLE DISCHARGE VELOCITY (FPS)	0.1491E+04	C2
BLADE INLET RELATIVE VELOCITY(FPS)	0.2706E+03	W2
BLADE INLET RADIAL VELOCITY (FPS)	0.2589E+03	V2
BLADE INLET RELATIVE MACH NUMBER	0.1809E+00	MW2
REYNOLDS NUMBERS		
BLADE PASSAGE REYNOLDS NO.	0.1310E+05	NREB
TURBINE DISC REYNOLDS NO.	0.2930E+06	NRED
JOURNAL DIAMETER REYNOLDS NO.	0.7325E+05	NREJ
ALTERNATOR GAP REYNOLDS NO.	0.3447E+05	NREG

CR-2363-J

Figure 5. Partial Admission Radial Impulse Design Point Computer Printout (Continued)

DRAG COEFFICIENTS

TURBINE DISC DRAG COEFF.	0.7402E-02	CMD
JOURNAL DIAMETER DRAG COEFF.	0.5404E-02	CDS
ALTERNATOR GAP MOMENT COEFF.	0.1848E-02	CDG

100	80.0	3.313	1.326	5.0
200	.9806	.50		
300	1.00	5.05	.500	.500
400	.84	1.0	.0015	.0007
500	0.	200000.	300.	
600	630601023	2		
700	.002	43.	.004	
800	80.	60.	.9	
900	1.	0.	1.	

CR-2363-4

Figure 5. Partial Admission Radial Impulse Design Point Computer Printout (Continued)

ALTERNATOR ELECTROMAGNETIC DESIGN

Based on the design requirements shown in Table 4 for the partial admission turboalternator, the electromagnetic design was established. This design was based on the performance requirements expected from the turboalternator design point performance computer run, in conjunction with the existing drawings and completed turboalternator stator that have been completed except for winding of the stator.

CRYOSECTION DESIGN

The complete cryosection designed around the radial reaction and partial admission impulse turboalternator designs are shown in Table 4. The complete cryosection for this requirement would have been sized for the performance design conditions of 5 grams per second at a pressure ratio of 2.5, with the turbine inlet temperature of 80°K.

Included in the cryosection is a quick cooldown coil, a charcoal adsorber, and a cryogenic heat exchanger. The cryogenic heat exchangers considered included the plastic laminate version and also the spiral finned tube version. The former has a low pressure drop, whereas the latter has a higher pressure drop.

HEAT EXCHANGER DESIGN

Following are the details of the heat exchanger design for the Advanced Research Projects Agency:

Turbine inlet temperature = 80°K
Turbine inlet pressure = 48.7 psia
Turbine outlet pressure = 19.5 psia
Turbine η_{overall} turbine = 0.47

$$\begin{aligned}\text{Isentropic temperature ratio} &= \frac{T_1}{T_2} = \frac{P_1}{P_2}^{\frac{\sigma-1}{\sigma}} \\ &= (2.5)^{\frac{1.67-1}{1.67}} = (2.5)^{0.4012} \\ &= 1.44\end{aligned}$$

$$T_{\text{out isentropic}} = \frac{80}{1.44} = 55.5$$

$$80 - 55.5 = 24.5$$

$$\Delta T_{\text{actual}} = 0.47 \times 24.5 = 11.5$$

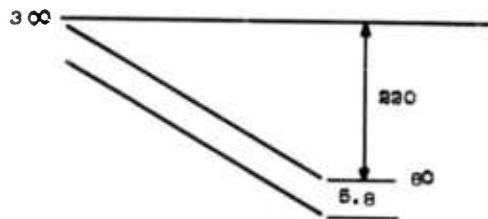
$$T_{\text{out actual}} = 80 - 11.5 = 68.5^\circ\text{K}$$

$$\text{Flow} = 0.005 \text{ kilograms per second}$$

$$\text{Say } \Delta T_{\text{load}} = \frac{1}{2} \times 11.5 = 5.8^\circ\text{K}$$

$$\begin{aligned}\dot{Q}_{\text{load}} &= \dot{m} C_p \Delta T = 0.005 \times 5200 \times 5.8 \\ &= 150 \text{ watts}\end{aligned}$$

$$\Delta T \text{ available to heat exchanger} = 5.8^\circ\text{K}$$



$$\begin{aligned}\epsilon &= 1 - \frac{\Delta T_{\text{end}}}{\Delta T_{\text{max}}} \\ &= 1 - \frac{5.8}{225.8} = 1 - 0.026 \\ \epsilon &= 0.974\end{aligned}$$

The design cycle for 98 percent is:

$$\begin{aligned}0.98 &= 1 - \frac{\Delta T_{\text{end}}}{220 + \Delta T_{\text{end}}} \\ 215.6 + 0.98 \Delta T_{\text{end}} - 220 - \Delta T_{\text{end}} &= - \Delta T_{\text{end}}\end{aligned}$$

$$\Delta T_{\text{end}} = \frac{220 - 215.6}{0.98} = \frac{4.4}{0.98}$$

$$\Delta T_{\text{end}} = 4.4898$$

$$T_{\text{cold in}} = 80 - 4.4898 = 75.510$$

$$\epsilon = \frac{300-80}{300-75.510} = \frac{220}{224.49} = 0.9800$$

GAS BEARING AND ROTOR DYNAMICS

BEARING DESIGN REQUIREMENTS

The journal and thrust bearing overall design requirements include:

- Lubricant: helium gas from cycle working fluid
- Ultimate design life: 10,000 hours or more
- Shock and vibration loads: (to be determined)
- Acceleration load: design for 3.0 g in any direction while operating
- Design cryogenic temperature: 80°K (144° R)
- Design speed: 141,300 rpm
- Maximum operating temperature: 125° F (585° R)
- Ambient pressure: 19.5 psia
- Starting: many start-stop cycles
- Orientation: both vertical and horizontal

In addition, requirements as a consequence of the operating environment include a maximum speed of 200,000 rpm. This maximum speed will only be experienced at the maximum operating temperature at the start of the system cooldown. After cooldown has started, the speed will be gradually decreased until the design speed of 141,300 rpm is reached at the design temperature of 80°K.

The above requirements assume:

- No operating pressure thrust load (A large load capability will be included for contingencies.)
- No change in the actual operating ambient pressure throughout the temperature range and intended operating mode
- Design speed close enough to the 150,000-rpm radial reaction turbine design speed that the bearing designs are essentially the same

- 3.0-g operating load as the largest load anticipated to be practical for the design of cryogenic turboalternators for continuous operation (Higher bearing loads are possible, but higher friction losses are not consistent with the objectives of reasonably high turboalternator overall efficiency. Therefore, once shock and vibration levels that the turboalternator can tolerate are determined by analysis and environmental tests, isolation of the turboalternator will be made to prevent adverse operating modes on the bearings. The 3.0-g maximum load requirement may then also be relaxed.)

BEARING SELECTIONS

Only self-acting gas bearings were considered for this design. Externally pressurized bearings were not considered for the following reasons:

- Refrigerator cycle efficiency requires a low ambient pressure, near atmospheric, in the rotor housings.
- Refrigerator cycle efficiency would be lowered because a portion of the cycle gas would have to be diverted through the bearings.
- Ducting the bearing exhaust gas involves a mechanical and thermal heat leak complication that is considered impractical.
- The bearings must be isolated from the rotor cavity by noncontacting seals. The design of the seals could be equally as complicated as the design of the bearing itself.

Tilting pad journal bearings (Figures 6 and 7) were selected for the journals because of:

- Confidence in ultimate success
- Prior manufacturing and cryogenic test experience
- Broad stability range
- Inherent self-alignment
- Reasonable tolerance to dirt ingestion and thermal distortion

A double-acting hydrodynamic thrust bearing with a gimbal system mount was selected because of:

- Confidence in the ultimate success
- Prior manufacturing and cryogenic test experience
- Suitability for any attitude, plus g-loading
- Suitability for complete self-alignment

A spiral groove, inward pumping geometry (Figures 8 and 9) was selected for the turboalternator designs because a stable configuration could be obtained

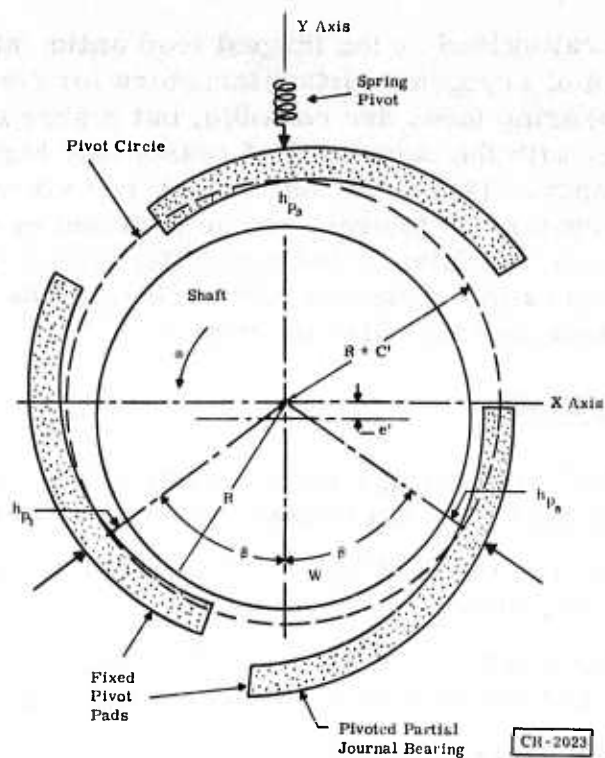


Figure 6. Schematic Diagram of Pivoted Pad Journal Bearing

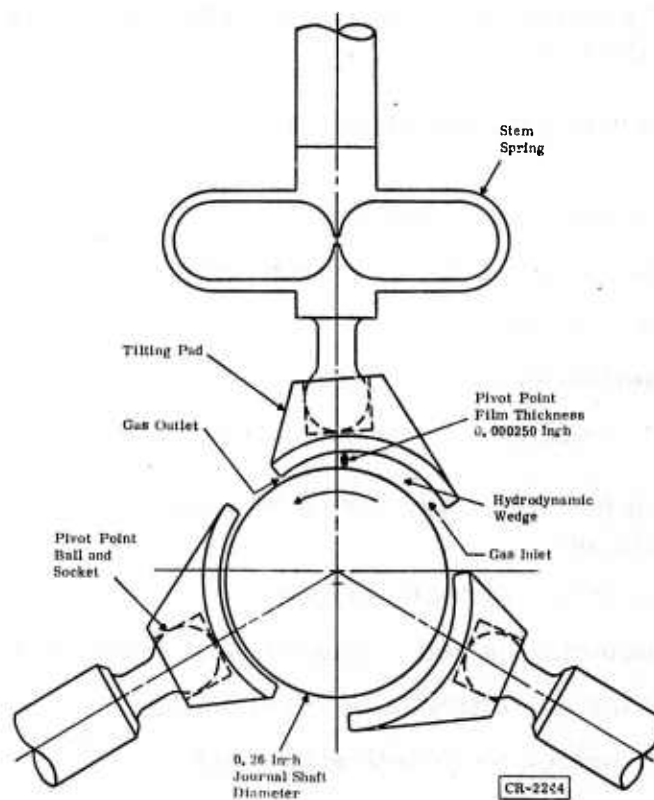


Figure 7. Cryogenic Turboalternator Tilting Pad Journal Bearing

that operated with a greater load capacity and less power loss than any other configuration.

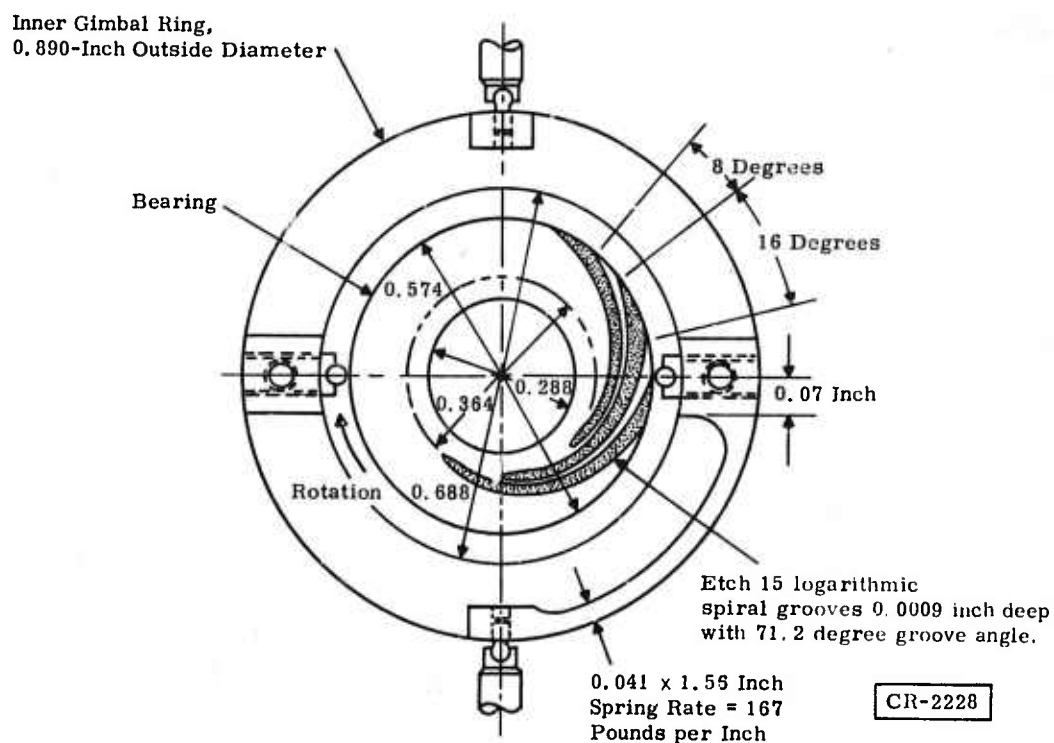


Figure 8. Gimbal-Mounted Spiral Groove Thrust Bearing

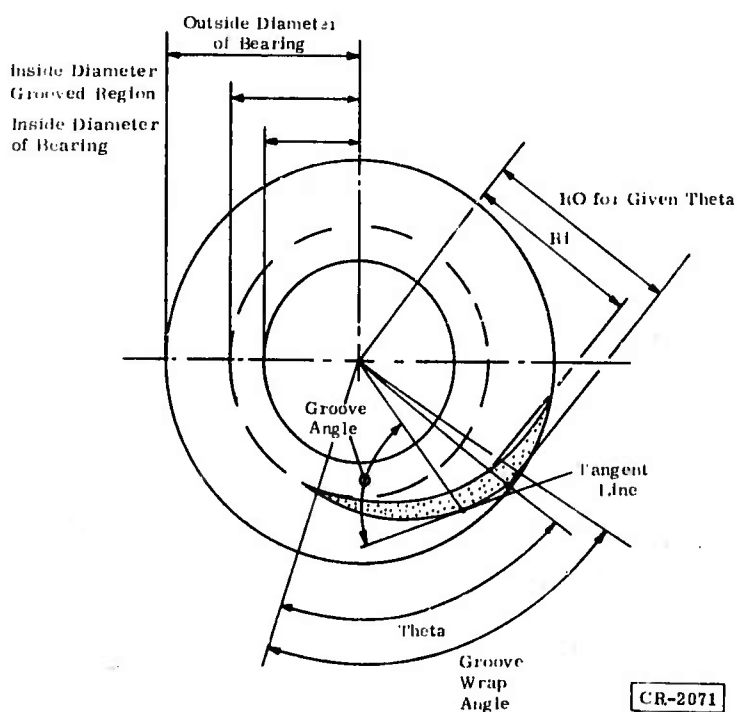


Figure 9. Schematic Diagram of Spiral Groove Thrust Bearing

JOURNAL BEARING DESIGN

Procedure

The procedure for journal bearing design consists of the following steps:

1. Set up the criterion for selection.
2. Select the bearing parameters and performance characteristics for the preliminary design.
3. Determine the first bending critical speed of the rotating assembly.
4. Determine the stability and response of the rotor/journal bearing combination.

Many of the selection criteria are based upon engineering judgments, some of which are based upon past experience. For instance, the principal journal bearing goal is to determine a design capable of maintaining a fluid film separation of the bearing surfaces in the cryogenic environment. All that is required is a nonzero minimum film thickness, but there are two other film thicknesses that are usually considered. One is the pivot film thickness chosen as a design goal in advance of thermal distortion data. The second film thickness is chosen as the absolute minimum acceptable film thickness, which should take into account basic equation accuracy, numerical solution accuracy, and anticipated manufacturing tolerances. Similar considerations apply to critical speeds and other aspects of the design.

The criteria used in designing the journal bearings are:

- Pivot film thickness of 100 microinches (at 3-g steady-state load, without bearing surface distortion)
- Absolute minimum film thickness of 50 microinches
- Minimum power loss
- Shoe pitch, roll, and radial translational natural frequencies with undistorted bearing surfaces must be 25 percent above or 5 percent below the operating speed extremes
- First bending critical speed 25 percent above the operating speed range
- Whirl threshold speed above the operating speed range
- Maximum nondimensional pivot film thickness (hp) of 0.75, for pad stability
- Minimum nondimensional pivot film thickness of 0.20, to limit bearing friction
- Maximum pivot point stress (hertz) of 100,000 psi

The journal bearings were designed using a selector computer program (Program JSELECT)* that contained:

- Coefficient of nondimensional polynomials for single-pad load, power loss, radial stiffness, and pitch axis stiffness versus bearing number (Λ) at a constant nondimensional pivot film thickness (h_p) of 0.20, 0.25, 0.30, 0.40, 0.50, 0.60, and 0.75 microinches
- Logic to internally computed coefficients of nondimensional polynomials for single-pad load, power loss, radial stiffness, and pitch axis stiffness and load versus h_p at constant Λ
- Coefficient of nondimensional polynomials for pad inertia versus shaft mass for constant Λ at the threshold of translatory whirl instability
- Routine based on beam theory for computing two rigid body natural frequencies and the first bending critical speed of a system consisting of four bars, three masses, and two bearings
- Routine for computing the increase in journal diameter due to centrifugal force
- Logic for testing film thicknesses relative to input criteria
- Logic for testing the proximity of the following frequencies relative to the end points of an operating speed range:
 - Shaft rigid body translations and rotations
 - Shoe radial translation
 - Shoe pitch axis rotation
 - Translatory self-excited whirl
- Logic for varying the machined-in clearance, preload, and preload spring stiffness, if frequency or film thickness tests are not passed
- Logic for computing performance characteristics if the machined-in clearance, preload, and preload spring stiffness are specified
- Logic to determine the pivot ball radius so the hertz stress will be 100,000 psi

The original pad data contained in the selector program were produced by a numerical solution of the transient Reynolds equation. Because the results are based on a disturbance from equilibrium, both steady-state and stability data were obtained simultaneously. All pad design data are based on a pad arc length of 100 degrees, with a pivot location of 65 percent and a length-to-diameter ratio of one.

*See Reference 1, Appendix VI.

Performance

Figure 10 shows the general arrangement of a tilting pad journal bearing. The principal features of this design are:

- Bearing consisting of three pads, each of which has an arc of 100 degrees
- Pads that are free to pivot by virtue of a ball-socket joint, located 65 degrees from the gas inlet edge

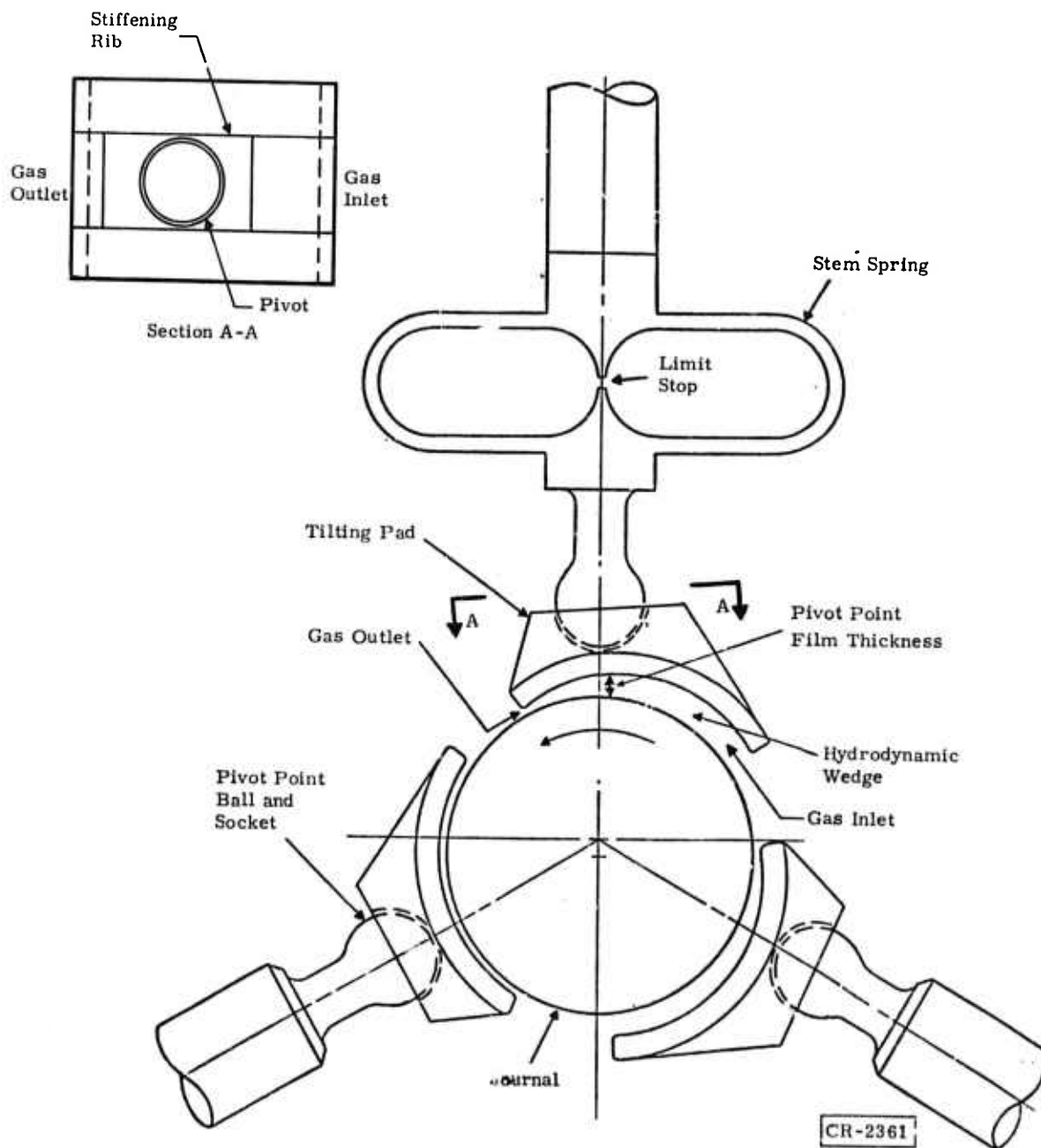


Figure 10. Tilting Pad Journal Bearing

- Low inertia pads, to provide high-speed stability
- Soft spring mount of one pad, to provide a relatively constant preload while accommodating centrifugal and thermally induced dimensional changes
- Pad spring mounting designed with a limit stop to prevent excessive journal displacement during high g-loading

The potential for long, trouble-free life has been incorporated into the journal bearing design by virtue of:

- Low journal bearing startup loads (A separating, fully fluid film will therefore be generated quickly, and wear debris will be minimized.)
- Rotating assembly balanced precisely, to minimize journal bearing pad pitch motions and therefore to minimize rubbing motion at the pivots
- Capacitance probes incorporated as monitoring devices, to ensure that the bearings are assembled and function properly
- Weight of rotating assembly minimized, to reduce bearing reaction forces during high g-loading
- All bearing surfaces hardened and ground to maximize wear life
- Shaft sufficiently stiff to place the first bending critical speed well above the maximum operating speed
- Journal bearing pivots designed with low hertz stresses to minimize fatigue and wear

Bearing pads are made from titanium carbide. The relatively low density but high hardness of this material provides the combination required for both maximum tracking and maximum wear capabilities. The pivots are made from tungsten carbide, while the journals are manufactured from 304L stainless steel and are nitrided. These combinations provide reduced wear and maximum life capabilities.

Figure 11 gives the design specifications for the journal bearings. The three lumped weights and the distance between the weights are used in estimating the first bending critical speed. Poisson's ratio, Young's modulus, and the weight density of the journal material are used to determine the increase in journal diameter due to centrifugal force. The dimensions and weight density of the pad are used in computing the pitch axis inertia, which is critical to the stability of the system.

Figures 12, 13, and 14 show a set of design parameters for a machined-in clearance (difference between the pad and journal radii), C_p , of 0.000625 inch, with loadings of 0g, 1g, and 3g, respectively. Calculations were made for other values of C_p , which indicated that $C_p = 0.000625$ inch was the opti-

DESIGN SPEED (RPM)	141300.0
TEMP. AT DESIGN SPD (°F)	144.00
AMBIENT PRESS, DESIGN SPD (PSIA)	10.50
VISCOSITY, DESIGN (LR*SEC/IN**2)	0.1240E-08
MAX. SPEED (RPM)	200000.0
TEMP. AT MAX SPD (°F)	585.00
AMBIENT PRESS, MAX SPD (PSIA)	10.50
VISCOSITY, MAX (LR*SEC/IN**2)	0.3070E-08
JOURNAL DIA. (IN)	0.500
ROTOR WEIGHT (LB)	0.3020
LEFT OVERHUNG WT. (LB)	0.0507
WT. BETWEEN RRGs. (LB)	0.2200
RIGHT OVERHUNG WT. (LB)	0.0310
LEFT WT. TO LEFT RRG. (IN)	0.3860
LEFT RRG. TO CG (IN)	1.8850
CG TO RIGHT RRG. (IN)	1.6800
RT RRG TO RT OVERHUNG WT (IN)	0.2750
JOURNAL WALL THICKNESS (IN)	0.2500
YOUNG*INERTIA, (LB*IN**2)	0.1720E 06
PERCENT OF PAD FOR PAD THICK	0.1800
PAD LENGTH (IN)	0.5000
POISSON'S RATIO (NU)	0.2600
YOUNG'S MODULUS (PSI)	0.2000E 08
WT DEN OF J. MAT. (LB/IN**3)	0.2830
WT DEN OF PAD MAT (LB/IN**3)	0.2100
ANGLE BETWEEN PIVOTS (DEG)	120.0000
MINIMUM PIVOT FILM TH. (IN)	0.000100
SPRING STIFFNESS (LB/IN)	0.1500E 04
MACHINED IN CLEARANCE (IN)	0.000625
BALL RADIUS (IN)	0.062000
SOCKET RADIUS (IN)	0.063500

CR-2452

Figure 11. Design Specifications for Gas-Lubricated Journal Bearings

imum in the sense of providing the broadest acceptable operating range for power loss, stiffness, minimum film thickness, and critical frequencies. Past test experience has indicated that a soft mounting spring will allow the system to tolerate a wider range of off-design conditions than will a stiff mounting spring. Startup is also facilitated by positioning the pad mounting spring to produce a zero speed separation between the shaft and the pad of 0 to 300 microinches. These two conditions, combined with the design goal to keep the minimum pad critical frequency at least 25 percent above the operating speed, to ensure stable operation, led to the selection of a 1500-pound per-inch mounting spring and a nondimensional pivot film thickness of $H_p = 0.45$ for the design point.

Figures 15, 16, and 17 give bearing parameters and performance at design speed and maximum speed for 0-g, 1-g, and 3-g operation. A maximum

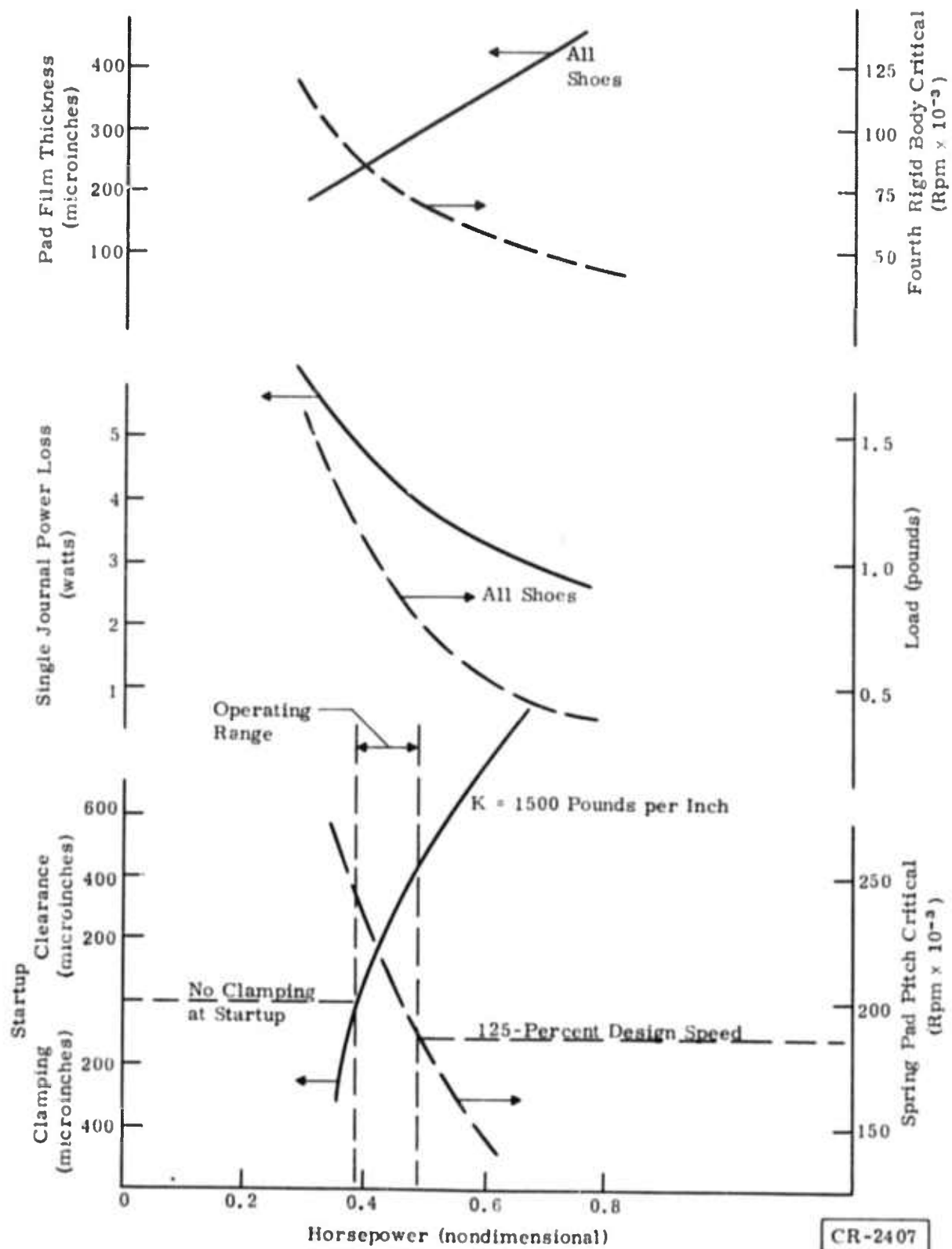


Figure 12. Turboalternator Journal Bearing (0-g Operation)
 $(C_p = 0.000625$ Inch and $N_{Design} = 141,300$ Rpm)

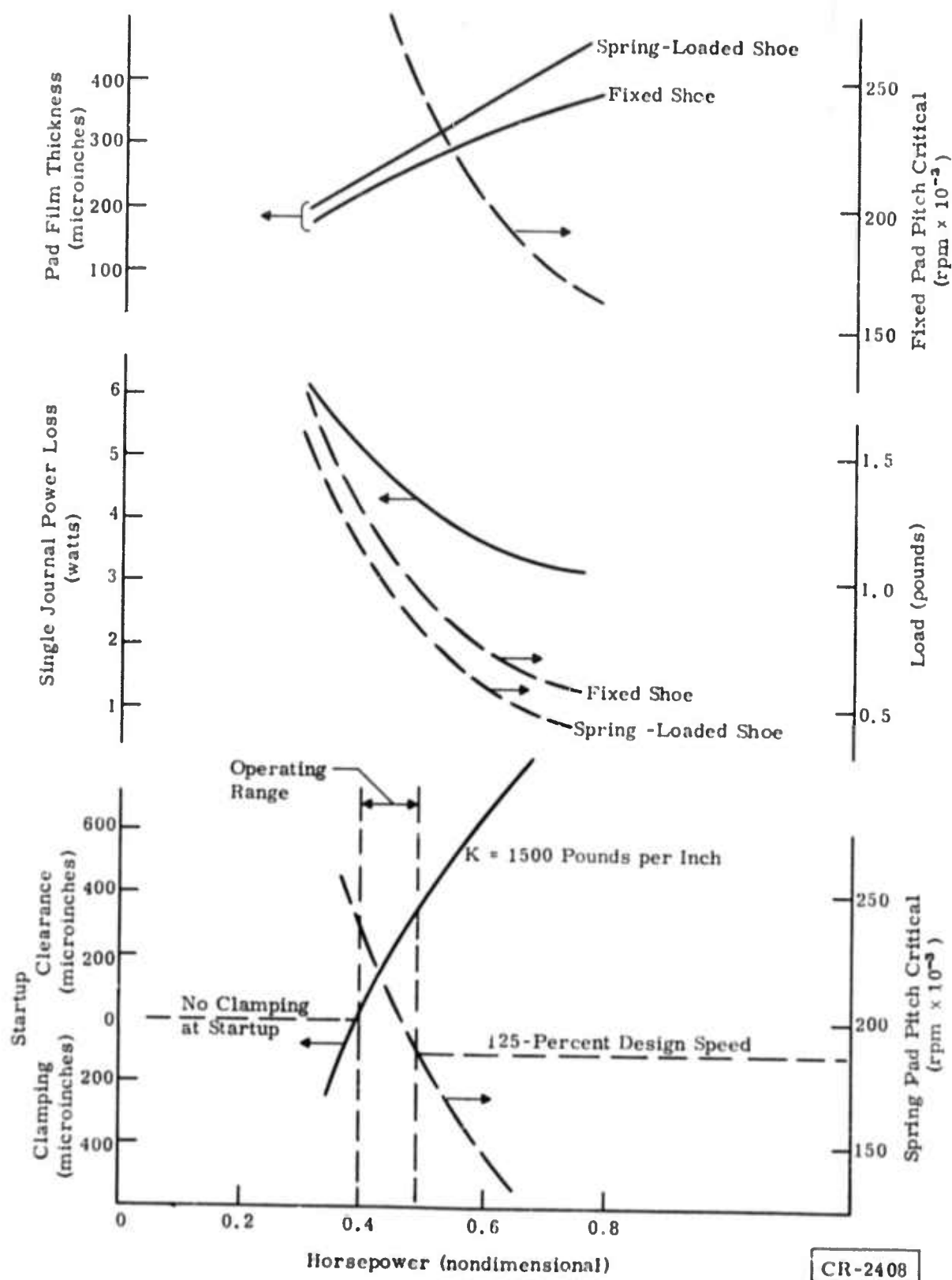


Figure 13. Turboalternator Journal Bearing (1-g Operation)
 $(C_p = 0.000625$ Inch and $N_{\text{Design}} = 141,300$ Rpm)

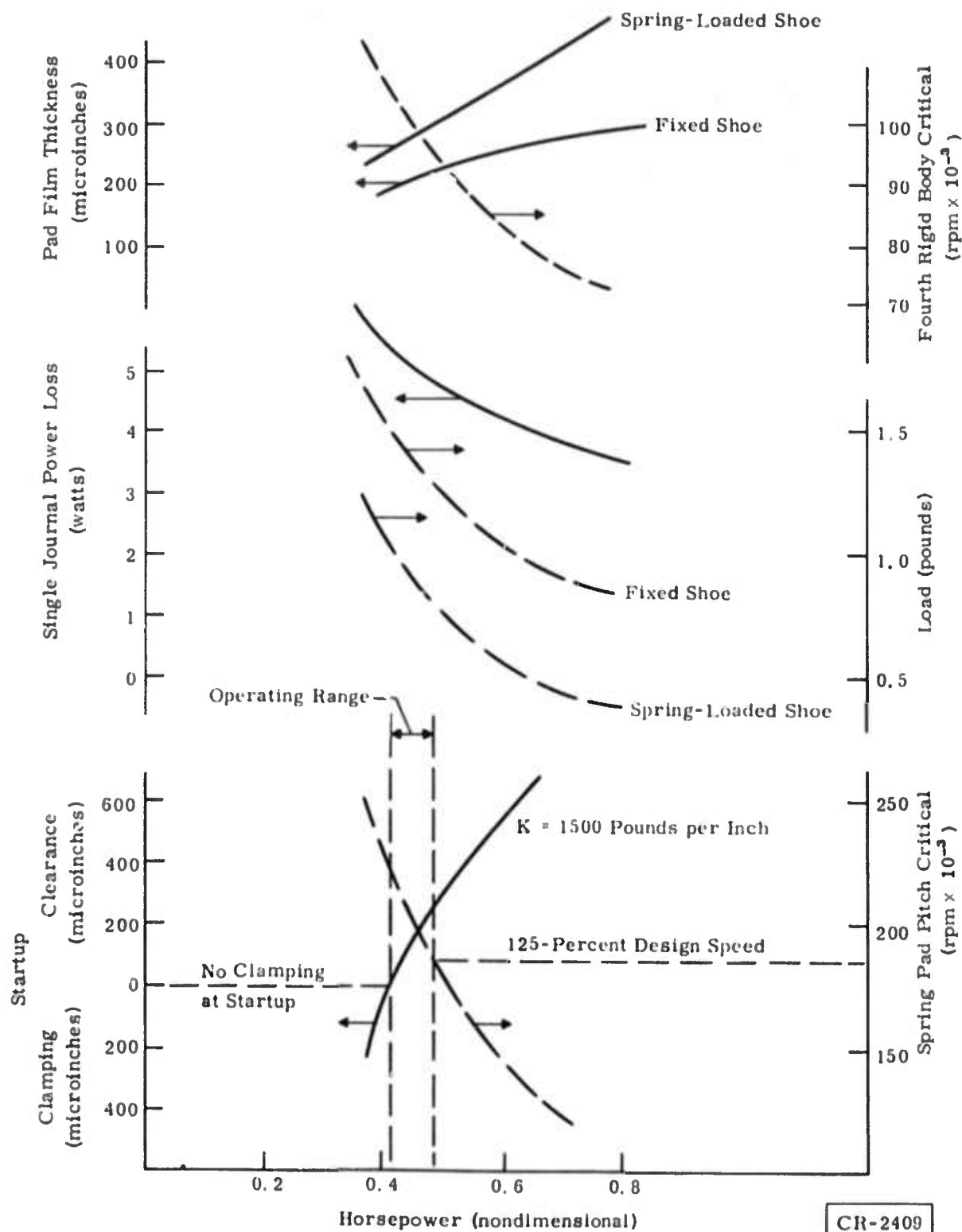


Figure 14. Turboalternator Journal Bearing (3-g Operation)
 $(C_p = 0.000625$ Inch and $N_{\text{Design}} = 141,300$ Rpm)

CONDITIONS AT DESIGN SPEED

LAMRDA (ND)	0.9469
AMBIENT PRESSURE (PSIA)	19.50
CLEARANCE (IN)	0.000610
JOURNAL DIAMETER (IN)	0.500029
BRG. TRANSVERSE STIFF. (LB/IN)	10055.71
BRG. VERTICAL STIFF. (LB/IN)	4579.63
BRG. POWER LOSS (WATTS)	4.3015

SHOES WITH FIXED PIVOTS

LOAD (LB)	0.9112
PIVOT FILM THICKNESS (IN)	0.000276
PITCH STIFFNESS (IN-LB/RAD)	57.0941
PITCH CRITICAL FREQ. (RPM)	203488.1

SHOES WITH SPRING MID. PIVOTS

LOAD (LB)	0.9112
PIVOT FILM THICKNESS (IN)	0.000275
PITCH STIFFNESS (IN-LB/RAD)	57.7091
PITCH CRITICAL FREQ (RPM)	204581.2
TRANS. CRITICAL FREQ (RPM)	350361.2
STIFF OF PRELOAD SPRING (LB/IN)	1500.0
PIVOT SOCKET RADIUS (IN)	0.0635
PIVOT BALL RADIUS (IN)	0.0620

GENERAL CONDITIONS

WHIRL SPEED LIMIT (RPM)	451772.9
FIRST BENDING CRIT. SPD. (RPM)	268878.6
SHAFT RIGID BODY CRIT SPD (RPM)	77525.5
SHAFT RIGID BODY CRIT SPD (RPM)	52521.4
SHAFT RIGID BODY CRIT SPD (RPM)	47291.1
SHAFT RIGID BODY CRIT SPD (RPM)	32315.6
SHOE PITCH INERTIA (IN-LB-SEC ²)	0.1257E-06
WEIGHT OF SHOE (LB)	0.002252
THICKNESS OF SHOE (IN)	0.0450
MACHINED-IN CLEARANCE (IN)	0.000625
START-UP CLAMPING FORCE (LB)	0.
START-UP CLEAR ON TOP SHOE (IN)	0.00026

CR-2410-1

Figure 15. Journal Bearing Performance
(0-g Operation)

SPRING STIFFNESS (LB/IN)	0.1500E+04
MACHINED IN CLEARANCE (IN)	0.000625
STARTING PIVOT FILM THICK.(ND)	0.450000
BALL RADIUS (IN)	0.062000
SOCKET RADIUS (IN)	0.063500
G LOADING	0.

*****GAS LUBRICATED JOURNAL BEARINGS*****

CONDITIONS AT MAXIMUM SPEED

LAMBDA (ND)	3.483
AMBIENT PRESSURE (PSIA)	19.50
CLEARANCE (IN)	0.000596
JOURNAL DIAMETER (IN)	0.500058
BEARING X-STIFFNESS (LB/IN)	10013.786
BEARING Y-STIFFNESS (LB/IN)	4562.432
BEARING POWER LOSS (WATTS)	16.39

SHOES WITH FIXED PIVOTS

LOAD (LB)	1.2961
PIVOT FILM THICKNESS (IN)	0.000346
PITCH STIFFNESS (IN LB/RAD)	63.1129
PITCH CRITICAL (RPM)	213951.8

SHOES WITH SPRING MTD. PIVOTS

LOAD (LB)	1.2961
PIVOT FILM THICKNESS (IN)	0.000347
PITCH STIFFNESS (IN LB/RAD)	63.0344
PITCH CRITICAL (RPM)	213818.8
TRANSLATION CRITICAL (RPM)	357253.1

CR-2410-2

Figure 15. Journal Bearing Performance
(0-g Operation) (Continued)

****CONDITIONS AT DESIGN SPEED****

LAMBDA (ND)	0.9469
AMBIENT PRESSURE (PSIA)	19.50
CLEARANCE (IN)	0.000610
JOURNAL DIAMETER (IN)	0.500029
BRG. TRANSVERSE STIFF. (LB/IN)	12276.59
BRG. VERTICAL STIFF. (LB/IN)	5319.93
BRG. POWER LOSS (WATTS)	4.5670

SHOES WITH FIXED PIVOTS

LOAD (LB)	1.0622
PIVOT FILM THICKNESS (IN)	0.000248
PITCH STIFFNESS (IN-LB/RAD)	72.7662
PITCH CRITICAL FREQ. (RPM)	229725.0

SHOES WITH SPRING MTD. PIVOTS

LOAD (LB)	0.9112
PIVOT FILM THICKNESS (IN)	0.000275
PITCH STIFFNESS (IN-LB/RAD)	57.7091
PITCH CRITICAL FREQ (RPM)	204531.2
TRANS. CRITICAL FREQ (RPM)	359361.2
STIFF OF PRELOAD SPRING (LB/IN)	1500.0
PIVOT SOCKET RADIUS (IN)	0.0635
PIVOT BALL RADIUS (IN)	0.0620

****GENERAL CONDITIONS****

WHIRL SPEED LIMIT (RPM)	451772.3
FIRST BENDING CRIT. SPD. (RPM)	269413.5
SHAFT RIGID BODY CRIT SPD (RPM)	35509.5
SHAFT RIGID BODY CRIT SPD (RPM)	56530.3
SHAFT RIGID BODY CRIT SPD (RPM)	51976.5
SHAFT RIGID BODY CRIT SPD (RPM)	34737.6
SHOE PITCH INERTIA (IN-LB-SEC ²)	0.1257E-06
WEIGHT OF SHOE (LB)	0.002252
THICKNESS OF SHOE (IN)	0.0450
MACHINED-IN CLEARANCE (IN)	0.000625
START-UP CLAMPING FORCE (LB)	0.
START-UP CLEAR ON TOP SHOE (IN)	0.00021

CR-2411-1

Figure 16. Journal Bearing Performance
(1-g Operation)

SPRING STIFFNESS (LB/IN)	0.1500E+04
MACHINED IN CLEARANCE (IN)	0.000625
STARTING PIVOT FILM THICK.(ND)	0.450000
BALL RADIUS (IN)	0.062000
SOCKET RADIUS (IN)	0.063500
G LOADING	1.0000

*****GAS LUBRICATED JOURNAL BEARINGS*****

CONDITIONS AT MAXIMUM SPEED

LAMBDA (ND)	3.483
AMBIENT PRESSURE (PSIA)	19.50
CLEARANCE (IN)	0.000596
JOURNAL DIAMETER (IN)	0.500058
BEARING X-STIFFNESS (LB/IN)	11976.448
BEARING Y-STIFFNESS (LB/IN)	5217.438
BEARING POWER LOSS (WATTS)	17.17

SHOES WITH FIXED PIVOTS

LOAD (LB)	1.4501
PIVOT FILM THICKNESS (IN)	0.000320
PITCH STIFFNESS (IN LB/RAD)	74.1412
PITCH CRITICAL (RPM)	231892.5

SHOES WITH SPRING MTD. PIVOTS

LOAD (LB)	1.2991
PIVOT FILM THICKNESS (IN)	0.000346
PITCH STIFFNESS (IN LB/RAD)	63.2513
PITCH CRITICAL (RPM)	214186.3
TRANSLATION CRITICAL (RPM)	357794.7

CR-2411-2

Figure 16. Journal Bearing Performance
(1-g Operation) (Continued)

****CONDITIONS AT DESIGN SPEED****

LAMBDA (ND)	0.9469
AMBIENT PRESSURE (PSIA)	19.50
CLEARANCE (IN)	0.000610
JOURNAL DIAMETER (IN)	0.500029
BRG. TRANSVERSE STIFF. (LB/IN)	17201.64
BRG. VERTICAL STIFF. (LB/IN)	6961.61
BRG. POWER LOSS (WATTS)	5.0738

SHOES WITH FIXED PIVOTS

LOAD (LB)	1.3642
PIVOT FILM THICKNESS (IN)	0.000206
PITCH STIFFNESS (IN-LB/RAD)	106.0393
PITCH CRITICAL FREQ. (RPM)	277317.3

SHOES WITH SPRING MTD. PIVOTS

LOAD (LB)	0.9112
PIVOT FILM THICKNESS (IN)	0.000275
PITCH STIFFNESS (IN-LB/RAD)	57.7091
PITCH CRITICAL FREQ (RPM)	204581.2
TRANS. CRITICAL FREQ (RPM)	359361.2
STIFF OF PRELOAD SPRING (LB/IN)	1500.0
PIVOT SOCKET RADIUS (IN)	0.0635
PIVOT BALL RADIUS (IN)	0.0620

****GENERAL CONDITIONS****

WHIRL SPEED LIMIT (RPM)	451772.8
FIRST BENDING CRIT. SPD. (RPM)	270691.0
SHAFT RIGID BODY CRIT SPD (RPM)	100824.6
SHAFT RIGID BODY CRIT SPD (RPM)	64693.0
SHAFT RIGID BODY CRIT SPD (RPM)	60821.3
SHAFT RIGID BODY CRIT SPD (RPM)	39638.3
SHOE PITCH INERTIA (IN-LB-SEC ²)	0.1257E-06
WEIGHT OF SHOE (LB)	0.002252
THICKNESS OF SHOE (IN)	1.0450
MACHINED-IN CLEARANCE (IN)	0.000625
START-UP CLAMPING FORCE (LB)	0.
START-UP CLEAR ON TOP SHOE (IN)	0.00012

CR-2412-1

Figure 17. Journal Bearing Performance
(3-g Operation)

SPRING STIFFNESS (LB/IN)	0.1500E+04
MACHINED IN CLEARANCE (IN)	0.000625
STARTING PIVOT FILM THICK.(ND)	0.450000
BALL RADIUS (IN)	0.062000
SOCKET RADIUS (IN)	0.063500
G LOADING	3.0000

*****GAS LUBRICATED JOURNAL BEARINGS*****

CONDITIONS AT MAXIMUM SPEED

LAMBDA (ND)	3.483
AMBIENT PRESSURE (PSIA)	19.50
CLEARANCE (IN)	0.000596
JOURNAL DIAMETER (IN)	0.500058
BEARING X-STIFFNESS (LB/IN)	16294.734
BEARING Y-STIFFNESS (LB/IN)	6656.919
BEARING POWER LOSS (WATTS)	18.74

SHOES WITH FIXED PIVOTS

LOAD (LB)	1.7521
PIVOT FILM THICKNESS (IN)	0.000278
PITCH STIFFNESS (IN LB/RAD)	97.5424
PITCH CRITICAL (RPM)	265983.0

SHOES WITH SPRING MTD. PIVOTS

LOAD (LB)	1.2901
PIVOT FILM THICKNESS (IN)	0.000346
PITCH STIFFNESS (IN LB/RAD)	63.2513
PITCH CRITICAL (RPM)	214186.3
TRANSLATION CRITICAL (RPM)	357794.7

CR-2412-2

Figure 17. Journal Bearing Performance
(3-g Operation) (Continued)

speed of 200,000 rpm was strived for, but the possibility of critical bearing pad frequencies within 25 percent of the maximum speed range does exist. Because of this, it will be necessary to thoroughly monitor the pad operation during the early development stages, to determine what the critical pad frequencies are. It may be necessary to limit the maximum speed to something less than 200,000 rpm, based on these results.

Figures 18 through 21 give performance as a function of the eccentricity ratio, e/Co , at design and maximum speeds for 1-g and 3-g loadings, respectively. Figures 22 through 25 list the performance parameters used to create these plots. The "C" is the displacement directed between the fixed pivots and the "Co" is the pivot circle clearance taken at the concentric position. Shoe 3 on the pivot film thickness graph refers to the spring-loaded shoe; Shoes 1 and 2 refer to the fixed pivot shoes. The Y axis on the stiffness curve passes through the journal center and the spring-mounted pivot; the X axis is orthogonal to the Y axis, with the origin at the center of the zero-applied load pivot circle.

A complete summary of the selected design is shown in Table 5.

Table 5
TURBOALTERNATOR TILTING PAD JOURNAL
GAS BEARING DESIGN SUMMARY

Characteristic	Parameter
Type	Three-shoe, tilting pad
Pad wrap angle	100 degrees
Pad pivot location, from leading edge	65 percent
Pad material and weight density	Titanium carbide, 0.21 pounds per cubic inch
Pad surface finish	4 rms
Diameter	0.5 inch
Pad length	0.5 inch
Angle between pivots	120 degrees
Journal material and weight density	304 stainless steel, 0.28 pounds per cubic inch
Journal wall thickness	0.25 inch
Cold machined-in clearance	0.000625 inch
Ball material and surface finish	Tungsten carbide, 4 rms
Socket material and surface finish	Titanium carbide, 4 rms
Preload spring stiffness	1500 pounds per inch
Shoe pitch inertia	1.289×10^{-7} inch-pound-square seconds
Nominal weight of shoe	3.2×10^{-3} pounds
Nominal thickness of shoe	0.045 inch

CR-2417

TILTING AND BEARING LUBRICATED.
 SPEED: 141500 RPM ALB PRESS: 19.500 PSIA CLEARANCE: .0015425 IN
 TEST: 140 DEG A JOURNAL DIA: .500 IN RTD 3RD ST: 1500 LB/IN
 APP 10 0000 070

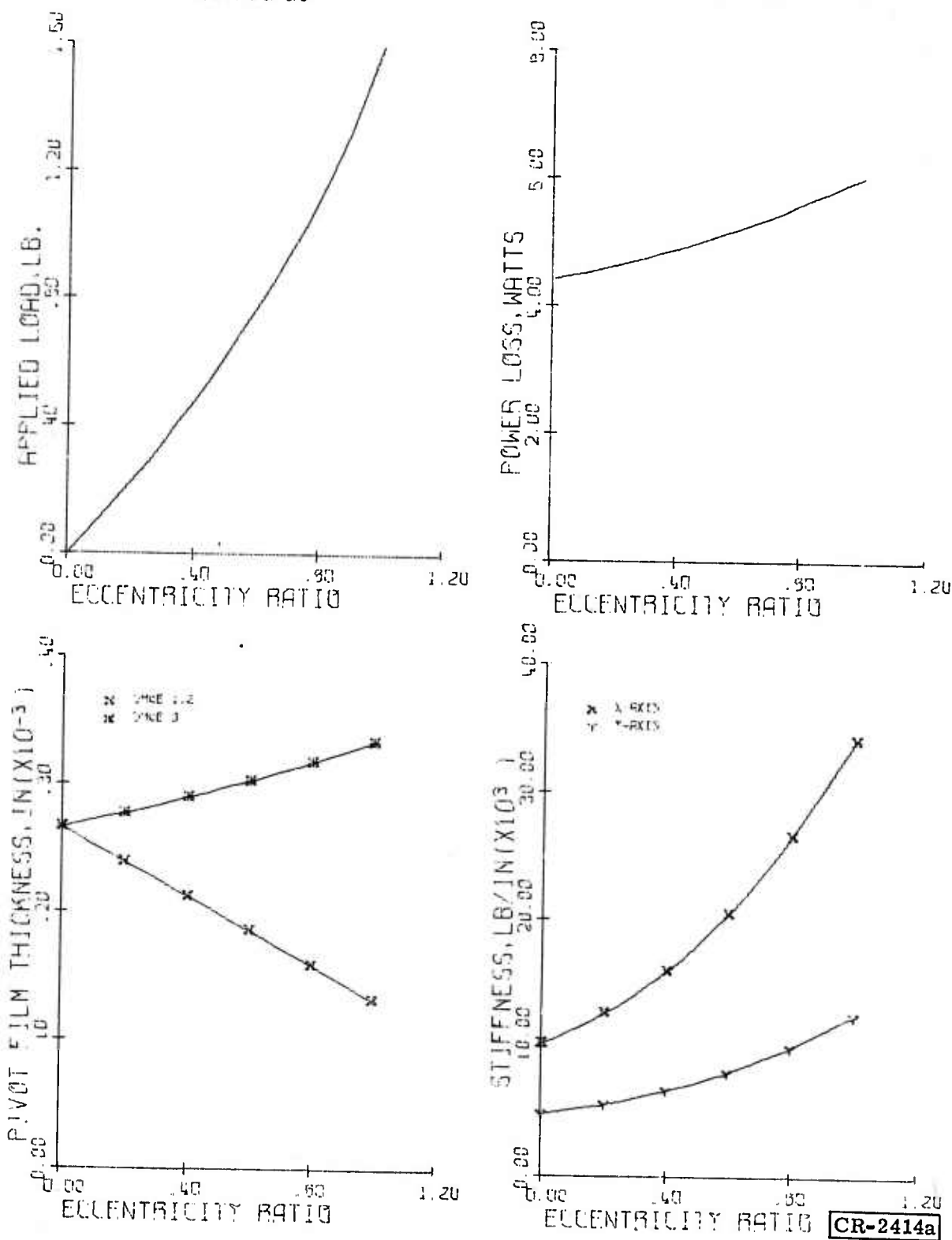


Figure 18. Turboalternator Journal Bearing Performance as a Function of Pivot Circle Eccentricity (1-g Design Speed)

TILTING PAD HELIUM LUBRICATED.
 SPEED = 300000 RPM
 TEMP = 599 DEG R
 APPA 1G MAX 5FD
 LOAD VECTOR BETWEEN FIXED PIVOTS
 19 500 PSTG
 500 IN
 CLEARANCE
 MTD SFR 51F
 1500 LB/IN

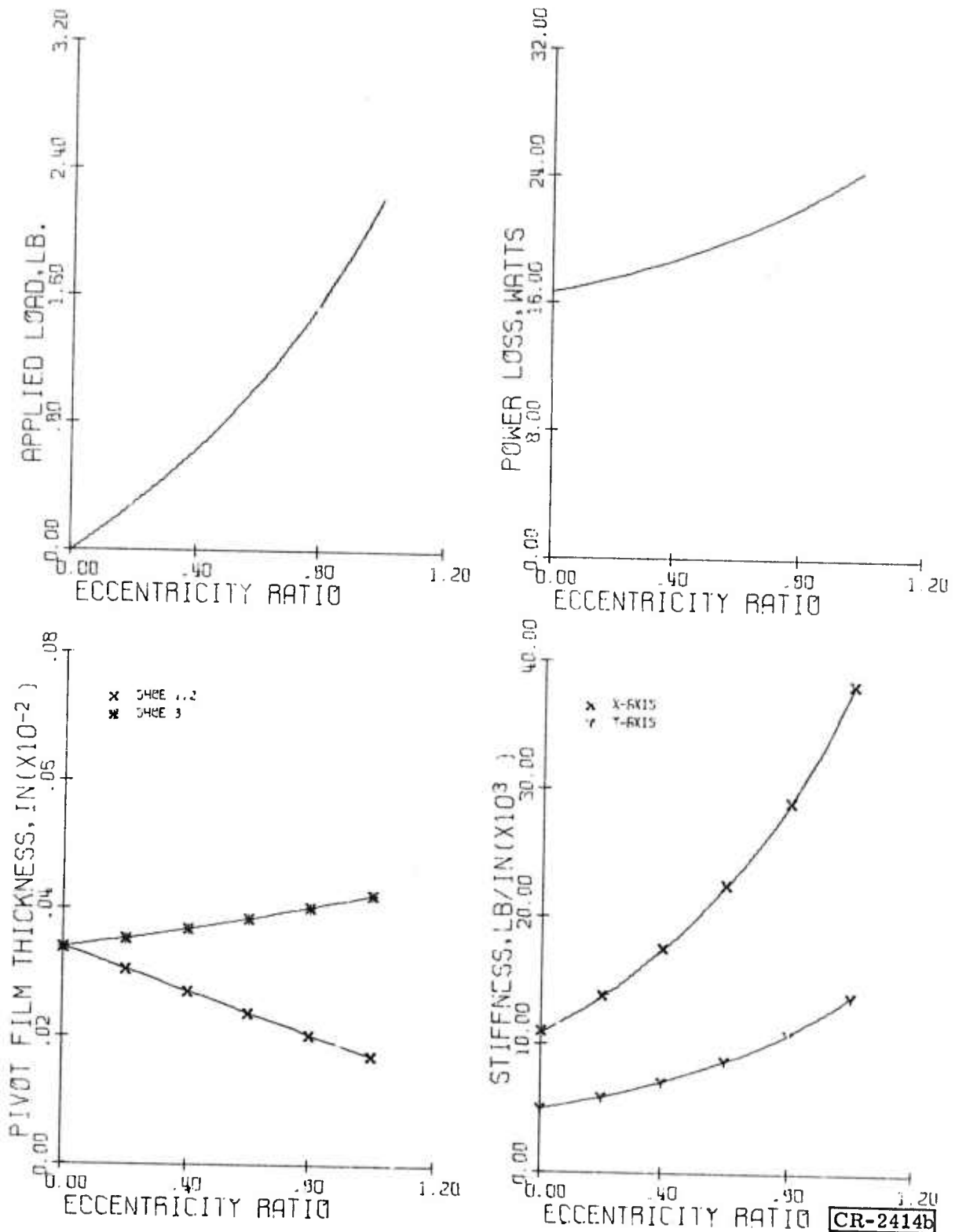


Figure 19. Turboalternator Journal Bearing Performance as a Function of Pivot Circle Eccentricity (1-g Maximum Speed)

ALL TESTS PRO HCLM LUBRICATED. 1000 RPM ON NEW FIXED PIVOTS
 SMOOT - 4.500 IN. 19.507 IN. 1500 RPM
 TEST - 1.44 LBS. R. 1000 DIS. 1500 RPM 1500 RPM 1500 RPM
 1000 30 0.00 370

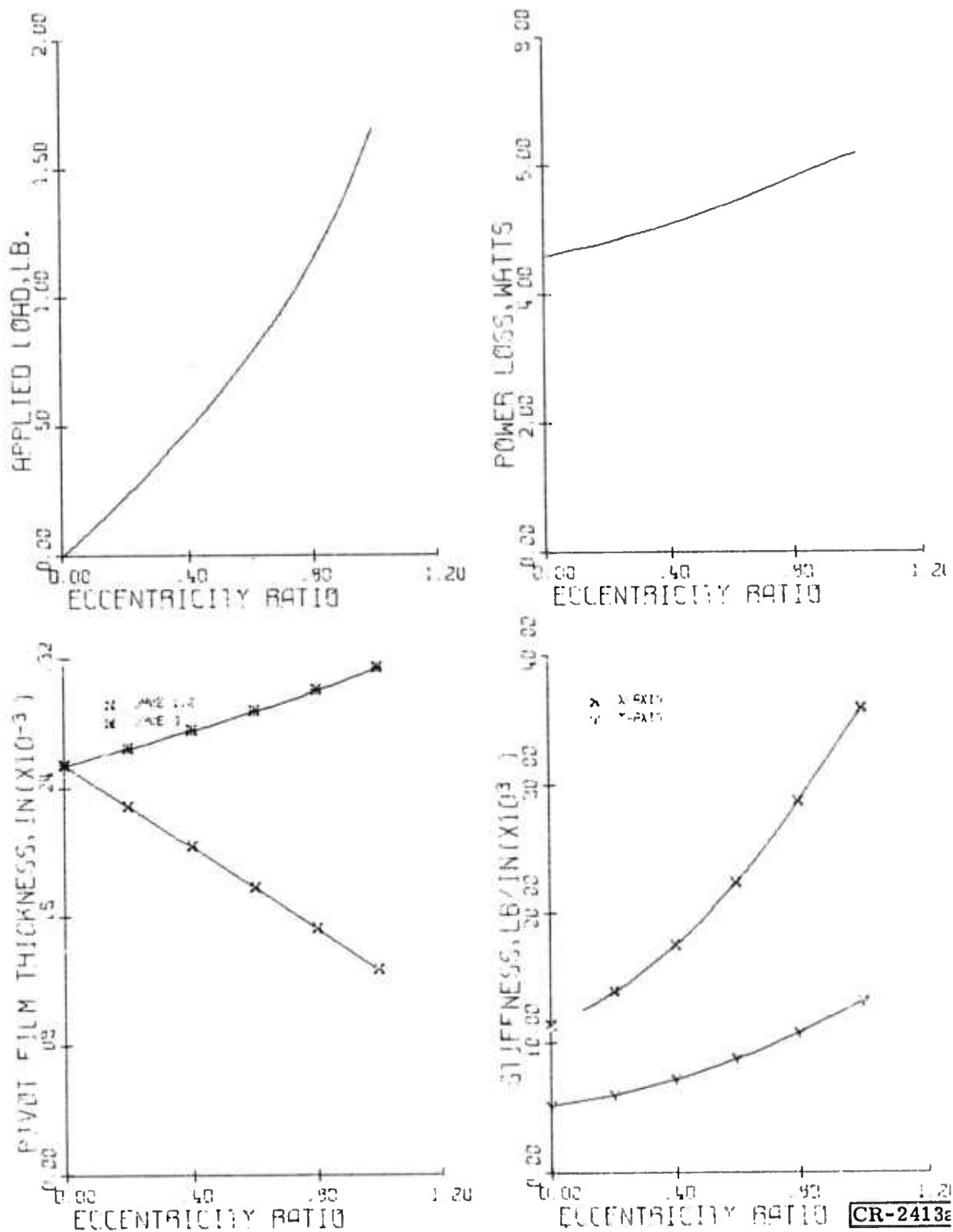


Figure 20. Turboalternator Journal Bearing Performance as a Function of Pivot Circle Eccentricity (3-g Design Speed)



TILTING PIVOT BEARING LUBRICATED.
 SPEED = 20000 RPM
 TEMP = 597 DEG F
 JOURNAL DIA = 1.000 IN
 PIVOT CLEARANCE = .0005 IN
 KTD YEA STF = 1500 LB/IN
 1000 VECTORS OF INERTIAL FORCE
 1000 VECTORS OF INERTIAL FORCE
 1000 VECTORS OF INERTIAL FORCE

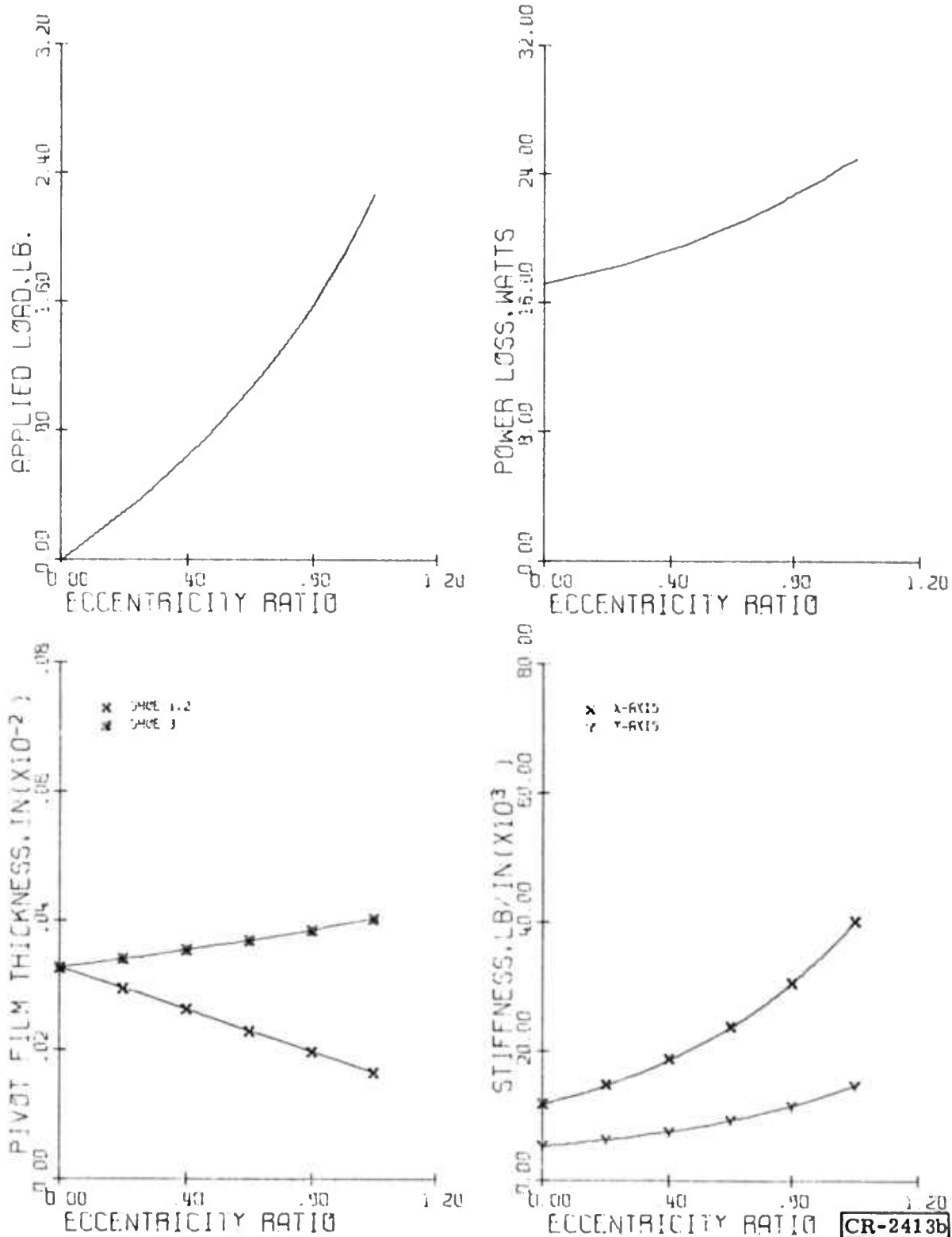


Figure 21. Turboalternator Journal Bearing Performance as a Function of Pivot Circle Eccentricity (3-g Maximum Speed)

RUN NO 1	
INPUT	
ROTATIONAL SPEED,RPM	0.1413E 06
AMBIENT PRESSURE,PSIA	0.1950E 02
MACHINED-IN CLEARANCE,IN	0.6250E-03
VISCOSITY,LR-S/IN**2	0.1240E-08
FIXED PIVOT FILM TK,IN	0.2480E-03
BRG. FACE TO PIVOT,IN	0.8800E-01
AMBIENT TEMPERATURE,DEG R	0.1448E 03
JOURNAL DIAMETER,IN	0.5000E 00
PRELOAD SPR. STIFF,LB/IN	0.1500E 04
PAD LENGTH,IN	0.5000E 00
SPRING PIVOT FILM TK,IN	0.3750E-03
FIXED PIVOT SPACING,DEG	0.1200E 03
OUTPUT	
CONC. PIVOT FILM TK,IN	
PIVOT CIRCLE ECC RATIO,NO	0.10 0.20 0.30 0.40 0.50
APPLIED LOAD, LB	0.1097E 00 0.2255E 00 0.3481E 00 0.4820E 00 0.6255E 00
POWER LOSS, WATTS	0.4426E 01 0.4529E 01 0.4642E 01 0.4757E 01 0.4903E 01
PVT FILM TK, SHOES 1,2,IN	0.2668E-03 0.2534E-03 0.2401E-03 0.2268E-03 0.2134E-03
PIVOT FILM TK, SHOE 3, IN	0.2668E-03 0.2726E-03 0.2785E-03 0.2843E-03 0.2900E-03
BRG STIFF X DIR, LB/IN	0.1040E 05 0.1151E 05 0.1281E 05 0.1433E 05 0.1611E 05
BRG STIFF, Y DIR, LB/IN	0.4699E 04 0.5061E 04 0.5482E 04 0.5977E 04 0.6558E 04
PIVOT CIRCLE CLEARANCE,IN	0.2668E-03 0.2598E-03 0.2522E-03 0.2459E-03 0.2393E-03
PIVOT CIRCLE ECC RATIO,NO	0.60 0.70 0.80 0.90 1.00
APPLIED LOAD, LB	0.7746E 00 0.9413E 00 0.1123E 01 0.1333E 01 0.1596E 01
POWER LOSS, WATTS	0.5222E 01 0.5486E 01 0.5611E 01 0.5829E 01 0.6036E 01
PVT FILM TK, SHOES 1,2,IN	0.1868E-03 0.1734E-03 0.1601E-03 0.1468E-03 0.1334E-03
PIVOT FILM TK, SHOE 3, IN	0.3043E-03 0.3120E-03 0.3193E-03 0.3268E-03 0.3358E-03
BRG STIFF X DIR, LB/IN	0.2064E 05 0.2348E 05 0.2673E 05 0.3035E 05 0.3418E 05
BRG STIFF, Y DIR, LB/IN	0.8842E 04 0.8971E 04 0.1004E 05 0.1123E 05 0.1248E 05
PIVOT CIRCLE CLEARANCE,IN	0.2259E-03 0.2196E-03 0.2131E-03 0.2067E-03 0.2006E-03

Figure 22. Helium-Lubricated Hydrodynamic Tilting Pad Journal Bearing Performance Characteristics for Load Between Fixed Pivots (Design Speed, Run 1)

RUN NO 1	
INPUT	
ROTATIONAL SPEED,RPM	0.2000E 06
AMBIENT PRESSURE,PSIA	0.1950E 02
MACHINED-IN CLEARANCE,IN	0.6250E-03
VISCOSITY,LR-S/IN**2	0.3070E-08
FIXED PIVOT FILM TK,IN	0.3200E-03
BRG. FACE TO PIVOT,IN	0.8800E-01
AMBIENT TEMPERATURE,DEG R	0.3850E 03
JOURNAL DIAMETER,IN	0.5000E 00
PRELOAD SPR. STIFF,LB/IN	0.1500E 04
PAD LENGTH,IN	0.5000E 00
SPRING PIVOT FILM TK,IN	0.3460E-03
FIXED PIVOT SPACING,DEG	0.1200E 03
OUTPUT	
CONC. PIVOT FILM TK,IN	
PIVOT CIRCLE ECC RATIO,NO	0.10 0.20 0.30 0.40 0.50
APPLIED LOAD, LB	0.1425E 00 0.2938E 00 0.4558E 00 0.6333E 00 0.8273E 00
POWER LOSS, WATTS	0.1671E 02 0.1712E 02 0.1759E 02 0.1813E 02 0.1875E 02
PVT FILM TK, SHOES 1,2,IN	0.3381E-03 0.3212E-03 0.3043E-03 0.2874E-03 0.2705E-03
PIVOT FILM TK, SHOE 3, IN	0.3381E-03 0.3455E-03 0.3529E-03 0.3603E-03 0.3682E-03
BRG STIFF X DIR, LB/IN	0.1102E 05 0.1231E 05 0.1381E 05 0.1554E 05 0.1754E 05
BRG STIFF, Y DIR, LB/IN	0.4919E 04 0.5339E 04 0.5827E 04 0.6392E 04 0.7044E 04
PIVOT CIRCLE CLEARANCE,IN	0.3381E-03 0.3293E-03 0.3205E-03 0.3117E-03 0.3030E-03
PIVOT CIRCLE ECC RATIO,NO	0.60 0.70 0.80 0.90 1.00
APPLIED LOAD, LB	0.1041E 01 0.1278E 01 0.1546E 01 0.1854E 01 0.2213E 01
POWER LOSS, WATTS	0.2023E 02 0.2112E 02 0.2212E 02 0.2321E 02 0.2440E 02
PVT FILM TK, SHOES 1,2,IN	0.2367E-03 0.2198E-03 0.2029E-03 0.1860E-03 0.1691E-03
PIVOT FILM TK, SHOE 3, IN	0.3848E-03 0.3933E-03 0.4021E-03 0.4117E-03 0.4214E-03
BRG STIFF X DIR, LB/IN	0.2246E 05 0.2549E 05 0.2901E 05 0.3315E 05 0.3817E 05
BRG STIFF, Y DIR, LB/IN	0.8655E 04 0.9648E 04 0.1080E 05 0.1216E 05 0.1382E 05
PIVOT CIRCLE CLEARANCE,IN	0.2865E-03 0.2776E-03 0.2693E-03 0.2612E-03 0.2531E-03

Figure 23. Helium-Lubricated Hydrodynamic Tilting Pad Journal Bearing Performance Characteristics for Load Between Fixed Pivots (Maximum Speed, Run 1)

RUN NO 2

INPUT

ROTATIONAL SPEED,RPM	0.1413E 06	AMBIENT TEMPERATURE,DEG R	0.1440E 03
AMBIENT PRESSURE,PSIA	0.1950E 02	JOURNAL DIAMETER,IN	0.5000E 00
MACHINED-IN CLEARANCE,IN	0.6250E-03	PRELOAD SPR. STIFF,LB/IN	0.1500E 04
VISCOSITY,LB-S/IN**2	0.1240E-08	PAD LENGTH,IN	0.5000E 00
FIXED PIVOT FILM TK,IN	0.2860E-03	SPRING PIVOT FILM TK,IN	0.2750E-03
BRG. FACE TO PIVOT,IN	0.8800E-01	FIXED PIVOT SPACING,DEG	0.1200E 03

OUTPUT

CONC. PIVOT FILM TK,IN	0.	0.10	0.20	0.30	0.40	0.50
PIVOT CIRCLE ECC RATIO,NO	0.	0.10	0.20	0.30	0.40	0.50
APPLIED LOAD, LB	0.	0.1119E 00	0.2296E 00	0.3539E 00	0.4898E 00	0.6306E 00
POWER LOSS, WATTS	0.	0.4604E-01	0.4710E-01	0.4827E-01	0.4956E-01	0.5096E-01
PVT FILM TK, SHOES 1,2,IN	0.2545E-03	0.2418E-03	0.2291E-03	0.2163E-03	0.2036E-03	0.1909E-03
PIVOT FILM TK, SHOE 3, IN	0.2545E-03	0.2597E-03	0.2649E-03	0.2700E-03	0.2760E-03	0.2814E-03
BRG STIFF X DIR, LB/IN	0.1141E 05	0.1263E 05	0.1404E 05	0.1569E 05	0.1761E 05	0.1984E 05
BRG STIFF, Y DIR, LB/IN	0.5057E 04	0.5457E 04	0.5920E 04	0.6459E 04	0.7087E 04	0.7820E 04
PIVOT CIRCLE CLEARANCE,IN	0.2545E-03	0.2474E-03	0.2410E-03	0.2342E-03	0.2277E-03	0.2210E-03

CONC. PIVOT FILM TK,IN	0.60	0.70	0.80	0.90	1.00
PIVOT CIRCLE ECC RATIO,NO	0.60	0.70	0.80	0.90	1.00
APPLIED LOAD, LB	0.7872E 00	0.9524E 00	0.1145E 01	0.1378E 01	0.1661E 01
POWER LOSS, WATTS	0.5422E 01	0.5614E 01	0.5814E 01	0.6022E 01	0.6204E 01
PVT FILM TK, SHOES 1,2,IN	0.1782E-03	0.1654E-03	0.1527E-03	0.1400E-03	0.1273E-03
PIVOT FILM TK, SHOE 3, IN	0.2479E-03	0.2935E-03	0.3807E-03	0.5023E-03	0.6142E-03
BRG STIFF X DIR, LB/IN	0.2242E 05	0.2537E 05	0.2869E 05	0.3228E 05	0.3593E 05
BRG STIFF, Y DIR, LB/IN	0.8667E 04	0.9639E 04	0.1073E 05	0.1191E 05	0.1311E 05
PIVOT CIRCLE CLEARANCE,IN	0.2147E-03	0.2081E-03	0.2020E-03	0.1958E-03	0.1896E-03

CR-2416a

Figure 24. Helium-Lubricated Hydrodynamic Tilting Pad Journal Bearing Performance Characteristics for Load Between Fixed Pivots (Design Speed, Run 2)

RUN NO 2

INPUT

ROTATIONAL SPEED,RPM	0.2500E 06	AMBIENT TEMPERATURE,DEG R	0.5850E 03
AMBIENT PRESSURE,PSIA	0.1950E 02	JOURNAL DIAMETER,IN	0.5000E 00
MACHINED-IN CLEARANCE,IN	0.6250E-03	PRELOAD SPR. STIFF,LB/IN	0.1500E 04
VISCOSITY,LB-S/IN**2	0.3070E-08	PAD LENGTH,IN	0.5000E 00
FIXED PIVOT FILM TK,IN	0.2780E-03	SPRING PIVOT FILM TK,IN	0.3460E-03
BRG. FACE TO PIVOT,IN	0.8600E-01	FIXED PIVOT SPACING,DEG	0.1200E 03

OUTPUT

CONC. PIVOT FILM TK,IN	0.	0.10	0.20	0.30	0.40	0.50
PIVOT CIRCLE ECC RATIO,NO	0.	0.10	0.20	0.30	0.40	0.50
APPLIED LOAD, LB	0.	0.1447E 00	0.2291E 00	0.4050E 00	0.6464E 00	0.8450E 00
POWER LOSS, WATTS	0.	0.1723E 02	0.1767E 02	0.1816E 02	0.1872E 02	0.1938E 02
PVT FILM TK, SHOES 1,2,IN	0.3284E-03	0.3100E-03	0.2937E-03	0.2774E-03	0.2611E-03	0.2448E-03
PIVOT FILM TK, SHOE 3, IN	0.3284E-03	0.3330E-03	0.3396E-03	0.3466E-03	0.3539E-03	0.3614E-03
BRG STIFF X DIR, LB/IN	0.1189E 05	0.1327E 05	0.1486E 05	0.1669E 05	0.1877E 05	0.2115E 05
BRG STIFF, Y DIR, LB/IN	0.5226E 04	0.5679E 04	0.6189E 04	0.6798E 04	0.7479E 04	0.8260E 04
PIVOT CIRCLE CLEARANCE,IN	0.3284E-03	0.3177E-03	0.3090E-03	0.3005E-03	0.2920E-03	0.2836E-03

CONC. PIVOT FILM TK,IN	0.60	0.70	0.80	0.90	1.00
PIVOT CIRCLE ECC RATIO,NO	0.60	0.70	0.80	0.90	1.00
APPLIED LOAD, LB	0.1081E 01	0.1304E 01	0.1560E 01	0.1897E 01	0.2269E 01
POWER LOSS, WATTS	0.2088E 02	0.2178E 02	0.2278E 02	0.2387E 02	0.2505E 02
PVT FILM TK, SHOES 1,2,IN	0.2284E-03	0.2121E-03	0.1958E-03	0.1795E-03	0.1632E-03
PIVOT FILM TK, SHOE 3, IN	0.3684E-03	0.3763E-03	0.3845E-03	0.3932E-03	0.4020E-03
BRG STIFF X DIR, LB/IN	0.2388E 05	0.2701E 05	0.3085E 05	0.3495E 05	0.4021E 05
BRG STIFF, Y DIR, LB/IN	0.9135E 04	0.1018E 05	0.1130E 05	0.1279E 05	0.1453E 05
PIVOT CIRCLE CLEARANCE,IN	0.2751E-03	0.2668E-03	0.2587E-03	0.2507E-03	0.2428E-03

CR-2416b

Figure 25. Helium-Lubricated Hydrodynamic Tilting Pad Journal Bearing Performance Characteristics for Load Between Fixed Pivots (Maximum Speed, Run 2)

THRUST BEARING DESIGN

Procedure

The selection criteria for the thrust bearing were essentially the same as those for the journal bearing; the design goal film thickness corresponding to the maximum load was assigned in advance of the thermal distortion data.

The design criteria used in selecting the thrust bearing were:

- Maximum design load: 3.0 g
- Minimum film thickness: 100 microinches with parallel, undistorted bearing surfaces at maximum load
- Stable operation with minimum possible gimbal pivot friction and damping from zero net load to maximum load
- Minimum power loss
- Minimum outside diameter
- Maximum gas film moment
- No rigid body natural frequencies in speed or load range
- Maximum stiffness over the operating range

The general thrust bearing design procedure consists of the following principal steps:

1. Set up the criterion for selection.
2. Optimize the load capacity with respect to the film thickness for axially stable face geometries.
3. Determine the bearing and gimbal ring moments of inertia and the pivot friction characteristics necessary to provide stability with a misaligned thrust runner for both axial translation of the rotor and angular rotation of the gimbal ring.

The spiral groove thrust bearing selector program for uniform clearance was used to obtain design and performance parameters. This same program was used for the spiral groove bearings, to compute the film righting moment at a load of approximately 3 g. Pivot characteristics were then computed so the pivot friction moment equaled the film moment with collar misalignment at the maximum load

The spiral groove thrust bearing selector program for uniform clearance was used to first evaluate the thrust bearing design. The program is based on analytical expressions for computing the load capacity of a spiral groove bearing with a uniform film thickness. In addition, the power loss, axial stiffness, and tilt stiffness are computed. Several other parameters, such as the Rey-

nolds number, are computed and listed to aid in the design selection. When the bearing design parameters have been selected, a plotting program is used to compute and plot performance characteristics for a double-acting bearing.

The principal parameters for the bearing design study are:

- Outside-diameter-to-inside-diameter ratio
- Design film clearance at which the load is to be optimized

For a small value of optimized film clearance, the load-versus-clearance curve will have a steep slope, maximizing the film thickness at a high load at the expense of the film thickness at a lower loading. This film thickness is normally selected as a compromise between the film thickness safety margin at the maximum load and the stiffness at normal operating conditions.

The design parameters are usually selected so:

- Mach number is less than 0.8 at the outside diameter.
- Minimum number of grooves is less than the maximum number of grooves. The minimum number is based on minimizing the groove entrance effects. The maximum number is based on manufacturing considerations.
- Relative swash amplitude is less than 0.15.
- Reynolds number is less than 1500.
- Bearing Λ is less than 50.
- Convective and transient inertias are much less than one.
- Steady-state and dynamic local compressibility are much less than one.
- Thrust runner tip speed is less than 800 feet per second.

On the basis of comparing the load capacity predicted by this program with available experimental data, the theoretical load capacity and stiffness are multiplied by 0.75, as a safety factor.

Performance

Figure 26 shows the general arrangement of the thrust bearing assembly. The principal features of the design are:

- Two spiral groove faces provide bidirectional axial load support (See Items 1 and 2, Figure 26).
- Each thrust bearing is independently gimbaled (Items 3 and 4).
- Ball-socket combinations are used for pivots (Item 5)

- One ball stem of each pivot pair is mounted on a leaf spring (Item 6).
- Leaf springs give design control over thrust bearing oscillation by determining the breakaway moment about the pivot axes.
- Design breakaway moment is slightly greater than the film moment that exists under normal operating conditions.
- Force on the ball-socket joint is controlled by positioning a set screw (Item 7).
- Thrust faces contain etched logarithmic spiral grooves that generate load support by hydrodynamic action (Item 8).
- Groove geometry is optimized for load capacity with respect to minimum film thickness.

The thrust faces are manufactured from beryllium-copper, because it is material that has been used successfully in the past for cryogenic expanders. All other parts are machined from 304L stainless steel. In addition, the gimbal balls are made from tungsten carbide, and the sockets are nitrided and lapped for wear resistance.

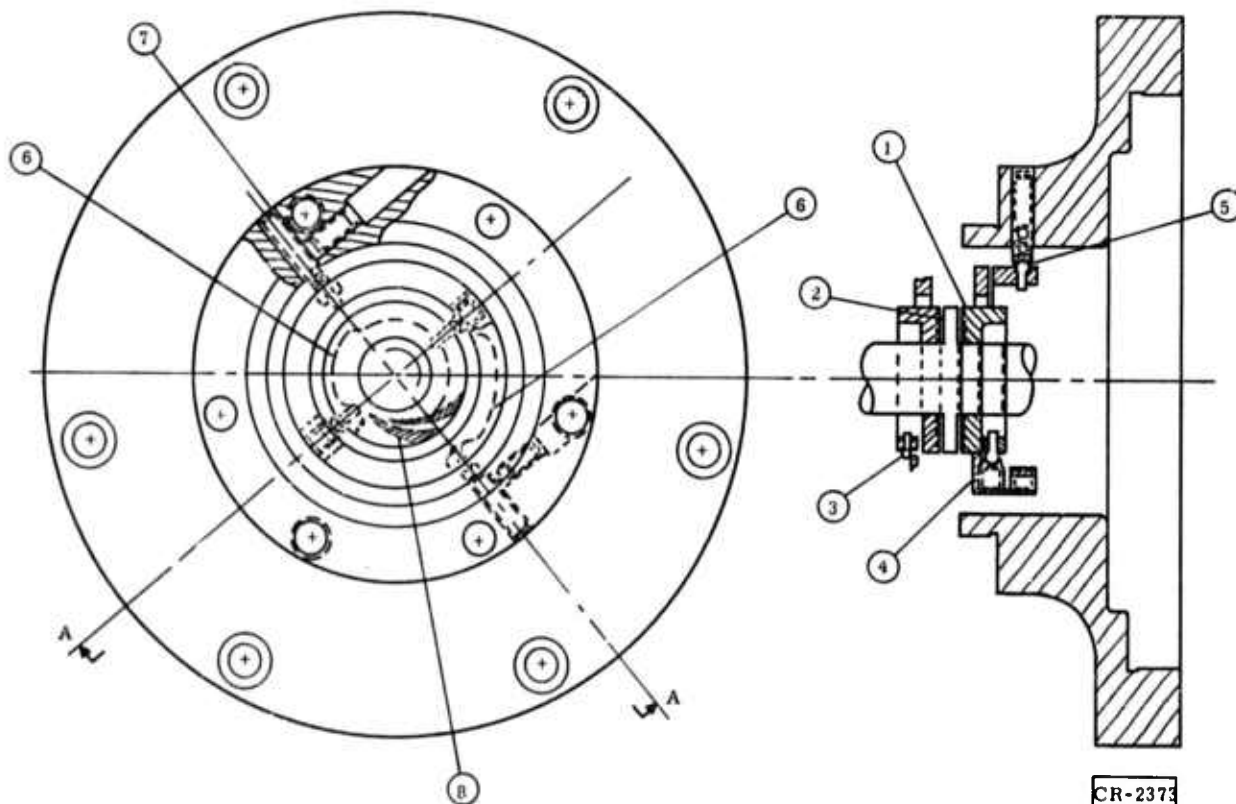


Figure 26. Typical Thrust Bearing Assembly

Using Figure 27 as a basis, the principal dimensions of the thrust face were established. To evaluate the sensitivity of the depth of the groove on

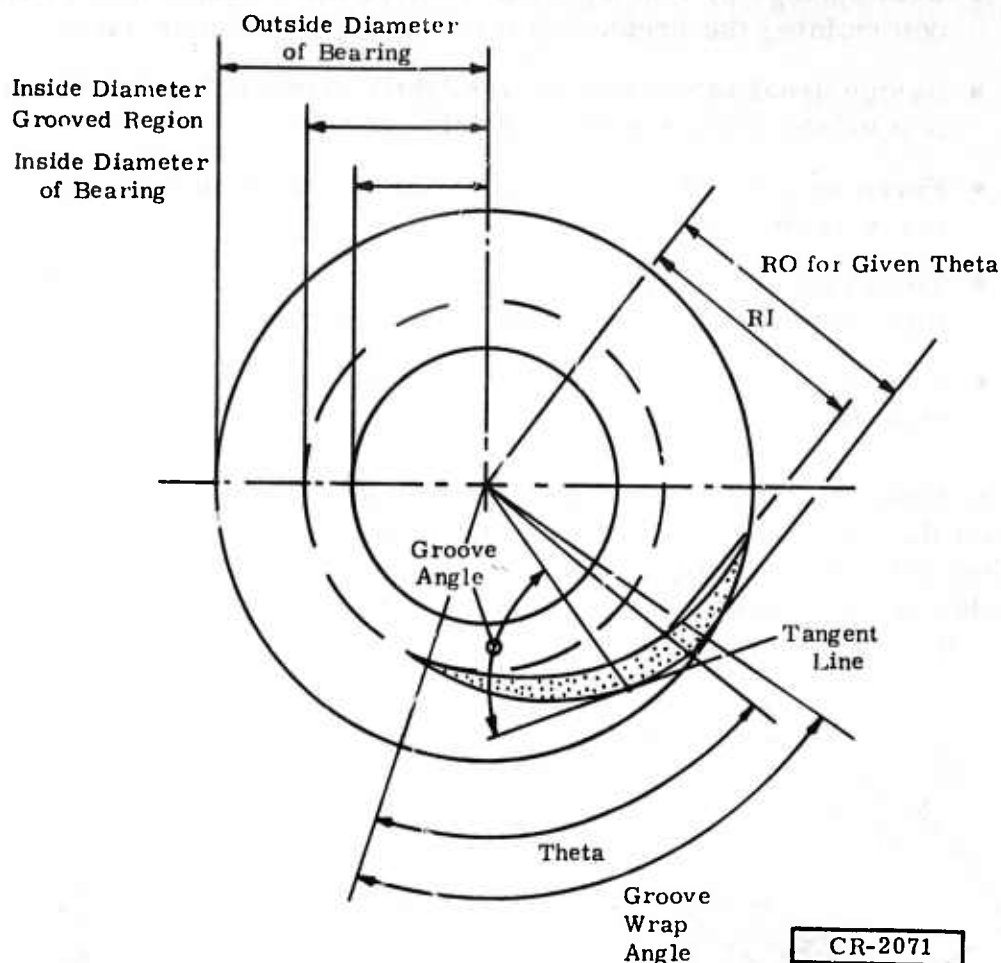


Figure 27. Geometry Showing Radial and Angular Coordinates for Drawing Logarithmic Spiral Grooves in Flat Thrust Face

this design, three different groove depth designs were considered. Figure 28 shows the load capacity as a function of the one-side film thickness for the three values of the groove depth considered and for an outside-diameter-to-inside-diameter ratio of 2.06. Figure 29 shows the power loss as a function of the one-side film thickness for the same three groove depths and outside-diameter-to-inside-diameter ratio. This ratio, which makes the bearing outside diameter 1.125 inches, was selected as the optimum compromise, based on minimizing power loss, maximizing load capacity, and minimizing groove entrance loss effects. Based on maximizing the film thickness at a 3g thrust load, a groove depth of 0.00152 inch was selected.

Figures 30 and 31 give bearing parameters and performance characteristics at design and maximum speeds. These computer outputs represent the design and maximum speed performance expected from one thrust bearing face only.

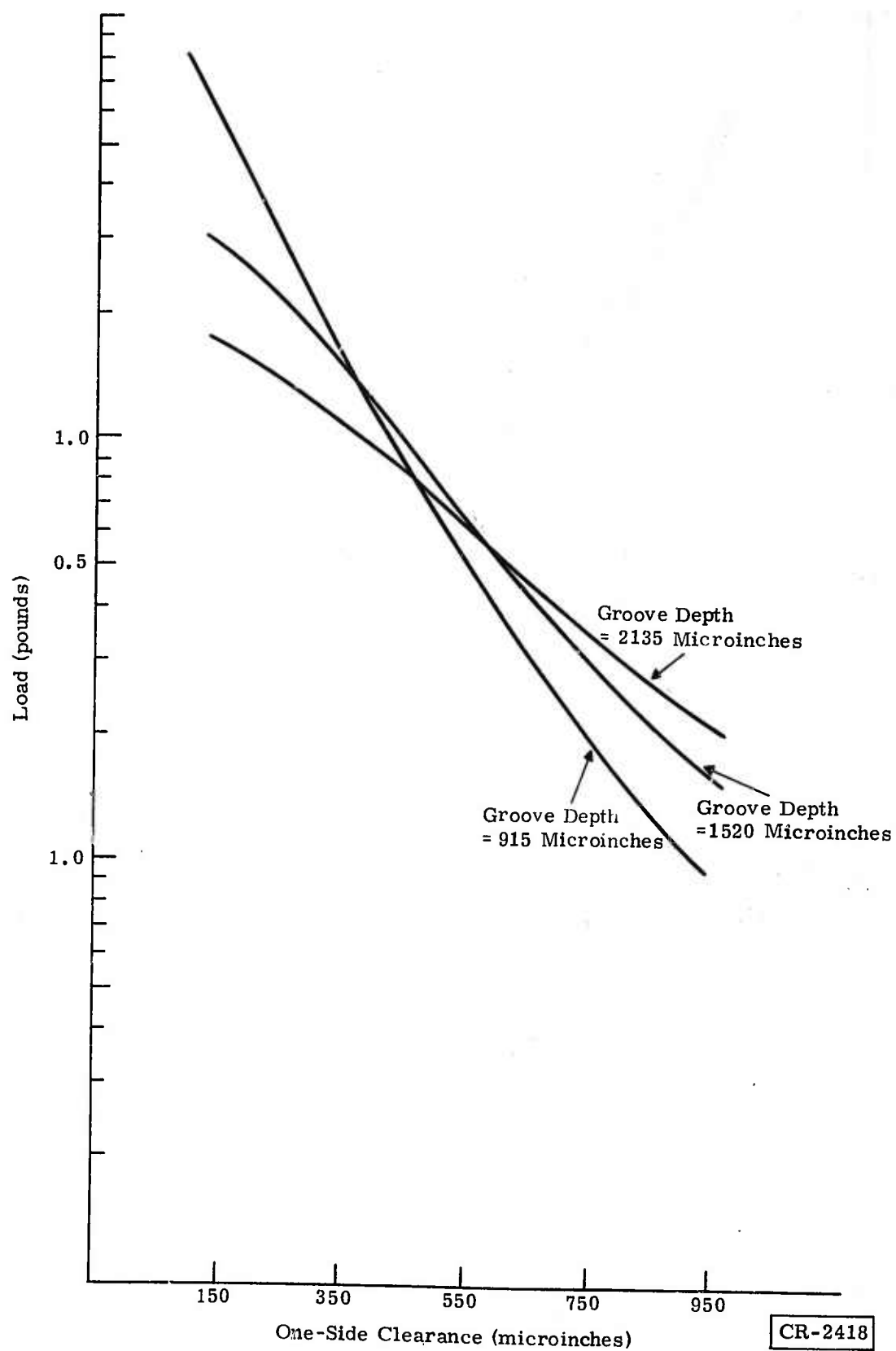


Figure 28. Load Capability Versus One-Side Clearance

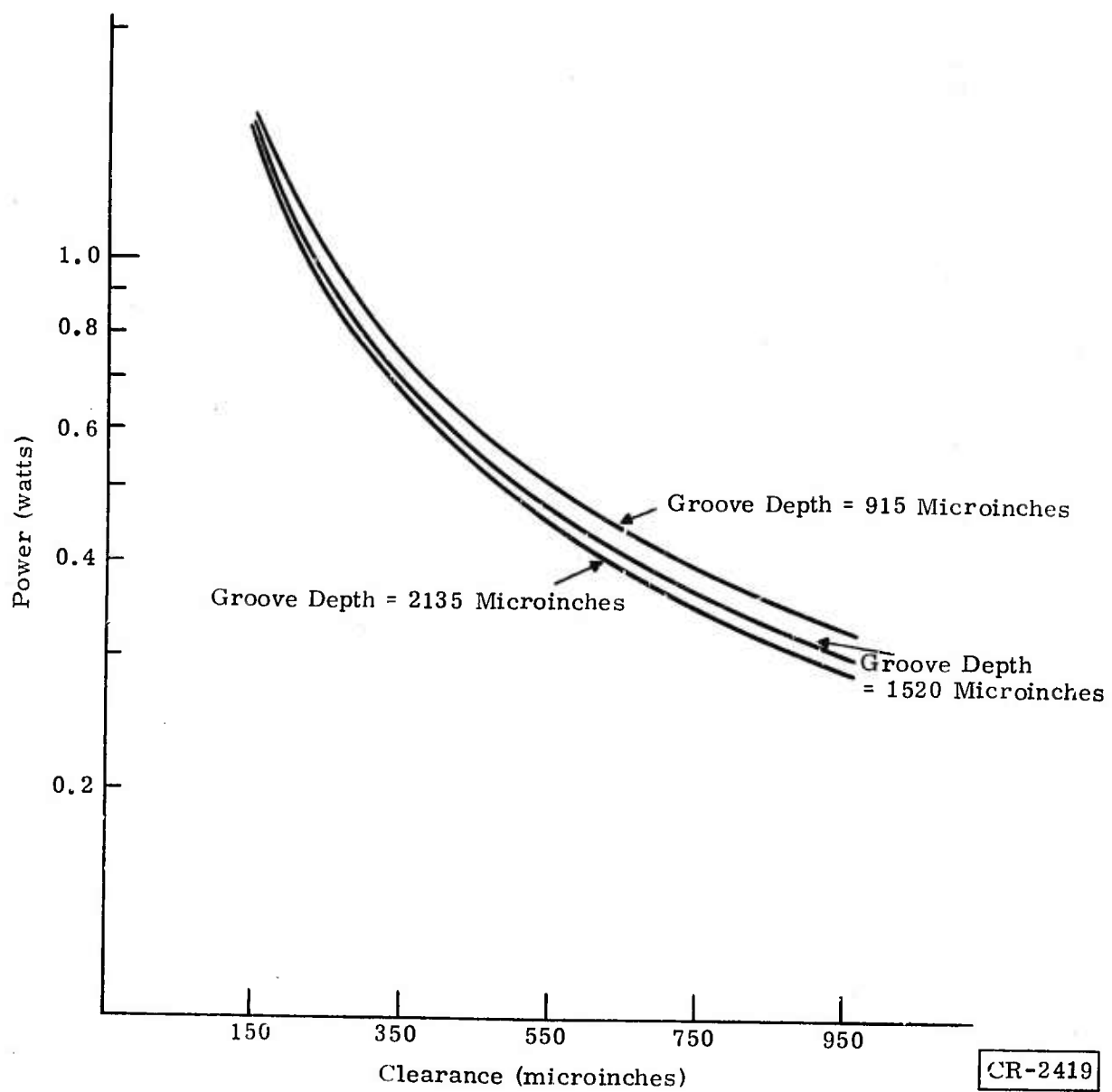


Figure 29. Power Versus One-Side Clearance

INPUT

DESIGN RUN NUMBER 430732

SPEED, RPM	0.1413E+06	GROOVE LT/BRG WIDTH	0.7300E+00
TEMPERATURE, DEG.R	0.1440E+03	GROOVE/RIDGE WIDTH	0.1930E+01
BEARING ID, IN.	0.5470E+00	GROOVE ANGLE, DEG	0.7120E+02
AMBIENT PRESS., PSIA	0.1950E+02	EXP COEFF. BRG, IN/IN F	0.7000E-05
SWASH ANGLE, DEG	0.1950E-02	EXP COEFF. RUN, IN/IN F	0.7000E-05
WT DEN BRG MAT, LB/IN3	0.2830E+00	MIN ALLOW. RIDGE W, IN	0.2300E-01
SHAFT WEIGHT, LB	0.3020E+00	CLEAR AT OPT GRV. D, IN	0.5000E-03

OUTPUT

MACH NO. AT OD	0.3736E+00	MIN. NO. GROOVES	27
GIMBAL MTD BRG TK., IN	0.1160E+00	VISCOSITY, LB-SEC/IN2	0.1240E-08
MAX NO. OF GROOVES	32	BEARING OD, IN.	0.1127E+01
MOLECULAR MFP, IN.	0.1393E-05	BRG. INER. IN-LB-SEC2	0.6427E-05
GROOVE DEPTH, IN.	0.1525E-02	TIP SPEED, FT/SEC	0.6947E+03

CLEARANCE, MICROINCHES	50	150	250
LOAD, LB	0.3421E+01	0.2979E+01	0.2203E+01
POWER, WATTS	0.3745E+02	0.1452E+02	0.9291E+01
RELATIVE SWASH AMPLITUDE	0.1701E+39	0.1533E+00	0.8653E-01
MAX DISTORTION TO CLEAR RAT.	0.1593E+01	0.1957E+00	0.7199E-01
AXIAL FREQUENCY, CPM	0.	0.2794E+05	0.2881E+05
TILT FREQUENCY, CPM	0	0.9123E+05	0.9407E+05
AXIAL STIFFNESS LB/IN	0.	0.6700E+04	0.7124E+04
TILT STIFFNESS IN-LB/RAD	0.	0.5866E+03	0.6237E+03
EFFECT. VIS. LB-SEC/IN**2	0.1062E-08	0.1174E-08	0.1199E-08
REYNOLDS NO.	0.2633E+02	0.7900E+02	0.1317E+03
LAMBDA	0.3687E+03	0.4097E+02	0.1475E+02
CONVECTIVE INERTIA RATIO	0.2387E-03	0.2149E-02	0.5968E-02
TRANSIENT INERTIA RATIO	0.	0.5187E+00	0.6006E+00
LOCAL COMPRESS. RATIO, SS	0.2883E+01	0.3203E+00	0.1153E+00
LOCAL COMPRESS. RATIO, DYN	0.	0.1474E-01	0.5473E-02

CLEARANCE, MICROINCHES	350	450	550
LOAD, LB	0.1509E+01	0.1004E+01	0.6708E+00
POWER, WATTS	0.6949E+01	0.5610E+01	0.4736E+01
RELATIVE SWASH AMPLITUDE	0.7865E-01	0.8973E-01	0.1136E+00
MAX DISTORTION TO CLEAR RAT.	0.3707E-01	0.2254E-01	0.1514E-01
AXIAL FREQUENCY, CPM	0.2554E+05	0.2109E+05	0.1695E+05

CR-2420-1

Figure 30. Helium-Lubricated Spiral Groove Thrust Bearing Parameters and Performance (Design Speed, One Side, Ratio of Outside Diameter to Inside Diameter = 2.06)

TILT FREQUENCY, CPM	0.8339E+05	0.6885E+05	0.5534E+05
AXIAL STIFFNESS LB/IN	0.5598E+04	0.3817E+04	0.2466E+04
TILT STIFFNESS IN-LB/RAD	0.4901E+03	0.3342E+03	0.2159E+03
EFFECT. VIS. LB-SEC/IN**2	0.1211E-08	0.1217E-08	0.1221E-08
REYNOLDS NO.	0.1843E+03	0.2370E+03	0.2897E+03
LAMBDA	0.7525E+01	0.4552E+01	0.3047E+01
CONVECTIVE INERTIA RATIO	0.1170E-01	0.1934E-01	0.2889E-01
TRANSIENT INERTIA RATIO	0.5941E+00	0.5443E+00	0.4829E+00
LOCAL COMPRESS. RATIO, SS	0.5884E-01	0.3559E-01	0.2383E-01
LOCAL COMPRESS. RATIO, DYN	0.2475E-02	0.1236E-02	0.6652E-03

CLEARANCE, MICROINCHES	650	750	850
LOAD, LB	0.4566E+00	0.3184E+00	0.2277E+00
POWER, WATTS	0.4118E+01	0.3655E+01	0.3294E+01
RELATIVE SWASH AMPLITUDE	0.1499E+00	0.1997E+00	0.2649E+00
MAX DISTORTION TO CLEAR RAT.	0.1087E-01	0.8175E-02	0.6373E-02
AXIAL FREQUENCY, CPM	0.1358E+05	0.1095E+05	0.8931E+04
TILT FREQUENCY, CPM	0.4433E+05	0.3575E+05	0.2916E+05
AXIAL STIFFNESS LB/IN	0.1582E+04	0.1029E+04	0.6844E+03
TILT STIFFNESS IN-LB/RAD	0.1385E+03	0.9009E+02	0.5992E+02
EFFECT. VIS. LB-SEC/IN**2	0.1224E-08	0.1226E-08	0.1227E-08
REYNOLDS NO.	0.3423E+03	0.3950E+03	0.4477E+03
LAMBDA	0.2182E+01	0.1639E+01	0.1276E+01
CONVECTIVE INERTIA RATIO	0.4035E-01	0.5372E-01	0.6899E-01
TRANSIENT INERTIA RATIO	0.4249E+00	0.3750E+00	0.3333E+00
LOCAL COMPRESS. RATIO, SS	0.1706E-01	0.1281E-01	0.9976E-02
LOCAL COMPRESS. RATIO, DYN	0.3815E-03	0.2311E-03	0.1467E-03

CLEARANCE, MICROINCHES	950	1050	1150
LOAD, LB	0.1666E+00	0.1245E+00	0.9487E-01
POWER, WATTS	0.3003E+01	0.2764E+01	0.2563E+01
RELATIVE SWASH AMPLITUDE	0.3478E+00	0.4509E+00	0.5771E+00
MAX DISTORTION TO CLEAR RAT.	0.5107E-02	0.4184E-02	0.3490E-02
AXIAL FREQUENCY, CPM	0.7373E+04	0.6159E+04	0.5202E+04
TILT FREQUENCY, CPM	0.2407E+05	0.2011E+05	0.1698E+05
AXIAL STIFFNESS LB/IN	0.4664E+03	0.3255E+03	0.2322E+03
TILT STIFFNESS IN-LB/RAD	0.4083E+02	0.2850E+02	0.2033E+02
EFFECT. VIS. LB-SEC/IN**2	0.1229E-08	0.1230E-08	0.1231E-08
REYNOLDS NO.	0.5003E+03	0.5530E+03	0.6057E+03
LAMBDA	0.1021E+01	0.8361E+00	0.6970E+00
CONVECTIVE INERTIA RATIO	0.8618E-01	0.1053E+00	0.1263E+00
TRANSIENT INERTIA RATIO	0.2988E+00	0.2702E+00	0.2463E+00
LOCAL COMPRESS. RATIO, SS	0.7986E-02	0.6538E-02	0.5450E-02
LOCAL COMPRESS. RATIO, DYN	0.9697E-04	0.6631E-04	0.4670E-04

CR-2420-2

Figure 30. Helium-Lubricated Spiral Groove Thrust Bearing Parameters and Performance (Design Speed, One Side, Ratio of Outside Diameter to Inside Diameter = 2.06) (Continued)

CLEARANCE, MICROINCHES	1250	1350	1450
LOAD, LB	0.7349E-01	0.5779E-01	0.4606E-01
POWER, WATTS	0.2391E+01	0.2243E+01	0.2113E+01
RELATIVE SWASH AMPLITUDE	0.7293E+00	0.9107E+00	0.1125E+01
MAX DISTORTION TO CLEAR RAT.	0.2956E-02	0.2536E-02	0.2199E-02
AXIAL FREQUENCY, CPM	0.4439E+04	0.3822E+04	0.3318E+04
TILT FREQUENCY, CPM	0.1449E+05	0.1248E+05	0.1083E+05
AXIAL STIFFNESS LB/IN	0.1691E+03	0.1253E+03	0.9448E+02
TILT STIFFNESS IN-LB/RAD	0.1480E+02	0.1097E+02	0.8272E+01
EFFECT. VIS. LB-SEC/IN**2	0.1231E-08	0.1232E-08	0.1232E-08
REYNOLDS NO.	0.6584E+03	0.7110E+03	0.7637E+03
LAMBDA	0.5900E+00	0.5058E+00	0.4384E+00
CONVECTIVE INERTIA RATIO	0.1492E+00	0.1740E+00	0.2008E+00
TRANSIENT INERTIA RATIO	0.2261E+00	0.2090E+00	0.1943E+00
LOCAL COMPRESS. RATIO, SS	0.4613E-02	0.3955E-02	0.3428E-02
LOCAL COMPRESS. RATIO, DYN	0.3372E-04	0.2489E-04	0.1873E-04

CLEARANCE, MICROINCHES	1550
LOAD, LB	0.3715E-01
POWER, WATTS	0.1999E+01
RELATIVE SWASH AMPLITUDE	0.1376E+01
MAX DISTORTION TO CLEAR RAT.	0.1925E-02
AXIAL FREQUENCY, CPM	0.2902E+04
TILT FREQUENCY, CPM	0.9475E+04
AXIAL STIFFNESS LB/IN	0.7228E+02
TILT STIFFNESS IN-LB/RAD	0.6328E+01
EFFECT. VIS. LB-SEC/IN**2	0.1233E-08
REYNOLDS NO.	0.8164E+03
LAMBDA	0.3837E+00
CONVECTIVE INERTIA RATIO	0.2294E+00
TRANSIENT INERTIA RATIO	0.1816E+00
LOCAL COMPRESS. RATIO, SS	0.3000E-02
LOCAL COMPRESS. RATIO, DYN	0.1434E-04

CR-2420-3

Figure 30. Helium-Lubricated Spiral Groove Thrust Bearing Parameters and Performance (Design Speed, One Side, Ratio of Outside Diameter to Inside Diameter = 2.06) (Continued)

INPUT

DESIGN RUN NUMBER 430734

SPEED, RPM	0.2000E+06	GROOVE LT/BRG WIDTH	0.7300E+00
TEMPERATURE, DEG. R	0.5850E+03	GROOVE/RIDGE WIDTH	0.1930E+01
BEARING ID, IN.	0.5470E+00	GROOVE ANGLE, DEG	0.7120E+02
AMBIENT PRESS., PSIA	0.1950E+02	EXP COEFF. BRG, IN/IN F	0.7000E-05
SWASH ANGLE, DEG	0.1950E-02	EXP COEFF. RUN, IN/IN F	0.7000E-05
WT DEN BRG MAT, LB/IN ³	0.2830E+00	MIN ALLOW. RIDGE W, IN	0.2300E-01
SHAFT WEIGHT, LB	0.3020E+00	CLEAR AT OPT GRV. D, IN	0.5000E-03

OUTPUT

MACH NO. AT OD	0.2623E+00	MIN. NO. GROOVES	27
GIMBAL MTD BRG TK., IN	0.1160E+00	VISCOSITY, LB-SEC/IN ²	0.3066E-08
MAX NO. OF GROOVES	32	BEARING OD, IN.	0.1127E+01
MOLECULAR MFP, IN.	0.6888E-05	BRG. INER. IN-LB-SEC ²	0.6427E-05
GROOVE DEPTH, IN.	0.1525E-02	TIP SPEED, FT/SEC	0.9834E+03

CLEARANCE, MICROINCHES	50	150	250
LOAD, LB	0.7654E+01	0.8631E+01	0.6840E+01
POWER, WATTS	0.1186E+03	0.5955E+02	0.4083E+02
RELATIVE SWASH AMPLITUDE	0.1701E+39	0.2054E+00	0.6459E-01
MAX DISTORTION TO CLEAR RAT.	0.3144E+01	0.5003E+00	0.1972E+00
AXIAL FREQUENCY, CPM	0.	0.3418E+05	0.4721E+05
TILT FREQUENCY, CPM	0.	0.1116E+06	0.1541E+06
AXIAL STIFFNESS LB/IN	0.	0.1002E+05	0.1912E+05
TILT STIFFNESS IN-LB/RAD	0.	0.8776E+03	0.1674E+04
EFFECT. VIS. LB-SEC/IN**2	0.1678E-08	0.2404E-08	0.2631E-08
REYNOLDS NO.	0.3710E+01	0.1113E+02	0.1855E+02
LAMBDA	0.1291E+04	0.1434E+03	0.5163E+02
CONVECTIVE INERTIA RATIO	0.3363E-04	0.3027E-03	0.8408E-03
TRANSIENT INERTIA RATIO	0.	0.6314E-01	0.9793E-01
LOCAL COMPRESS. RATIO, SS	0.1009E+02	0.1121E+01	0.4037E+00
LOCAL COMPRESS. RATIO, DYN	0.	0.4460E-01	0.2218E-01

CLEARANCE, MICROINCHES	350	450	550
LOAD, LB	0.4838E+01	0.3280E+01	0.2217E+01
POWER, WATTS	0.3153E+02	0.2593E+02	0.2216E+02
RELATIVE SWASH AMPLITUDE	0.5248E-01	0.5725E-01	0.7079E-01
MAX DISTORTION TO CLEAR RAT.	0.1048E+00	0.6494E-01	0.4415E-01

CR-2421-1

Figure 31. Helium-Lubricated Spiral Groove Thrust Bearing Parameters and Performance (Maximum Speed, One Side, Ratio of Outside Diameter to Inside Diameter = 2.06)

AXIAL FREQUENCY, CPM	0.4426E+05	0.3737E+05	0.3040E+05
TILT FREQUENCY, CPM	0.1445E+06	0.1220E+06	0.9925E+05
AXIAL STIFFNESS LB/IN	0.1681E+05	0.1198E+05	0.7930E+04
TILT STIFFNESS IN-LB/RAD	0.1472E+04	0.1049E+04	0.6943E+03
EFFECT. VIS. LB-SEC/IN**2	0.2742E-08	0.2808E-08	0.2852E-08
REYNOLDS NO.	0.2597E+02	0.3339E+02	0.4081E+02
LAMBDA	0.2634E+02	0.1594E+02	0.1067E+02
CONVECTIVE INERTIA RATIO	0.1648E-02	0.2724E-02	0.4069E-02
TRANSIENT INERTIA RATIO	0.1025E+00	0.9598E-01	0.8618E-01
LOCAL COMPRESS. RATIO, SS	0.2060E+00	0.1246E+00	0.8341E-01
LOCAL COMPRESS. RATIO, DYN	0.1061E-01	0.5419E-02	0.2951E-02

CLEARANCE, MICROINCHES	650	750	850
LOAD, LB	0.1522E+01	0.1068E+01	0.7676E+00
POWER, WATTS	0.1943E+02	0.1736E+02	0.1572E+02
RELATIVE SWASH AMPLITUDE	0.9200E-01	0.1213E+00	0.1597E+00
MAX DISTORTION TO CLEAR RAT.	0.3195E-01	0.2419E-01	0.1895E-01
AXIAL FREQUENCY, CPM	0.2453E+05	0.1989E+05	0.1628E+05
TILT FREQUENCY, CPM	0.8008E+05	0.6492E+05	0.5315E+05
AXIAL STIFFNESS LB/IN	0.5163E+04	0.3393E+04	0.2274E+04
TILT STIFFNESS IN-LB/RAD	0.4520E+03	0.2971E+03	0.1991E+03
EFFECT. VIS. LB-SEC/IN**2	0.2883E-08	0.2906E-08	0.2924E-08
REYNOLDS NO.	0.4823E+02	0.5564E+02	0.6306E+02
LAMBDA	0.7638E+01	0.5737E+01	0.4467E+01
CONVECTIVE INERTIA RATIO	0.5684E-02	0.7567E-02	0.9719E-02
TRANSIENT INERTIA RATIO	0.7641E-01	0.6777E-01	0.6046E-01
LOCAL COMPRESS. RATIO, SS	0.5972E-01	0.4486E-01	0.3492E-01
LOCAL COMPRESS. RATIO, DYN	0.1705E-02	0.1038E-02	0.6616E-03

CLEARANCE, MICROINCHES	950	1050	1150
LOAD, LB	0.5639E+00	0.4228E+00	0.3229E+00
POWER, WATTS	0.1439E+02	0.1328E+02	0.1235E+02
RELATIVE SWASH AMPLITUDE	0.2085E+00	0.2690E+00	0.3430E+00
MAX DISTORTION TO CLEAR RAT.	0.1525E-01	0.1253E-01	0.1048E-01
AXIAL FREQUENCY, CPM	0.1348E+05	0.1129E+05	0.9551E+04
TILT FREQUENCY, CPM	0.4400E+05	0.3684E+05	0.3118E+05
AXIAL STIFFNESS LB/IN	0.1559E+04	0.1093E+04	0.7827E+03
TILT STIFFNESS IN-LB/RAD	0.1365E+03	0.9569E+02	0.6853E+02
EFFECT. VIS. LB-SEC/IN**2	0.2938E-08	0.2950E-08	0.2960E-08
REYNOLDS NO.	0.7048E+02	0.7790E+02	0.8532E+02
LAMBDA	0.3576E+01	0.2927E+01	0.2440E+01
CONVECTIVE INERTIA RATIO	0.1214E-01	0.1483E-01	0.1779E-01
TRANSIENT INERTIA RATIO	0.5436E-01	0.4927E-01	0.4500E-01
LOCAL COMPRESS. RATIO, SS	0.2796E-01	0.2289E-01	0.1908E-01
LOCAL COMPRESS. RATIO, DYN	0.4385E-03	0.3006E-03	0.2120E-03

CR-2421-2

Figure 31. Helium-Lubricated Spiral Groove Thrust Bearing Parameters and Performance (Maximum Speed, One Side, Ratio of Outside Diameter to Inside Diameter = 2.06) (Continued)

	1250	1350	1450
CLEARANCE, MICROINCHES			
LOAD, LB	0.2507E+00	0.1975E+00	0.1577E+00
POWER, WATTS	0.1155E+02	0.1085E+02	0.1024E+02
RELATIVE SWASH AMPLITUDE	0.4321E+00	0.5382E+00	0.6632E+00
MAX DISTORTION TO CLEAR RAT.	0.8896E-02	0.7645E-02	0.6640E-02
AXIAL FREQUENCY, CPM	0.8162E+04	0.7038E+04	0.6117E+04
TILT FREQUENCY, CPM	0.2665E+05	0.2297E+05	0.1997E+05
AXIAL STIFFNESS LB/IN	0.5717E+03	0.4250E+03	0.3211E+03
TILT STIFFNESS IN-LB/RAD	0.5005E+02	0.3721E+02	0.2811E+02
EFFECT. VIS. LB-SEC/IN**2	0.2968E-08	0.2975E-08	0.2981E-08
REYNOLDS NO.	0.9274E+02	0.1002E+03	0.1076E+03
LAMBDA	0.2065E+01	0.1771E+01	0.1535E+01
CONVECTIVE INERTIA RATIO	0.2102E-01	0.2452E-01	0.2828E-01
TRANSIENT INERTIA RATIO	0.4139E-01	0.3830E-01	0.3565E-01
LOCAL COMPRESS. RATIO, SS	0.1615E-01	0.1385E-01	0.1200E-01
LOCAL COMPRESS. RATIO, DYN	0.1534E-03	0.1134E-03	0.8542E-04

	1550
CLEARANCE, MICROINCHES	
LOAD, LB	0.1274E+00
POWER, WATTS	0.9698E+01
RELATIVE SWASH AMPLITUDE	0.8094E+00
MAX DISTORTION TO CLEAR RAT.	0.5822E-02
AXIAL FREQUENCY, CPM	0.5356E+04
TILT FREQUENCY, CPM	0.1743E+05
AXIAL STIFFNESS LB/IN	0.2461E+03
TILT STIFFNESS IN-LB/RAD	0.2155E+02
EFFECT. VIS. LB-SEC/IN**2	0.2986E-08
REYNOLDS NO.	0.1150E+05

	LAMBDA
CONVECTIVE INERTIA RATIO	0.3232E-01
TRANSIENT INERTIA RATIO	0.3334E-01
LOCAL COMPRESS. RATIO, SS	0.1050E-01
LOCAL COMPRESS. RATIO, DYN	0.6545E-04

CR-2421-3

Figure 31. Helium-Lubricated Spiral Groove Thrust Bearing Parameters and Performance (Maximum Speed, One Side, Ratio of Outside Diameter to Inside Diameter = 2.06) (Continued)

The following input is printed with the output:

- Title indicating the gas, used as the lubrication
- Ratio of the outside diameter to the inside diameter
- Shaft rotational speed (rpm)
- Gas temperature ($^{\circ}$ R), used in computing the viscosity
- Bearing inside diameter (inches)
- Ambient pressure (psia)

- Thrust runner swash angle (peak to peak) (degrees)
- Weight density of the bearing material (pounds per cubic inch), used in calculating the moment of inertia for the tilt frequency output
- Shaft weight (pounds), used in computing the axial frequency output
- Groove-length-to-bearing-width ratio (nondimensional), measured radially
- Groove-length-to-ridge-width ratio (nondimensional), measured at a constant radius
- Groove angle (degrees), measured between tangent-to-groove and radial coordinates
- Coefficient of thermal expansion for the bearing material (inches per inch $^{\circ}$ F), used to compute dishing due to bearing film shear heating
- Coefficient of thermal expansion for the thrust runner material (inches per inch $^{\circ}$ F), used to compute dishing due to bearing film shear heating
- Minimum allowable ridge width (square inches) and minimum thickness of the ridge, used to compute the maximum bearing number
- Clearance at which the load capacity is to be optimized (inches)

The output consists of a group of overall performance factors that include:

- Mach number (nondimensional) based on helium and the thrust bearing outside diameter, used to indicate the potential of the compressibility effects at the tip of the thrust bearing
- Viscosity (pound-seconds per square inch), based on the appropriate gas at the input temperature.
- Molecular mean free path, which accounts for the deviation of gas from a continuum as a function of the temperature, pressure, and clearance space and which is reflected as a change in the effective viscosity
- Minimum number of grooves computed on the basis that the pressure ripple across the grooves is 10 percent of the pressure rise along the grooves, related to the assumption that the edge correction is negligible
- Maximum number of grooves, which is a manufacturing and structural consideration based on an input quantity that limits the ridge wall thickness
- Estimated moment of inertia of the bearing, with respect to a diameter, through the midplane (pound-square second)
- Assumed thickness of the thrust disk, based on dividing the annular width of the thrust disk by 2.5

- Bearing outside diameter obtained from the inside diameter and the ratio of the outside diameter to the inside diameter
- Groove depth (inches)
- Thrust runner tip speed (feet per second)

Individual performance items are then tabulated in 16 columns, for one thrust face only, with a heading for the land film clearance in microinches:

- Load capacity (pounds), including the 0.75 safety factor referred to above.
- Power loss (watts)
- Relative swash amplitude (nondimensional), the ratio of the calculated swash amplitude to the maximum swash amplitude at contact (The calculated swash amplitude is based on the swash angle, the film tilt stiffness, and the moment of inertia of the bearing, calculated on the basis of an assumed thickness-to-diameter ratio.)
- Ratio of the distorted minimum film thickness to the undistorted minimum film thickness (Distortion is assumed to be parabolic, and the heat input is calculated from the bearing power loss. Thermal expansion coefficients for the bearing and runner are part of the program input.)
- Axial frequency (cycles per minute), the natural frequency based on the axial film stiffness and the weight of the rotor
- Tilt frequency (cycles per minute), the natural frequency based on the film tilt stiffness and the bearing moment of inertia
- Axial stiffness (pounds per inch), including the 0.75 safety factor referred to above
- Tilt stiffness of the gas film (pounds per radian)
- Effective viscosity (pound-second per square inch), used in calculating bearing performance and based on the film thickness, viscosity, and molecular mean free path (The mean free path effect reduces the viscosity and therefore reduces the load capacity. This effect becomes more pronounced as the film thickness decreases.)
- Reynolds number (nondimensional), the ratio of inertia to viscous forces, indicating whether the assumption of laminar flow used in the present analysis is valid (The value should be less than 1500.)
- Convective inertia ratio (nondimensional), based on the groove width and the tangential velocity, indicating whether the assumption of the negligible inertia effect is valid (The ratio should be very much less than one.)
- Transient inertia ratio (nondimensional), based on the nominal bearing gap and the axial oscillation, indicating whether the as-

sumption of the negligible inertia effect is valid (The ratio should be very much less than one.)

- Local compressibility ratio, steady-state (nondimensional), based on the tangential velocity, indicating whether the assumption of quasi-incompressibility is valid (In this analysis, a sectionally linear pressure profile is assumed. To be valid, the magnitude of the circumferential pressure fluctuation must be small compared to the local pressure level. This ratio should be very much less than one.)
- Local compressibility ratio, dynamic (nondimensional), based on axial oscillation and referring to the assumption defined above (This ratio should be very much less than one.)

Figures 32 and 33 give the performance, at design and maximum speeds, resulting from the interaction of both thrust faces, with a total axial clearance between the thrust bearings set at 0.002 inch and the spiral groove depth set at 0.00152 inch. Figures 34 and 35 give load, stiffness, and power loss for the double-acting bearing for both design and maximum speed conditions. All graphs are given in terms of clearance on the side, with maximum load.

The spiral grooves are manufactured by photoetching using a mask. The nomenclature used in drawing the mask is given in Figure 9; the coordinates for the mask are given in Figure 36.

Table 6 is a design summary for the Advanced Research Projects Agency spiral groove thrust bearing.

Table 6
TURBOALTERNATOR SPIRAL GROOVE THRUST
BEARING DESIGN SUMMARY

Characteristic	Parameter
Outside diameter	1.125 inches
Inside diameter	0.287, 0.547 inch
Inside diameter, grooved region	0.703 inch
Number of grooves	30
Groove angle	71.2 degrees
Groove width to ridge width at constant radius	1.93 (nondimensional)
Angular spacing at inside diameter of grooved region	
Groove width	7.904 degrees
Ridge width	4.096 degrees
Depth of groove	0.00152 inch
Collar swash angle	0.00195 degree
Total axial clearance	0.002 inch
Bearing material, coating, and surface finish	Beryllium copper, none, 8 rms
Collar material, coating, and surface finish	304L, nitride, 4 rms

CR-2427

```

RUN NO. 1

***INPUT***
SPEED, RPM          0.1413E 04  GROOVE 11/RND WIDTH  0.7100E 00
TEMPERATURE, DEGR.  0.1440E 03  GROOVE/P1001 WIDTH  0.1910E 01
AMBIENT PRESS., PSIA 0.1050E 02  GROOVE ANGLE, DEG  0.7120E 02
READING ID, IN.      0.1125E 01  INITIAL CLEAR, IN  0.5000E-04
READING ID, IN.      0.5470E 00  TOTAL AXIAL CLEAR, IN 0.2000E-02
CLEAR DPT BY DPTH, IN 0.5000E-01

***OUTPUT***
CLEARANCE, MICROINCHES  50.0000  97.5000  145.0000  192.5000  240.0000  287.5000  335.0000
LOAD, LB                0.3374E 01  0.3267E 01  0.2948E 01  0.2609E 01  0.2236E 01  0.1881E 01  0.1554E 01
POWER, WATTS            0.1005E 02  0.2271E 02  0.1657E 02  0.1334E 02  0.1135E 02  0.1001E 02  0.0904E 01
AXIAL STIFFNESS LB/IN   0.      0.4549E 04  0.6540E 04  0.7237E 04  0.7105E 04  0.6659E 04  0.5876E 04
TILT STIFFNESS IN-LB/RAD 0.      0.3075E 03  0.5731E 03  0.6122E 03  0.6277E 03  0.5818E 03  0.5134E 03

CLEARANCE, MICROINCHES  382.5000  430.0000  477.5000  525.0000  572.5000  620.0000  667.5000
LOAD, LB                0.1208E 01  0.1045E 01  0.0800E 00  0.0612E 00  0.5004E 00  0.4532E 00  0.3644E 00
POWER, WATTS            0.0114E 01  0.2750E 01  0.7317E 01  0.6904E 01  0.6470E 01  0.6445E 01  0.6255E 01
AXIAL STIFFNESS LB/IN   0.0111E 04  0.4179E 04  0.3441E 04  0.2819E 04  0.2311E 04  0.1904E 04  0.1503E 04
TILT STIFFNESS IN-LB/RAD 0.4377E 03  0.1651E 03  0.3007E 03  0.2463E 03  0.2019E 03  0.1663E 03  0.1303E 03

CLEARANCE, MICROINCHES  715.0000  762.5000  810.0000  857.5000  905.0000  952.5000  1000.0000
LOAD, LB                0.2007E 00  0.2271E 00  0.1726E 00  0.1244E 00  0.8056E-01  0.3959E-01  0.
POWER, WATTS            0.0101E 01  0.4970E 01  0.5002E 01  0.5009E 01  0.5759E 01  0.5729E 01  0.5710E 01
AXIAL STIFFNESS LB/IN   0.1141E 04  0.1142E 04  0.0946E 03  0.0946E 03  0.0242E 03  0.7835E 03  0.7707E 03
TILT STIFFNESS IN-LB/RAD 0.1141E 03  0.0970E 02  0.0724E 02  0.0701E 02  0.7201E 02  0.6045E 02  0.6779E 02

```

Figure 32. Helium-Lubricated Spiral Groove Thrust Bearing Performance (Design Speed, Two Sides, Ratio of Outside Diameter to Inside Diameter = 2.06)

```

RUN NO. 2

***INPUT***
SPEED, RPM          0.2000E 04  GROOVE 11/RND WIDTH  0.7100E 00
TEMPERATURE, DEGR.  0.5050E 03  GROOVE/P1001 WIDTH  0.1910E 01
AMBIENT PRESS., PSIA 0.1050E 02  GROOVE ANGLE, DEG  0.7120E 02
READING ID, IN.      0.1125E 01  INITIAL CLEAR, IN  0.5000E-04
READING ID, IN.      0.5470E 00  TOTAL AXIAL CLEAR, IN 0.2000E-02
CLEAR DPT BY DPTH, IN 0.5000E-01

***OUTPUT***
CLEARANCE, MICROINCHES  50.0000  97.5000  145.0000  192.5000  240.0000  287.5000  335.0000
LOAD, LB                0.7527E 01  0.0705E 01  0.0540E 01  0.7035E 01  0.6902E 01  0.5914E 01  0.4971E 01
POWER, WATTS            0.1250E 03  0.0744E 02  0.6093E 02  0.5704E 02  0.5052E 02  0.4534E 02  0.4150E 02
AXIAL STIFFNESS LB/IN   0.      0.      0.0000E 04  0.1622E 05  0.1892E 05  0.1895E 05  0.1740E 05
TILT STIFFNESS IN-LB/RAD 0.      0.      0.7052E 03  0.1417E 04  0.1653E 04  0.1650E 04  0.1528E 04

CLEARANCE, MICROINCHES  382.5000  430.0000  477.5000  525.0000  572.5000  620.0000  667.5000
LOAD, LB                0.4124E 01  0.1397E 01  0.2783E 01  0.2273E 01  0.1052E 01  0.1503E 01  0.1212E 01
POWER, WATTS            0.1055E 02  0.1623E 02  0.3430E 02  0.3007E 02  0.3164E 02  0.3063E 02  0.2980E 02
AXIAL STIFFNESS LB/IN   0.1535E 05  0.1306E 05  0.1091E 05  0.0040E 04  0.7477E 04  0.0707E 04  0.5194E 04
TILT STIFFNESS IN-LB/RAD 0.1341E 04  0.1141E 04  0.0532E 03  0.7097E 03  0.6532E 03  0.5422E 03  0.4537E 03

CLEARANCE, MICROINCHES  715.0000  762.5000  810.0000  857.5000  905.0000  952.5000  1000.0000
LOAD, LB                0.0671E 00  0.7584E 00  0.5772E 00  0.4164E 00  0.2700E 00  0.1320E 00  0.
POWER, WATTS            0.2913E 02  0.2050E 02  0.2016E 02  0.2784E 02  0.2762E 02  0.2749E 02  0.2744E 02
AXIAL STIFFNESS LB/IN   0.4399E 04  0.3785E 04  0.3322E 04  0.2905E 04  0.2756E 04  0.2424E 04  0.2501E 04
TILT STIFFNESS IN-LB/RAD 0.3043E 03  0.1304E 03  0.2007E 03  0.2600E 03  0.2400E 03  0.2202E 03  0.2255E 03

TRACE OF CALLS IN REVERSE ORDER
CALLING ROUTINE 10  ARGUMENT 1  ARGUMENT 2  ARGUMENT 3  ARGUMENT 4  ARGUMENT 5
.FPOF. 31  026751  000000000042  350625010233
.FPOF. 1434 031545
.FPOF. 5  046262  000000000005
END OF FILE READING FILE CODE 10
OPTIONAL RETURN NOT REQUESTED

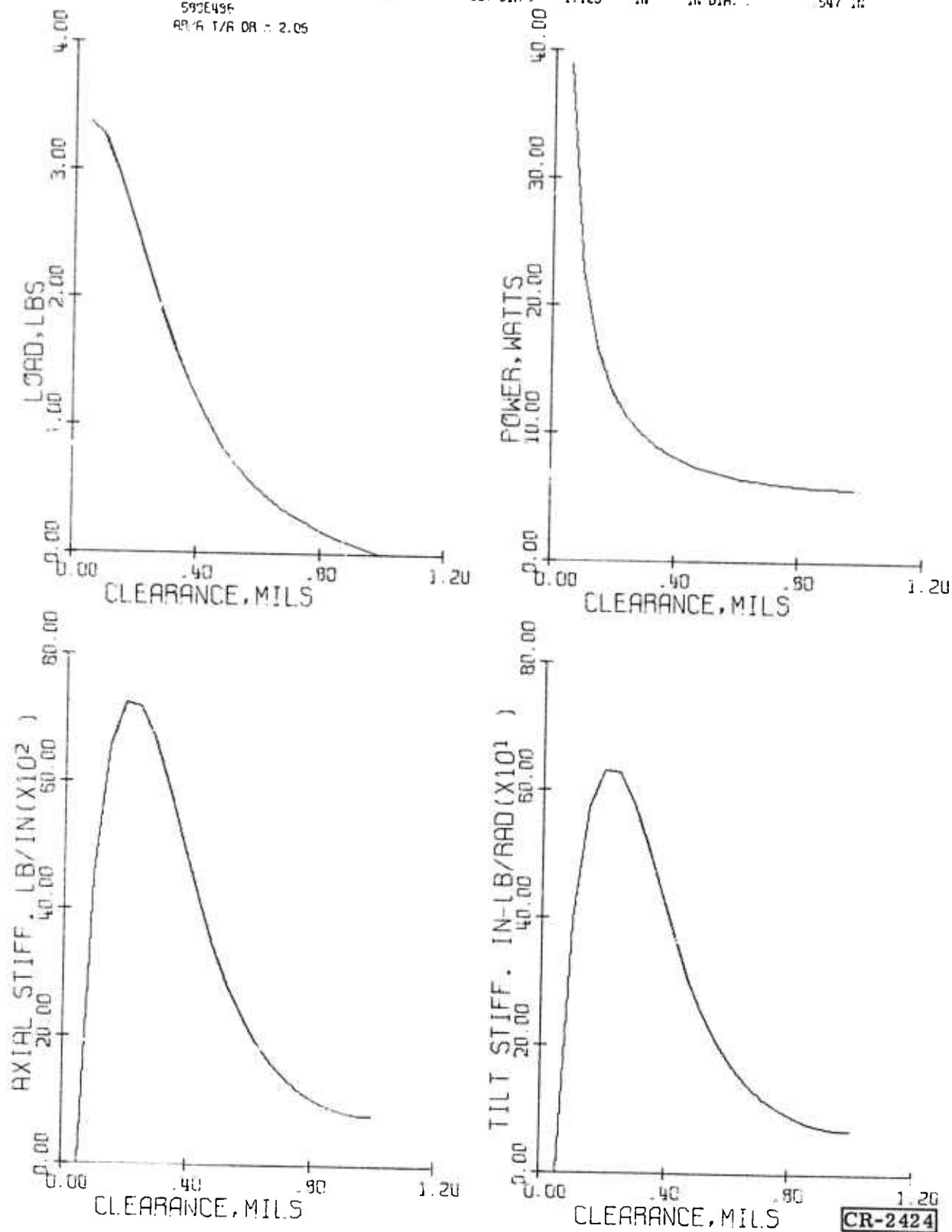
```

Figure 33. Helium-Lubricated Spiral Groove Thrust Bearing Performance (Maximum Speed, Two Sides, Ratio of Outside Diameter to Inside Diameter = 2.06)

HEI IUM LUBRICATED.
 SPEED = 141300
 TEMP = 144.0
 592E496
 R/A T/A OR = 2.05

PERFORMANCE AS A FUNCTION OF LOADED SIDE CLEARANCE

RPM 19500 PSIA 1000 TOT AXIAL CLEAR = 2.0 MILS
 DEG R 1.125 IN IN DIA. = 547 IN



CR-2424

Figure 34. Spiral Groove Thrust Bearing Characteristics (Design Speed)

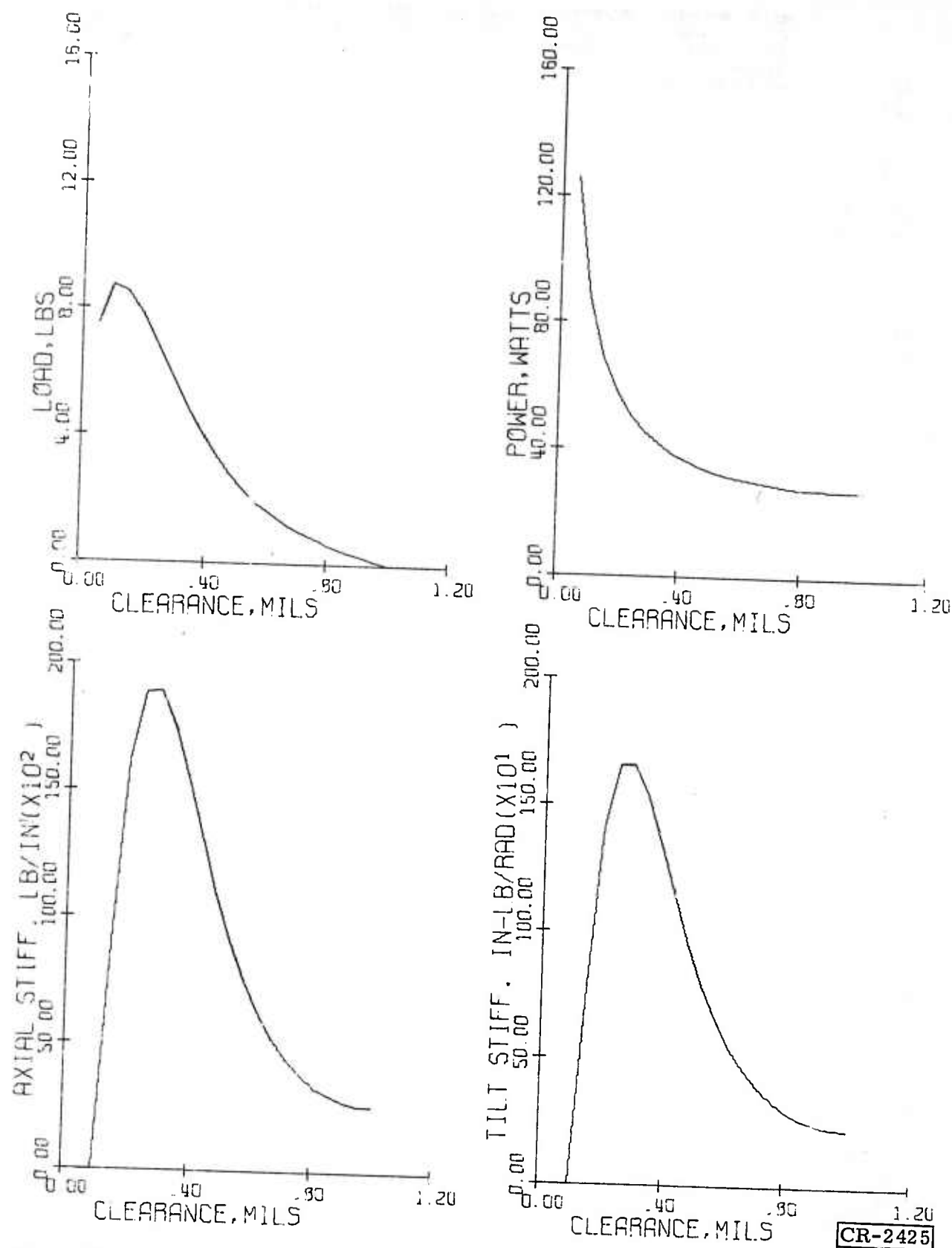


Figure 35. Spiral Groove Thrust Bearing Characteristics (Maximum Speed)

DEFINITIONS

RI = RADIAL COORDINATE OF INBOARD EDGE OF SPIRAL GROOVE
 RO = RADIAL COORDINATE OF OUTBOARD EDGE OF SPIRAL GROOVE
 THETA = GROOVE ANGULAR COORDINATE MEASURED CLOCKWISE FOR ONE THRUST FACE AND COUNTER CLOCKWISE FOR THE OTHER
 WRAP ANGLE = THE ANGULAR EXTENT OF A GROOVE MEASURED FROM OD OF GROOVED REGION TO ID OF GROOVED REGION

SPECIFICATIONS

NUMBER OF GROOVES = 30
 OD OF BEARING = 1.125 INCHES
 ID OF BEARING = 0.547 INCHES
 ID OF GROOVED REGION = 0.703 INCHES
 GROOVE ANGLE = 71.200 DEGREES
 GROOVE TO RIDGE WIDTH RATIO AT CONSTANT RADIUS = 1.930
 GROOVE WRAP ANGLE = 79.134 DEGREES
 ANGULAR SPACING AT ID OF GROOVED REGION
 GROOVE WIDTH = 7.904 DEGREES
 RIDGE WIDTH = 4.096 DEGREES
 COORDINATES OF FIRST GROOVE
 RADIUS SCALE FACTOR = 1.000

THETA	RI	RO
DEG.	IN.	IN.
0	0.000	0.352
5	0.345	0.362
10	0.356	0.373
15	0.367	0.384
20	0.378	0.396
25	0.389	0.408
30	0.401	0.420
35	0.413	0.433
40	0.425	0.446
45	0.438	0.459
50	0.451	0.473
55	0.465	0.487
60	0.479	0.502
65	0.493	0.517
70	0.508	0.533
75	0.524	0.549
80	0.539	0.566
85	0.556	0.583

CR-2426

Figure 36. Radial and Angular Coordinates for Drawing Logarithmic Spiral Grooves in Flat Thrust Face

TURBINE WHEEL THERMAL AND STRESS ANALYSIS

The impulse and reaction turbine wheels for the 80°K turboalternator tests have been designed. The extreme operating conditions for both wheels are:

<u>Condition</u>	<u>Temperature (°K)</u>	<u>Speed (rpm)</u>
C	80	150,000
W	320	200,000

The thermostructural response of both wheels to these operating conditions has been calculated using the finite element technique, which permits thermal and centrifugal effects to be treated simultaneously. The results are presented below.

IMPULSE WHEEL

The impulse wheel (Figure 37) is made of 6Al-4V titanium and fits onto a stainless steel shaft.* The thermal expansion of titanium is less than that of

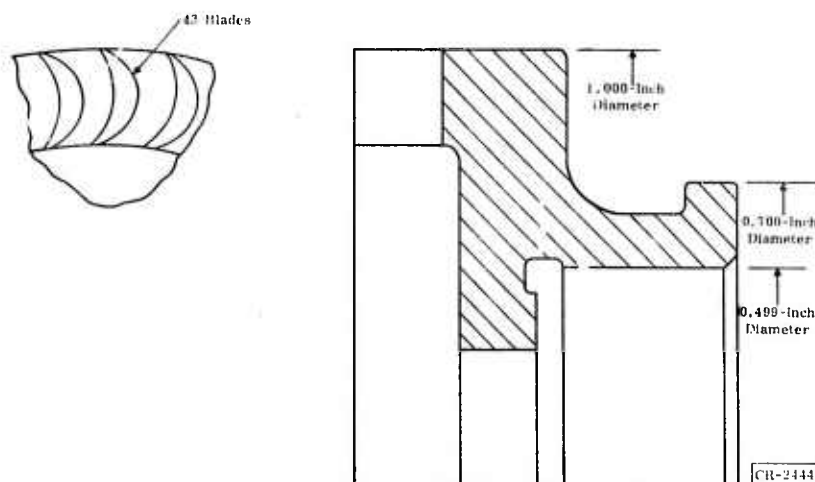


Figure 37. Impulse Wheel

steel. The wheel-shaft assembly is made at room temperature; therefore, as Condition C is approached, the wheel contracts less than the shaft and becomes loose on the shaft, unless the wheel-shaft assembly is made with an interference fit at room temperature. The stresses due to the interference fit are reduced as the temperature is lowered from room temperature and are increased as the temperature is raised from room temperature. The thermal stresses are, therefore, much higher for Condition W than for Condition C. Because

*It was originally planned that this wheel would be made of 6061-T6 aluminum, to minimize the manufacturing effort. However, the difference in thermal expansions between the wheel and the shaft result in prohibitively high (100,000 psi) wheel stresses at Condition C.

Condition W also has a higher speed, this is the critical condition, from a stress standpoint.*

The process followed in the analysis is to determine the room temperature interference required to maintain wheel-to-shaft contact in Condition C and then determine the stresses in Condition W with this interference fit.

The interference fit required is 0.5 mil (0.0005 inch) on the radius or 1.0 mil (0.001 inch) on the diameter. This fit is sufficient to offset the differential thermal expansion and centrifugal forces tending to separate the wheel and shaft in Condition C, so the wheel can resist the operating torque. The states of stress and displacement in the wheel at Condition C, with this value of interference fit, are presented in Figures 38 and 39. Because the state of stress is triaxial, stress results are presented in the form of von Mises effective stress contours.

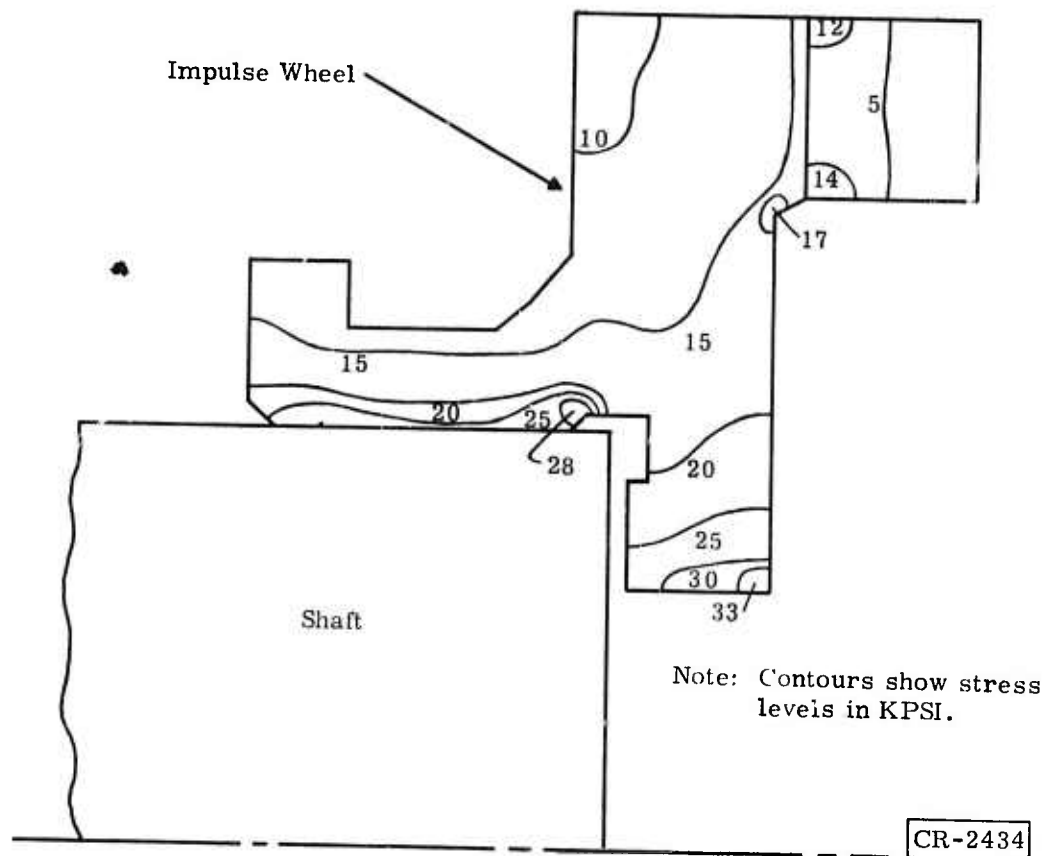


Figure 38. Impulse Wheel Effective Stress Contours (0.5-Mil Fit on Radius, Condition C)

*The wheel is subjected to Condition C for most of its life; it is subjected to Condition W for only brief periods. Thus, the stresses at Condition C are important in determining its useful life in regard to creep behavior.

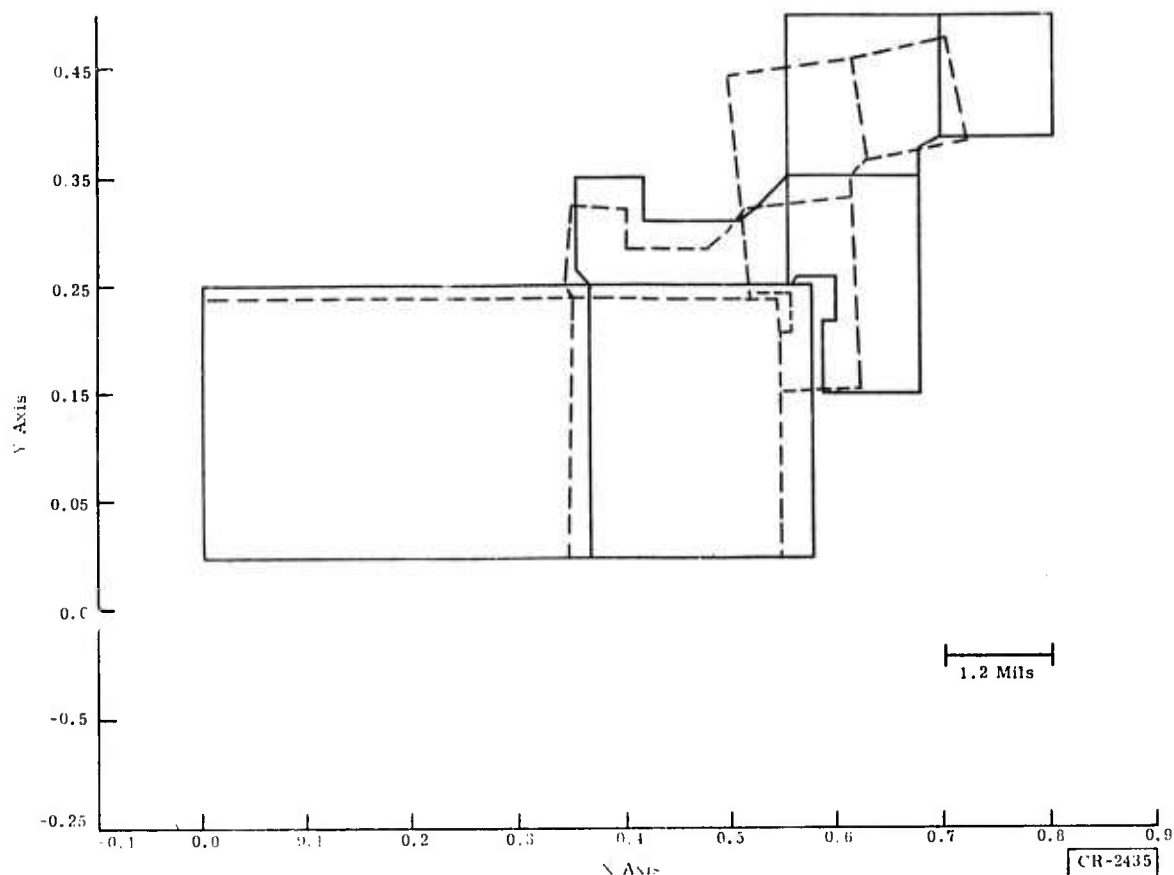


Figure 39. Impulse Wheel Displacement (0.5-Mil Fit on Radius, Condition C)

The states of stress and displacement in the wheel at Condition W were calculated using the 0.5-mil (on the radius) interference fit. These fits are presented in Figures 40 and 41.

From Figures 38 and 40, it is observed that the maximum effective stresses in the impulse wheel are 33,000 psi for Condition C and 59,000 psi for Condition W. This wheel must be designed to withstand local yielding (instantaneous plasticity) and long-term creep. The yield stress of 6Al-4V titanium is above 120,000 psi for Condition W (the exact value depends on the processing) and will be even greater for Condition C. Because the yield stress is much higher than the maximum effective (applied) stress for both conditions, local yielding will not occur.

Because the wheel is exposed to Condition W for only a very small fraction of its lifetime, long-term creep, if it occurs, will occur mainly for Condition C. A simple technique used to design against creep in titanium in the aircraft industry is to assume that no creep will occur if the applied stresses are less than one-third of the yield stress. For Condition C, this situation is satisfied. A more exact method used to design against creep is to use the Larson-Miller parameter, ϕ , and experimentally obtained creep-rupture curves, as shown

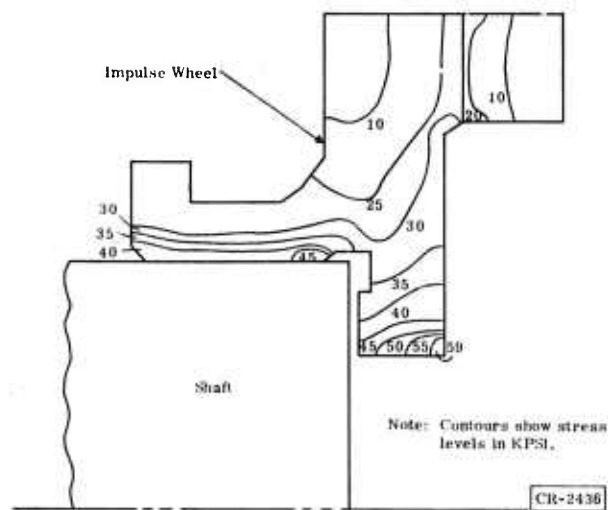


Figure 40. Impulse Wheel Effective Stress Contours
(0.5-Mil Fit on Radius, Condition W)

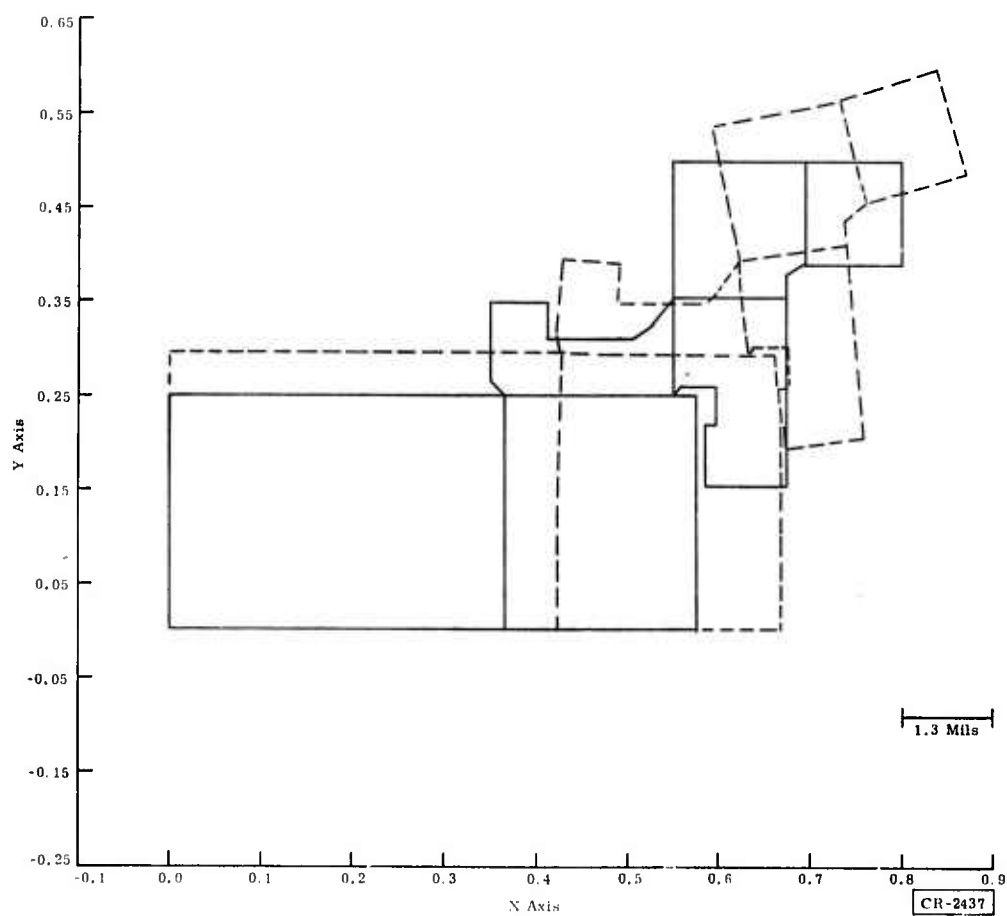


Figure 41. Impulse Wheel Displacement (0.5-Mil Fit on Radius,
Condition W)

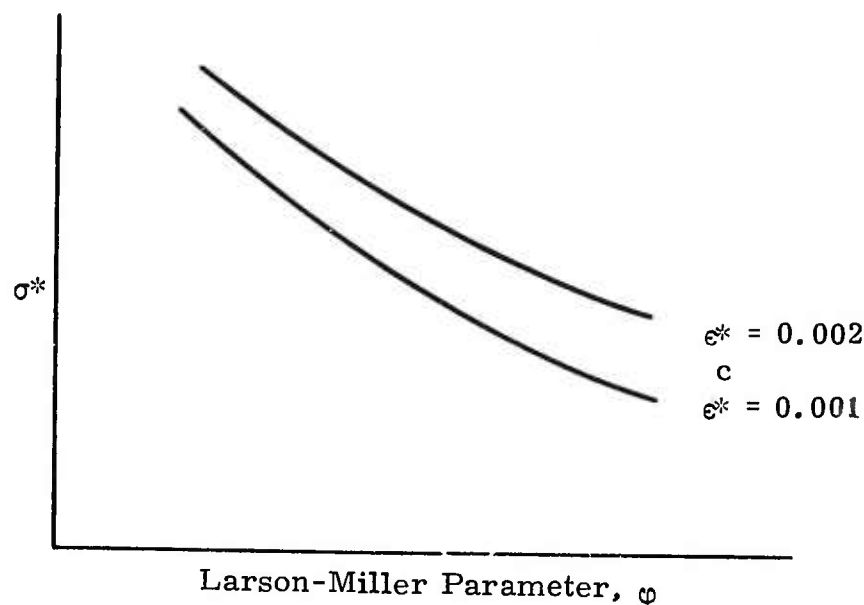


Figure 42. Larson-Miller Parameter (ϕ) and Experimentally Obtained Creep-Rupture Curves

schematically in Figure 42. Such curves define the maximum applied stress, σ^* , that can be present if a structure is to creep no more than amount ϵ^* .

The parameter, ϕ , is defined for titanium by the relationship:

$$\phi = T (20 + \log_{10} t) \times 10^{-3}$$

where T is the temperature ($^{\circ}\text{R}$) and t is the exposure time (hours). It is desired that the impulse wheel have a design life of 20 years. Thus, for Condition W the value of ϕ is 15.2, and for Condition C the value of ϕ is 1.9. From the General Electric Materials Data Book (Ref. 2), the value of ϕ^* corresponding to $\epsilon^* = 0.001$ (1/10-percent creep) is greater than 85,000 psi for both Conditions C and W. The applied stresses for both conditions are below this level.

Thus it can be shown, using two different techniques, that the impulse wheel will have the desired lifetime (creep will be less than 1/10 percent) of 20 years.

The value of the interference fit is critical. If the fit is too large, the stresses in the wheel hub for Condition W will be large enough to cause local yielding; if it is too small, the radial contact stresses at the wheel-shaft interface will become zero, and the wheel will slip on the shaft. Results obtained using different values of interference fit have been used to obtain the curves present in Figures 43 and 44. Figure 43 shows the value of the minimum (radial compression) contact stress in the interface region as a function of the value of the interference fit for Condition C. The acceptable minimum value of the contact stress depends upon the torque to be transmitted and the size of the contact region. Arbitrarily selecting this minimum value to be 1000 psi,

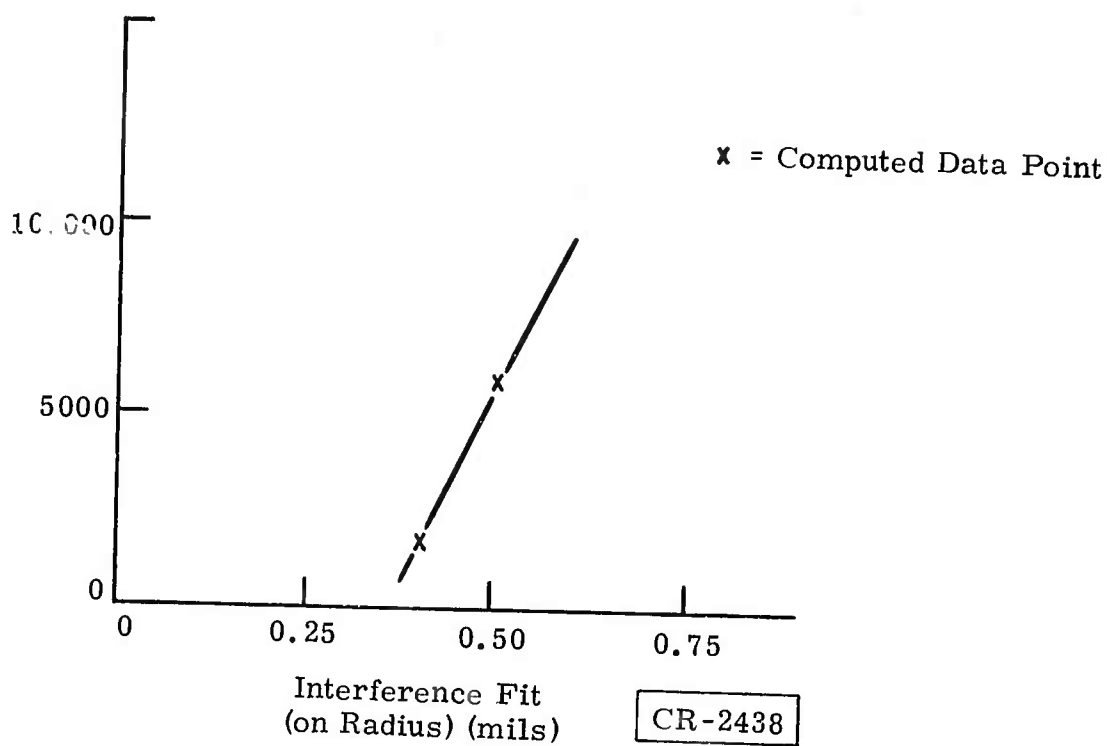


Figure 43. Minimum Contact Stress Versus Interference Fit (Condition C)

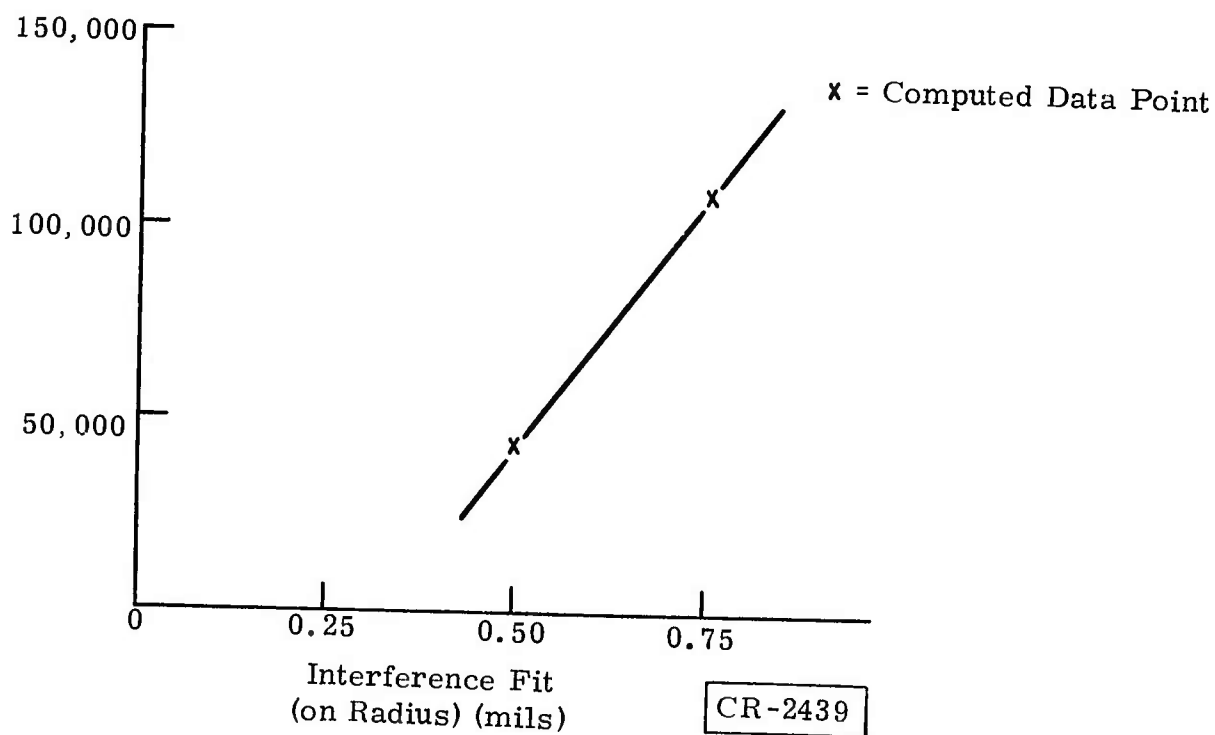


Figure 44. Maximum Effective Stress in Hub Versus Interference Fit (Condition W)

Figure 43 shows that the lowest acceptable interference fit is about 0.4 mils (on the radius). Figure 44 shows the value of the maximum effective stress in the hub as a function of the value of the interference fit for Condition W. The maximum value of the effective stress must be less than the yield stress of the wheel. For a yield stress of 120,000 psi, Figure 44 shows that the largest acceptable interference fit is 0.8 mil (on the radius). Thus, the interference fit, δ , desired can be given as:

$$\delta = 0.5^{+0.3}_{-0.1} \text{ mil}$$

REACTION WHEEL

The reaction wheel is shown in Figure 45. Because the wheel is made of 6Al-4V titanium and fits onto a stainless steel shaft, its thermostructural re-

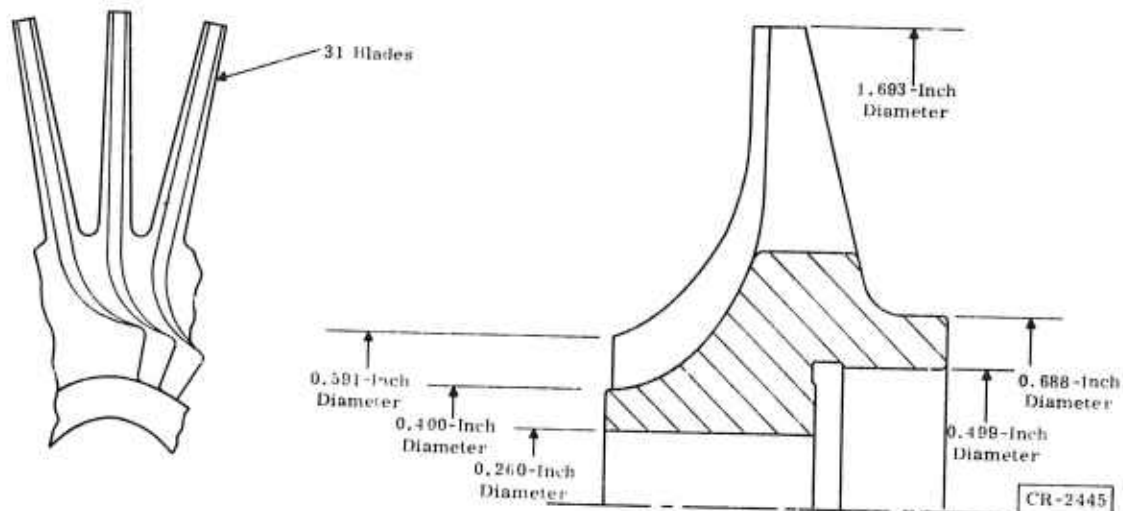


Figure 45. Reaction Wheel

sponse is similar to that of the impulse wheel, and the same process is followed in its analysis as was followed for the impulse wheel (to determine the room temperature interference required to maintain wheel-to-shaft contact in Condition C and then to determine the stresses in Condition W with this interference fit).

The interference fit required is 0.5 mil (0.0005 inch) on the radius or 1.0 mil (0.001 inch) on the diameter. This fit is sufficient to offset the differential thermal expansion and centrifugal forces tending to separate the wheel and shaft in Condition C, so the wheel can resist the operating torque. The states of stress and displacement in the wheel at Condition C, with this value of interference fit, are presented in Figures 46 and 47. As in the case of the impulse wheel, the state of stress is presented in the form of von Mises effective stress contours. The state of stress in the wheel at Condition W was calculated using the 0.5-mil (on the radius) interference fit (Figure 48).

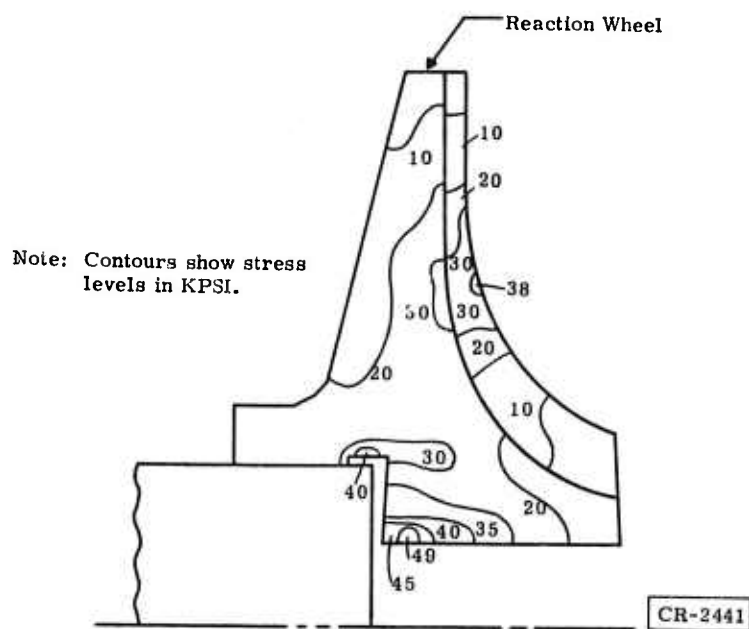


Figure 46. Reaction Wheel Effective Stress Contours (0.5-Mil Fit on Radius, Condition C)

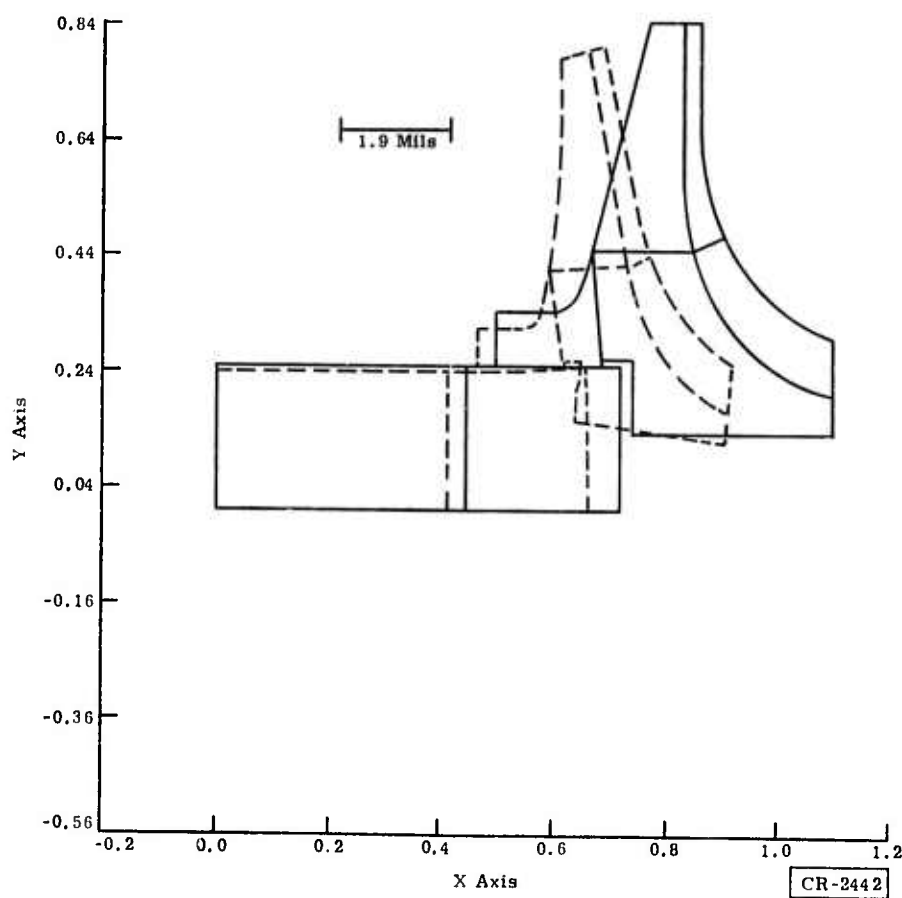


Figure 47. Reaction Wheel Displacements (0.5-Mil Fit on Radius, Condition C)

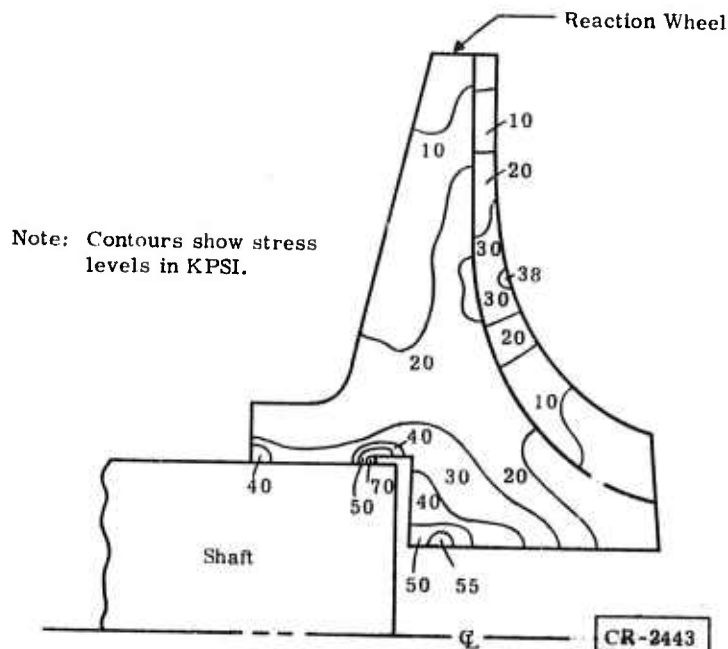


Figure 48. Reaction Wheel Effective Stress Contours (0.5-Mil Fit on Radius, Condition W)

From Figures 46 and 48, it is observed that the maximum effective stresses in the reaction wheel are 49,000 psi for Condition C and 70,000 psi for Condition W. By the same arguments used for the impulse wheel, it can be shown that local yielding will not occur for the reaction wheel. Similarly, because this wheel is subjected to the same exposure temperature and life-time requirements as the impulse wheel, the values of the Larson-Miller parameter, ϕ , are 1.9 for Condition C and 15.2 for Condition W. Because the reaction wheel is made of 6Al-4V titanium, the value of σ^* corresponding to $\epsilon^* = 0.001$ is greater than 85,000 psi for both Conditions C and W. The applied stresses for both conditions are below this value; thus, the reaction wheel will have the desired lifetime of 20 years.

An analysis of the allowable limits on the interference fit was not made for this wheel, but the limits should be very close to those obtained for the impulse wheel, because the design of both wheels in the interface region is similar.

ALTERNATOR DESIGN BASIS

Methods for calculating alternator performance have been outlined in Reference 3. Also, basic design data relating the frequency, flux, and core loss were reported. These methods and results have been applied to predict performance of the Advanced Research Projects Agency Big Bertha alternator.

Special materials are used in the stator core and rotor field to maximize alternator efficiency. A nickel-iron-molybdenum alloy (79-16-4 percent) having

very low hysteresis and eddy current loss is used for the stator laminations. A cobalt-platinum permanent magnet field produces flux that is compatible in density with the stator material. There are negligible losses in the rotor. This magnet material is also compatible with the joining and surface hardening processes involved in its fabrication. An overall picture of the alternator features and performance is described in Table 7.

Table 7
CALCULATED ALTERNATOR FEATURES AND PERFORMANCE

Alternator Features	Performance (Computer Design D-30907)
<u>Stator</u>	
Outside diameter punching	1.804 inch
Inside diameter	0.558 inch
Length	0.874 inch
Material	Hymu 80, 0.004 inch
Number of slots	12
Spiral	21 degrees
Tooth width	0.084 inch
Circuits	2
Connection	Wye
Pitch	83.3 percent
Conductors per slot	48
Wire	21.0113 HF
Turns in series, per phase	48
Pitch factor	0.966
Distribution factor	0.966
Skew factor	0.993
Stacking factor	0.94
Resistance (85°K)	0.0903 ohms
Leakage reactance	4.70 ohms
<u>Rotor Field</u>	
Diameter	0.500 inch
Length	0.7815 inch
Material	Co-Pt
Air gap	0.029 inch
<u>Performance (85°K)</u>	
Power factor	1.0
Output	397.2 watts
Line-to-line volts, no load	118.2
Line-to-line volts, full load	116.3
Current	1.976 amperes
Current density	4930 amperes per square inch
Core loss	2.70 watts
Copper loss	1.06 watts
Electromagnetic efficiency	99.0 percent

CR-2455

This alternator is conservatively designed on the rising side of the efficiency curve. It appears by calculation that its output might be doubled with little, if any, sacrifice in efficiency. This feature may be particularly desirable during cooldown, when the upper turboalternator, which has the greatest burden for cooldown, is overloaded. Rated performance has been calculated at 85°K and is reported in Table 7. Its electromagnetic efficiency is 99.0 percent.

The alternator is so efficient, compared with its driving turbine, that optimization of the alternator frequency to increase its efficiency a mere 0.1 or 0.2 percent would probably degrade the turbine performance several percent. Hence, little or no recognition of optimum alternator speed has been used to influence the turbine design.

Bearing losses that are not included in the above analysis should not be completely ascribed to the turbine, except for the thrust bearing. Journal bearings do more than support the shaft weight, including the wheel and the field. They also hold critical alignments between the wheel, the nozzle, and the thrust runner assemblies. Division of the bearing losses would have necessarily been arbitrary. Therefore, the criteria for alternator performance was chosen as simply its electromagnetic efficiency, to preclude any argument as to what its share of the parasitic losses should have been.

The electrical circuit of this alternator has four parallel paths for the line current: two in circuits and two through conductors in-hand. This arrangement was made to reduce voltage, because low voltage reduces the need for heavy insulation, and the voltage should be significantly below the corona start voltage. There is also a heat leak penalty for carrying larger currents. The alternator lead heat leak with the optimum cross section alternator leads will be a total of about 0.24 watt, a small but significant amount, compared with the 3.76-watt loss in the alternator. A three-phase winding has the least current and copper section in its leads for the least number of phases and, hence, it has the least heat leak.

DESIGN FOR OPEN CYCLE TESTS

It is necessary to design the turboalternator so that it can be operated in the open cycle with stored gas, for both the bearing tests and the shock and vibration tests.

The turboalternator open cycle test station supplied by high-pressure helium trailers can provide a flow to the test station at conditions of:

- Reference pressure: 91.5 psig
- Temperature: 68.0°F
- Mass flow: 2.86 grams per second (22.76 pounds per hour)

At this flow rate, the cost for gas would be approximately \$90 per hour, and the maximum running time for a full 79,535-cubic-foot trailer would be about 60 hours. A smaller, 43,832-cubic foot trailer is also available.

This maximum requires too much gas to be practical; hence, a design study was conducted for a turboalternator operating at very low flows. The radial reaction turboalternator should be the full admission type. It is not appropriate to operate this turboalternator with a partial admission nozzle. Therefore, only the impulse type turbine will be considered for the very low flows.

A series of design runs were conducted to evaluate the performance of low-flow, partial admission, impulse turbines. Starting with the design point conditions for Design Case 630601023, the flow was gradually decreased, and the various performance aspects were examined.

Turboalternator design computer runs were conducted down to very low flows, to where there was no net power available to drive the turbine at the target design speed of 141,300 rpm. These runs were made for the conditions at 80°K with a 2.5 pressure ratio of the design conditions and with the use of helium gas. The turbine wheel design remained the same, but the arc of admission was varied (Figure 49). The zero net power point ended up to be 1.353 grams per second.

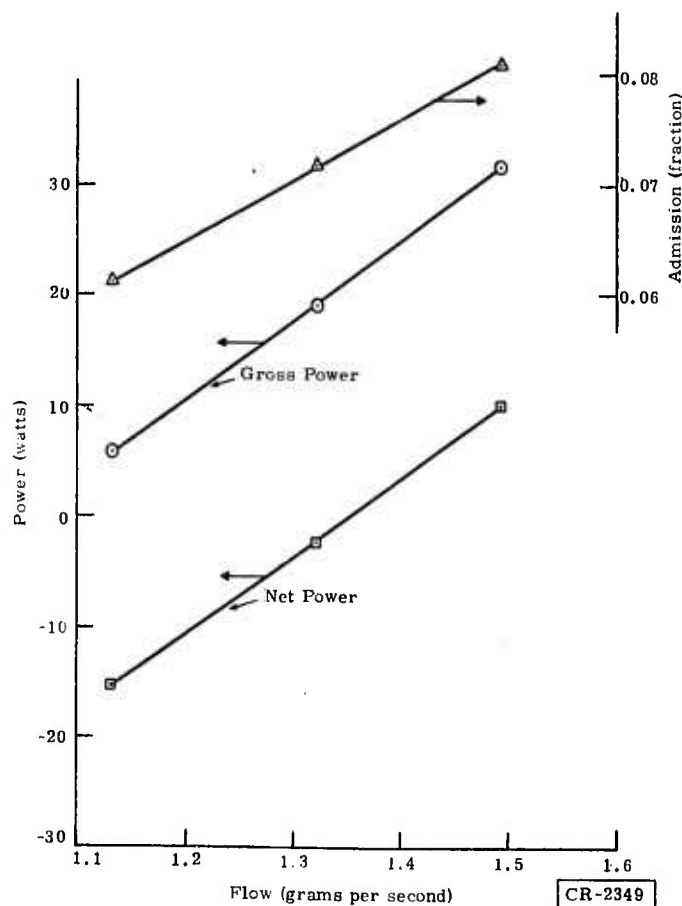


Figure 49. Flow as a Function of Power

At a flow rate of 1.49 grams per second, there is a net power available of 9.86 watts. This power will be used as the design basis. The corresponding admission fraction for the turbine wheel is 0.0807. Hence, an alternate turbine nozzle design will be made for an admission fraction of this value, modified from the larger performance design admission fraction of 0.2708.

This 1.49 grams per second amounts to using a large helium trailer continuously for 115 hours, and the hourly gas charge would be \$47 per hour. This 1.49-gram-per-second flow amounts to 5.04 standard bottles of helium to be used each hour. The corresponding figure for a nitrogen gas bottle is 0.497 bottles per hour.

The use of a higher pressure ratio can be considered for operation, rather than the design pressure ratio of 2.5, up to the limit of the stored gas or the facility compressor. Relative to available power at room temperature, there should be no problem, because the higher available head will allow a much lower pressure ratio to be used to drive the turbine up to the speed desired. Further, the use of nitrogen at room temperature, with a higher head and a higher mass flow available for the same small admission nozzle, will allow operation at pressure ratio lower than the design pressure ratio. Hence, it is concluded that a special partial admission nozzle with a minimum flow is feasible to adequately drive the turboalternator at the design speed.

Shock, vibration, and gas bearing start-stop tests at room temperature will be made. Start-stop tests for this type of turbine require only an acceleration to get the gas bearings started. It is estimated that a 0.04 admission fraction should be adequate for this. Hence, the 0.0807 admission nozzle design will be used with only half of the nozzle openings. Should this require too high a pressure, the nozzle could be opened with the addition of more slots, or widening of the existing slots.

The same 0.04 nozzle should also be suitable for driving the turboalternator for shock and vibration tests at room temperature at the design speed.

TURBOALTERNATOR TEST PLANS

Turboalternator tests for extreme environments were to be conducted for performance, bearing materials, shock, and vibration.

TEST 80°K TURBOALTERNATOR

Functional Tests

The parts for the 80°K Big Bertha turboalternator made during the Phase II portion of the program were to first be assembled and tested to assure acceptable functional operation at the open cycle test station with the 0.04 admission fraction nozzle with the impulse turbine wheel.

Warm Performance

Warm performance tests were to be conducted to calibrate nozzles and test-evaluate the gas bearings and rotating assembly at room temperature, at the laboratory open cycle test station. Pressure differences across the rotating assembly were to be evaluated relative to the characteristic performance parameters, such as the pressure ratio and the velocity ratio. The data were to be reduced with an existing performance data reduction program. Both helium and nitrogen gases would have been used.

Cold Performance

Cold performance tests with liquid nitrogen precooling were to be conducted in a manner similar to that for the warm performance tests, but only helium gas would have been used. After these tests, any adjustment in the nozzle could have been resolved for subsequent gas bearing and shock and vibration tests.

Shock and Vibration

Shock and vibration tests were to be conducted operating the turboalternator at room temperature. Tests would have been conducted on appropriate shock and vibration test equipment, in line with the test plan developed in Phase II. Only a low-flow nozzle would have been used, as in the bearing tests, because it is most practical to drive the turboalternator with stored high-pressure gas in the vicinity of the General Electric shock and vibration test equipment.

Gas Bearing Materials Tests

Gas bearing tests would have been conducted at the gas bearing test station. A special low flow nozzle was to be used with an impulse turbine wheel, to minimize the stored gas required. All tests were to be conducted with no alternator load. The turboalternator was to be installed under a bell jar, to prevent outside contaminants from entering the test unit.

Warm start-stop tests were to be conducted at room temperature, using a timed solenoid-actuated turbine inlet gas valve, and a strip chart recorder would have been used to trace the acceleration and deceleration paths for each start-stop cycle. Cold start-stop evaluation tests would have been conducted using the same bell jar arrangement, with the incoming gas precooled in a dewar of liquid nitrogen.

TEST 80°K CRYOSECTION SYSTEM

The cryogenic heat exchanger system from Phase II would have been incorporated in the closed cycle cryosection test station in the cryogenic refrigeration system.

eration laboratory at the Research and Development Center. The 80°K turboalternator was to be plumbed to the cryogenic heat exchanger. All the necessary plumbing and accessories were to be incorporated, to completely function-performance-test this 80°K system. The high-pressure helium gas source would have been provided by the Research and Development Center facility compressor. Performance data were to be obtained, and through the extension of the existing data reduction programs, complete performance data would have been reduced and analyzed.

All performance tests would have been conducted, using the large nozzles designed for highest efficiency. Either one or two sets of wheels and nozzles were to be used, to evaluate both partial admission and full admission turbine performance.

Warm performance and functional tests would have been conducted to calibrate the large nozzles and to test-evaluate the gas bearings and rotating assembly at room temperature, at the laboratory open cycle test station. Only small pressure ratios are possible, because of the relatively large nozzle openings.

Warm performance tests would have been continued after the turboalternator was installed with the cryogenic heat exchanger in the cryosection test station. Tests were to be conducted as a closed cycle, with the facility compressor.

Cold performance evaluation tests would have been conducted at the closed cycle test station, as a continuation of the above warm, closed cycle performance tests. A liquid nitrogen, fast-cooldown coil would have been incorporated.

JOURNAL BEARING MATERIAL EVALUATION TESTS

During the development of turboalternators under U.S. Air Force Contract No. F33615-71-C-1003, difficulties were encountered in manufacturing satisfactory tilting pad journal bearings made of 304L stainless steel, with a nitrided, hardened case. The problems were caused in the nitriding process. The nitrided case was either nonuniform, or the depth was much greater than that specified, causing excessive distortion and cracking, so the pads could not be machined to drawing specifications. A few of the nitrided journal bearings were successfully manufactured, but when tested in a turboalternator assembly, the bearings appeared to distort as the operating temperature approached 100°K, damaging the journal surfaces.

In view of the above difficulties, other materials were investigated. One of the most promising materials was Kentanium, Grade K-165, manufactured by Kennametal, Inc., at Latrobe, Pennsylvania. Kentanium is the trade name for a series of hard carbide alloys of sintered powdered metal, with titanium

carbide as the principal ingredient. Nickel and nickel-molybdenum are used as the binder materials.

Because Kentanium has a lower coefficient of thermal expansion, the machined-in clearance will be larger at low temperatures, in comparison to stainless steel pads, because the pad radius will not shrink as much. This is in the proper direction for increased stability and increased load capability for the low viscosity to be experienced at low temperatures, because the non-dimensional film thickness is decreased for the same actual pivot film thickness. With this trend, together with the load capability increase, a slight increase in bearing friction will be experienced.

Three samples of Kentanium recommended for use at extreme temperatures were obtained: Grades K-151A, K-152B, and K-165. The hardness of these materials ranges from 90.0 to 93.5 Rockwell A.

Test samples of each grade were prepared for cryogenic testing by grinding a V-notch across one surface and shocking the materials by quenching it repeatedly in the liquid nitrogen, from room temperature. No fractures or cracks were visible upon examination of the samples under a 60-power microscope.

Friction and wear tests were also made on the Kentanium samples and on a sample of nitrided 316 stainless steel in a Dow Corning testing machine. The samples were all tested under the same conditions, riding against a rotating ring of 316 stainless steel 1-3/8 inches in diameter, nitrided and ground on the outside diameter to a 2-rms finish, representative of the journal surface on a finished shaft. Grade K-165 gave the best results, by producing the least amount of wear and the lowest dynamic coefficient of friction, 0.55.

Based on the above test results, a set of six Kentanium (K-165), tilting pad journal bearings were made to the design shown in Figure 50, for the Tiny Tim turboalternator (0.261-inch-diameter shaft). Before the Kentanium journal bearings were tested, the Air Force contract was terminated.

To evaluate the Kentanium journal bearing material for use in the Advanced Research Projects Agency Big Bertha turboalternator (0.5-inch-diameter shaft), tests were continued on the Tiny Tim turboalternator assembly under the Advanced Research Projects Agency contract.

The Tiny Tim turboalternator assembly consisted of a 0.5-inch-diameter, 37-blade, aluminum turbine wheel. New tungsten carbide journal bearing pivot balls, 0.077 inch in diameter, were also used in this assembly. The tungsten carbide balls were brazed to the end of the 304L stainless steel pivot stems, to provide a hard homogeneous material that will withstand the comparatively high-hertz stress incurred on the tip of the pivot ball by the new flat-bottom journal bearing pivot sockets. The journal bearing radial clearances were ad-

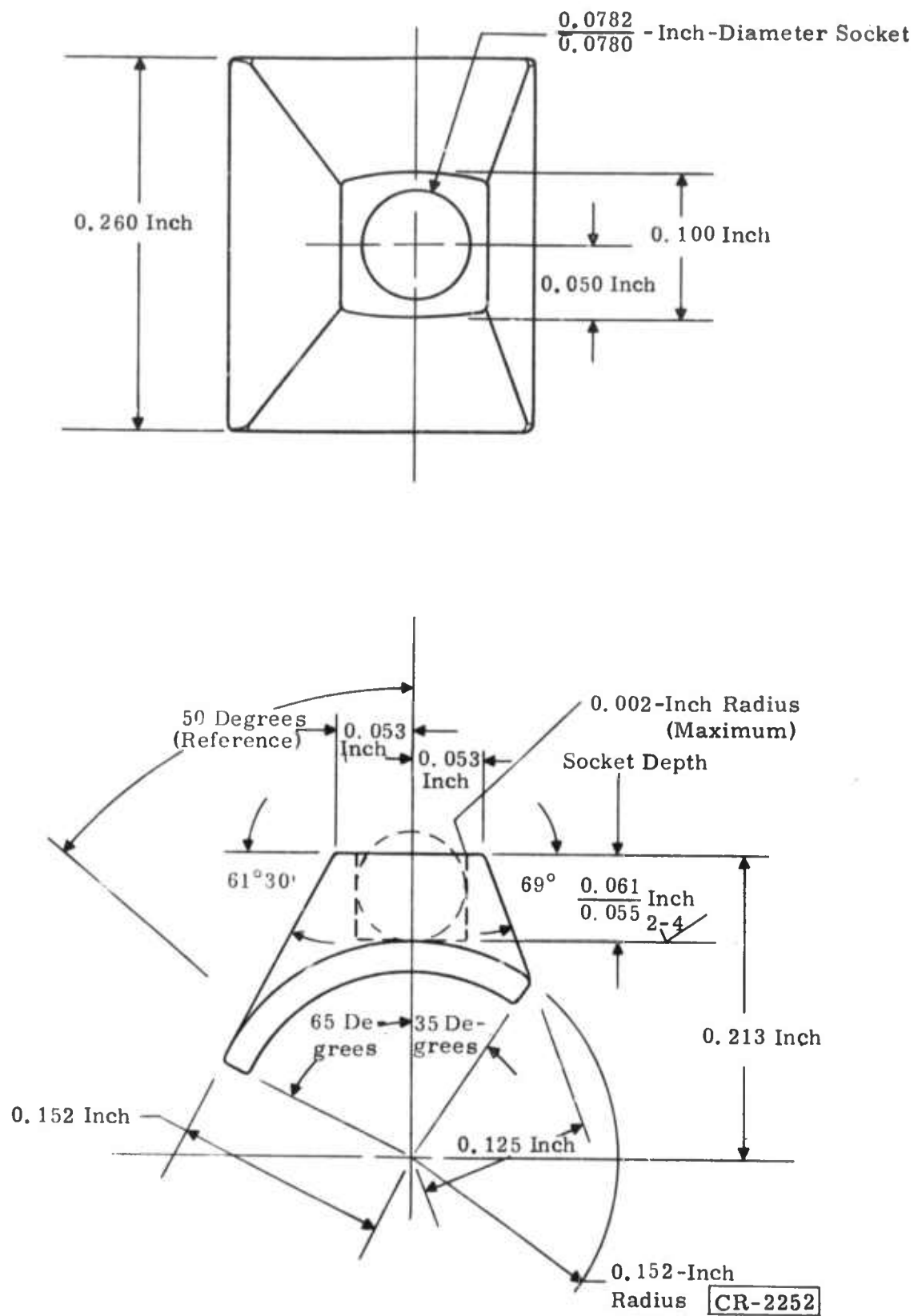


Figure 50. Tiny Tim Kentanium Tilting Pad Journal Bearing

justed to 250 microinches, and the thrust bearings were shimmed to give the shaft a total axial travel of 0.0008 inch and a wheel-to-nozzle axial clearance of 0.0015 to 0.0023 inch.

Turboalternators are initially assembled with the shaft magnetized, to allow the shaft to fall freely while the above clearance adjustments are made.

After the turboalternators are assembled and the clearance adjustments are made, evaluation tests are performed in an open cycle test station at room temperature and near liquid nitrogen temperature. A schematic diagram of the test station is shown in Figure 51. High-pressure gas (helium or nitrogen) is supplied from the gas cylinder banks and is expanded across the turbine to atmospheric pressure. Liquid nitrogen temperature tests are performed by precooling the helium gas, using a cooling coil immersed in liquid nitrogen.

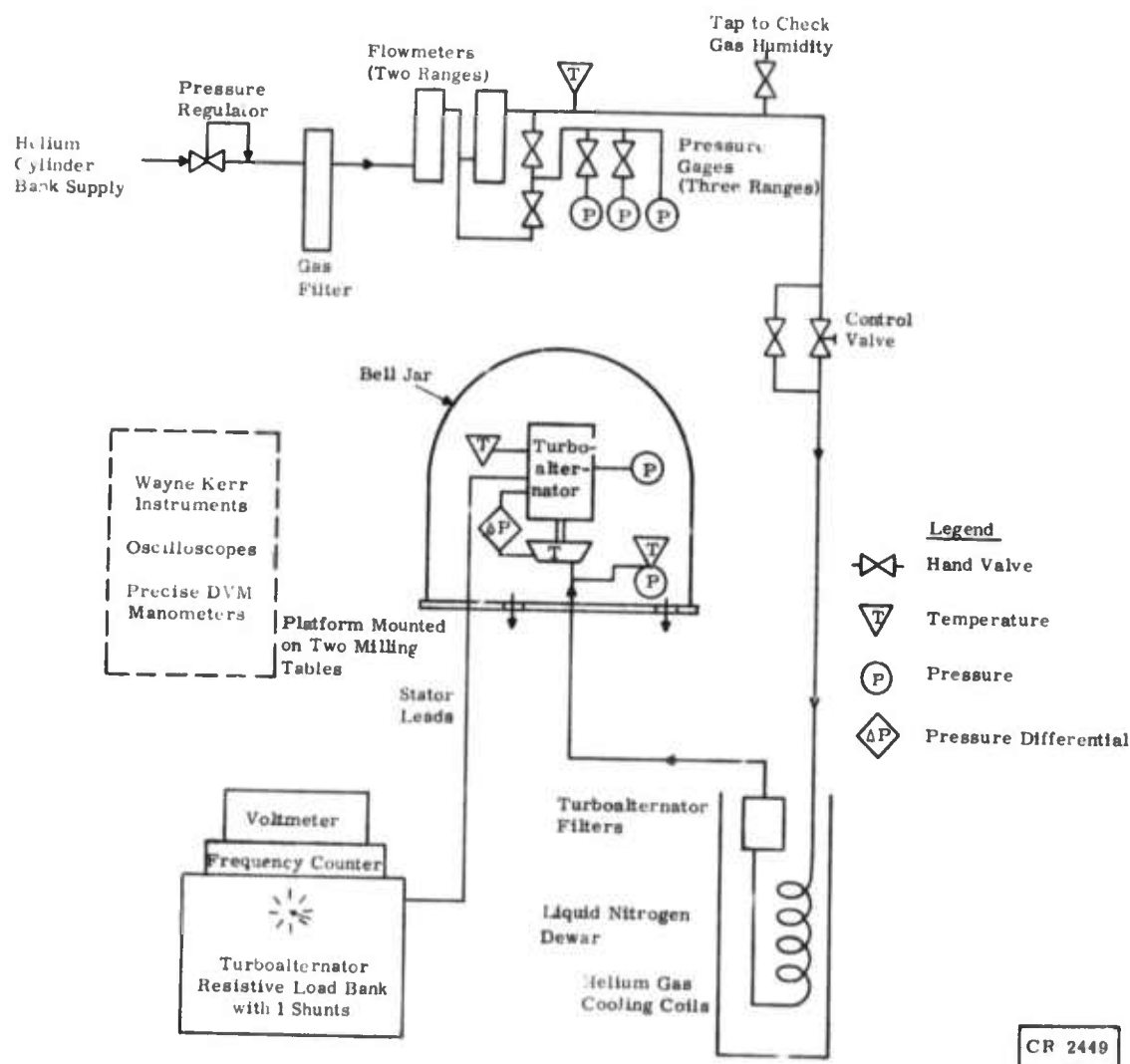


Figure 51. Schematic Diagram of Open Cycle Turboalternator Test Station

Complete instrumentation, consisting of speed, gas flow, pressure, temperature, and gas bearing and rotor dynamic characteristics, are used to evaluate the performance. Noninductive, resistive, three-phase load banks are used to load the alternator. Voltmeter measurements are made across the loads and current shunts and are connected in series with the load to determine the power output.

Linear capacitance proximity probes are used to adjust the bearing clearances and to continuously monitor the operation of the turboalternator bearings and shaft during the evaluation performance tests. Viewing the output signals from the proximity probes on an oscilloscope provides an excellent means of monitoring the operation of the turboalternators.

Figure 52 shows a two-stage turboalternator mounted on two indexing tables in the open cycle test station. The indexing tables are used to orient

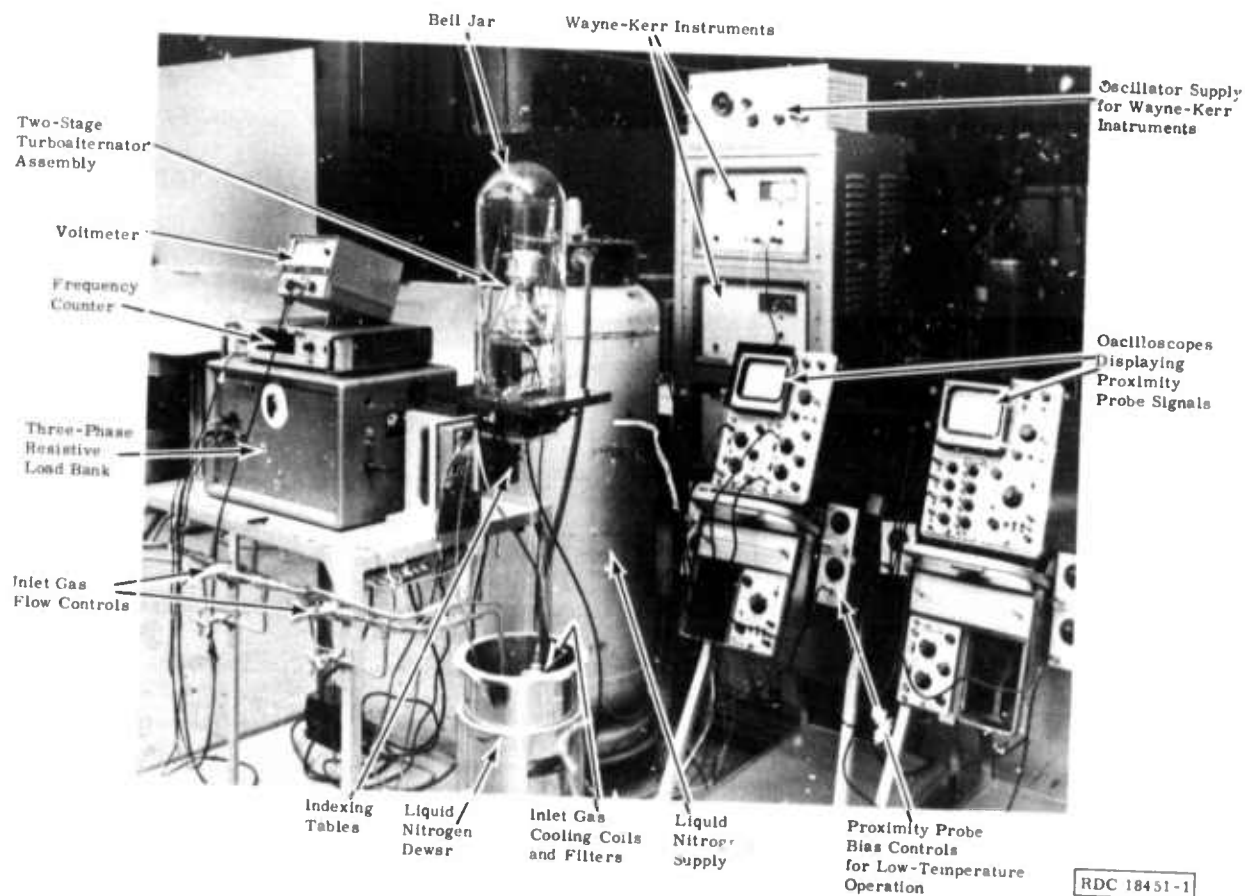


Figure 52. Open Cycle Turboalternator Test Station

the turboalternator in any plane. Figure 53 is a closeup view of a two-stage turboalternator assembly mounted on the open cycle support. The temporary gas inlet fixtures, gas lines, pressure taps, and electrical connections are identified.

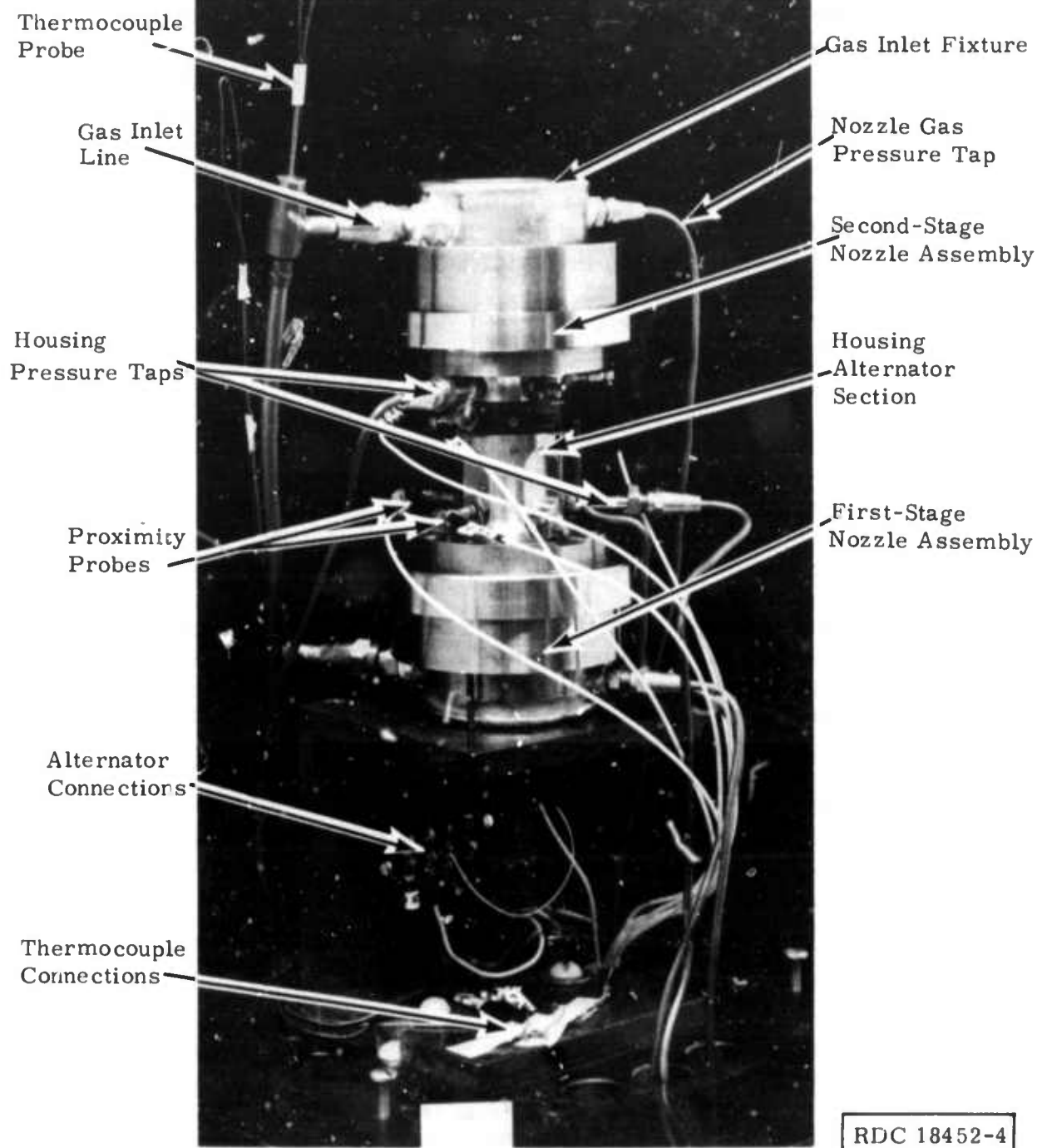


Figure 53. Two-Stage Turboalternator Assembly
on Open Cycle Support Stand

Preliminary room temperature tests were made on the turboalternator using the Kentanium journal bearing pads at speeds on the order of 100,000 rpm. The proximity probe signals indicated very stable operation, and the shaft orbit probe signals produced exceptionally small orbits of 30 to 40 microns at each end of the shaft. Figure 54 is a photograph of the oscilloscope displaying the shaft orbits. The upper orbit was obtained by two proximity probes mounted 90 degrees apart on the radius of the housing at the thrust end of the shaft. The lower orbit was obtained by two similar probes mounted at the turbine end of the shaft. The thrust proximity probe viewing the end of the shaft, monitoring the axial motion, also showed very stable operation, as shown in Figure 55.

This turboalternator assembly was operated in a vertical position only thrust end up, at 100,000 rpm for 1/2 hour and was subjected to six start-stop operations as a preliminary test on the Kentanium journal bearing pads, before disassembly to magnetize the shaft magnet. During the tests, the turboalternator operated very smoothly, starting at a low nozzle inlet pressure of 2.5 to 3.0 inches of mercury, and after the inlet gas was turned off, the turbine coasted to a smooth stop, with the shaft gently settling on the inner thrust bearing as the speed decreased.

The turboalternator was then partially disassembled, to magnetize the shaft magnet. A careful examination of the shaft journal surfaces under a 60-power microscope gave no indication of any wear or discoloration, as experienced in some assemblies in the past. Therefore, the shaft magnet was magnetized, and the turboalternator was reassembled.

The operation of the turboalternator, after reassembly, was identical to that during the initial tests. A proximity probe was installed to monitor the outer thrust bearing motion. The pad proximity probe used in some of the previous assemblies was not installed, because the new design of the journal bearing pads, with the flat-bottom pivot sockets, required an 11-degree change in the angle of the probe viewing surface, and this change would not allow positioning of the probe without interfering with the pad motion.

Six start-stops were repeated, to test the operation of the turboalternator after reassembly and to check the position of the outer thrust probe during operation. The turboalternator was then prepared for cold, open cycle testing, to evaluate the operation with the Kentanium pads at temperatures approaching that of liquid nitrogen.

The turboalternator was prepared for cold, liquid nitrogen temperature, open cycle testing. In this test, the gas to the turbine was precooled by flowing the gas through a coil immersed in liquid nitrogen. Strips of plastic material were attached to the turboalternator support stand, to direct the cold nozzle exhaust gas around the turboalternator housing, cooling the whole assembly. A bell jar was placed over the turboalternator assembly, to isolate

**Best Available
Copy
for all Pictures**

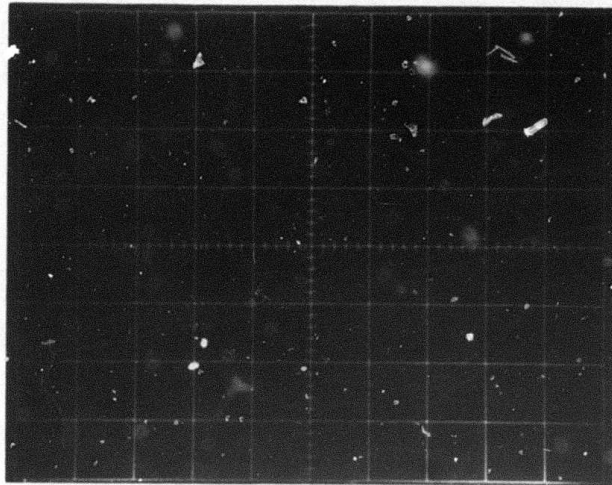


Figure 54. Shaft Orbits of Turboalternator Assembly with Kentanium Journal Bearings Operating at Room Temperature and 100,000 Rpm (Oscilloscope sensitivity is 400 microinches per centimeter.)

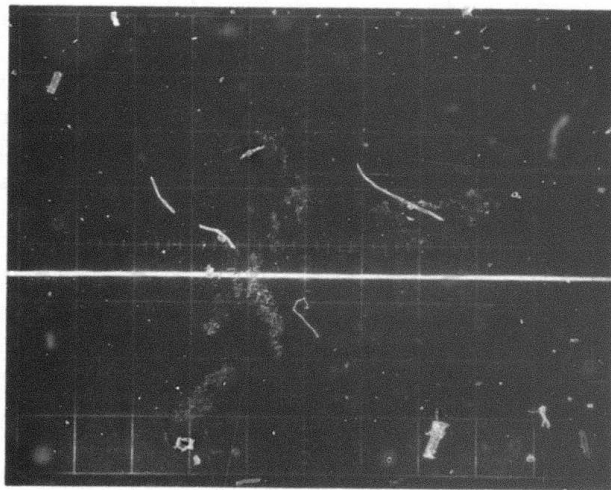


Figure 55. Thrust Probe Signal of Turboalternator with Kentanium Journal Bearings Operating at Room Temperature and 100,000 Rpm (Oscilloscope sensitivity is 400 microinches per centimeter vertically and 1.0 milliseconds per centimeter horizontally.)

the system from ambient moisture. The sealed housing was not assembled onto the turboalternator, because performance data were not to be taken during the bearing evaluation test run.

The turboalternator was operated for 1 hour at room temperature, 100,000 rpm, and no load, to purge the system with dry (5-ppm moisture content) helium gas. Then liquid nitrogen was gradually added to the dewar containing the cooling coil, to slowly cool the turboalternator assembly. In previous cold tests on this Air Force turboalternator, using the nitrided journal bearings, turboalternators operated roughly and were damaged as the gas inlet temperature approached 100°K.

After 2-1/2 hours of cooling and gradually increasing the alternator load to 165.5 ohms (approximately 16 watts) at 100,000 rpm, the turboalternator continued to operate very well with the gas inlet temperature at 93°K and the average stator temperature of 102°K. The only problem encountered was that one of the orbit proximity probe connections opened, so only the shaft orbit at the turbine end could be monitored. Otherwise, the turboalternator operation was essentially the same as it had been at room temperature.

The turbine end shaft orbit remained the same. A slight increase in the axial motion of the shaft and the outer thrust bearing were noted. As the next load point of 142 ohms was applied to the alternator, the turbine operation became unstable in the axial plane. The proximity probes viewing the shaft and the outer thrust showed comparatively large oscillations and indicated that the shaft was touching the thrust bearings. The alternator load was reduced immediately, and smooth operation was obtained again. The unstable operation may have been caused by the outer thrust bearing touching the proximity probe as the gas flow to the turbine was increased to maintain the speed at 100,000 rpm, with the increase in the alternator load.

Because the operation of the turboalternator seemed to be limited to the above conditions, it was decided to remove the alternator load and test the journal bearing at temperatures of approximately 100°K with start-stop tests. Ten start-stop tests were successfully made with the turbine starting at nozzle inlet pressures ranging from 3.2 to 3.8 inches of mercury and coasting to smooth stops when the gas was turned off.

The assembly was allowed to warm up to room temperature, and the turboalternator continued to operate satisfactorily. The proximity probe viewing the outer thrust bearing definitely appeared to be positioned closer to the bearing than during the initial adjustment, indicating that the diameter of the gimbal pivot balls should be increased further, to eliminate this type of shift in the thrust bearings.

The turboalternator was then partially disassembled, to allow examination of the shaft journal surfaces by viewing them between the journal bearings,

using a 60-power microscope. There were no indications of wear or discoloration on the shaft journal surfaces.

After successfully operating the turboalternator with the Kentanium journal bearings at temperatures approaching that of liquid nitrogen, it was decided to further evaluate the journal bearings by setting up a special experiment to operate the turboalternator at temperatures near that of liquid helium. In the past, 58°K has been the lowest temperature at which a turboalternator has satisfactorily operated. This operation was accomplished as part of a U.S. Army contract, using a slightly different turboalternator operating in a refrigerator system.

A schematic diagram of the experimental liquid helium open cycle turboalternator test station is shown in Figure 56. The liquid nitrogen test station

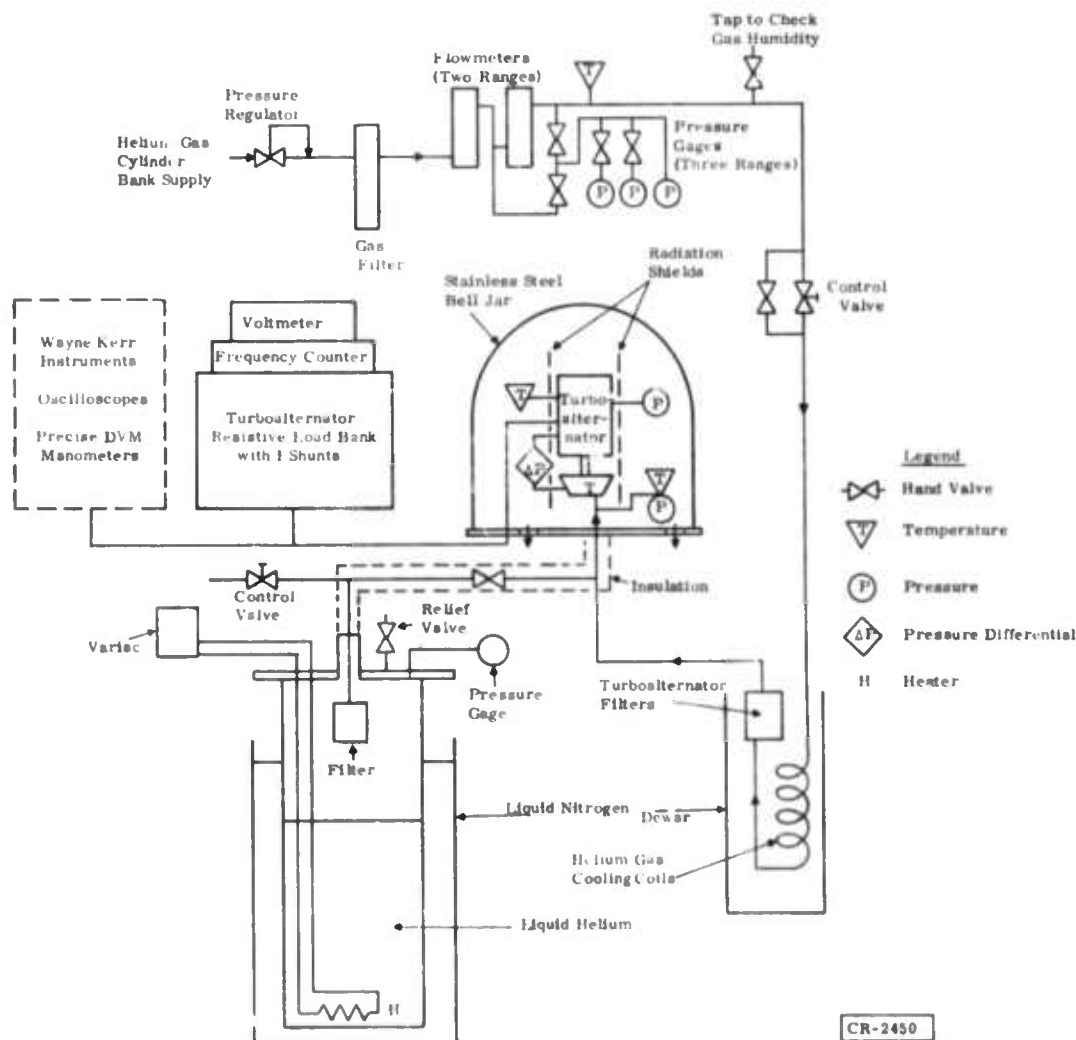


Figure 56. Schematic Diagram of Liquid Helium Open Cycle Turboalternator Test Station

was modified by adding a sealed liquid helium dewar with a control valve and a short insulated line to the turboalternator inlet gas supply. A heater located at the bottom of the dewar was used to control the gas boil-off rate from the liquid helium, to drive the turbine and maintain a pressure of approximately 15 psig in the dewar.

In the liquid nitrogen open cycle tests, the turbine inlet gas temperature was measured by a copper-constantan thermocouple, with the reference junction at liquid nitrogen temperature. Because the sensitivity of the copper-constantan thermocouples drops off quite rapidly below liquid nitrogen temperature, a germanium temperature sensor, calibrated from 75°K down to 4.2°K by Scientific Instruments, Inc., was installed in the nozzle exhaust, to monitor temperatures below liquid nitrogen temperature. To reduce the radiation losses from the turboalternator, 12 layers of aluminized Mylar were wrapped around the plastic gas shields used to direct the cold gas from the exhaust back around the turboalternator assembly to cool the whole unit. A stainless steel can was placed over the turboalternator assembly, to isolate the system from ambient moisture. Another radiation shield was installed in the can above the turboalternator assembly, to improve the thermal isolation.

The liquid helium dewar used held a maximum of 33 liters of liquid. This amount of liquid, when converted to gas, would operate the turbine for approximately 1 hour, depending on the operating speed and the alternator load applied. Therefore, to conserve the liquid helium, the test was started by operating the system as an open cycle liquid nitrogen station to precool the turboalternator to temperatures near that of liquid nitrogen. The same procedures and cooling rates described above for the initial liquid nitrogen test were repeated.

Figures 57 and 58 show the proximity probe signals obtained at the beginning of the test, with the turboalternator operating at room temperature and 100,000 rpm and with no load on the alternator. (The faint shadows seen on the orbit probe signals in the oscilloscope photographs were caused by the proximity probe instrumentation, especially with the higher sensitivities used during this test.)

After 2-1/2 hours of cooling, the turboalternator continued to operate satisfactorily at 100,000 rpm with a 990-ohm load (approximately 3.0 watts) as the inlet gas temperature reached 95°K and with an average stator temperature of 113°K. Figures 59 and 60 show the proximity probe signals obtained. The turbine was allowed to operate at the above conditions for about 1 hour while the liquid helium was transferred into the dewar. The liquid helium dewar was sealed, and the heater was adjusted to increase the gas boil-off rate. The gas flow from the liquid helium dewar was gradually increased to the turboalternator by opening the line control valve and closing the control valve from the liquid nitrogen cooling system. The turboalternator load was then gradually increased, increasing the gas flow through the turbine to maintain the speed at 100,000 rpm. As the turbine cooled, the operation remained

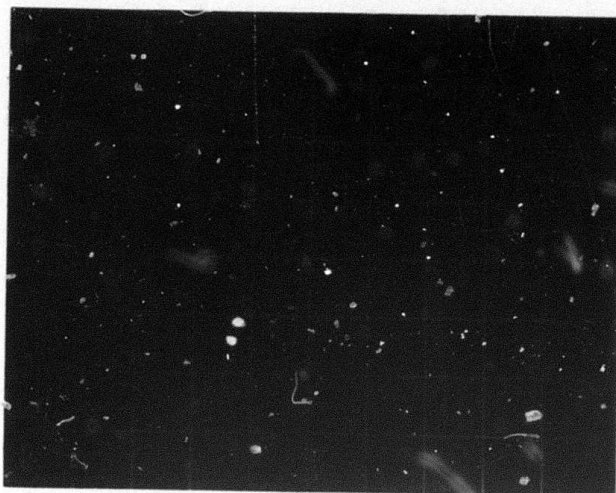


Figure 57. Shaft Orbits of Turboalternator with Kentanium Journal Bearings Operating at No Load, Room Temperature, and 100,000 Rpm Before Liquid Helium Boil-Off Test (Oscilloscope sensitivity is 200 microinches per centimeter.)

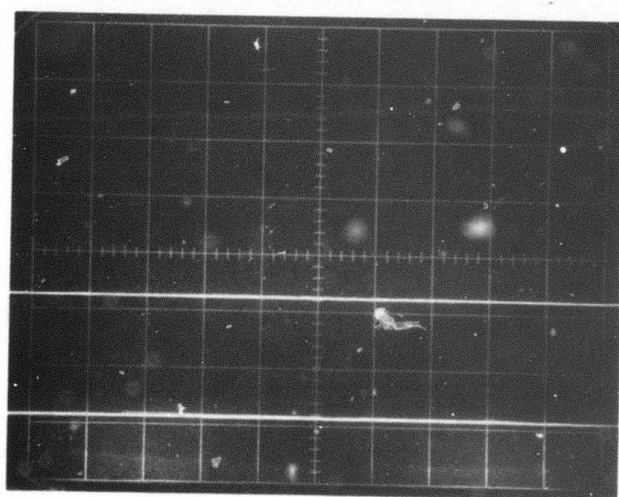


Figure 58. Shaft Axial Motion (upper trace) and Outer Thrust Bearing Motion (lower trace) of Turboalternator with Kentanium Journal Bearings Operating at No Load, Room Temperature, and 100,000 Rpm (Oscilloscope sensitivity is 400 microinches per centimeter vertically and 1.0 millisecond per centimeter horizontally.)

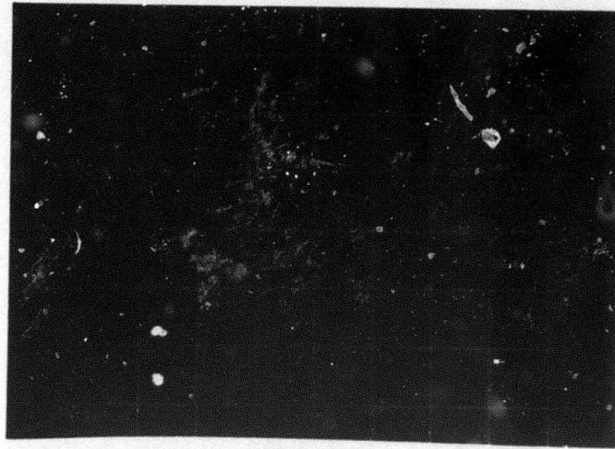


Figure 59. Shaft Orbits of Turboalternator Operating at 95° K and 100,000 Rpm with 3.0-Watt Load Before Liquid Helium Boil-Off Test (Oscilloscope sensitivity is 200 microinches per centimeter.)

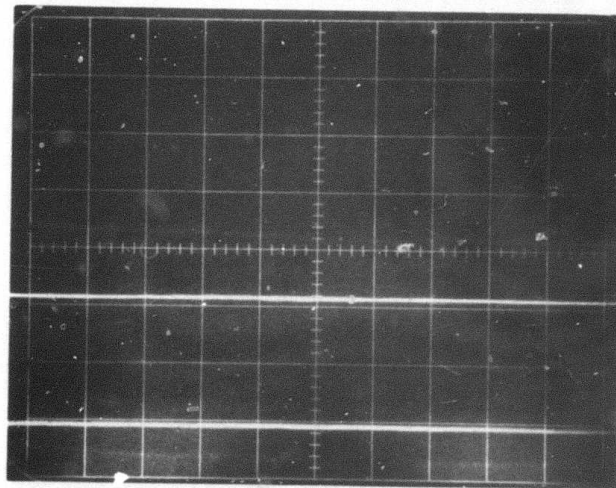


Figure 60. Shaft Axial Motion (upper trace) and Outer Thrust Bearing Motion (lower trace) of Turboalternator Operating at 95° K and 100,000 Rpm with 3.0-Watt Load (Oscilloscope sensitivity is 200 microinches per centimeter.)

the same, with the exception of one of the orbit probes opening at the turbine end of the shaft, so only the thrust-end shaft orbit could be monitored.

After 15 minutes of operation, the turbine exhaust temperature reached 28°K at 100,000 rpm with a 326.5-ohm load (6.78 watts). Twenty minutes later, the turbine exhaust temperature reached 14°K with a 165.5-ohm load (13.4 watts). Figures 61 and 62 show the proximity probe signals obtained. A slight oscillation on the order of 80 microinches was noted in the axial motion of the shaft, with very little change noted in the outer thrust bearing signal.

As the alternator load was increased to 142 ohms, the exhaust temperature decreased to 9.8°K, but the operation of the outer thrust bearing became rough (Figure 63). This condition indicated that the shaft thrust surface was intermittently touching the thrust bearings, causing the rough operation noted. The shaft thrust orbit also became slightly larger in diameter. To avoid damaging the turboalternator parts, the alternator load was quickly reduced to 199-ohms, and the turbine returned to smooth operation at 14°K and 100,000 rpm. The turbine continued to operate satisfactorily under the above conditions for approximately 10 minutes, before the liquid helium supply was depleted. The total running time below liquid nitrogen temperature was approximately 50 minutes.

This experiment was very successful, achieving a very significant milestone in the development of turboalternators for cryogenic refrigeration. This is the lowest known temperature ever achieved with a turboexpansion machine anywhere in the world. It is the first step in establishing the feasibility of operating turboalternators with extremely low-viscosity helium gas-lubricated bearings. The 9.8°K helium gas is probably the lowest viscosity fluid ever used in a hydrodynamic bearing system.

The problem encountered with the thrust bearings at the low temperature in the above test should be eliminated by increasing the diameter of the gimbal pivot balls to reduce the clearance between the ball and the socket of the pivots. This increase would allow finer adjustment of the thrust bearing clearances and should considerably stiffen the operation of the thrust bearings.

The liquid helium experiment was repeated, in an effort to obtain a few data points at the low temperatures. The same cooldown procedures were used, and similar operation was observed with the turbine operating at 90,000 rpm. As the exhaust temperature reached 16.0°K, both orbit signals were lost, due to either shorts in the connectors or open circuits in the probes. This time the turboalternator operation became rougher as the 142-ohm load was applied. Figures 64 and 65 show the increase in the shaft axial motion. After the oscilloscope photographs were taken, the turbine suddenly stopped, and the helium gas supply was quickly turned off. Efforts were made to restart the turbine, but it would not spin and lift off of the bearings.

The system was allowed to return to room temperature. The turbine then started normally, as gas was applied to the nozzle, and operated satisfactorily with no significant change noted. A frozen contaminate particulate

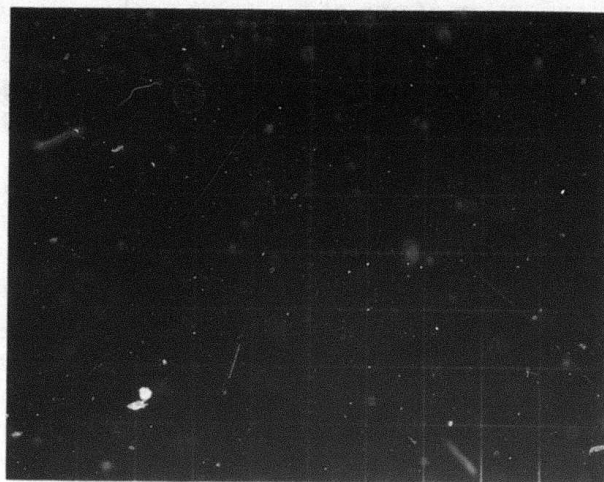


Figure 61. Shaft Thrust End Orbit of Turboalternator Operating at 14°K and 100,000 Rpm with 13.4-Watt Load (Oscilloscope sensitivity is 200 microinches per centimeter.)

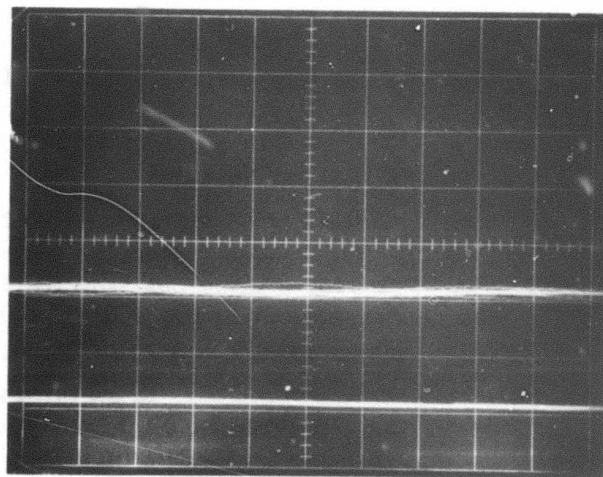


Figure 62. Shaft Axial Motion (upper trace) and Outer Thrust Bearing Motion (lower trace) of Turboalternator Operating at 14°K and 100,000 Rpm with 13.4-Watt Load (Oscilloscope sensitivity is 200 microinches per centimeter.)

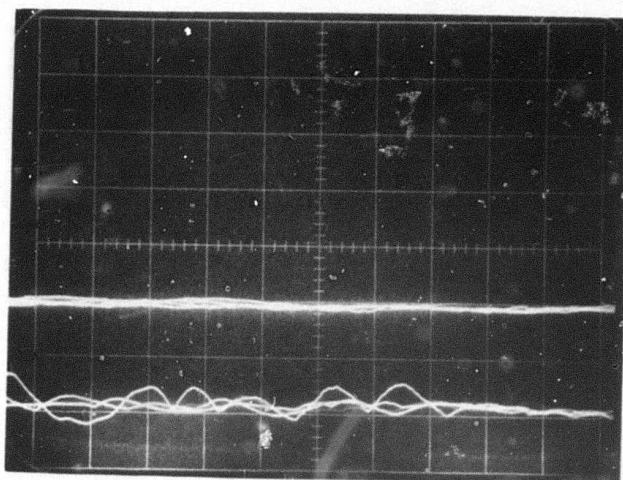


Figure 63. Shaft Axial Motion (upper trace) and Outer Thrust Bearing Motion (lower trace) for Turbo-alternator Operating at 9.8°K and 100,000 Rpm with 142-Ohm Load (Oscilloscope sensitivity is 200 microinches per centimeter.)

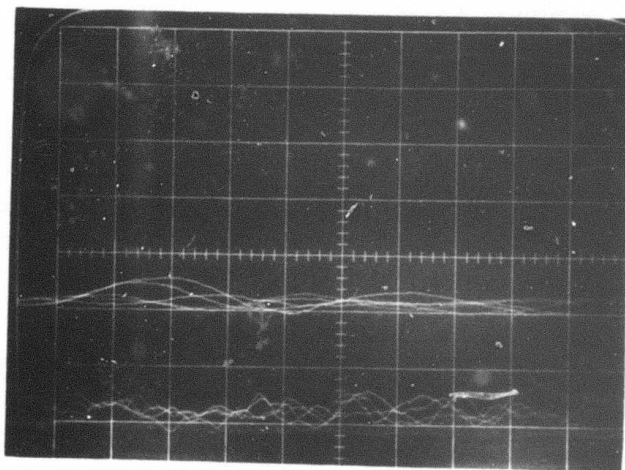


Figure 64. Second Liquid Helium Boil-Off Test: Shaft Axial Motion (upper trace) and Outer Thrust Bearing Motion (lower trace) with Turbo-alternator Operating at 16°K and 90,000 Rpm with 142-Ohm Load (Oscilloscope sensitivity is 200 microinches per centimeter.)

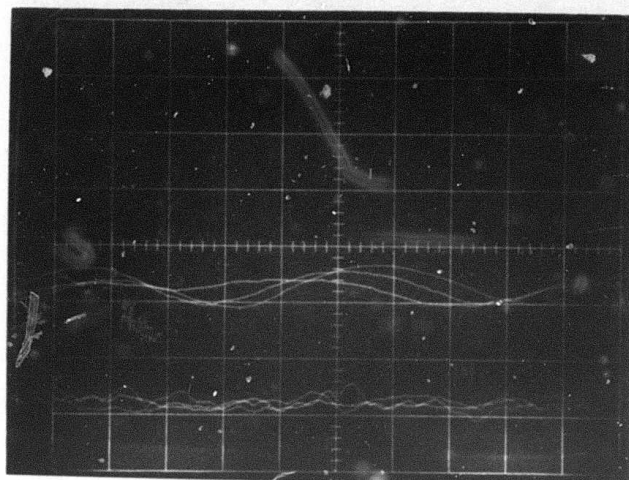


Figure 65. Later Photograph of Second Liquid Helium Boil-Off Test: Shaft Axial Motion (upper trace) and Outer Thrust Bearing Motion (lower trace) with Turboalternator Operating at 16°K and 90,000 Rpm with 142-Ohm Load (Oscilloscope Sensitivity is 200 microinches per centimeter.)

from the system must have been carried into the nozzle, restricting the clearance between the turbine wheel and nozzle and causing the turbine to stop.

The data obtained during the last low-temperature test are listed in Table 8. A photograph of the liquid helium boil-off open cycle turboalternator test station is shown in Figure 66.

Table 8
TURBOALTERNATOR DATA OBTAINED
DURING SECOND LIQUID HELIUM BOIL-OFF TEST

Time	Data Point	Speed (rpm)	Nozzle Inlet Pressure (inches of mercury)	Load Resistance (ohms)	Alternator Voltage, Line-Neutral (volts)	Total Electric Power (watts)	Turbine Exhaust Temperature (°K)
11:21	1	90,300	6.2	432.0	25.0	3.81	77*
11:30	2	92,400	8.5	326.5	25.4	5.94	42.0
11:36	3	89,200	10.5	248.0	24.5	7.27	29.6
11:43	4	90,180	13.2	199.0	24.9	9.39	23.0
11:45	5**	--	19.3	142.0	--	--	16.0

*Approximate

**The turbine was stopped during this period.

CR-2456

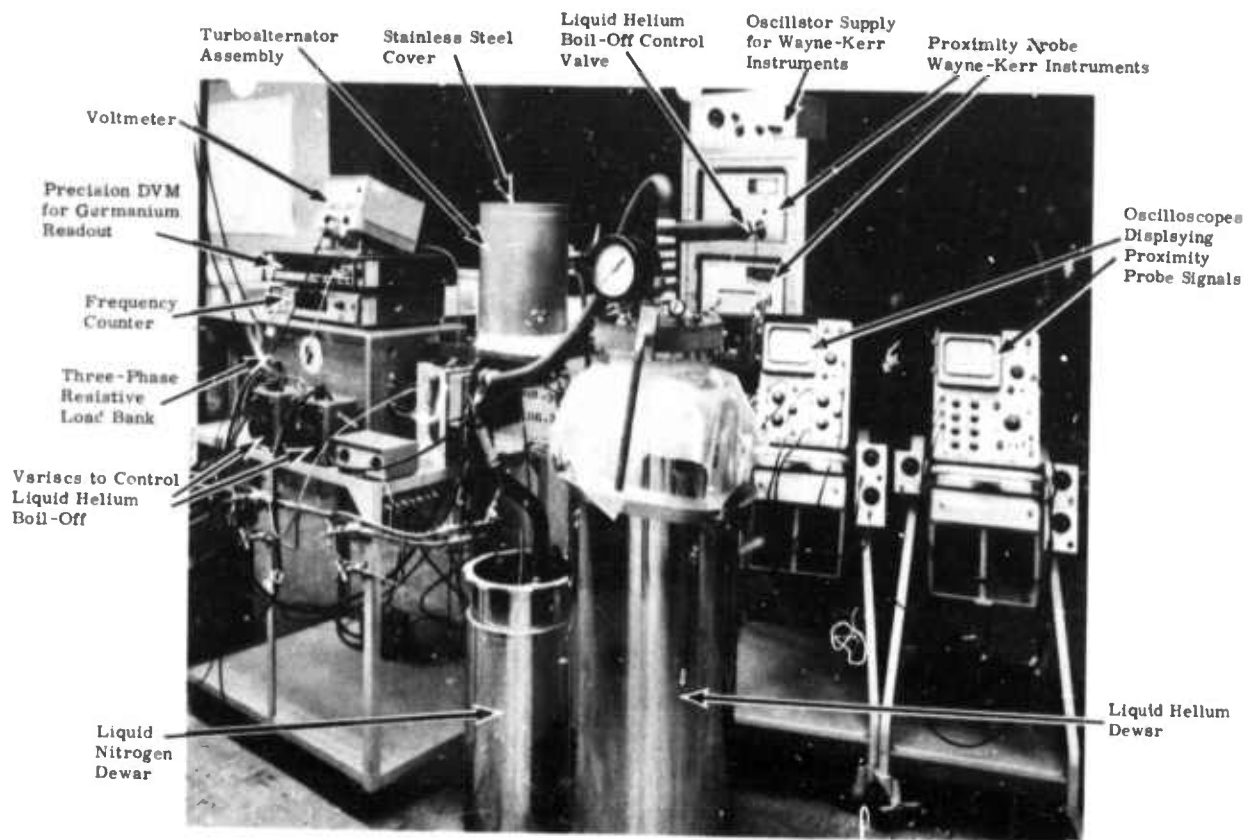


Figure 66. Liquid Helium Boil-Off Open Cycle Turboalternator Test Station

CONTRACT TURBOALTERNATOR MECHANICAL DESIGN

From the above design analysis and investigative bearing materials test results, a final design for the contract was established, and work on component parts was initiated in the shop.

For the Advanced Research Projects Agency contract, a Big Bertha turboalternator with a 0.5-inch-diameter shaft was designed. A mechanical arrangement layout was made, based on the design approach used in the second-generation Tiny Tim turboalternator frame size, which uses the 0.26-inch-diameter shaft described above.

The single-stage turboalternator was designed to incorporate elements that could readily be developed to provide suitable performance and that could be adaptable to quantity production.

The design layout of the single-stage turboalternator is shown in Figure 67.

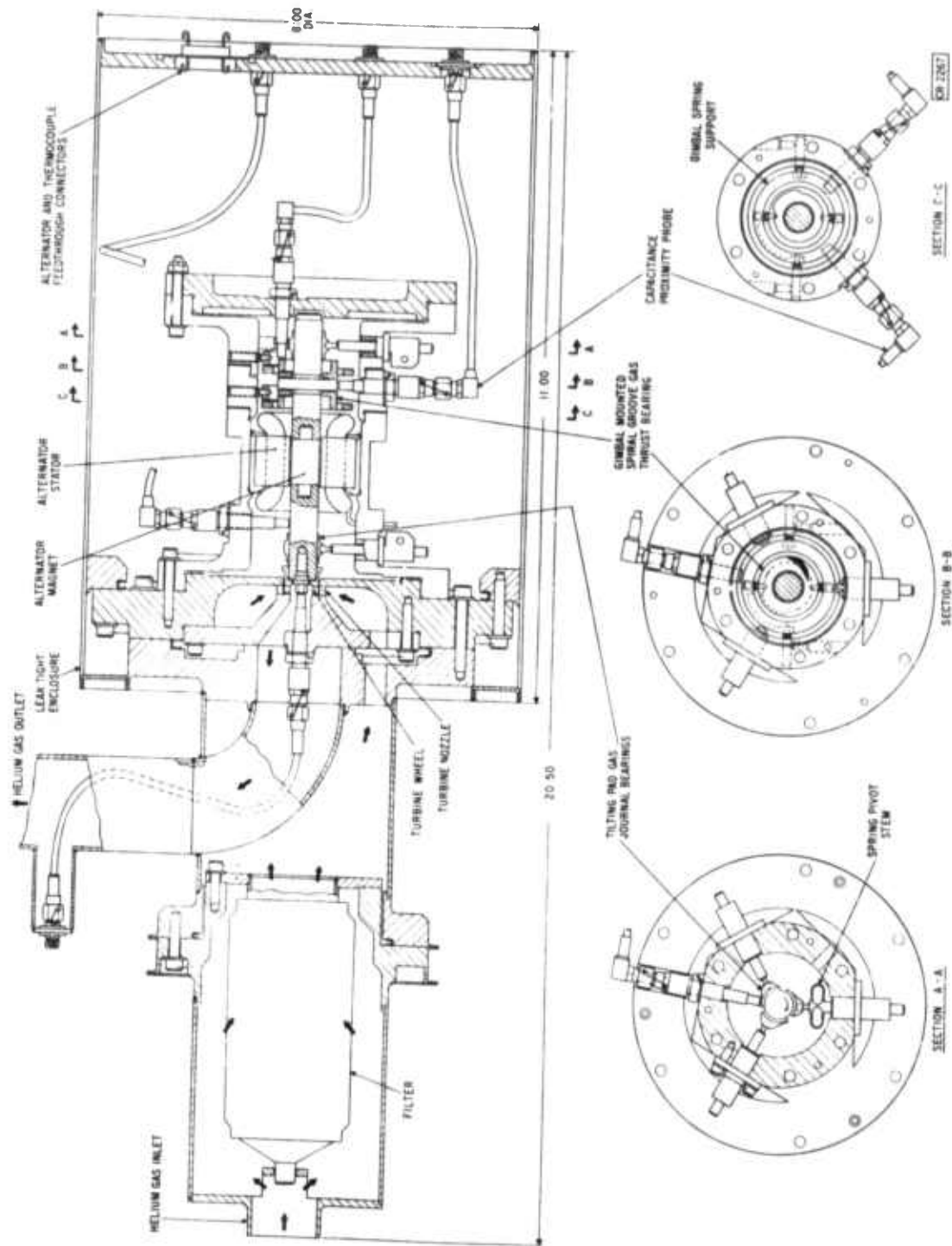


Figure 67. Single-Stage Big Bertha Cryogenic Turboalternator (0.50-Inch-Diameter Shaft)

The turboalternator is mounted on gas-lubricated journal bearings. Three hardened pads at each journal bearing support the 0.50-inch-diameter shaft with an operating gas film thickness on the order of 400 microinches. These journal bearings are of the self-acting, tilting pad type and are capable of stable operation throughout the operating range and at any attitude.

Two inward pumping, self-acting, spiral groove thrust bearings position the shaft axially. Like the journal bearings, the thrust bearings are gas-lubricated and typically operate with a 600-microinch gas film thickness. The entire bearing system is self-aligning, because the thrust bearings are gimbal-mounted and the journal tilting pads are individually self-aligning. Satisfactory operation of the complete bearing system can therefore be somewhat independent of the accuracy with which adjacent parts are manufactured. The radial inflow wheel is convenient for close blade-tip axial clearances to minimize leakage. Neither the turbine wheel nor the nozzle was final-designed from an aerodynamics standpoint.

The turbine energy is absorbed by a two-pole permanent magnet alternator. This compact alternator is a very practical device for extracting energy at cryogenic temperatures, when that energy will be dissipated at a remote location. The two-pole magnet operates within the stator, which is wound three-phase in a core of low-loss iron laminations.

The vacuum-tight enclosure shown would be welded for the final assembly, but the design allows the use of replaceable static seals for initial tests. Proximity probes would be installed to monitor the position of the rotor and gas-bearing elements. An axial probe on the outer thrust bearing is shown to monitor thrust-bearing motion.

High-speed gas bearing turboalternators require very close tolerances to operate properly. The aerodynamic components also require close clearances to achieve maximum performance potentials. Therefore, it is most desirable to establish the assembly procedures of a candidate design at the inception of the design. The results can lead to minimizing the number of critical tolerances on manufactured parts and also can lead to a design that will provide the least development effort. Detailed assembly procedures were about to be initiated on this contract.

STATUS OF TURBOALTERNATOR PARTS

The majority of the manufacturing drawings have been completed for the Advanced Research Projects Agency turboalternator, and parts were in various stages of completion when this portion of the contract was terminated. Several of the turboalternator parts were photographed, as shown in Figure 68. The inventory listed in Table 9 outlines the quantities and the status of the parts.

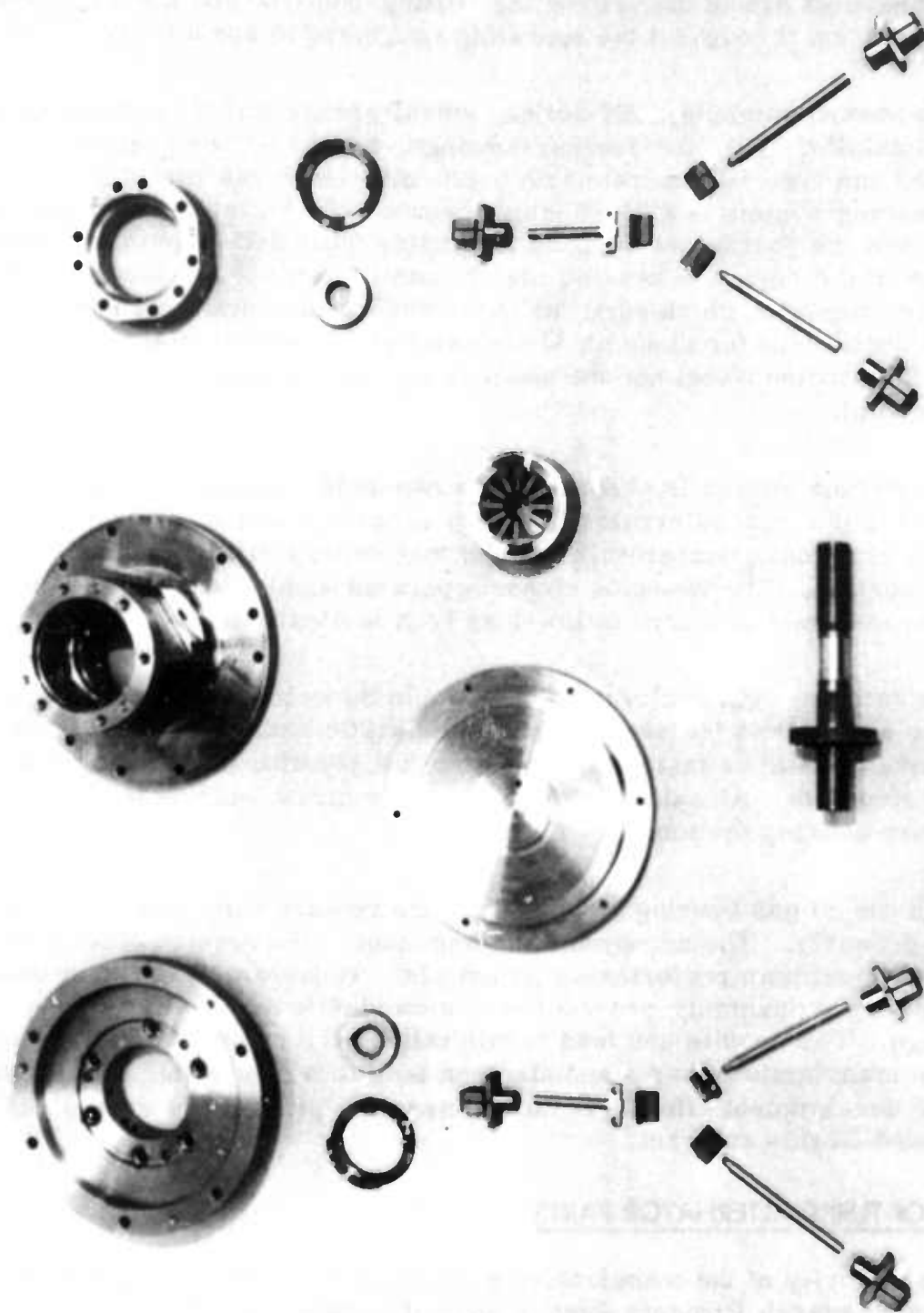


Figure 68. Turboalternator Parts

Table 9
INVENTORY OF TURBOALTERNATOR PARTS
(BIG BERTHA FRAME SIZE)
(Assembly Drawing 588E486G1)

Quantity	Part	Name	General Electric Drawing	Remarks
2	4	Housing Stator Section	588E444P1	Complete, except for final inspection and deburring
1	4	Housing Stator Section	588E444P1	25-percent complete
8	5	Shafts	588E456P1	Brazed assemblies as received from vendor
4	5	Shafts	588E456P1	All bad magnet-to-shaft brazes - joint broke in bend test
3	8	Stator	423D434G1	Punchings ascribed -- windings not started
1	9	Outer Thrust Gimbal Assembly	--	--
2	--	Housing Outer Gimbal	588E455P1	Complete except for final inspection and deburring
2	--	Housing Outer Gimbal	588E455P1	25-percent complete
6	--	Outer Thrust Bearings	423D470P2	Spiral grooves etched, spring calibration and final inspection required
30	--	Gimbal Pivot Stems	664B374G1	Balls brazed to stems -- balls must be cleaned and lapped, and stems must be cut
17	--	Gimbal Pivot Screws	664B311P3	As received from nitriding, case depth only 1 to 1-1/2 mils
17	--	Gimbal Pivot Screws	664B311P4	As received from nitriding, case depth only 1 to 1-1/2 mils
9	--	Gimbal Rings	543C607	Machining complete springs, uncalibrated
1	10	Nozzle Assembly	423D630G1	Not started
1	11	Turbine Wheel	423D631P1	Not started
1	12	Gas Inlet and Discharge Cylinder	423D632G1	Not started
1	12	Gas Inlet and Discharge Cylinder	543C605G1	Obsolete design, 50-percent complete
1	13	Filter Housing	423D633G1	Not started
1	14	Cover -- Turbo Section	423D634G1	Not started
1	17	Probes	543C169G1	Twenty-one probes only, not calibrated, still on Air Force contract
1	18	Probes	543C169G2	Ten probes only, not calibrated, still on Air Force contract
30	20	Bearing Pads	543C184P1	Kentanium as cast from vendor
1	21	Inner Thrust Gimbal Assembly	543C185G1	--
2	--	Housing Inner Gimbals	423D464P1	Machining complete
2	--	Housing Inner Gimbals	423D464P1	25-percent complete
6	--	Inner Thrust Bearings	423D470P1	Spiral grooves etched, spring calibration and final inspection required
8	22	Bearing Stem (spring loaded)	543C495	25-percent complete CR-2454a

Table 9 (Cont'd)

**INVENTORY OF TURBOALTERNATOR PARTS
(BIG BERTHA FRAME SIZE)
(Assembly Drawing 588E486G1)**

Quantity	Part	Name	General Electric Drawing	Remarks
21	23	Bearing Stem Supports	543C193P1	Complete
24	24	Bearing Stems	543C193P2	Tungsten carbide bails brazed to stems, 60-percent complete
25	24	Bearing Stems	543C193P2	Obsolete design -- nitrided, not finished
2	24	Bearing Stem Samples	543C193P2	Machined from tungsten carbide to establish procedures for 1/2-inch radius on tip of bail
1	28	Filter	664B360	As received from Microporous Filter Division of Circle Seal Corporation
2	29	End Cap	664B361P1	Machining complete
2	31	Locking Plate	664B363P1	Complete
4	32	Locking Plate	664B363P2	Complete
3	33	Locking Plate	664B363P3	Complete
2	34	Locking Plate	664B363P4	Complete
8	35	Probe Viewer Screw	211A2220P1	Machining complete
2	--	Electrical Headers	664B361P2	For single probe feedthrough
10	--	Weldable Probe Lead Feedthroughs	Microdot, Inc. 053-0728-0001	Leak tight as received and after cooling to liquid nitrogen temperature
20	--	Probe Lead Connectors	Microdot, Inc. 132-0300-0004	As received
8	--	Probe Lead Connectors	Microdot, Inc. 132-0118-0004	As received
7	--	Thermocouple and Alternator Lead Feedthroughs	Ceramaseal, Inc. 78952	Two tested -- leak tight as received and after cooling to liquid nitrogen temperature (one leaked 7×10^{-6})
3	--	Set of Experimental Kryptonium Shaft Sections (as received from vendor)	--	--
1	--	Assembly Fixtures	--	--
1	--	Shaft Holder	423D444P1	Complete
2	--	Dummy Shaft	423D444P2	Complete
1	--	Thrust Bearing Center Fixture	423D444P3	Complete
1	--	Shaft Magnetizing Support	423D444P4	Complete
2	--	Shaft Extensions	423D444P8	Complete
1	--	Gage Shaft	543C187P1	Not started
1	--	Gage Shaft Support	543C187P2	Complete
1	--	Centering Screw	543C187P3	Complete
4	--	Shaft Storage Boxes	--	Wooden
3	--	Bellows	664B318	Obsolete turbo cover
1	--	Fixture for Brazing Carbide Bails onto Stems	543C495 543C193 664B374	--

CR-2425b

Section 3

REFRIGERATOR TRANSIENT ANALYSIS

For transient or off-design analysis of refrigerator subsystem performance, a generic transient refrigerator model was developed and implemented in digital form. The existing model is restricted to a representation of the refrigerator cryosection, assuming a compressor with constant suction and discharge pressures.

A completely modular approach has been used. Separate and independent models (in the form of subroutines) were made for the following types of devices:

- Heat exchanger
- Thermal load
- Turboalternator
- Joule-Thomson valve
- Liquid accumulator

Each of these subroutines is of general form and will be utilized as many times as is required for the distribution of devices in the refrigerator configuration being represented. The particular structure of the configuration is then defined by a specific interconnection subroutine that equates the input to a given device to the output of some other device.

The heat exchanger model contains the general equations for terminal temperatures of an ideal counterflow device under balanced or unbalanced flow conditions. The mass flow for each side is continuously variable, and the effects of changing flow magnitudes and the degree of balance or unbalance are continuously computed. The effects of changes in specific heat with temperature for the working fluid are also continuously determined.

The transient behavior of each heat exchanger is approximated by treating the core temperature as a variable that responds to changing fluid temperature and flow conditions in a first-order exponential manner. Two such core temperatures (one for each terminal end of the heat exchanger) are continuously computed, and their associated time constants are separately and continuously adjusted for changing specific heat as the temperatures vary.

The thermal load model is conceptually similar to that for the heat exchanger, except there is only one flow passage and one single lumped thermal mass with varying specific heat. The thermal load subroutine contains models for selectable heat leak, constant heat flow, or radiation types of loads. Provision has been made to handle varying liquid/vapor mixtures for the coolest load of a heat leak type.

The turboalternator model approximates the mechanical performance of the turbine and alternator by linear torque-speed functions and their combined shaft moment of inertia. The turbine flow and torque-speed characteristics are continuously computed as ideal functions of the inlet temperature. The alternator shaft power and the turbine outlet temperature are continuously computed from the energy balance relationships.

The Joule-Thomson valve is modeled as an ideal device in which the flow is determined as a function of its input temperature and the output temperature is determined from the assumption of constant enthalpy over the specified pressure drop. Provision is made for adjustment of the valve flow during cooldown, according to some arbitrarily chosen control function. The liquid/vapor proportions are continuously computed from an energy balance calculation. In the associated liquid accumulator, it is assumed that the liquid fraction entering is accumulated, and its total is continually integrated. An option can be made to simulate the draining off of accumulated liquid at a specified rate. The temperature of the vapor leaving the accumulator is a function of the temperature of the vapor entering and the presence or absence of the accumulated liquid.

The transient computation for a given refrigerator configuration is made on a stepwise, completely modular basis. At any given time the state of all variables is known and, in particular, the inputs to every subsystem device are available. The response of each individual device to its inputs over a specified time step is then computed on a first-order basis. The resulting set of individual outputs is then applied to the interconnection subroutine to establish the updated set of input data for the next time step. As in any first-order integration process, the instantaneous accuracy and stability of the numerical procedure will be directly related to the arbitrarily selected magnitude of the time step. Provided that the step size is consistent with numerical stability, the procedure will provide an ultimate steady-state solution without a cumulative error.

The refrigerator model was run as a test case, simulating the cooldown from ambient temperature for a practical configuration containing five heat exchangers, three thermal loads, two turboalternators, and a Joule-Thomson valve and accumulator. The configuration and modular model structure are shown in Figure 69.

The run was made on a full transient basis to the point of liquid accumulation. At that point, the time constants for some of the larger thermal masses were arbitrarily shortened, and the model was allowed to rapidly approach the design steady state.

TRANSIENT COOLDOWN RESULTS

A generic, modular model for transient or off-design simulation of cryogenic refrigerator system operation was developed and implemented in digital

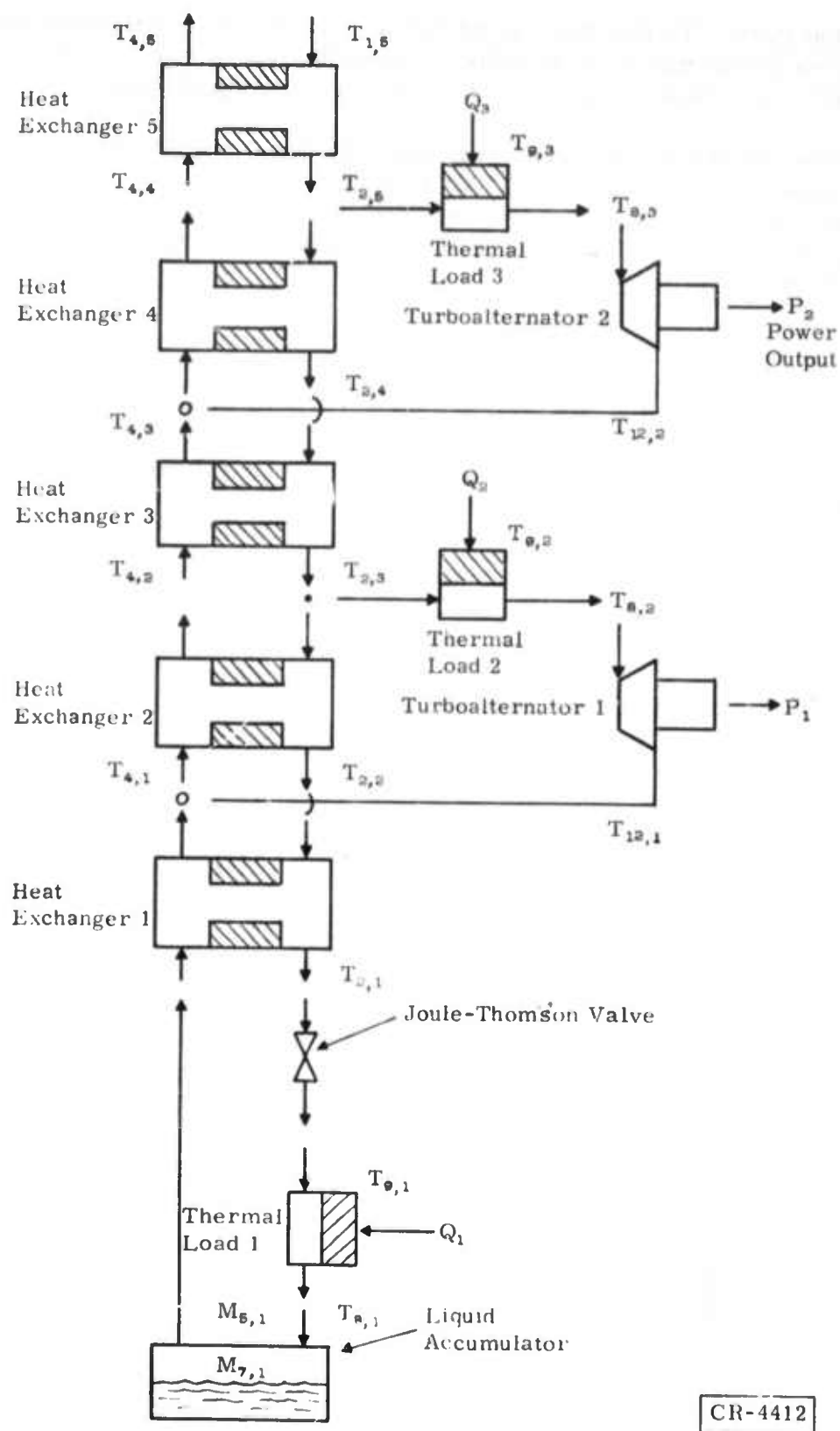


Figure 69. Model for Transient Analysis

computation form. To test the model and ultimately use it for estimation of the cooldown performance of an actual system design, a variety of synthetic cases were run, followed by a test for a realistic configuration.

With the aid of manual monitoring and occasional adjustment in computation step size, the model program successfully simulated the complete transient cooldown for a design cryosection from an ambient temperature start to the beginning of helium liquefaction. The general configuration was that shown in Figure 69.

STARTING AND CONTROLLED CONDITIONS

The cooldown run was started with all devices at an ambient temperature of 322°K, with the turbines at rest, and with the helium flow present. The initial transient occurrence is the acceleration of the turboalternators to operating speed in the first few seconds. Their speed and power curves are shown in Figure 70.

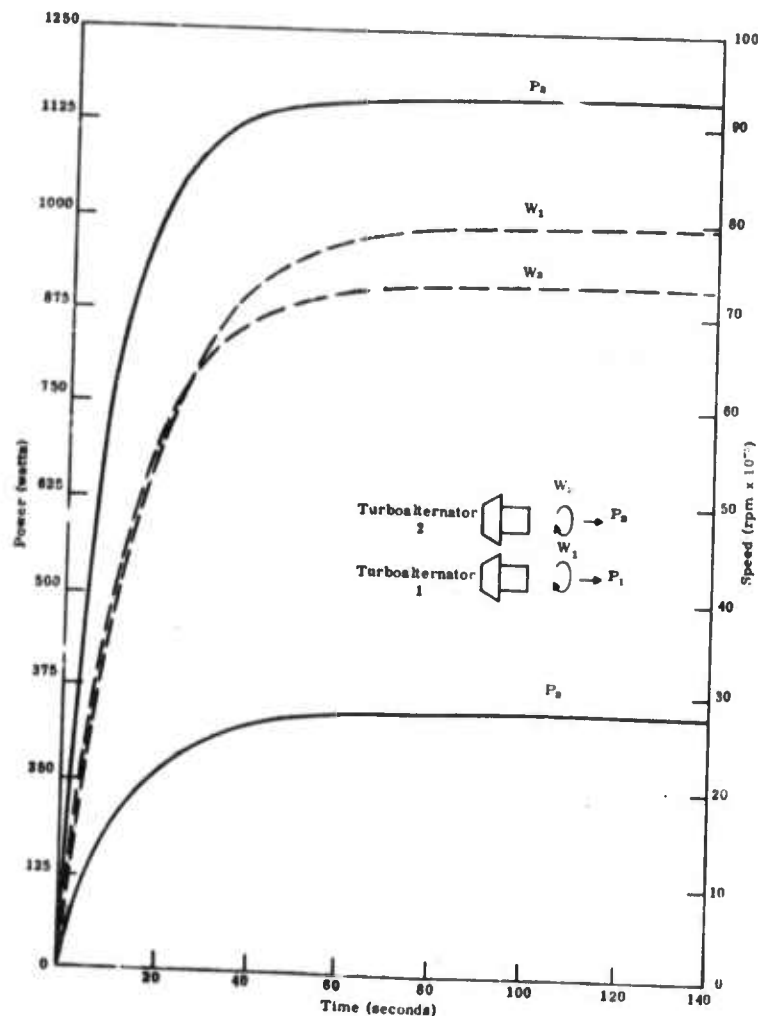


Figure 70. Turboalternator Startup

Compressor/intercooler heating is simulated by an exponential rise in the temperature of the fluid supplied to the cryosection (input to the top heat exchanger). This temperature trace is shown in Figure 71.

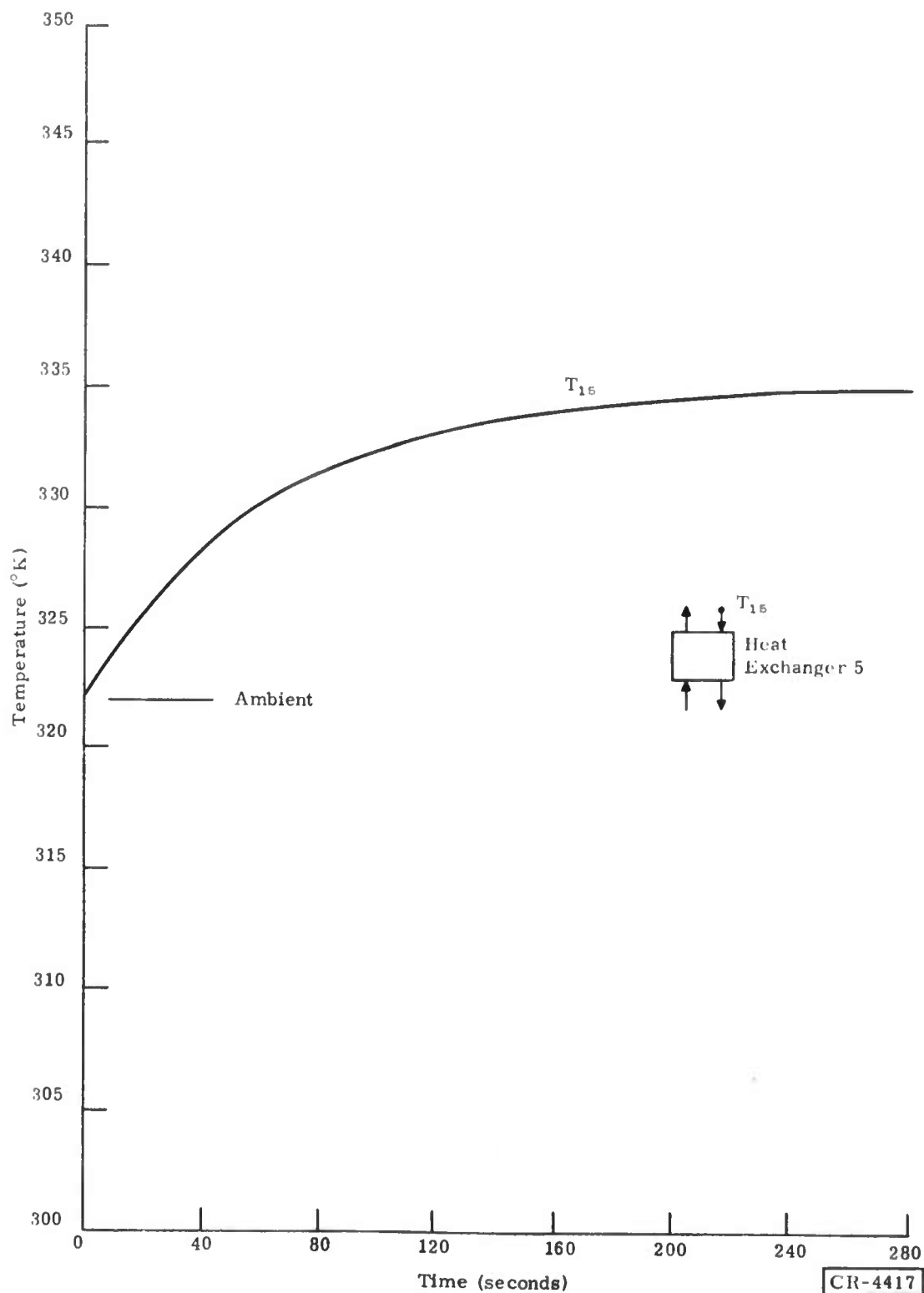


Figure 71. Input (Compressor/Intercooler) Startup

The large load (616 pounds of copper) at the cold end was considered to be a dominant factor in the cooldown performance. Under normal (uncontrolled) conditions, the flow and consequent cooling at this point would be very small for much of the cooldown cycle. As an experiment, it was assumed that a controlled bypass was present at the Joule-Thomson valve, and the corresponding initial flow was set at 7.1 grams per second (twice the design flow rate) to facilitate the bottom loop cooling. This rate was maintained until it became apparent that it was no longer effective, and at that point (46.7 hours) the rate was reduced to 3.55 grams per second (design flow rate). Finally, near the point of liquefaction, the flow rate was permitted to assume its normal (uncontrolled) level. The flow rate schedule is shown in Figure 72.

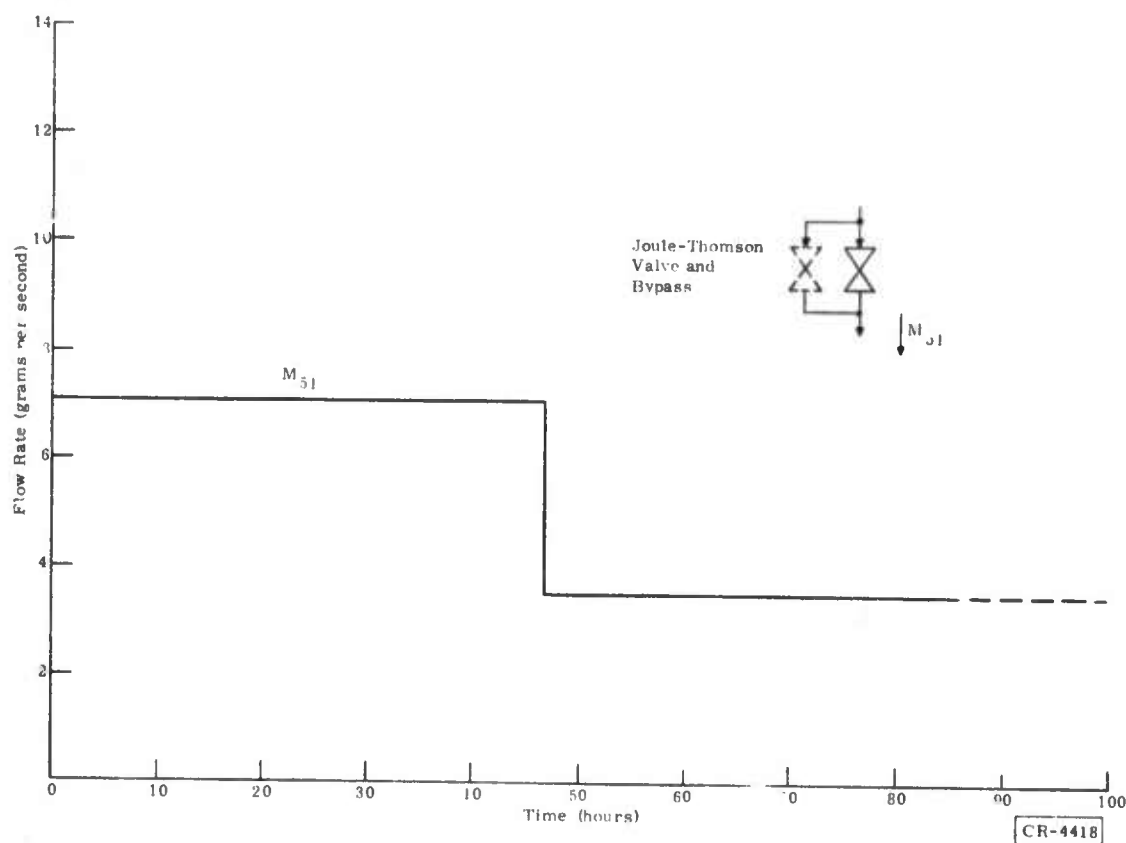


Figure 72. Controlled Joule-Thomson Valve and Bypass Flow Rate

TRANSIENT RUN

Under the initial and controlled conditions described above, the model was allowed to run to the point of liquefaction (87.5 hours). At that point, cooldown of the large warm-end devices was incomplete; however, with the small step sizes necessary, much computation time would have been required simply to run these out with no real addition to the transient picture. The run was therefore stopped at that point, and time constants were artificially altered to permit a runout to near steady-state, with a small amount of additional computation.

The transient temperature traces for the five heat exchangers is shown in Figure 73. In each case the outlet temperature on the high-pressure side is plotted. Figure 74 shows an expanded plot of the response of the three coolest heat exchangers to flow switching in the Joule-Thomson loop.

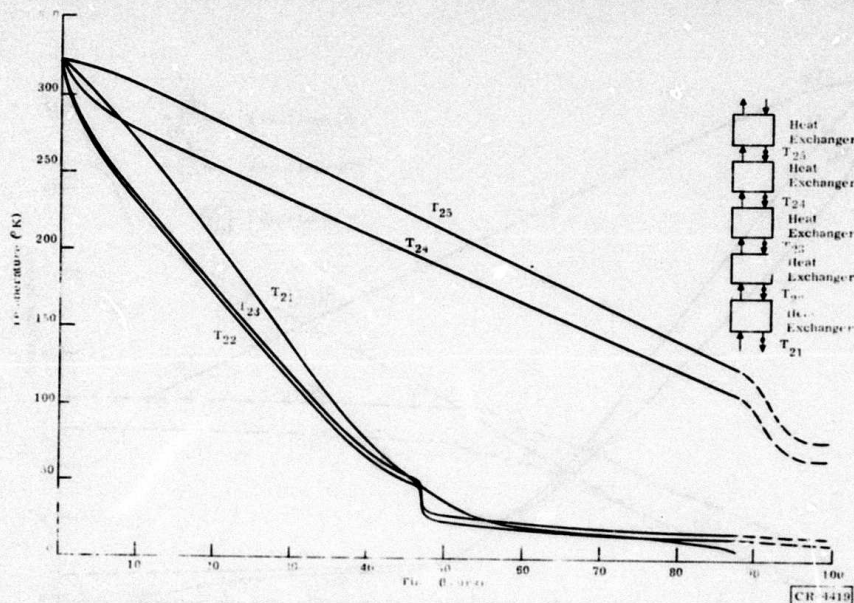


Figure 73. Heat Exchanger Temperatures

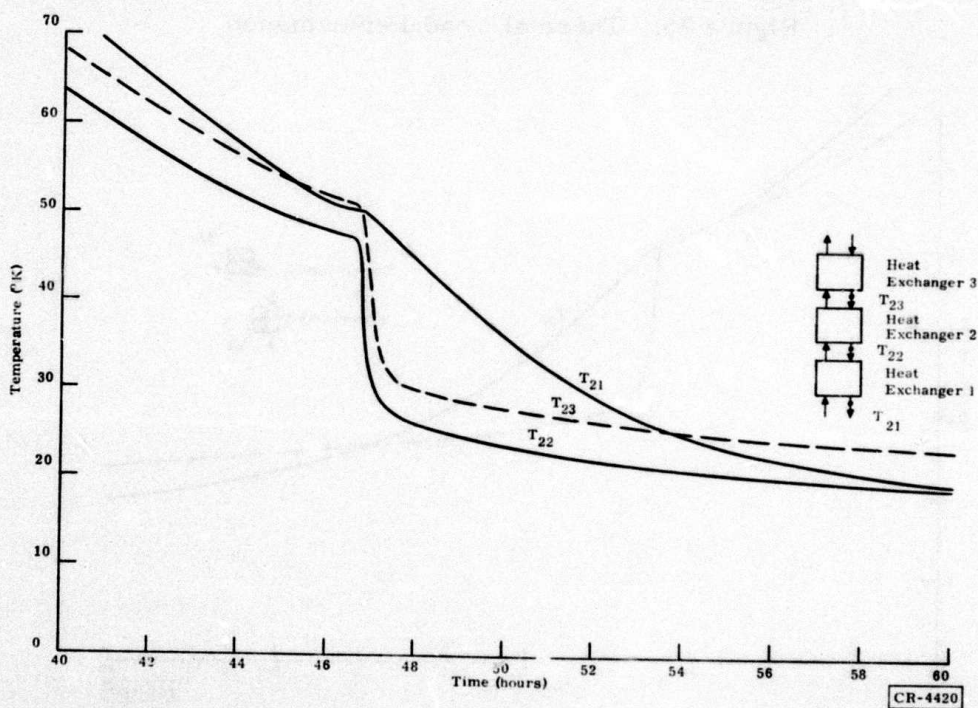


Figure 74. Heat Exchanger Response to Flow Switching

The response of the three thermal loads is shown in Figure 75. The variables plotted are the temperatures of the load masses and the heat flow absorbed from an ambient temperature source. Figure 76 shows an expanded plot of the load temperature response to the flow switching effects.

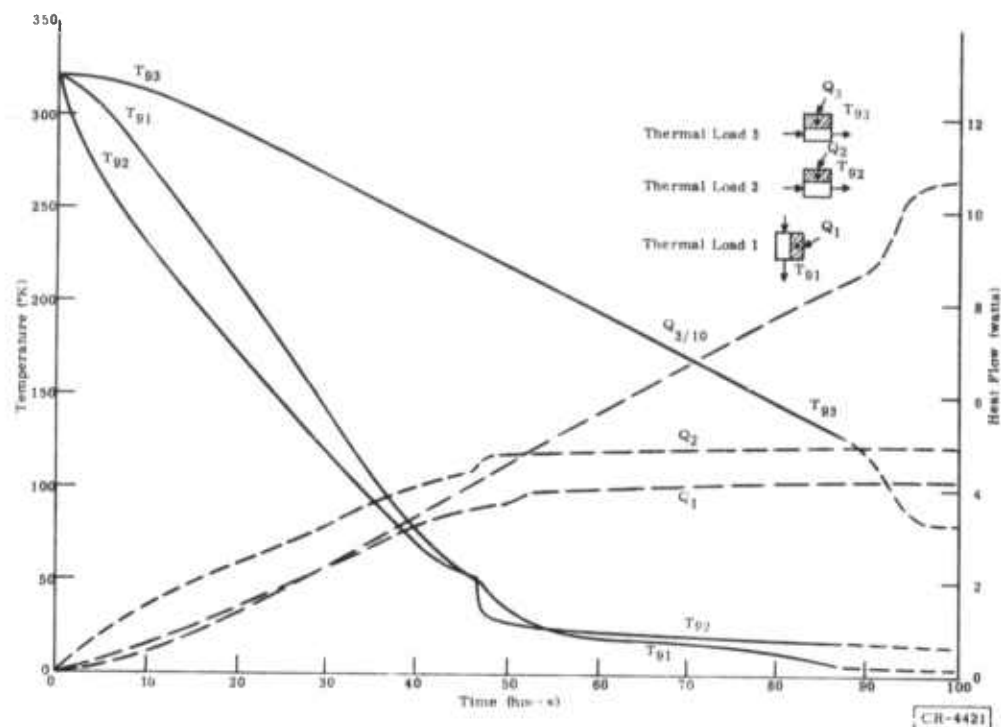


Figure 75. Thermal Load Performance

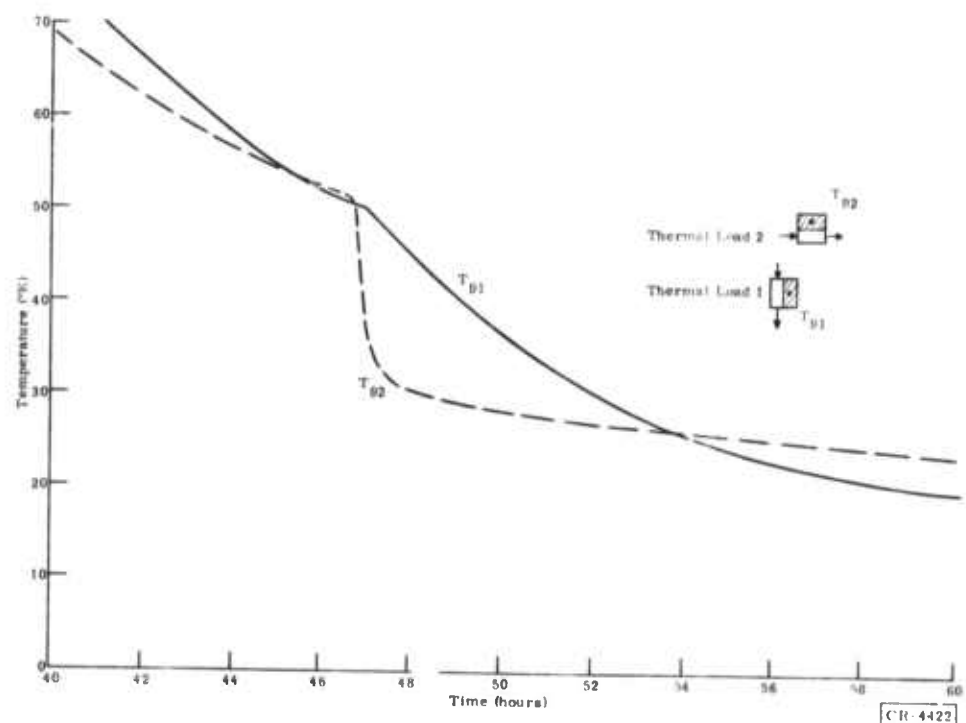


Figure 76. Thermal Load Response to Flow Switching

Turboalternator performance during cooldown is plotted in Figure 77, where speed and load power for the two turboalternators are shown. A test of the model integrity is the low-temperature performance of the bottom heat exchanger shown in Figure 78. The characteristic switchover of the terminal temperatures in the vicinity of 20° K is dependent upon the proper incorporation of real gas properties.

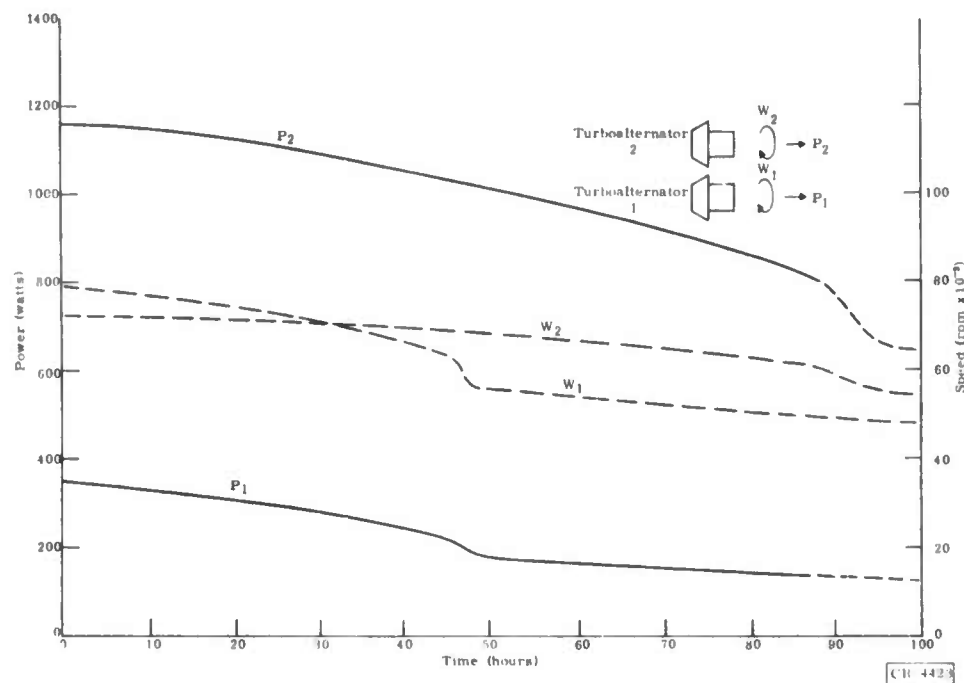


Figure 77. Turboalternator Performance

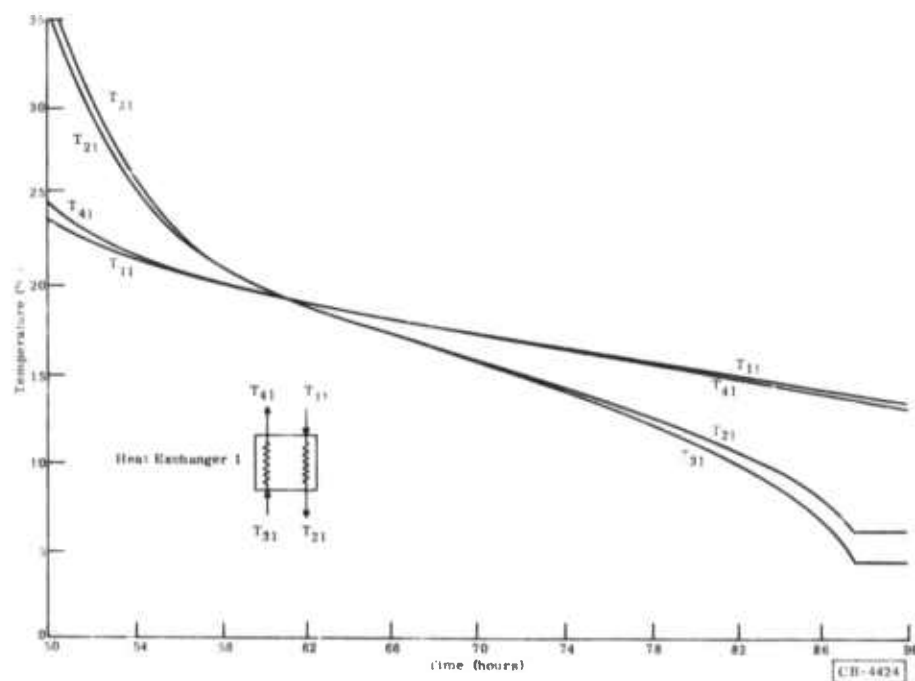


Figure 78. Heat Exchanger 1 Low-Temperature Performance

Following the point of liquefaction, time constants were arbitrarily adjusted to permit more rapid computation. Slewing in this manner constitutes an example of the way the model might be used to seek a new balance, given any initial starting point (e.g., an off-design condition). In this case, the stable balance point is the system design point, and the results test the integrity of the model mechanization and parameters. The computation was allowed to proceed until it was apparent that all variables were closely approaching their proper values and was arbitrarily halted when the remaining errors were on the order of 1 percent. The comparison between the known design point and the last recorded model variable set is given in Table 10.

Table 10
END-OF-RUN TRANSIENT DATA

Device	Variable	Design Value	Calculated Value
Heat Exchanger 5	T ₁₅	335.0	335.0000
	T ₂₅	77.54	77.9982
	T ₄₅	331.0	331.0090
Heat Exchanger 4	T ₂₄	65.78	66.1633
	T ₄₄	72.15	72.6465
Heat Exchanger 3	T ₂₃	13.91	14.0536
	T ₄₃	64.97	65.4396
Heat Exchanger 2	T ₂₂	11.44	11.5564
	T ₄₂	12.07	12.2095
Heat Exchanger 1	T ₂₁	6.214	6.2229
	T ₄₁	11.33	11.4442
Thermal Load 3	Q ₃	106.2	105.989
	T ₆₃	80.00	80.4605
	T ₉₃	81.00	81.4564
Thermal Load 2	Q ₂	5.00	4.9978
	T ₈₂	14.00	14.1503
	T ₉₂	14.20	14.3439
Thermal Load 1	Q ₁	4.20	4.2002
	T ₈₁	4.40	4.4000
	T ₉₁	4.50	4.4832
Turboalternator 2	P ₂	650.0	651.669
	W ₂	54.555	54.6334
	M ₄₂	8.3	8.2762
	T ₁₂₂	64.97	65.4215
Turboalternator 1	P ₁	127.7	126.355
	W ₁	47.970	48.093
	M ₄₁	9.2	9.1530
	T ₁₂₁	11.33	11.4467
Joule-Thomson/Liquefier	M ₅₁	3.55	3.54746
	M ₇₁	0.11	0.1174

CR-4425

DISCUSSION AND CONCLUSIONS

A generic mathematical model for transient/off-design simulation of a refrigeration system cryosection was developed and successfully tested for a realistic design case. The model is completely modular in structure and is therefore applicable to a wide variety of system configurations. It contains considerable sophistication in its representation of component devices and reproduces the results of more complex design programs with good accuracy. Using proper step sizes, the computation of a complete cooldown transient was accomplished in a stable and realistic manner. Various physical phenomena known to be characteristic of the devices involved were exhibited by the model performance.

On the other hand, the model must be recognized as a developmental version in which a number of modifications or improvements are needed to produce an efficient analytical tool. Such improvements include incorporation of automatic control of the computation step size, general incorporation of more efficient computation procedures, addition of other devices and effects, and review of the theoretical representation of thermal time constants. The completely modular nature of the model structure should greatly aid in any such future development, because modifications can be made in a building block manner.

The test run results show reasonable behavior of the design system and its individual devices over a complete cooldown cycle. The total time of 87.5 hours from ambient start to liquefaction of the helium is not an unreasonable result, considering the massive thermal load to be cooled. However, it must be recognized that this is an isolated test case for the transient calculation. Until parallel model and physical tests are compared, it will not be known to what degree the transient modeling is accurate. Also, in this particular case, flow switching control was introduced on an intuitive basis; without a set of comparative runs, it cannot be said whether this shortened or prolonged the total cooldown cycle.

In general, it can be said that the modeling effort is successful and opens up the potential for new and better understanding of the behavior of systems of this kind. This is certainly true of its use for comparative evaluation of alternative configurations and off-design conditions. The absolute transient results are indicative, but their accuracy remains to be verified by physical test correlation.

MODELING EXPERIENCE

In common with many digital transient calculations, this model must deal with the problem of widely differing time constants. In the present example, a time constant ratio on the order of 100 to 1 exists between major devices at ambient temperature, and this ratio is increased to nearly 1000 to 1 at cry-

ogenic operating temperatures. In the rather complex, interconnected loop arrangement present, the effective dynamics depend upon not only these values, but also various loop gains that vary with the temperature.

In the simple computational form used, the same time increment is used throughout the system, and this increment is adjusted arbitrarily as conditions vary. For example, near the liquefaction point, it is necessary to use very short time steps for cold loop stability, and these same short time steps (0.1 second) are used at the warm end with very long time constants (on the order of 1000 seconds).

A further development of the model program should provide for different computation rates at fast and slow portions of the system and should consider means for automatically adjusting these rates as the run proceeds. General purpose analysis programs incorporating such features exist (e.g. General Electric computer program ADA), and the relative merits of using these versus augmenting the special purpose model with similar features should be investigated.

The modeling representation of the device structure is believed to be at a level adequate for the present purpose. The device left in the most elementary form is the turboalternator. However, it is easily made more detailed, if required, and can be made to yield electrical losses or respond to changes in the resistance load or input pressure with a high degree of fidelity. The modular form used facilitates replacement of any given device model, if desired.

From a transient viewpoint, future investigation should review the theoretical transient behavior of heat exchangers, possibly arriving at a different approach to the heat exchanger representation, to more accurately model the true transient behavior.

As it stands, the model is limited to a constant pressure configuration; consequently, no compressor model is required. The addition of the compressor and pressure variation effects on the other devices is an area for future development.

Once a system is represented in mathematical form, it is possible to compute many functions in addition to the primary variables. For example, in an early experiment the energy and the rate of energy flow from each individual system device were continuously computed during a cooldown transient. Observations of this type and/or many types of transient switching effects are readily generated with this type of model.

TEST CASE EXPERIENCE

The experimental transient cooldown cases that were run led to some insight into the essential behavior of this type of system. In elementary terms,

one can observe the bootstrapping effect by which the turboalternators gradually pull down the temperature of the relatively massive heat exchangers, until finally the coldest exchanger reaches the region in which real gas properties provide Joule-Thomson cooling to flip it over and past the turbine in a slingshot manner.

It was found that slight changes in the flow rate have a pronounced effect on the dynamics of the Joule-Thomson loop of the system (presumably loop gain). The flow rate programming used in the case described above under "Transient Cooldown Results" was an attempt to use this effect to enhance the cooling of the large, coldest load. By experiment, it was found that the initial value chosen (twice the normal flow) resulted in the highest initial rate of cooling for the No. 1 load. The fact that this was not optimum everywhere is indicated by the fact that in approximately 46 hours the system was tending to level off at too high a temperature for liquefaction. At that point the flow rate was reduced to normal (design) flow, and a rapid dip in the Joule-Thomson loop temperature resulted. This experience suggests that there is a need for investigation of the optimum flow control over the entire cooldown transient. Whether the flow control is beneficial in the cooldown of the entire system is not clear; however, it certainly appears possible to alter the performance at a given load point relative to other load points.

Whether the total time to liquefaction (87.5 hours) is a good measure of the corresponding cooldown for the physical system is not known and will not be known until some correlation with physical data is made. However, assuming the functions to be of realistic form, regardless of the absolute magnitudes, the load curves of Figure 75 show a very slow (flat) cooling period from the flow switching point at about 47 hours and onward. This situation suggests at least the possibility that a more optimum flow schedule might have reduced the temperature at 47 hours by a few degrees, displacing the curves accordingly and reducing the time to liquefaction by many hours.

MODEL DESCRIPTION

The cryogenic refrigeration system model, as it presently exists, assumes the presence of an external source and a sink for working fluid at a constant pressure and pressure difference. The system model contains four component device models:

- Heat exchanger
- Thermal load
- Turboalternator
- Joule-Thomson valve/liquefier

The system model also contains three auxiliary functions:

- Interconnections

- Temperature-enthalpy relations
- Miscellaneous time functions

The System Model structure is completely modular, and there can be as many heat exchangers, thermal loads, or turboalternators as are desired, with or without a Joule-Thomson/liquefier stage, arranged in any physically consistent combination.

The heat exchanger model will accomodate balanced or unbalanced flow conditions, automatically determining the condition existing for each system heat exchanger, individually and at any point in time.

The thermal load model will accomodate three types of heat loads:

- Constant Q. The rate at which energy is received from some external source is a constant specified value.
- Heat Leak. The temperature of some external source is held at a specified value, and the flow of heat is proportional to the difference between the temperature of that external source and the temperature of the thermal load mass.
- Radiation. The temperature of some external source is held at a specified value, and the flow of energy is proportional to the difference in the fourth powers of the source and the load temperatures.

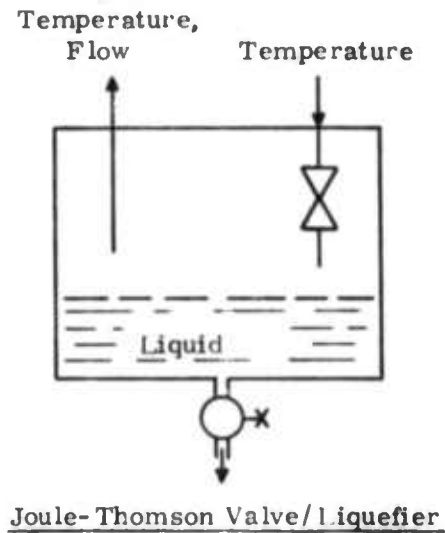
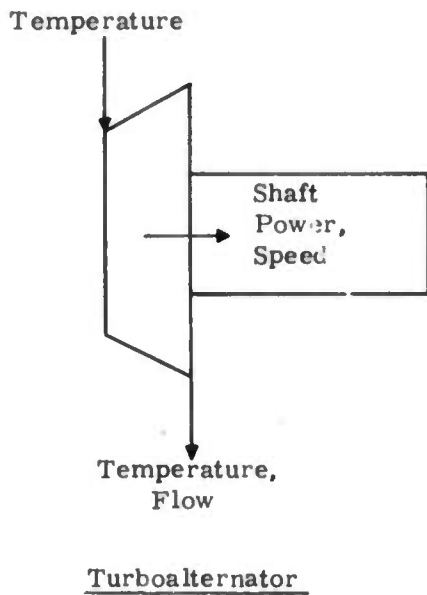
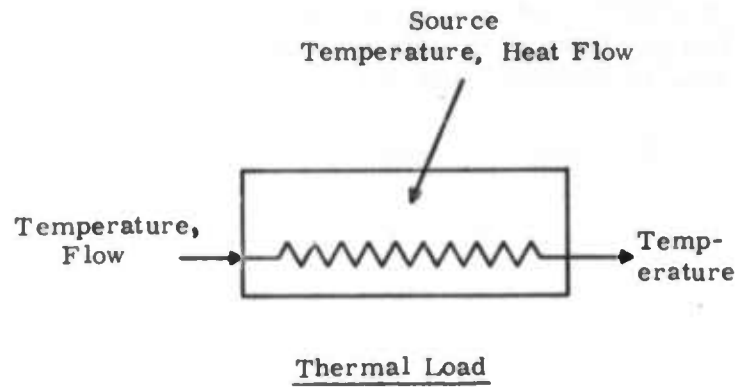
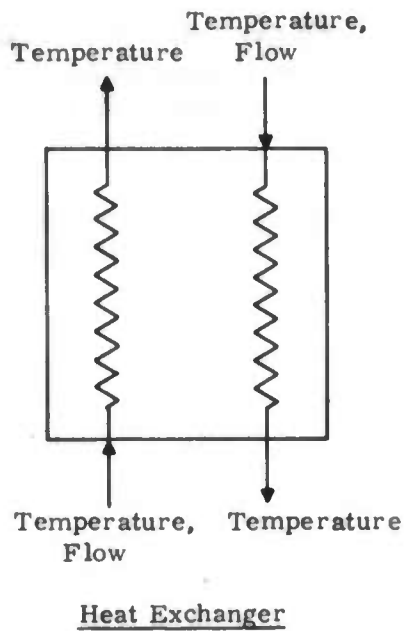
For each individual load in the system, it is necessary to specify which of the three types of heat loads is represented. The system may contain any mixture of types.

Real gas temperature-enthalpy relations are used in both the heat-exchanger model and the thermal load model, as well as in the Joule-Thomson valve/liquefier calculations, thereby effectively accounting for the changes in the specific heat of the working fluid during transient temperature changes.

The Joule-Thomson/liquefier model will simulate the accumulation and/or boiling off of liquid and has a provision for the simulation of draining of accumulated liquid for external purposes.

The turboalternator model simulates the conversion of thermal power to mechanical (shaft) power and includes the effect of energy storage by virtue of the moment of inertia of the rotating assembly.

The basic input-output functions for the four component devices are shown in Figure 79. For each system heat exchanger, inputs of temperature and mass flow at both high- and low-pressure sides result in determination of the corresponding output temperatures for the high- and low-pressure sides.



CR-4426

Figure 79. Component Devices

For each thermal load, an input temperature and the mass flow, plus specified load source parameters, will result in determination of an output temperature plus information regarding the source temperature or the heat flow (depending upon the load type).

For each turboalternator, an input (high-pressure gas) temperature will result in determination of an output (low-pressure gas) temperature and mass flow, plus the shaft speed and power.

For the Joule-Thomson valve/liquefier, an input (high-pressure gas) temperature will result in output (low-pressure gas) temperature and mass flow, plus information regarding the rate of liquefaction and liquid accumulation.

For every different system configuration (with respect to the numbers and arrangement of component devices), it is necessary to specify a corresponding set of interconnections. As suggested in Figure 79, these interconnection specifications will be temperatures and mass flow values to be equated as the output for one device becomes the input to a second device to which it is attached. In most cases these are direct relationships. The exception is the determination of the temperature when two values of flow are mixed. In that case, the resulting temperature is assumed to be the weighted mean of the temperatures in the two lines, where the weighting factors are the relative mass flow values.

The temperature interconnection specifications are the temperatures at all nodes, and the mass flow interconnection specifications are sums of the mass flows in the shunt devices (turboalternators and the Joule-Thomson/liquefier). As an example, a simple assembly of component devices is shown in Figure 80, and the corresponding interconnection specifications are given in Table 11.

The component device models and, consequently, the complete system model are mechanized on a time varying (transient) basis. Each heat exchanger model and each thermal load model contain the simulation of a thermal mass, represented by a first-order exponential response to the input temperature functions. The basic computational form used in these models is illustrated as shown in Figure 81.

The output temperature of the device (T_{out}) is some function of its inputs (e.g., input temperature T_{in} and mass flow M) and time (t). It is assumed that this relationship can be expressed:

$$T_{out} = F(T_{in}, M) + G e^{-Ht} \quad (1)$$

where the function, F , is the final (steady-state) solution for the output, T_{out} . Given the present set of inputs, T_{in} and M , $G e^{-Ht}$ is the present instantaneous

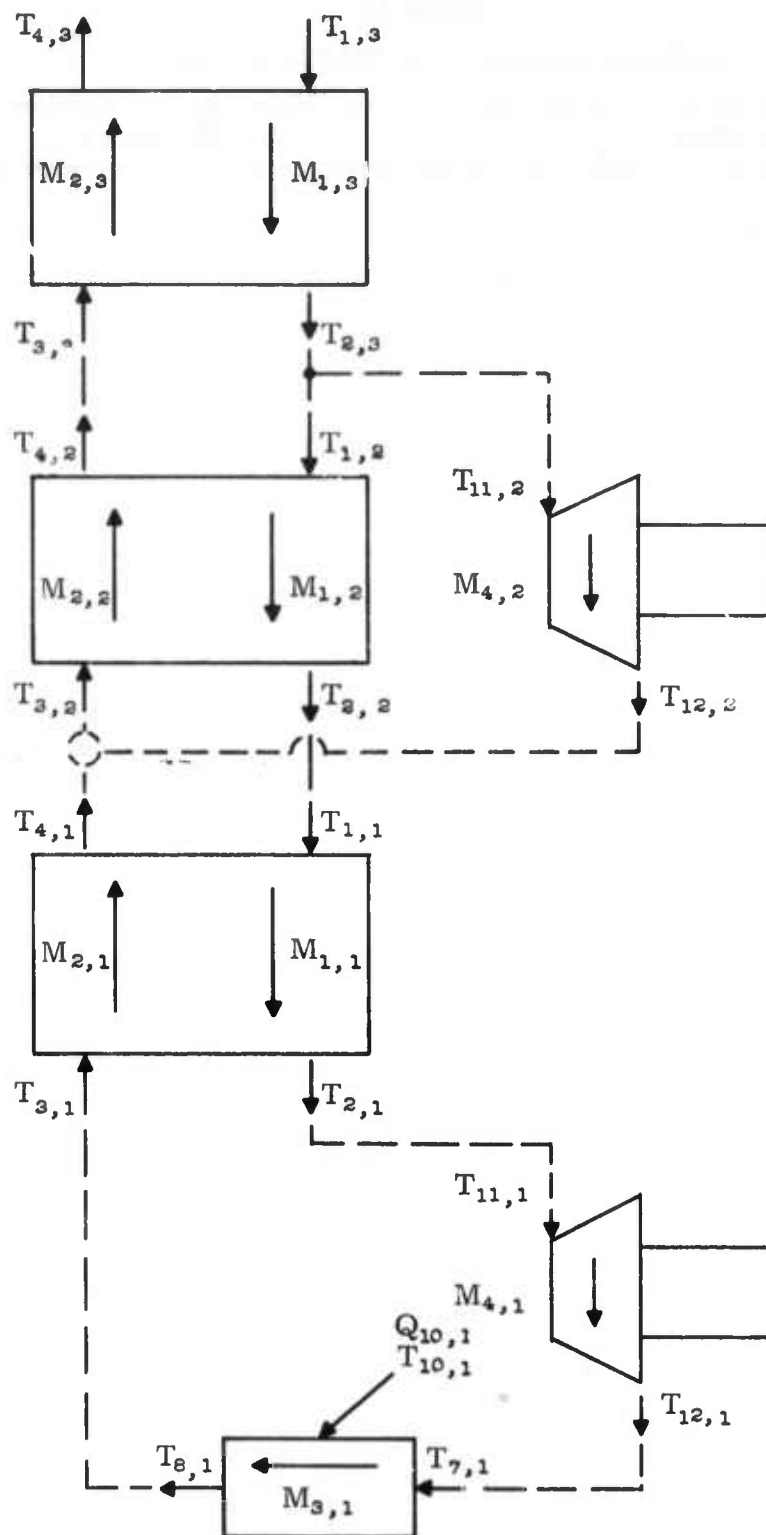


Figure 80. Example of Interconnection

Table 11
INTERCONNECTION SPECIFICATIONS

Temperature/Flow	Specifications
Temperature	$T(1, 2) = T(2, 3)$ $T(11, 2) = T(2, 3)$ $T(1, 1) = T(2, 2)$ $T(11, 1) = T(2, 1)$ $T(7, 1) = T(12, 1)$ $T(3, 1) = T(8, 1)$ $T(3, 2) = \frac{M(2, 1) \times T(4, 1) + M(4, 2) \times T(12, 2)}{M(2, 1) + M(4, 2)}$
Mass flow	$T(3, 3) = T(4, 2)$ $M(1, 1) = M(4, 1)$ $M(2, 1) = M(4, 1)$ $M(3, 1) = M(4, 1)$ $M(1, 2) = M(4, 1)$ $M(2, 2) = M(4, 1) + M(4, 2)$ $M(1, 3) = M(4, 1) + M(4, 2)$ $M(2, 3) = M(4, 1) + M(4, 2)$

CR-4428

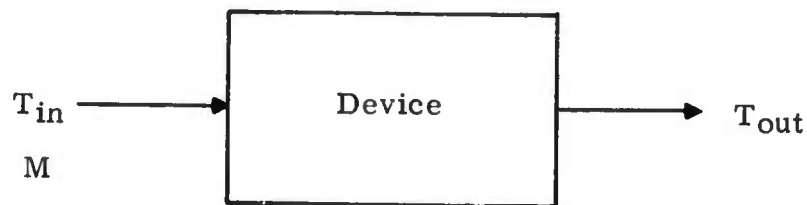


Figure 81. Computational Form

error by which the output departs from the solution dictated by the present inputs, and H is the decrement (reciprocal of the time constant) for the device.

Differentiating Equation 1 with respect to time and substituting:

$$\frac{d}{dt} (T_{out}) = -H G e^{-Ht} = -H (T_{out} - F) \quad (2)$$

then, in incremental form:

$$\Delta T_{\text{out}} = H (F - T_{\text{out}}) \Delta t$$

and finally, for numerical calculation purposes:

$$(T_{\text{out}})_{i+1} = (T_{\text{out}})_i + H (F - T_{\text{out}})_i \Delta t \quad (3)$$

For the heat exchanger model, decrement H has the form:

$$H = \frac{2hA}{M_c C_c} \quad (4)$$

where:

h = Surface heat transfer coefficient

A = Surface area

M_c = Core mass

C_c = Core specific heat

Because the specific heat of the core material, C_c , changes with the temperature, the core temperatures at both ends of each heat exchanger are continuously calculated and are used to adjust separate values for H at the warm and cold ends of each device.

For the thermal load model, the form of the decrement will vary among the three types; however, the core temperature is continuously calculated in all cases and is used for temperature adjustment.

In the case of the turboalternator model, the procedure is to calculate the turbine and alternator load torques separately and to use any torque difference to accelerate or decelerate the total shaft moment of inertia. In incremental form:

$$\begin{aligned} \frac{\Delta W}{\Delta t} &= \frac{1}{J} (L_T - L_A) \\ W_{i+1} &= W_i + \frac{1}{J} (L_T - L_A)_i \Delta t \end{aligned} \quad (5)$$

where:

W = Shaft speed

J = Shaft moment of inertia

L_T = Turbine torque

L_A = Alternator torque

Initial values must be specified for all incremented functions. These values will be two output and two core temperatures for each heat exchanger, one output and one core temperature for each thermal load, shaft speed for each turboalternator, and any liquid accumulation in the liquefier. It is desirable, though not necessary, that the other variables in the system be given initial values for a printout record of the complete initial state.

Given such a set of initial conditions, the system program will first run through all interconnections to provide inputs to all devices consistent with the initial conditions. For that set of inputs, it will individually compute a set of outputs for every device in the system, for one increment in time. When this is complete, it will again go through all interconnections to update the set of inputs to match the output results just obtained. The procedure is then repeated for the second time step, and so forth.

A reset counter is used to command a selected printout at a specified number of time steps. A continuous counter is used to accumulate the total elapsed transient time. Any desired switching logic can be inserted to change any device parameter at a specified time or at a specified value of any system variable.

The calculation will continue indefinitely, unless logic for some specified stopping criteria is inserted. It will therefore carry out the transient calculation until the steady-state condition is reached. By the form of the incremental calculation, this will be the true steady-state value without cumulative error because, by Equation 3, transient adjustment of any given system variable will cease only when the variable exactly equals the number calculated to be its steady-state value relative to its surrounding inputs.

The basic model layout and sequence of operations is shown in flowchart form in Figure 82.

HEAT EXCHANGER MODEL

Each heat exchanger in the system is treated as a four-terminal device, with two inputs and two outputs, having a capacity for internal energy storage. The energy storage characteristics are represented by a pair of first-order time constants, one for the warm end and one for the cold end of the device, and these constants are made functions of their corresponding local core temperatures.

The model variables consist of four terminal fluid temperatures, two core temperatures, two decrements (time constant reciprocals), and two mass flows:

- T_1 = Warm side incoming fluid temperature
- T_2 = Warm side outgoing fluid temperature

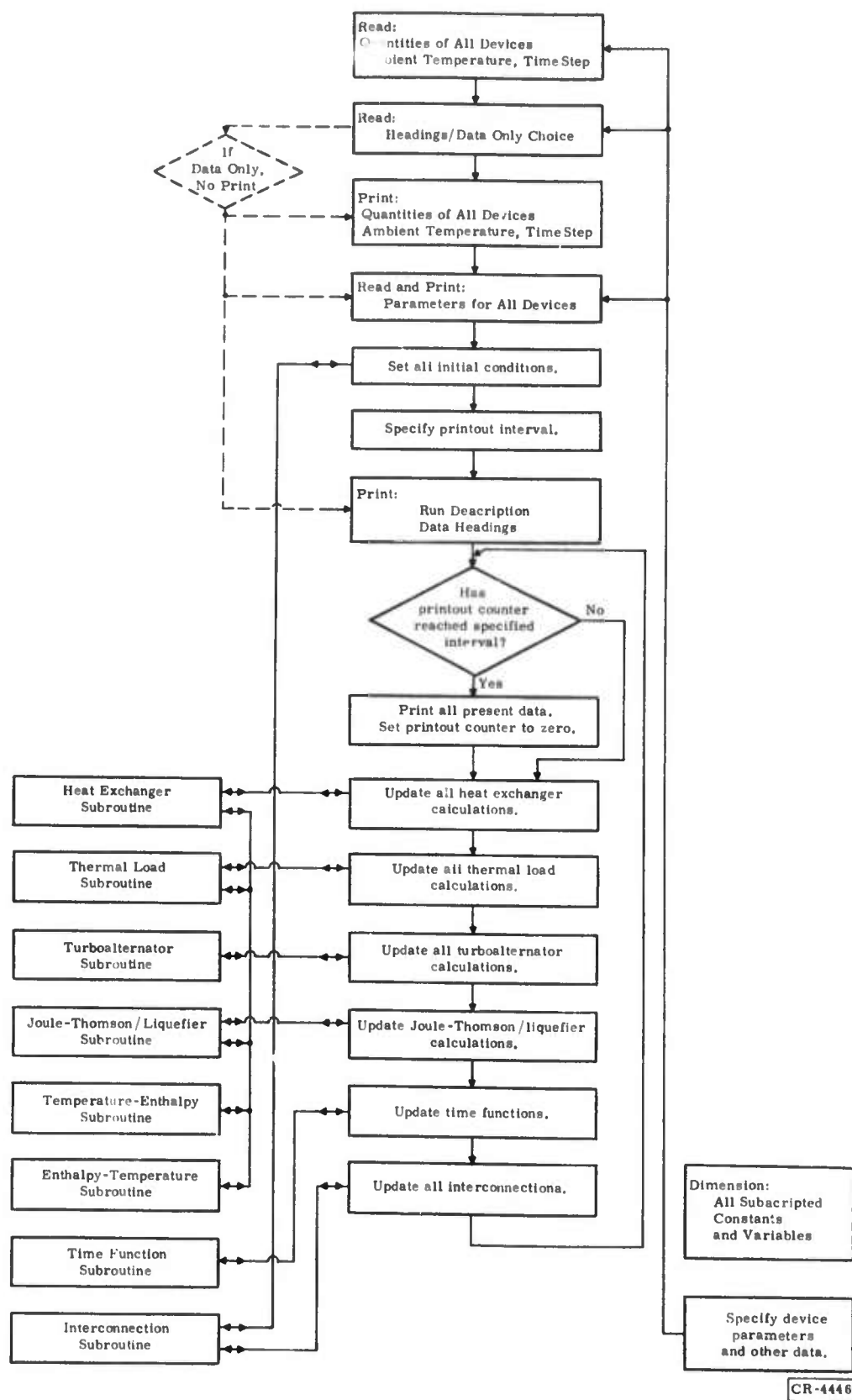


Figure 82. Flowchart of Basic Model Layout

- T_3 = Cold side incoming fluid temperature
- T_4 = Cold side outgoing fluid temperature
- T_6 = Warm end core temperature
- T_8 = Cold end core temperature
- H_6 = Warm end decrement
- H_8 = Cold end decrement
- M_1 = Warm side mass flow
- M_2 = Cold side mass flow

Schematically, the device is represented as shown in Figure 83.

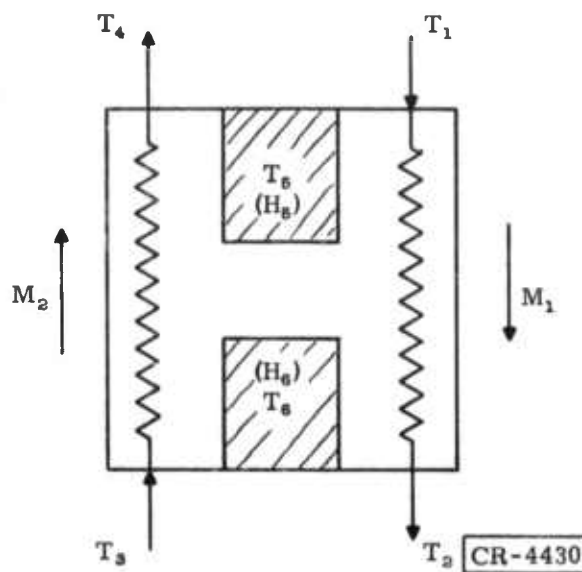


Figure 83. Schematic Diagram of Heat Exchanger Model

The parameters that characterize a particular heat exchanger are contained in two specified constants, K_1 and K_2 . K_1 is defined as:

$$K_1 = M_{\min} \times N_{tu}$$

$$= \frac{hA}{2C}$$

where:

M_{\min} = Lesser of rated M_1 and M_2

N_{tu} = Number of transfer units

h = Core-fluid heat transfer coefficient

A = Surface area

C = Fluid C_p

K_2 is defined as:

K_2 = Decrement at ambient temperature

$$= \frac{2hA}{M_c C_c}$$

where:

M_c = Core mass

C_c = Core thermal conductivity

In general, the heat exchanger will be in some initial thermal state, and certain inputs (T_1 , M_1 , T_3 , and M_2) will be applied. The first step will then be calculation of the steady-state (final) output and core temperatures (F_2 , F_4 , F_5 , and F_6), which would ultimately result from these inputs:

$$F_2, F_4, F_5, F_6 = f(T_1, M_1, T_3, M_2, K_1) \quad (6)$$

The second step will be calculation of the decrements for the present core temperatures prevailing:

$$\begin{aligned} H_5 &= K_2 \times f(T_5) \\ H_6 &= K_2 \times f(T_6) \end{aligned} \quad (7)$$

The final step will be calculation of the new state temperatures at the end of a time increment, $U1$, using first-order integration:

$$T_{i+1} = T_i + U1 \times H_i \times (F_i - T_i) \quad (8)$$

The form of the equations for the F-functions of Equation 6 will vary, depending upon the state of the mass flow balance or unbalance. Also, when a heat exchanger is used at near liquid temperatures, its performance is significantly influenced by variations in the fluid specific heat.

The model logic is arranged in such a way that no individual heat exchanger is committed to a balanced or unbalanced flow condition, even though that may be its steady-state design. Under transient conditions, the actual flow conditions will be determined at each time step, and it is possible for a given heat exchanger to change from a balanced to an unbalanced flow or vice-versa, from one time step to the next.

Equations For Balanced Flow, $M_1 = M_2$

For temperature inputs T_1 and T_3 , mass flow inputs $M_1 = M_2$, and heat exchanger parameter K_1 :

$$F_2 = \frac{T_1 + \frac{K_1}{M_1} T_3}{1 + \frac{K_1}{M_1}} \quad (9)$$

$$F_4 = \frac{\frac{K_1}{M_1} T_1 + T_3}{1 + \frac{K_1}{M_1}} \quad (10)$$

$$F_6 = \frac{\left(\frac{1}{2} + \frac{K_1}{M_1}\right) T_1 + \frac{1}{2} T_3}{1 + \frac{K_1}{M_1}} \quad (11)$$

$$F_8 = \frac{\frac{1}{2} T_1 + \left(\frac{1}{2} + \frac{K_1}{M_1}\right) T_3}{1 + \frac{K_1}{M_1}} \quad (12)$$

Equations For Unbalanced Flow, $M_1 > M_2$

For temperature inputs T_1 and T_3 , mass flow inputs M_1 and M_2 , and heat exchanger parameter K_1 :

$$F_2 = \frac{\left(1 - \frac{M_2}{M_1}\right) T_1 + \left[1 - e^{-K_1\left(\frac{1}{M_2} - \frac{1}{M_1}\right)}\right] \frac{M_2}{M_1} T_3}{1 - \frac{M_2}{M_1} e^{-K_1\left(\frac{1}{M_2} - \frac{1}{M_1}\right)}} \quad (13)$$

$$F_4 = \frac{\left[1 - e^{-K_1\left(\frac{1}{M_2} - \frac{1}{M_1}\right)}\right] T_1 + \left[\left(1 - \frac{M_2}{M_1}\right) e^{-K_1\left(\frac{1}{M_2} - \frac{1}{M_1}\right)}\right] T_3}{1 - \frac{M_2}{M_1} e^{-K_1\left(\frac{1}{M_2} - \frac{1}{M_1}\right)}} \quad (14)$$

$$F_6 = \frac{\left[1 - \frac{1}{2} \left(1 + \frac{M_2}{M_1}\right) e^{-K_1\left(\frac{1}{M_2} - \frac{1}{M_1}\right)}\right] T_1 + \left[\frac{1}{2} \left(1 - \frac{M_2}{M_1}\right) e^{-K_1\left(\frac{1}{M_2} - \frac{1}{M_1}\right)}\right] T_3}{1 - \frac{M_2}{M_1} e^{-K_1\left(\frac{1}{M_2} - \frac{1}{M_1}\right)}} \quad (15)$$

$$F_8 = \frac{\left[\frac{1}{2} \left(1 - \frac{M_2}{M_1} \right) \right] T_1 + \left[\frac{1}{2} \left(1 + \frac{M_2}{M_1} \right) - \frac{M_2}{M_1} e^{-K_1 \left(\frac{1}{M_2} - \frac{1}{M_1} \right)} \right] T_3}{1 - \frac{M_2}{M_1} e^{-K_1 \left(\frac{1}{M_2} - \frac{1}{M_1} \right)}} \quad (16)$$

Equations For Unbalanced Flow, $M_2 > M_1$

For temperature inputs T_1 and T_3 , mass flows inputs M_1 and M_2 , and heat exchanger parameter K_1 :

$$F_2 = \frac{\left[\left(1 - \frac{M_1}{M_2} \right) e^{-K_1 \left(\frac{1}{M_1} - \frac{1}{M_2} \right)} \right] T_1 + \left[1 - e^{-K_1 \left(\frac{1}{M_1} - \frac{1}{M_2} \right)} \right] T_3}{1 - \frac{M_1}{M_2} e^{-K_1 \left(\frac{1}{M_1} - \frac{1}{M_2} \right)}} \quad (17)$$

$$F_4 = \frac{\left[1 - e^{-K_1 \left(\frac{1}{M_1} - \frac{1}{M_2} \right)} \right] \frac{M_1}{M_2} T_1 + \left[1 - \frac{M_1}{M_2} \right] T_3}{1 - \frac{M_1}{M_2} e^{-K_1 \left(\frac{1}{M_1} - \frac{1}{M_2} \right)}} \quad (18)$$

$$F_5 = \frac{\left[\frac{1}{2} \left(1 + \frac{M_1}{M_2} \right) - \frac{M_1}{M_2} e^{-K_1 \left(\frac{1}{M_1} - \frac{1}{M_2} \right)} \right] T_1 + \left[\frac{1}{2} \left(1 - \frac{M_1}{M_2} \right) \right] T_3}{1 - \frac{M_1}{M_2} e^{-K_1 \left(\frac{1}{M_1} - \frac{1}{M_2} \right)}} \quad (19)$$

$$F_6 = \frac{\left[\frac{1}{2} \left(1 - \frac{M_1}{M_2} \right) e^{-K_1 \left(\frac{1}{M_1} - \frac{1}{M_2} \right)} \right] T_1 + \left[1 - \frac{1}{2} \left(1 + \frac{M_1}{M_2} \right) e^{-K_1 \left(\frac{1}{M_1} - \frac{1}{M_2} \right)} \right] T_3}{1 - \frac{M_1}{M_2} e^{-K_1 \left(\frac{1}{M_1} - \frac{1}{M_2} \right)}} \quad (20)$$

Adjustment for Variable Specific Heat

In the differential equations for an ideal counterflow device, mass flow and fluid specific heat enter as a product. This suggests that effects of varying

specific heat can be represented without theoretical error by making proportional adjustments in the mass flow variable while assuming a constant C_p .

At any given time, values for the four terminal Heat Exchanger 1 temperatures (T_1 , T_2 , T_3 , and T_4) are known. Using the proper functions for their respective pressures, corresponding enthalpy values E_1 , E_2 , E_3 , and E_4 are obtained. By taking the ratios of the enthalpy differences to the temperature differences, average values for specific heats are calculated for the high- and low-pressure sides. The ratios of these values to the nominal value for specific heat (5.2) are then used to adjust the actual mass flow values, M_1 and M_2 , to obtain the synthetic values, N_1 and N_2 :

$$N_1 = \frac{1}{5.2} \times \frac{E_2 - E_1}{T_2 - T_1} \times M_1 \quad (21)$$

$$N_2 = \frac{1}{5.2} \times \frac{E_4 - E_3}{T_4 - T_3} \times M_2 \quad (22)$$

These synthetic values for mass flow are then used to calculate F_2 , F_4 , F_5 , and F_6 , using the relations described for Equations 9 through 20.

Because the possibility of small or zero differences in enthalpy or temperature exists during transient operation, the model logic is designed to detect such cases and to bypass the calculation for that particular time step, thereby using the previously calculated values until numerical accuracy is restored.

It is also possible that during transient operation, the process of liquefaction and/or fluid drainage might reduce the return flow in Heat Exchanger 1 to zero. If this should occur, the model logic will set F_2 , F_4 , F_5 , and F_6 equal to the input fluid temperature, T_1 .

Decrements and Numerical Integration

The procedure to this point has been to produce a set of predicted final values (F_2 , F_4 , F_5 , and F_6) for the output and core temperatures corresponding to the present input temperature and mass flow conditions. To complete the vector set, the F -values for the independent input temperatures are made equal to their present values (it is assumed that these values are held constant for the current time step):

$$\begin{aligned} F_1 &= T_1 \\ F_3 &= T_3 \end{aligned} \quad (23)$$

For the same reason, the decrements for the two independent input temperature variables are set to zero:

$$H_1 = 0 \quad (24)$$

$$H_3 = 0$$

The decrements for the output fluid temperatures are assumed to be the same as those for the adjacent core temperatures. Those, in turn, are assumed to have a specified value, K_2 , at ambient temperature T_0 and to vary inversely with the present core temperatures, T_5 and T_6 .

$$\begin{aligned} H_2 &= K_2 \frac{T_0}{T_5} \\ H_4 &= K_2 \frac{T_0}{T_5} \\ H_5 &= K_2 \frac{T_0}{T_5} \\ H_6 &= K_2 \frac{T_0}{T_5} \end{aligned} \quad (25)$$

Finally, using the above values for present temperature T , predicted final temperature F , and decrement H , the new temperature, T' , at the end of a time step, $U1$, is computed for each of the six heat exchanger temperature variables and is repeated for all of the $N1$ heat exchangers present in the system:

$$T'_{ji} = T_{ji} + H_{ji} (F_{ji} - T_{ji}) U1 \quad \left| \begin{array}{l} j = 1 \text{ to } 6 \\ i = 1 \text{ to } N1 \end{array} \right. \quad (26)$$

Outline of Model Logic

The basic flowchart arrangement for the heat exchanger model is shown in Figure 84.

THERMAL LOAD MODEL

Each thermal load in the system is treated as a three-terminal device with the capacity for internal energy storage. The conceptual arrangement is shown schematically in Figure 85.

It is assumed that the device has thermal mass at a uniform temperature, T_9 , and that thermal energy flows to that mass at rate Q , from an external source at temperature T_{10} .

The thermal mass is in turn cooled by the flow of fluid that enters the device at temperature T_7 , leaves at temperature T_8 , and has rate of mass flow M_3 .

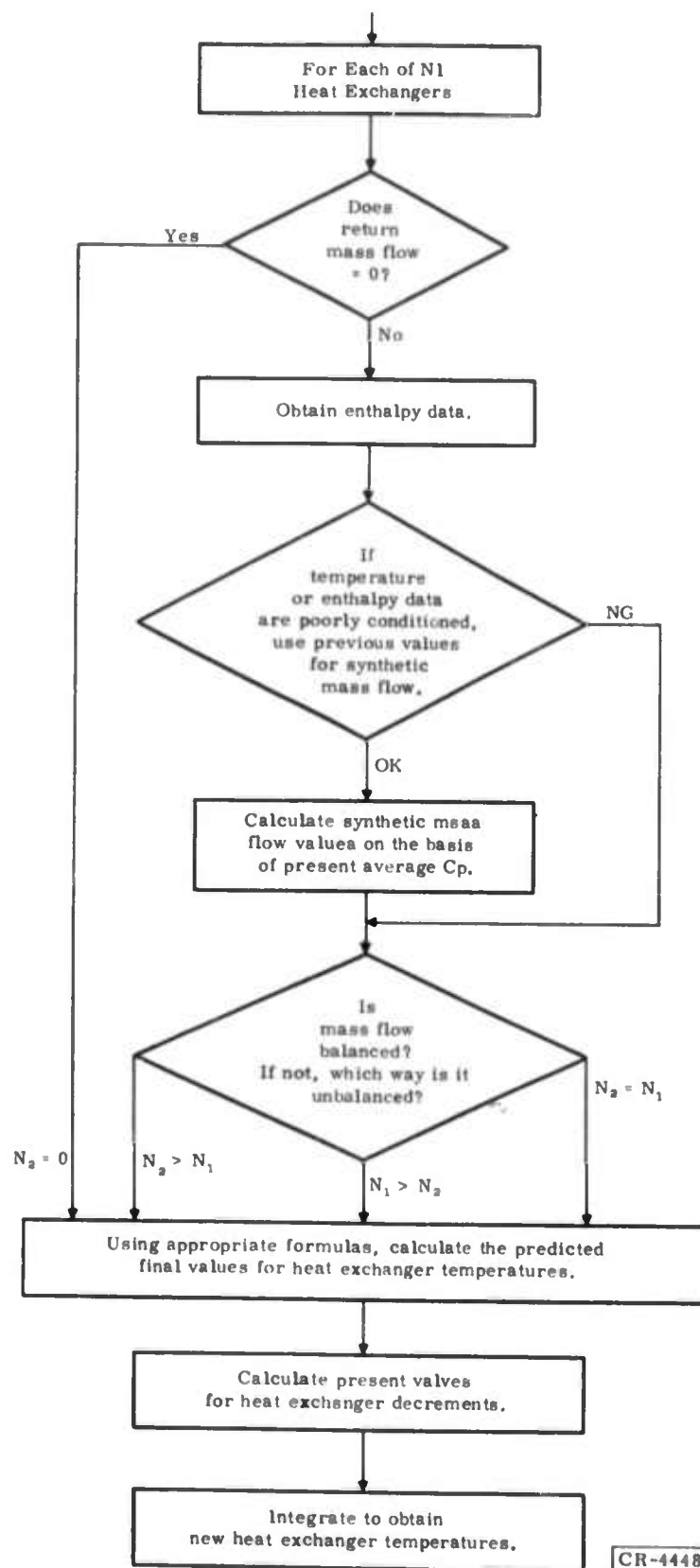


Figure 84. Flowchart of Heat Exchanger Model (Logic and Calculation Sequence)

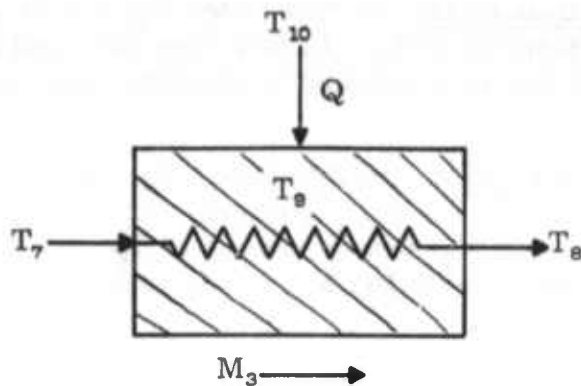


Figure 85. Schematic Diagram of Thermal Load Model

The difference between Q and the rate at which energy is transferred to the fluid will be the rate at which the energy stored in the thermal load mass is changing, and this will be determined by the basic time constant of the device. The temperature, T_θ , of the mass (physical structure) of the thermal load station is taken to be the thermal load temperature seen by external heat sources.

The six variables indicated in Figure 85 are:

- T_7 = Input fluid temperature
- T_8 = Exit fluid temperature
- T_θ = Thermal mass (structure) temperature
- T_{10} = External source temperature
- M_3 = Fluid mass flow
- Q = Heat flow from external source

To specify a particular thermal load, five parameters are required:

- K_3 = Fluid structure heat transfer coefficient ($h_1 A$)
- K_4 = Reciprocal of energy storage capacity ($1/M_s C_s$)
- K_5 = Fluid specific heat (C_p)
- K_6 = Structure external source heat transfer coefficient
- K_7 = Index indicating load type

Three load types are included in the model:

- Type 0 -- Constant Q . For this load type, Q will be specified, and the source temperature, T_{10} will then vary as a function of T_θ . An example would be a resistor, dissipating a fixed power, attached to the thermal load station.

- Type 1 -- Heat Leak. In this case, T_{10} will be specified and Q will vary as a function of T_9 . In both this case and the preceding Type 0 case, heat flow proportional to the difference between T_{10} and T_9 is assumed.
- Type 2 -- Radiation. In this case, T_{10} will be specified and Q will vary as a function of T_9 . However, heat flow proportional to the difference between the fourth powers of T_{10} and T_9 is assumed. A Newton-Raphson solution for the resulting nonlinear relationship is incorporated.

The model is arranged in such a way that all of the logical decisions and pertinent parameters are exercised at each time step. It is therefore possible to switch from one load type to another or to modify any input parameter in any way desired at any time step.

In all cases, the value for fluid specific heat initially specified (K_5) is automatically adjusted by setting it equal to an average value at each time step:

$$K_5 = Cp = \frac{E_8 - E_7}{T_8 - T_7} \quad (27)$$

where E_8 and E_7 are the values for enthalpy corresponding to temperatures T_8 and T_7 for the appropriate fluid pressure. If these differences are too small for accuracy, the calculation is temporarily bypassed, and the preceding value is used.

The general computation procedure will be first to determine the predicted final value, F_9 , for the temperature of the thermal mass on the basis of incoming external energy rate Q or source temperature T_{10} , plus the cooling effect of the incoming fluid at temperature T_7 and mass flow M_3 :

$$F_9 = f(Q \text{ or } T_{10}, T_7, M_3, K_3, K_5, K_6) \quad (28)$$

The decrement for T_9 is then computed as a function of fluid mass flow M_3 and is corrected for core material temperature T_9 by its ratio to ambient temperature T_0 :

$$H_9 = \frac{T_0}{T_9} \times f(K_3, K_4, K_5, K_6, M_3) \quad (29)$$

The temperature, T_9 , is then incremented to a new value, T_9' , over the time step, $U1$, as:

$$T_9' = T_9 + U1 \times H_9 (F_9 - T_9) \quad (30)$$

Using the updated core temperature, T_9' , and the incoming fluid temperature, T_7 , the exit fluid temperature, T_8' , is determined:

$$T_8' = f(T_7, T_9', K_3, K_5, M_3) \quad (31)$$

Finally, either the rate of heat transfer, Q' , or the external source temperature, T'_{10} , is determined:

$$Q' = f(T_{10}, T'_9, K_6)$$

or:

$$T'_{10} = f(Q, T'_9, K_6) \quad (32)$$

Equations for Type 0 -- Constant Q

For input variables T_7 , M_3 , and Q , the predicted final core temperature, F_9 , is:

$$F_9 = T_7 + \frac{Q}{M_3 K_5 \left(1 - e^{-\frac{K_3}{M_3 K_5}}\right)} \quad (33)$$

The decrement for this temperature function is:

$$H_9 = M_3 K_5 K_4 \left(1 - e^{-\frac{K_3}{M_3 K_5}}\right) \frac{T_0}{T_9} \quad (34)$$

The incremented value for T_9 is:

$$T'_9 = T_9 + U_1 H_9 (F_9 - T_9) \quad (35)$$

The corresponding fluid exit temperature is:

$$T'_8 = T_7 e^{-\frac{K_3}{M_3 K_5}} + T'_9 \left(1 - e^{-\frac{K_3}{M_3 K_5}}\right) \quad (36)$$

The corresponding external source temperature is:

$$T'_{10} = T'_9 + \frac{Q}{K_6} \quad (37)$$

Equations for Type 1 -- Heat Leak

For input variables T_7 , M_3 , and T_{10} , the predicted final core temperature, F_9 , is:

$$F_9 = \frac{K_6 T_{10} + M_3 K_5 \left(1 - e^{-\frac{K_3}{M_3 K_5}}\right) T_7}{K_6 + M_3 K_5 \left(1 - e^{-\frac{K_3}{M_3 K_5}}\right)} \quad (38)$$

The decrement for this temperature function is:

$$H_g = K_6 + M_3 K_5 \left(1 - e^{-\frac{K_3}{M_3 K_5}} \right) K_4 \frac{T_0}{T_g} \quad (39)$$

The incremented value for T_g is:

$$T'_g = T_g + U_1 \times H_g (F_g - T_g) \quad (40)$$

The corresponding fluid exit temperature is:

$$T'_g = T_g e^{-\frac{K_3}{M_3 K_5}} + T'_g \left(1 - e^{-\frac{K_3}{M_3 K_5}} \right) \quad (41)$$

The corresponding external heat flow is:

$$Q' = K_6 (T_{10} - T'_g) \quad (42)$$

Equations for Type 2 -- Radiation

To determine the predicted final value for core temperature F_g in the radiation case, it is necessary to solve the fourth-order equation:

$$\frac{K_6}{M_3 K_5 \left(1 - e^{-\frac{K_3}{M_3 K_5}} \right)} (T_{10}^4 - F_g^4) + T_g - F_g = 0 \quad (43)$$

If the dummy variable, x , is substituted for F_g , then:

$$f(x) = \frac{K_6}{M_3 K_5 \left(1 - e^{-\frac{K_3}{M_3 K_5}} \right)} (T_{10}^4 - x^4) + T_g - x \quad (44)$$

and differentiating:

$$f'(x) = - \frac{4K_6}{M_3 K_5 \left(1 - e^{-\frac{K_3}{M_3 K_5}} \right)} x^3 - 1 \quad (45)$$

Then the Newton-Raphson relation is:

$$x_{n+1} = x_n - \frac{f(x_n)}{f'(x_n)} \quad (46)$$

to be used recurrently until a solution of sufficient accuracy is obtained. This is done in the model to a level of 10^{-5} , at which point the result is taken to be F_g .

The corresponding decrement, H_g , is:

$$H_g = K_4 M_3 K_5 \left(1 - e^{-\frac{K_3}{M_3 K_5}} \right) \frac{T_0}{T_g} \quad (47)$$

The incremented value for T_9 is:

$$T'_9 = T_9 + U1 \times H_9 (F_9 - T_9) \quad (48)$$

The corresponding value for T_8 is:

$$T'_8 = T_7 e^{-\frac{K_3}{M_3 K_6}} + T'_9 \left(1 - e^{-\frac{K_3}{M_3 K_6}} \right) \quad (49)$$

The corresponding value for Q is:

$$Q' = K_6 (T_{10}^4 - T_9'^4) \quad (50)$$

Liquid/Vapor Effects

For those cases in which a thermal load is located at the cold output of a liquefaction device, provision must be made for flow of a liquid/vapor mixture through the load. Under transient conditions, this mixture can vary from all vapor, to mixture in/vapor out, to mixture in/mixture out. In its present form, the model handles only a Type 1 (heat leak) load under these conditions.

For this portion of the model, the following additional variables and parameters are used:

Y_7 = Liquid fraction entering

Y_8 = Liquid fraction leaving

E_7 = Enthalpy of vapor entering

E_8 = Enthalpy of vapor leaving

K_{17} = Enthalpy of liquid

K_{15} = Temperature of liquid

The first step in this procedure is to determine whether liquefaction is a consideration. To accomplish this, the entering temperature (T_7), is compared with the liquid temperature, K_{15} . If T_7 is above the liquid temperature, liquefaction is not present, and the computation proceeds as described in the preceding paragraphs.

If the entering temperature, T_7 , is equal to the liquid temperature, K_{15} , a trial calculation of the liquid fraction is made. Assuming that the liquid both enters and leaves the load structure, the liquid fraction leaving is calculated as:

$$Y_8 = Y_7 - \frac{K_3 (T_9 - K_{15})}{M_3 (E_7 - K_{17})} \quad (51)$$

If this leaving fraction, Y_8 , is positive, the assumption is valid, and the derivative for the core temperature is calculated as:

$$\frac{d}{dt}(T_9) = K_4 \left[K_8 (T_{10} - T_9) - K_3 (T_9 - K_{15}) \right] \frac{T_0}{T_9} \quad (52)$$

Then the updated core temperature, T_9 , is:

$$T_9' = T_9 + \left[\frac{d}{dt}(T_9) \right] U_1 \quad (53)$$

The fluid exit temperature is the liquid temperature:

$$T_8 = K_{15} \quad (54)$$

The external heat flow to the load is:

$$Q = K_6 (T_{10} - T_9) \quad (55)$$

If the leaving liquid fraction calculated in Equation 51 is negative, it indicates that the entering liquid is evaporated within the device, and the assumption of the leaving liquid (with its associated constant temperature implication) is not valid. It is then necessary to calculate the fractional distance over the core, $Z1$, in which liquid is present as:

$$Z1 = \frac{M_3 (E_7 - K_{17}) Y_7}{K_3 (T_9 - K_{15})} \quad (56)$$

The core temperature derivative is then:

$$\begin{aligned} \frac{d}{dt}(T_9) = K_4 \left\{ K_8 (T_{10} - T_9) - K_3 Z1 (T_9 - K_{15}) \right. \\ \left. - M_3 K_6 (T_9 - K_{15}) \left[1 - e^{-\frac{K_3}{M_3 K_6} (1 - Z1)} \right] \right\} \frac{T_0}{T_9} \end{aligned} \quad (57)$$

The updated core temperature is:

$$T_9' = T_9 + \left[\frac{d}{dt}(T_9) \right] U_1 \quad (58)$$

The leaving fluid temperature is:

$$T_8 = T_9 - (T_9 - K_{15}) e^{-\frac{K_3}{M_3 K_6} (1 - Z1)} \quad (59)$$

The external heat flow is:

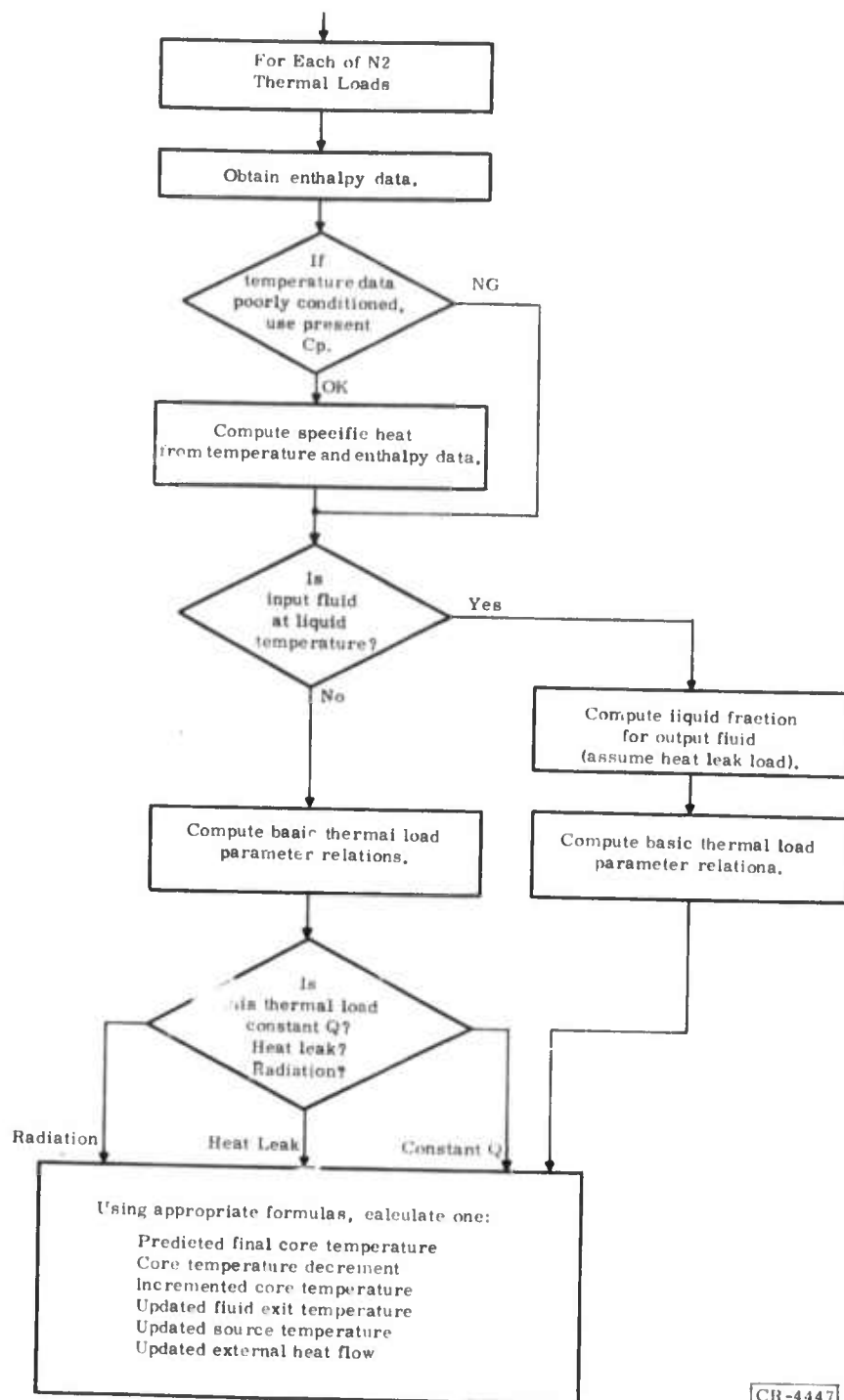
$$Q = K_6 (T_{10} - T_9) \quad (60)$$

The leaving liquid fraction is zero:

$$Y_8 = 0 \quad (61)$$

Outline of Model Logic

The basic flowchart arrangement for the thermal load model is shown in Figure 86.



CR-4447

Figure 86. Flowchart of Thermal Load Model (Logic and Calculation Sequence)

TURBOALTERNATOR MODEL

Each turboalternator in the system is treated as a three-terminal device with mechanical energy storage. The conceptual arrangement is shown schematically in Figure 87.

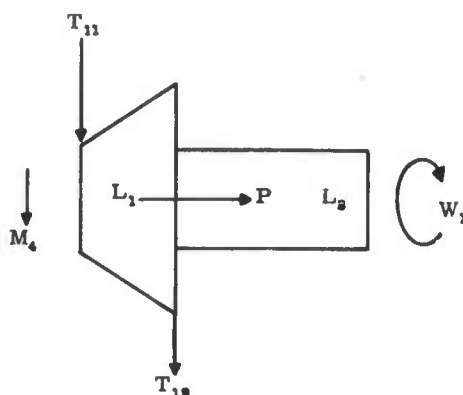


Figure 87. Schematic Diagram of Turboalternator Model

The system pressure and the pressure ratio are assumed constant. Under these conditions fluid is applied to the turbine at temperature T_{11} , mass flow M_4 results, and the fluid exits at temperature T_{12} . Mechanically, the assembly rotates at speed W_1 , at which the turbine develops driving torque L and delivers mechanical power P to the shaft assembly. The alternator in turn develops loading torque L_2 , and any difference between L_1 and L_2 will result in acceleration or deceleration of the assembly, with a consequent change in its stored energy.

In the present simplified form of the model, the torque-speed functions for both the turbine and the alternator are assumed to be linear. The alternator function is assumed to be constant, while the slope of the turbine function will depend upon the inlet temperature. The torque-speed relations are shown in Figure 88.

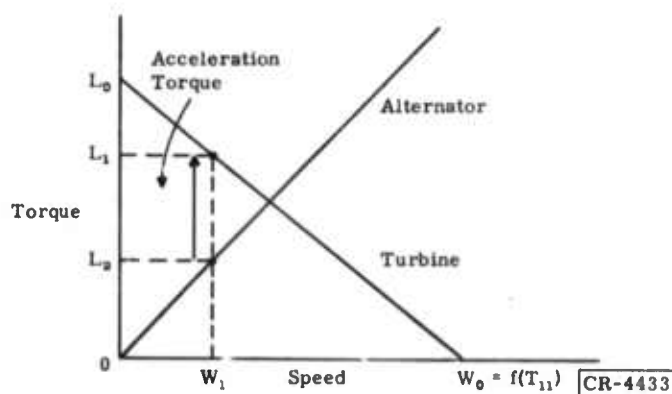


Figure 88. Torque-Speed Relations for Turboalternator Model

In particular, in the model, L_0 is assumed to be constant, W_0 is a function of input temperature T_{11} , and L_2 is proportional to W_1 .

The fluid exit temperature, T_{12} , is determined by making the product of mass flow M_4 and temperature difference $T_{11} - T_{12}$ proportional to the turbine shaft power, P . In the ideal case, in consistent units, this constant of proportionality will be the reciprocal of the fluid specific heat.

The model variables are:

T_{11} = Input fluid temperature

T_{12} = Exit fluid temperature

M_4 = Mass flow through turbine

W_1 = Assembly shaft speed

L_1 = Turbine torque

L_2 = Alternator torque

P = Turbine shaft power

W_0 = Turbine maximum speed

The specified model parameters are:

K_8 = Product of turbine mass flow and square root of inlet temperature

K_9 = Ratio of turbine maximum speed to square root of inlet temperature

K_{10} = Slope of alternator torque-speed function

K_{11} = Mechanical-thermal power conversion factor

K_{12} = Assembly shaft moment of inertia

L_0 = Turbine stalled torque

It is noted that the effective mechanical time constant for the assembly is:

$$\tau_M = \frac{1}{K_{12} \left(\frac{L_0}{W_0} + K_{10} \right)} \quad (62)$$

This constant will vary with the temperature as W_0 changes.

Model Equations

The mass flow, M_4 , is a function of the inlet temperature:

$$M_4 = \frac{K_8}{\sqrt{T_{11}}} \quad (63)$$

The turbine maximum speed is a function of the inlet temperature:

$$W_0 = K_9 \sqrt{T_{11}} \quad (64)$$

The turbine torque is a function of the ratio of the present speed to the maximum speed:

$$L_1 = L_0 \left(1 - \frac{W_1}{W_0} \right) \quad (65)$$

The alternator torque is proportional to the speed:

$$L_2 = K_{10} W_1 \quad (66)$$

Acceleration is proportional to the torque difference:

$$L_3 = K_{12} (L_1 - L_2) \quad (67)$$

Speed is incremented for a given acceleration and time step, $U1$:

$$W_1' = W_1 + U1 \times L_3 \quad (68)$$

A new value for the shaft power is determined as the product of the turbine torque and speed:

$$P' = L_1 \times W_1' \quad (69)$$

A new exit fluid temperature is determined:

$$T_{12}' = T_{11} - \frac{K_{11}}{M_4} P' \quad (70)$$

Optional Algebraic Solution

To avoid the effects of the normally short turboalternator time constant, a direct algebraic solution for the shaft speed can be used as:

$$W_1 = \frac{W_0 L_0}{K_{10} W_0 + L_0} \quad (71)$$

Typically, the speed can be computed transiently for a sufficient time to permit acceleration to normal operating speed and then it can be updated algebraically for subsequent time steps.

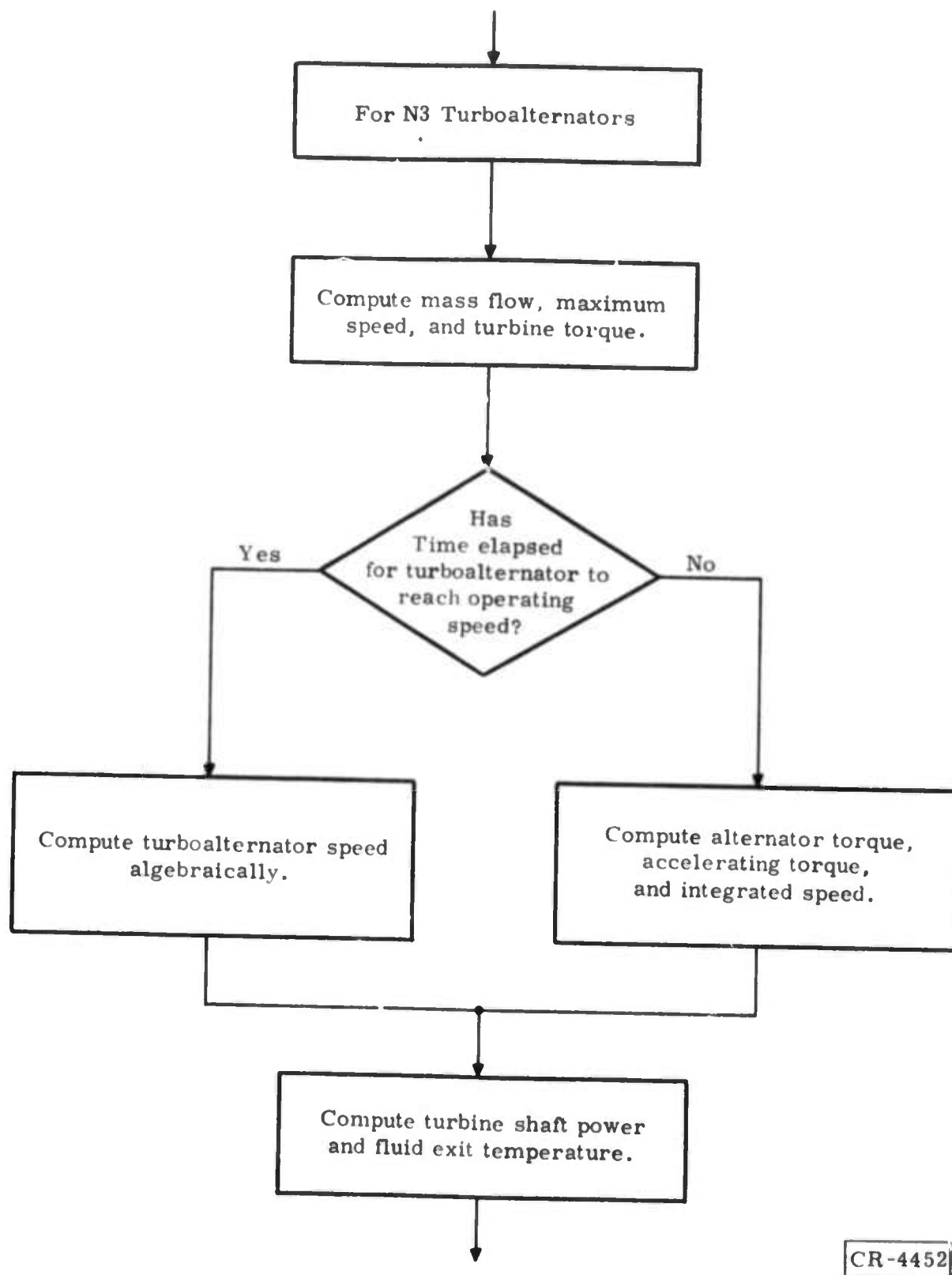
Outline of Model Logic

The basic flowchart arrangement for the turboalternator model is shown in Figure 89.

JOULE-THOMSON LIQUEFIER MODEL

The Joule-Thomson valve and liquefier reservoir combination is treated as a three-terminal device with provision for valve adjustment to increase high-temperature flow and with provision for liquid drainage. The conceptual arrangement is shown in Figure 90.

The device is assumed to be operating across the difference between two constant pressures, utilizing the nonlinear temperature-enthalpy relations at near-liquid temperatures in an idealized fashion, to achieve the desired functions.



CR-4452

Figure 89. Flowchart of Turboalternator Model (Logic and Calculation Sequence)

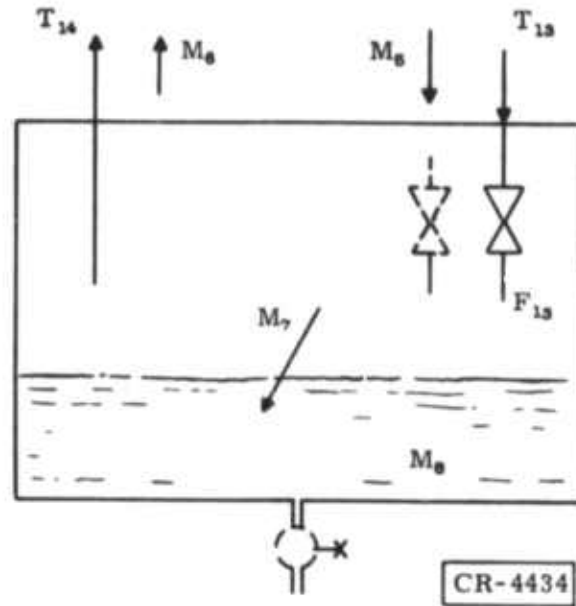


Figure 90. Conceptual Arrangement of Joule-Thomson Liquefier Model

The flow through the Joule-Thomson valve is assumed to be a function of the inlet temperature, T_{13} , as:

$$M_6 = \frac{K_{13}}{T_{13}} \quad (72)$$

Because the normal design operating point for the valve is at near liquid temperature, the flow will be extremely small for most of a cooldown transient, effectively blocking any cooling operation of the lowest flow loop of the system.

Assuming that some compensation for this effect will be made in a practical system, a flow bypass function is included in the model. The flow bypass function provides preselected flow, K_{14} , to exist above a preselected temperature, K_{13} , below which the design characteristics of the valve take over. This procedure is illustrated in Figure 91.

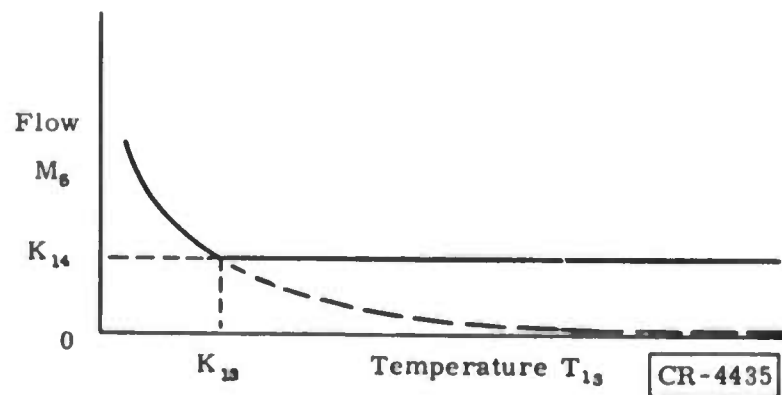


Figure 91. Flow Bypass Function Procedure

With the flow into the device established, the remainder of the problem involves determination of the thermal state existing and applying mass and energy flow balance relations.

The input temperature, T_{13} , is known, and the enthalpy, E_{13} , for that temperature at the input high pressure is also known. The valve output temperature, F_{13} , is then determined for the same enthalpy and for the lower exit pressure. Several possibilities are then considered.

If there is no liquid (M_8) present and the valve exit temperature, F_{13} , is above the liquid temperature, K_{15} , then the fluid is assumed to simply flow through the device and:

$$\left. \begin{array}{l} M_8 = M_5 \\ T_{14} = F_{13} \end{array} \right| \begin{array}{l} M_8 = 0 \\ F_{13} > K_{15} \end{array} \quad (73)$$

If the valve exit temperature calculation results in a value for F_{13} below the liquid temperature, K_{15} , it is assumed that liquefaction is taking place. Under this condition, the output temperature, T_{14} , is taken to be the liquid temperature, K_{15} , and a corresponding enthalpy, E_{14} , is determined.

If an accumulation of liquid exists, it is assumed that the output temperature, T_{14} , is equal to the liquid temperature, K_{15} , with corresponding enthalpy E_{14} , regardless of the value of the valve exit temperature, F_{13} :

$$\left. \begin{array}{l} T_{14} = K_{15} \\ E_{14} = f(T_{14}) = f(K_{15}) \end{array} \right| \begin{array}{l} F_{13} < K_{15} \\ \text{or} \\ M_8 > 0 \end{array} \quad (74)$$

The rate at which liquefaction of the incoming fluid takes place (M_7) is determined by the energy balance relationship:

$$\begin{aligned} M_5 \times E_{13} &= M_7 \times K_{17} + (M_5 - M_7) \times E_{14} \\ M_7 &= \frac{E_{14} - E_{13}}{E_{14} - K_{17}} M_5 \end{aligned} \quad (75)$$

where K_{17} is the enthalpy of the liquid.

The above relationships permit positive liquefaction rate M_7 when the valve exit temperature (and consequently E_{13}) is sufficiently low; the relation-

ships also permit a negative liquefaction rate (boiling off) when the valve exit temperature rises while accumulated liquid remains to hold output enthalpy E_{14} constant. When all of the liquid is gone and T_{13} is above the liquefaction temperature, $E_{14} = E_{13}$ and rate M_7 is zero.

The output flow for device M_6 will be the difference between input flow M_5 and liquefaction rate M_7 :

$$M_6 = M_5 - M_7 \quad (76)$$

The quantity of the existing liquid, M_8 , is determined by integrating the liquefaction rate, M_7 , less any selected drain rate, K_{16} for time step U1:

$$M_8' = M_8 + U1 \times (M_7 - K_{16}) \quad (77)$$

Because it is possible for this integration to proceed through zero with a negative rate, logic is provided to arbitrarily limit such a result at $M_8 = 0$. The model variables are:

- T_{13} = Input temperature -- high-pressure side of Joule-Thomson valve
- E_{13} = Enthalpy for T_{13}
- F_{13} = Ideal temperature -- low-pressure side of Joule-Thomson valve
- T_{14} = Output temperature -- accumulator output at low pressure
- E_{14} = Enthalpy for T_{14}
- M_5 = Input mass flow -- Joule-Thomson valve plus bypass
- M_6 = Output mass flow -- accumulator output at low pressure
- M_7 = Mass flow to liquid
- M_8 = Accumulated liquid mass

The model specified parameters are:

- K_{13} = Temperature at which bypass is closed
- K_{14} = Total mass flow while bypass is open
- K_{15} = Liquid temperature
- K_{16} = Liquid drain flow rate
- K_{17} = Enthalpy of liquid
- K_{18} = Product of flow rate and square root of input temperature for Joule-Thomson valve

Outline of Model Logic

The basic flowchart arrangement for the Joule-Thomson/liqefier model is shown in Figure 92.

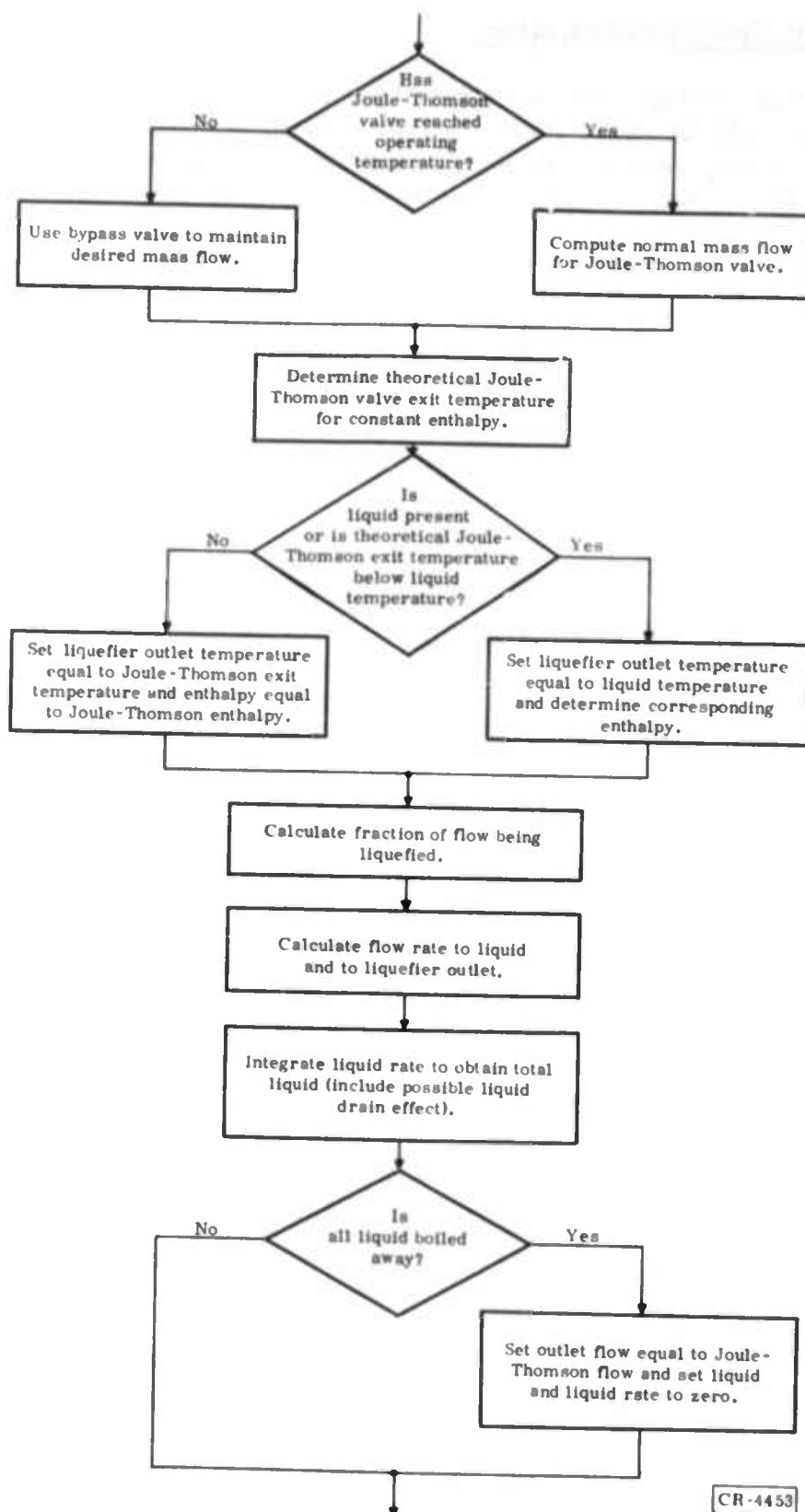


Figure 92. Flowchart of Joule-Thomson/Liquefier Model (Logic and Calculation Sequence)

Alternative (Split) Configuration

In certain refrigerator configurations the Joule-Thomson valve and liquid accumulator will be separated by an intervening thermal load, or other device. For these cases, separate models of the valve and accumulator devices are provided, based upon the preceding development.

The following additional variables are introduced:

T_{15} = Valve exit temperature

E_{15} = Valve exit enthalpy

Y_0 = Valve exit liquid fraction

M_9 = Accumulator entering flow

T_{18} = Accumulator entering temperature

E_{18} = Accumulator entering enthalpy

Y_1 = Accumulator entering liquid fraction

The basic flowchart arrangements for the separate Joule-Thomson valve and liquid accumulator models are shown in Figures 93 and 94.

AUXILIARY FUNCTIONS

Temperature-Enthalpy Relations

To model the system behavior properly at very low temperatures, it is necessary to account for the variation in the fluid specific heat. To accomplish this, temperature-enthalpy functions for the two pressures involved are included. The general form of the true function is shown in Figure 95.

Noting that the true function approaches the ideal linear perfect gas relationship asymptotically, a hyperbolic approximation was arbitrarily chosen for calculation purposes. The general relation used is:

$$\left(\frac{T - C_1}{C_3} \right)^2 - \left(\frac{E - C_2}{C_4} \right)^2 = 1 \quad (78)$$

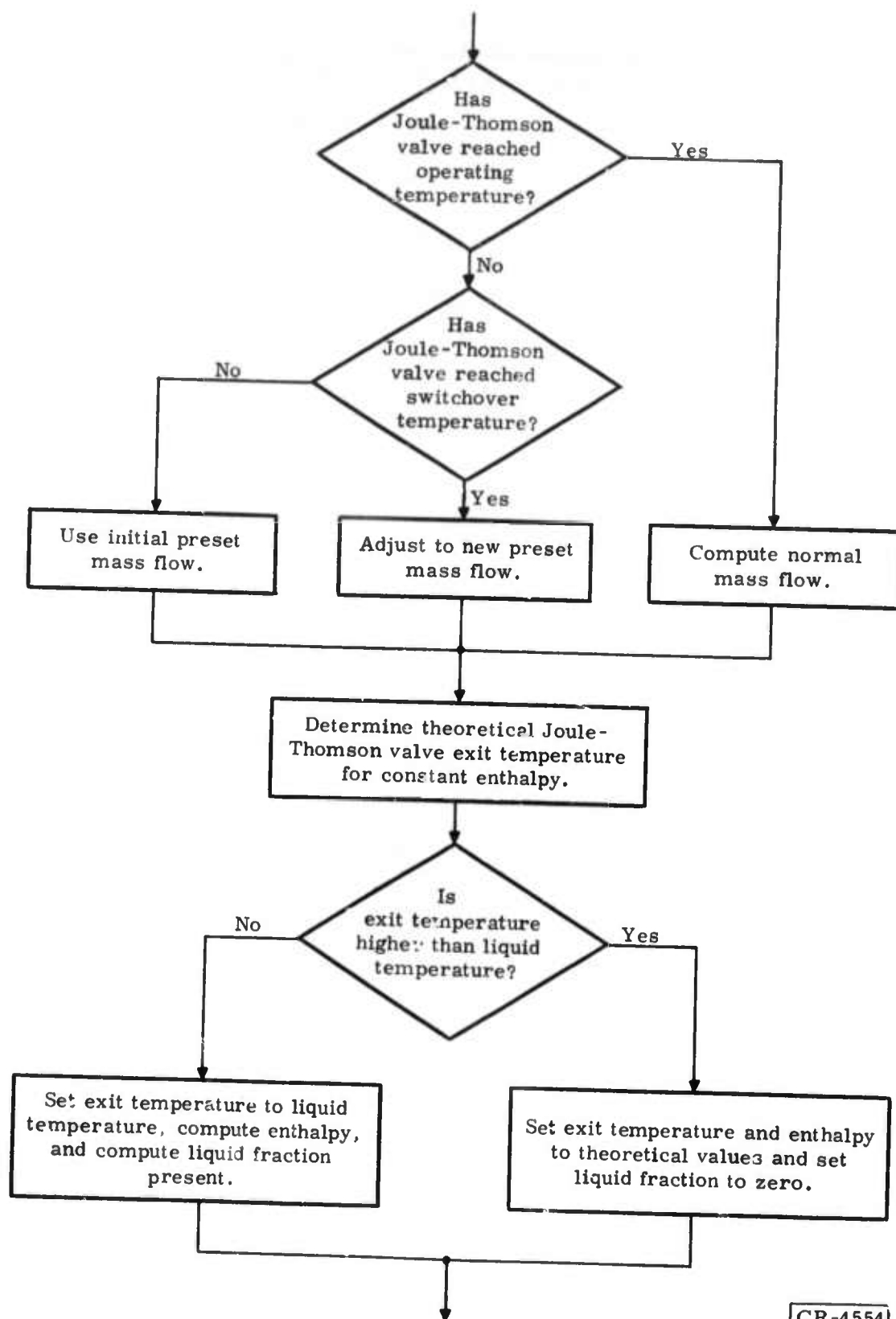
where:

T = Fluid temperature

E = Fluid enthalpy

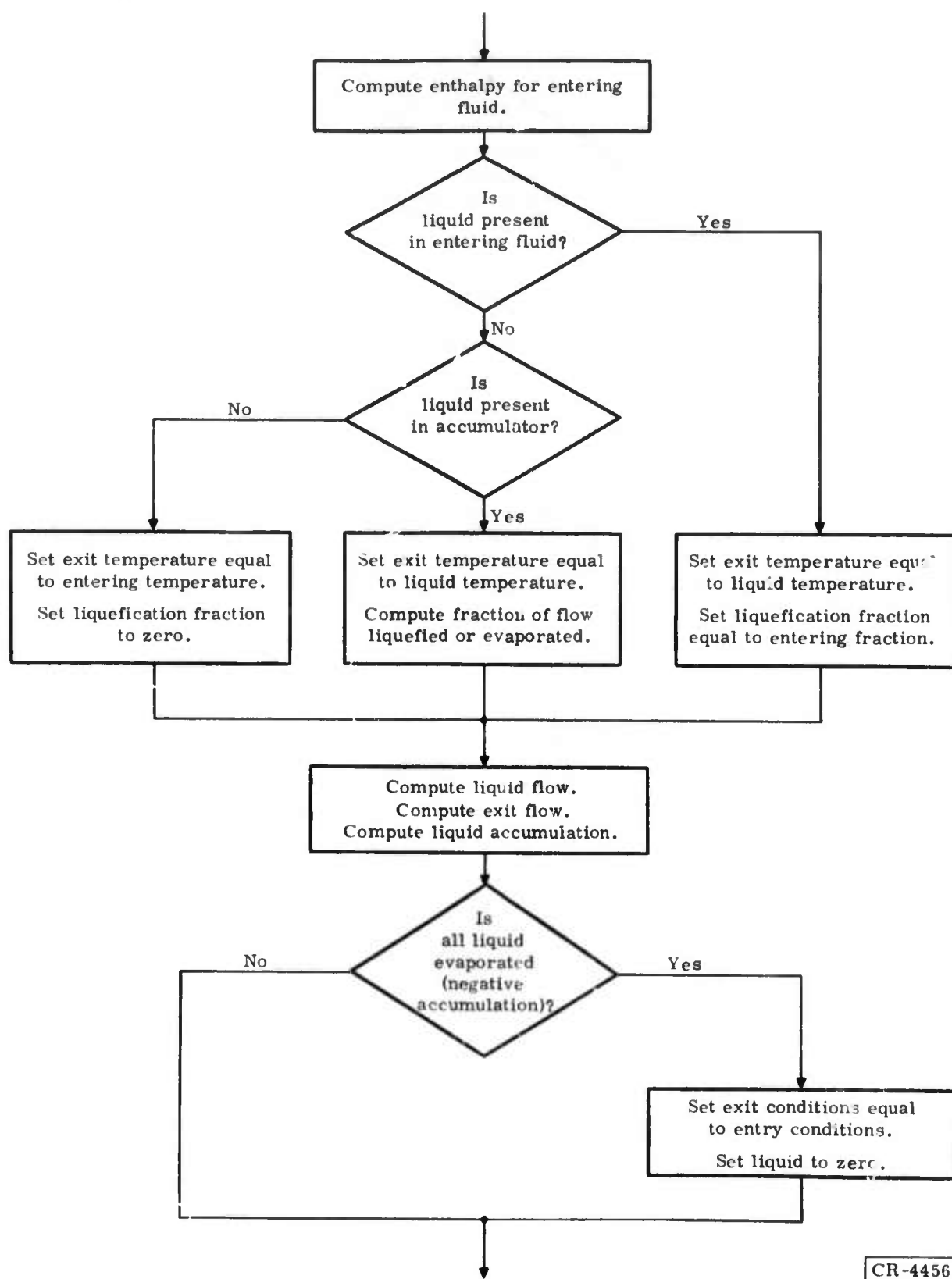
C_n = Constant parameter

This relation is equally useful for obtaining enthalpy for a given temperature and for obtaining temperature corresponding to a given value for en-



CR-4554

Figure 93. Flowchart of Joule-Thomson Valve Model (Logic and Calculation Sequence)



CR-4456

Figure 94. Flowchart of Liquid Accumulator Model (Logic and Calculation Sequence)

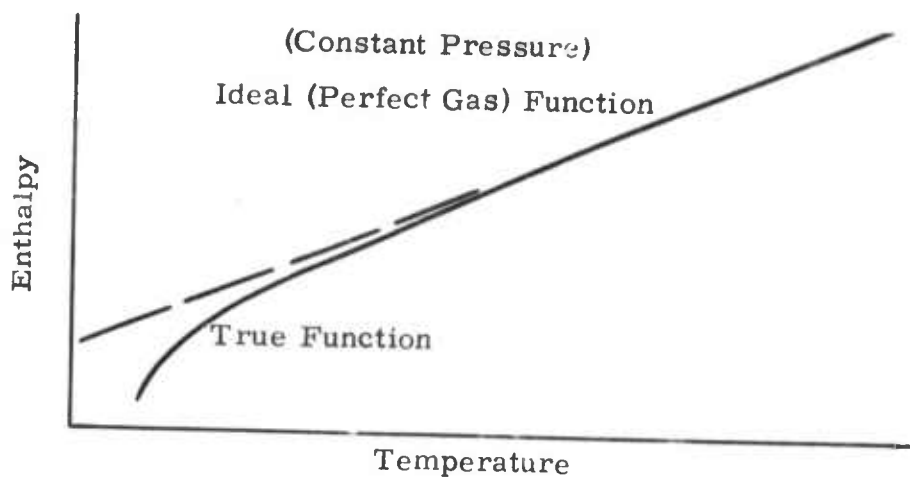


Figure 95. General Form of True Function

thality. In the latter case, the symbol F is used in place of T , because it is sometimes a trial value of temperature rather than the ultimate temperature used. The two relations are:

$$E = C_2 + \sqrt{\left(\frac{C_4}{C_3}\right)^2 (T - C_1)^2 - C_4^2} \quad (79)$$

$$F = C_1 + \sqrt{C_3^2 + \frac{(E - C_2)^2}{\left(\frac{C_4}{C_3}\right)^2}} \quad (80)$$

where F is the trial value for temperature T .

To prevent possible erroneous results from the dual-valued hyperbolic approximation near its point of reversal, the approximation is terminated by a linear segment at the low-temperature end, as illustrated in Figure 96.

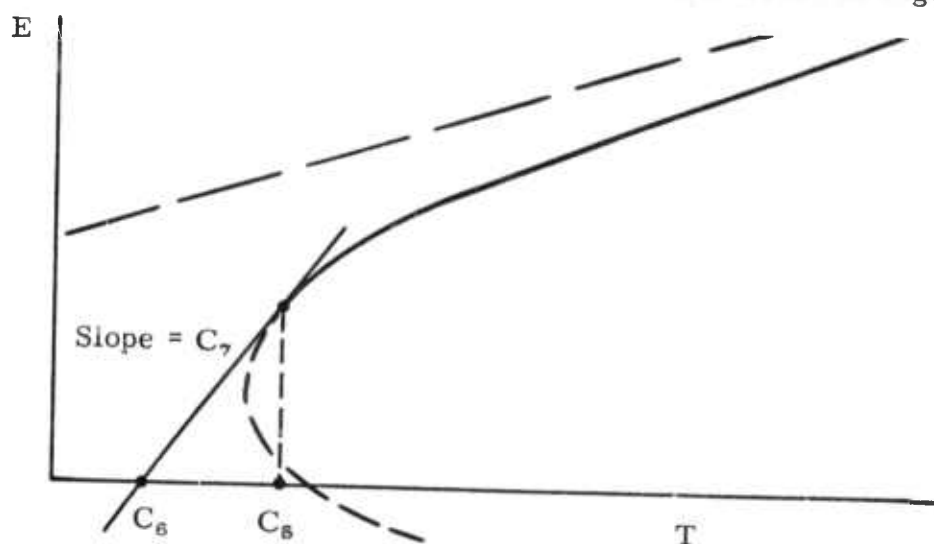


Figure 96. Approximation Terminated by Linear Segment at Low-Temperature End

The relations for this terminating segment are:

$$E = C_7 (T - C_8) \quad | \quad T < C_8 \quad (81)$$

$$F = C_8 + \frac{E}{C_7} \quad | \quad E < C_7 (C_8 - C_8) \quad (82)$$

There are two such temperature-enthalpy curves stored in the model, one for the high-pressure side and one for the low-pressure return. These curves are designated by a second subscript, Z, where:

Z = 1 for high-pressure curve

Z = 2 for low-pressure curve

The constant parameters will then be of the form:

$$C(n, Z) \quad | \quad \begin{array}{l} n = 1 \text{ to } 7 \\ Z = 1 \text{ to } 2 \end{array}$$

The calculation will be entered with a value for either T(J,1) or E(J,1) and a value for Z indicating high or low pressure. The output will then be the corresponding E(J,1) or F(J,1).

In some cases, a better empirical fit can be obtained by a displacement of the enthalpy reference axis (biasing E by a constant value). For this purpose, an additional bias parameter, C₈, is included so:

$$E' = E + C_8 \quad (83)$$

$$F' = f(E) = f(E' - C_8) \quad (84)$$

Miscellaneous Time Functions

In a transient model there are a few routine bookkeeping functions to be performed. These functions include integration of incremental time steps, U1, to determine the total elapsed time, U:

$$U' = U + U1 \quad (85)$$

and a counter to determine the elapsed intervals between the desired printout points:

$$I1' = I1 + U1 \quad (86)$$

It may also be desirable to change some load or other system parameter at some selected point in time (or when any other system variable reaches some preselected value). For example:

$$\begin{array}{l} X = A \quad | \quad U < Y \\ X = B \quad | \quad U > Y, T > Z \\ X = C \quad | \quad U > Y, T < Z \\ \text{Etc.} \end{array}$$

Because all computations are repeated from a fresh set of input data at each time step, the application of such switching logic is limited only by the ingenuity of the user.

MODEL NOMENCLATURE

The sets of system parameters and system variables are designated in vector form using a descriptive letter with two subscripts. For example, $T(J, I)$ represents the temperature at the J th point in a component device model, for the I th such device in the system.

The letter designations for the principal parameters and variables are:

K = Constant parameter

T = Temperature

F = Final (steady-state) temperature

E = Enthalpy

H = Decrement for transient temperature

M = Rate of mass flow

L = Torque

W = Shaft rotational speed

Q = Rate of heat flow

P = Mechanical power

These designations are numbered sequentially (first subscript) as they appear in the following hierarchy of component device models (listed with their descriptive abbreviations) (Table 12).

Table 12

FIRST SUBSCRIPT (J) ALLOCATION SEQUENCE

Letter	H-E	T-L	T-A	J-T/LIQ
K	1-2	3-7	8-12	13-18
T	1-6	7-10	11-12	13-18
F	1-6	9	--	13
E	1-4	7-8	--	13-18
H	1-6	9	--	--
M	1-2	3	4	5-9
L	--	--	0-3	--
W	--	--	0-1	--
Q	--	No Subscript	--	--
P	--	--	No Subscript	--

CR-4436

This basic numbering structure is illustrated in Figure 97 for Temperature and Enthalpy functions.

The basic numbering structure for mass flow functions is similarly illustrated in Figure 98.

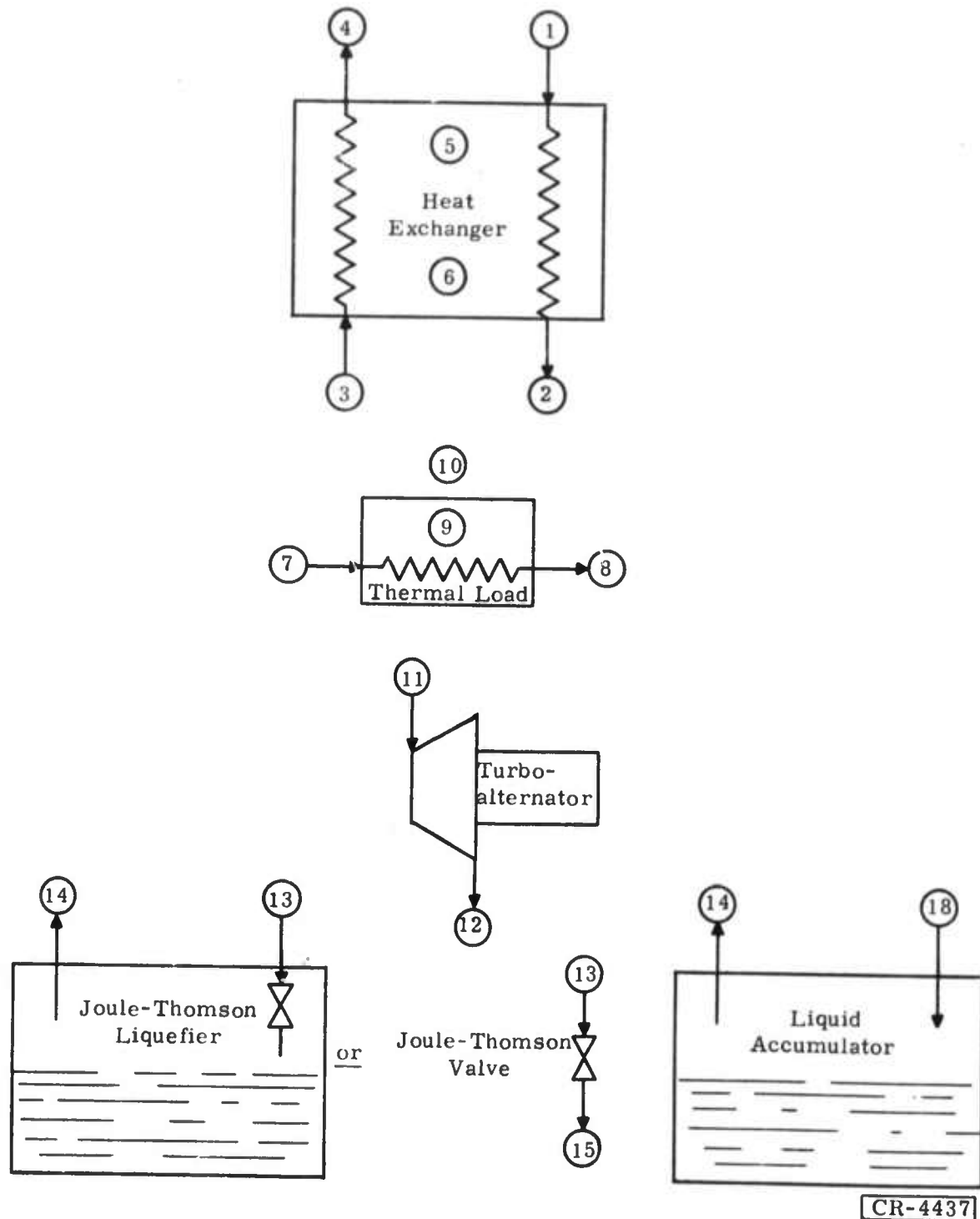


Figure 97. Basic Numbering Structure for Temperature and Enthalpy Functions

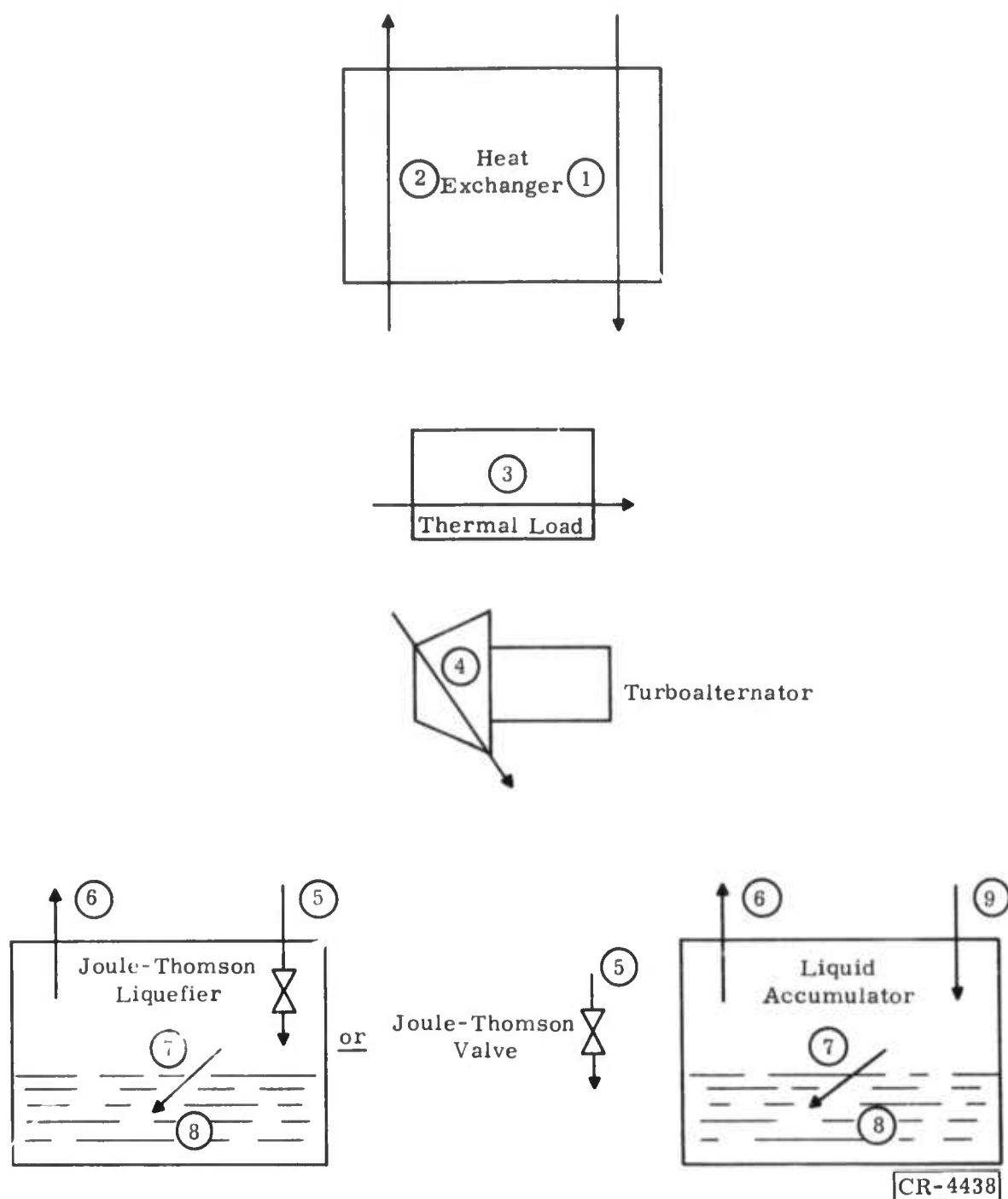


Figure 98. Basic Numbering Structure for Mass Flow Functions

For example, any temperature $T(9, I)$ will be the core temperature for some thermal load, and any mass flow rate $M(4, I)$ will be the flow rate for some turboalternator.

Three special cases are noted. Whereas M_{1-7} represents the mass flow rate, M_9 is the accumulated liquid mass rather than a rate. No first subscript

is used for heat flow rate Q or for mechanical power P , because these are associated exclusively with thermal loads and turboalternators, respectively.

The three directly related variables, present temperature T , final temperature F , and enthalpy E , will always be consistently numbered (when they have the same subscripts, they will refer to the same point in the system).

The second subscript, I , is used to number the devices of any given type sequentially, beginning with the device at the coldest point in the system. For example, $T(J, 1)$ will be a temperature for the bottom heat exchanger, coldest thermal load, lowest turboalternator, or the liquefier, depending upon the device type identification J . $T(J, 2)$ will refer to the next coldest device of that type, and so forth.

The use of this nomenclature is illustrated for a typical system assembly in Figures 99 through 101.

Detailed Model Nomenclature

Following is a list of the model nomenclature:

<u>Nomenclature</u>	<u>Description</u>
A	Dummy variable for intermediate computation
B	Dummy variable for intermediate computation
C	Dummy variable for intermediate computation
C (J, Z)	Constant parameter for temperature-enthalpy function, $J = 1$ to 7, $Z = 1$ for high pressure, $Z = 2$ for low pressure
D	Dummy variable for intermediate computation
E	Dummy variable for intermediate computation
E1	Dummy variable for intermediate computation
E2	Dummy variable for intermediate computation
E (J, I)	Enthalpy at point J for device I
F (J, I)	Final (steady-state) temperature at point J for device I
H (J, I)	Temperature decrement at point J for device I
I	Subscript for particular device of its type
I1	Counter to control printout
J	Subscript for point relative to device type
K (J, I)	Constant parameter for device I , $J = 1$ to 18
L (0, I)	Turbine stall torque for turboalternator I
L (1, I)	Turbine torque for turboalternator I

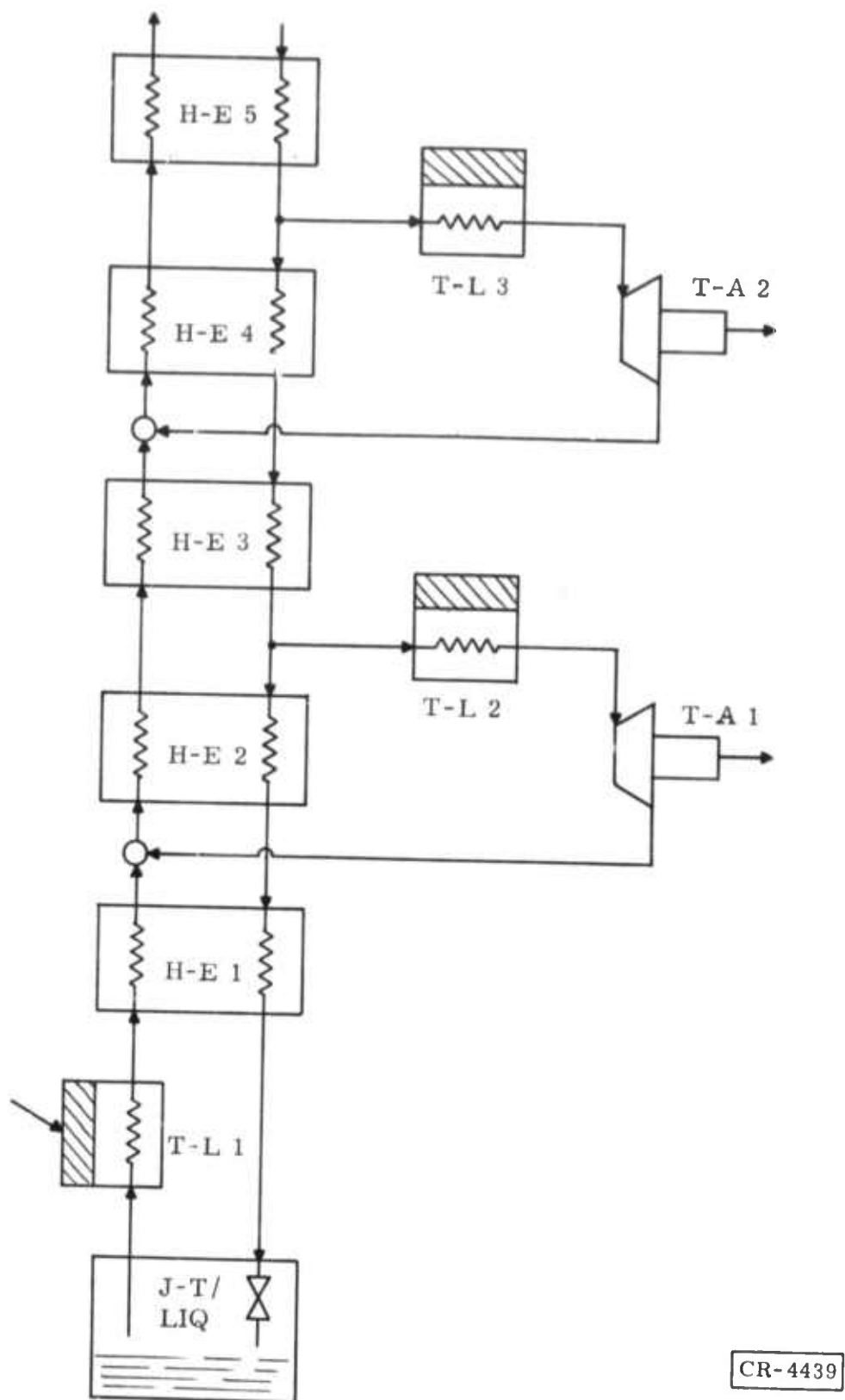
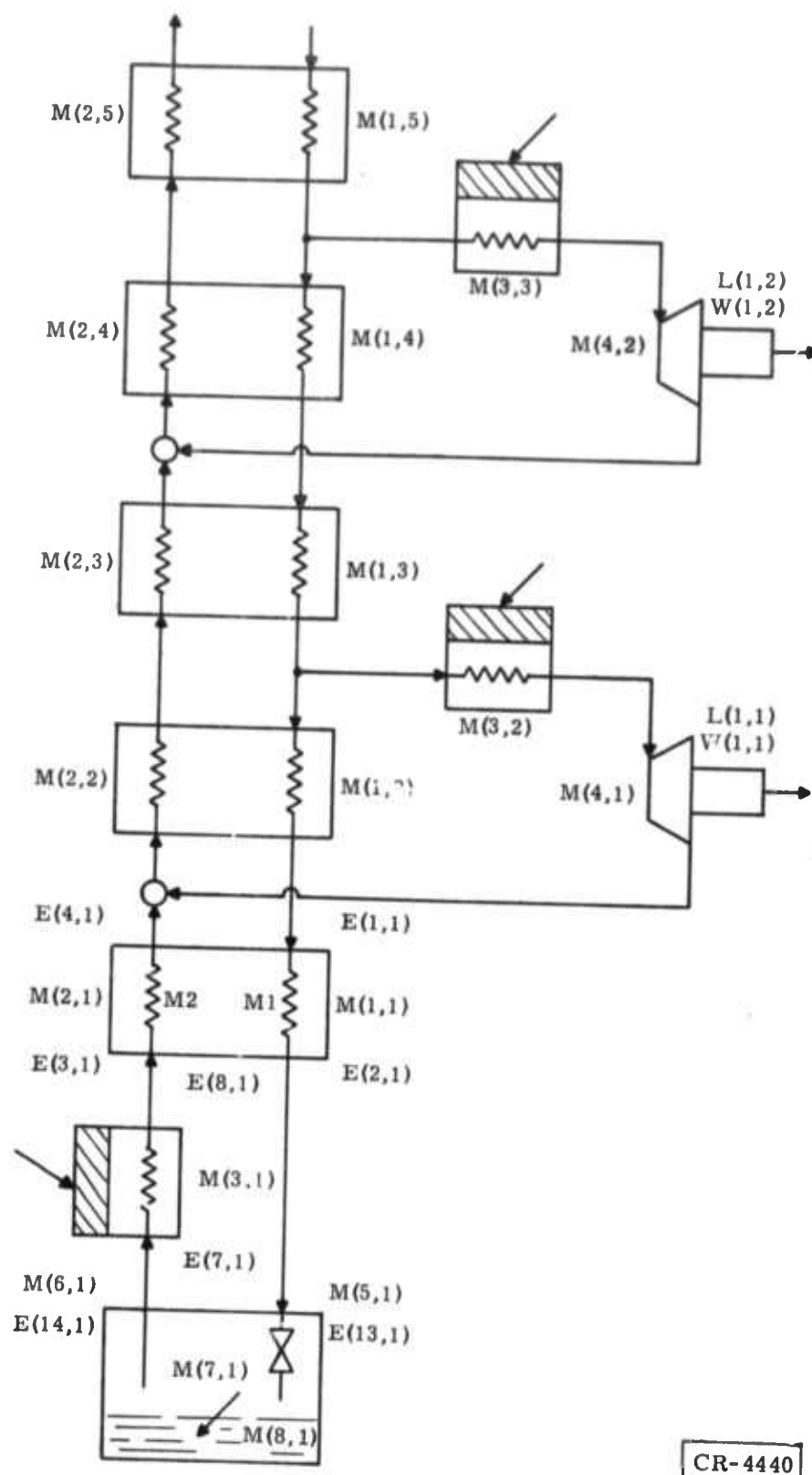


Figure 99. Example of Model Nomenclature for Devices



CR-4440

Figure 100. Example of Model Nomenclature for M (J,I) (Mass Flow), E (J,I) (Enthalpy), L (J,I) (Torque), and W (J,I) (Speed)

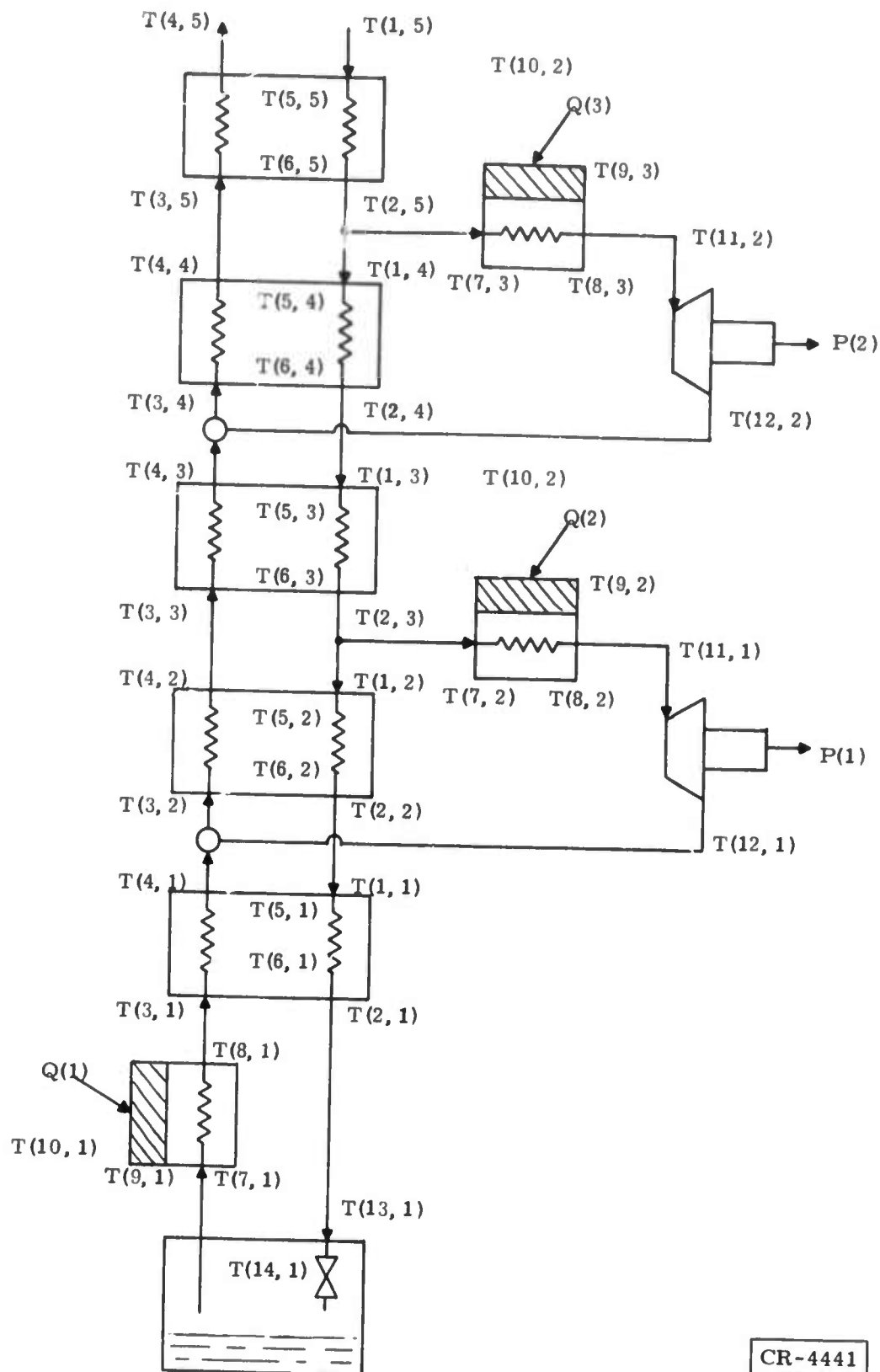


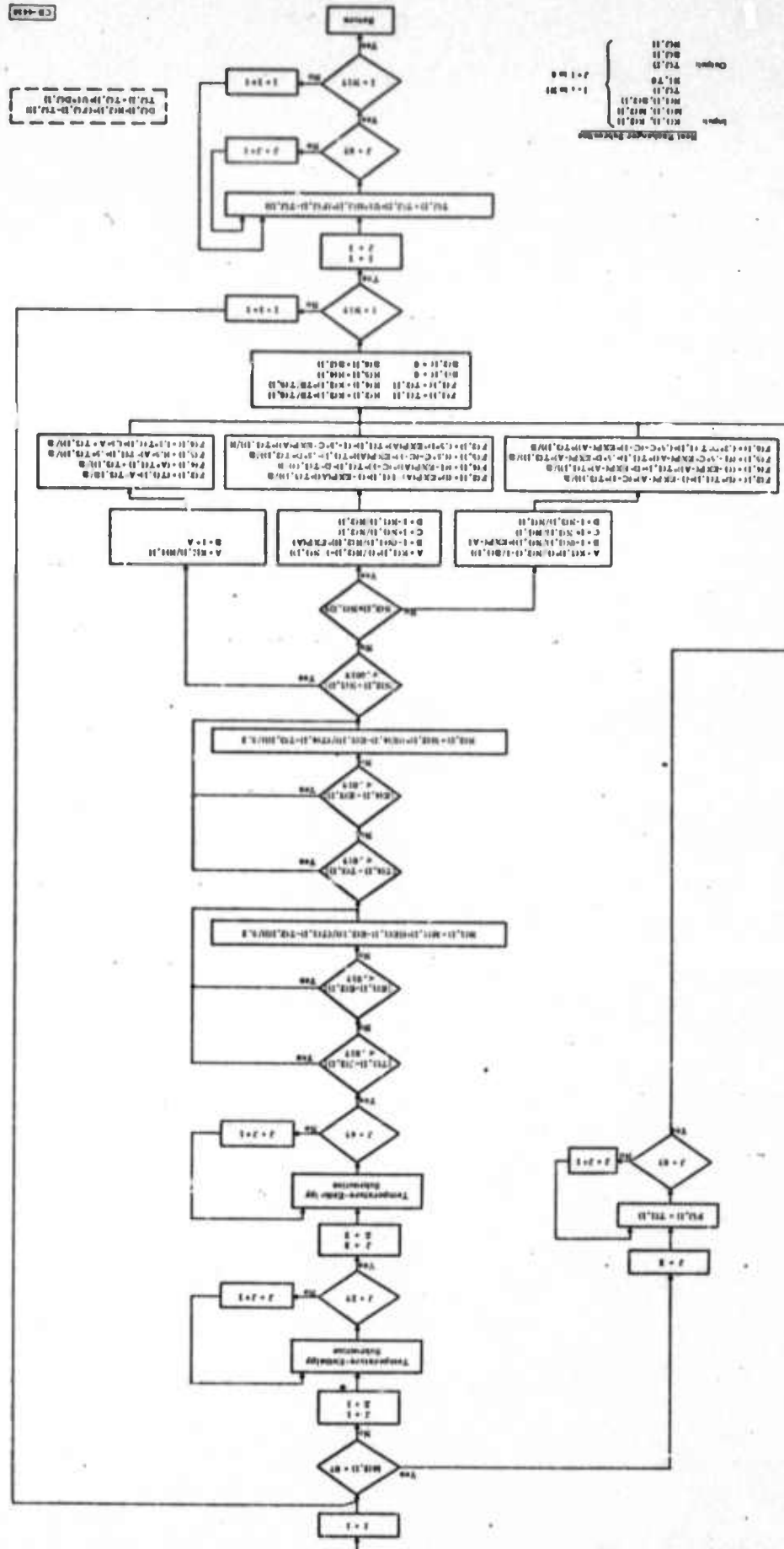
Figure 101. Example of Model Nomenclature for T (J,I) (Temperature), Q (I) (Heat Flow), and P (I) (Power)

<u>Nomenclature</u>	<u>Description</u>
L (2,I)	Alternator torque for turboalternator I
L (3,I)	Shaft acceleration for turboalternator I
M (J,I)	Mass flow rate at point J for device I, J = 1 to 7
M (8,1)	Accumulated liquid mass
N1	Number of heat exchangers (≥ 1)
N2	Number of thermal loads (≥ 1)
N3	Number of turboalternators (≥ 1)
N4	Joule-Thomson/Liquefier indicator (0 or 1)
N5	Print control (0 for data only, 1 for headings also)
N (J,I)	Synthetic mass flow, J = 1 or 2, heat exchanger I
P (I)	Shaft power for turboalternator I
Q (I)	Heat flow rate for thermal load I
T 0	Ambient temperature
T (J,I)	Temperature at point J for device I
U	Elapsed time
U1	Computation time step
V	Dummy variable for intermediate computation
W (0,I)	Maximum turbine speed for turboalternator I
W (1,I)	Shaft speed for turboalternator I
X	Dummy variable for intermediate computation
Y	Dummy variable for intermediate computation
Y0	Liquid fraction at Joule-Thomson valve output
Y1	Liquid fraction at accumulator input
Y7	Liquid fraction at thermal load input
Y8	Liquid fraction at thermal load output
Z	Dummy variable for intermediate calculation
Z1	Dummy variable for intermediate calculation

COMPONENT DEVICE SUBROUTINES

The complete subroutine mechanization of the principal component devices is shown in flowchart form in Figures 102 through 107.

Figure 102. Flowchart of Heat Exchanger Subroutine



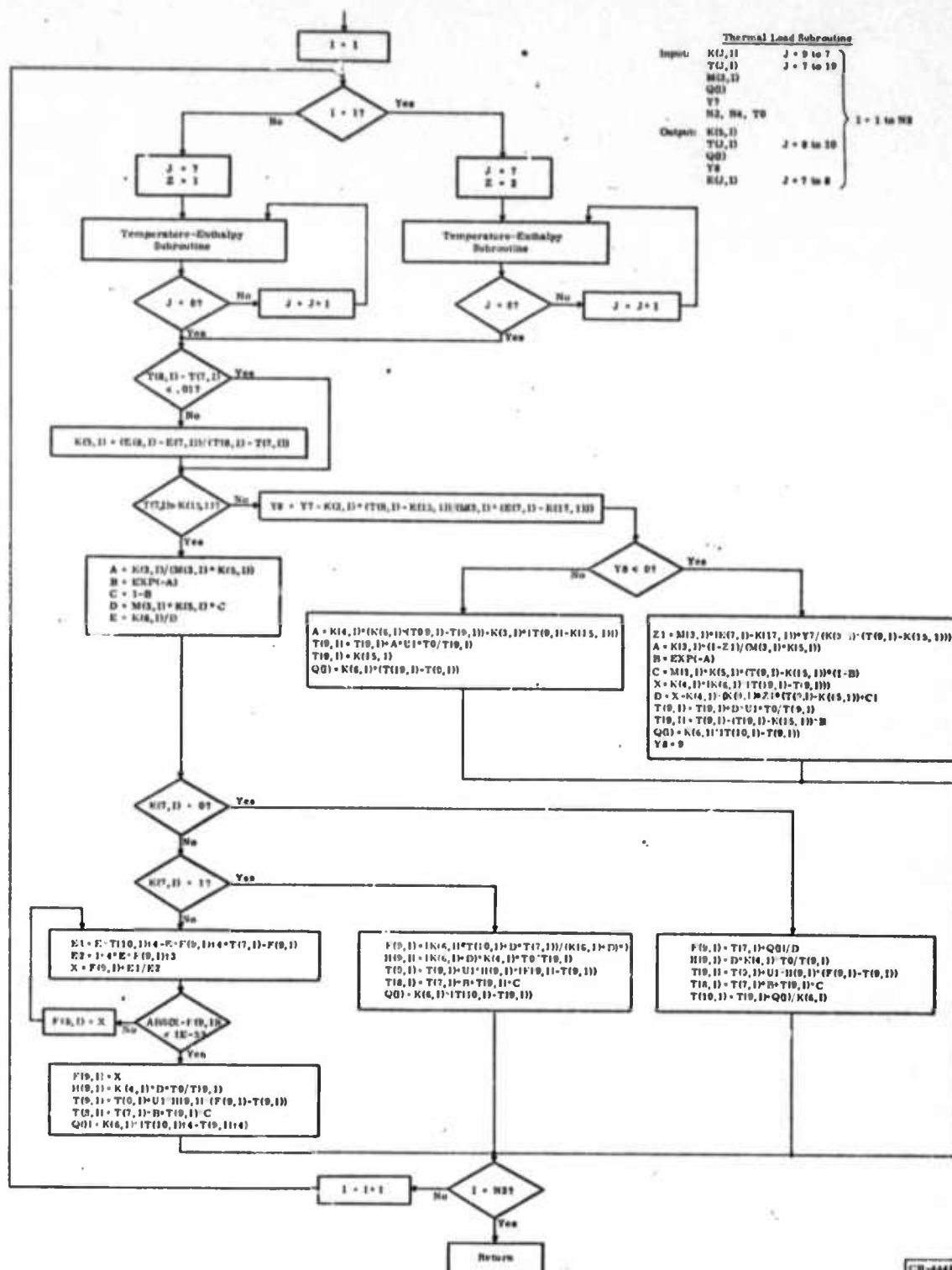
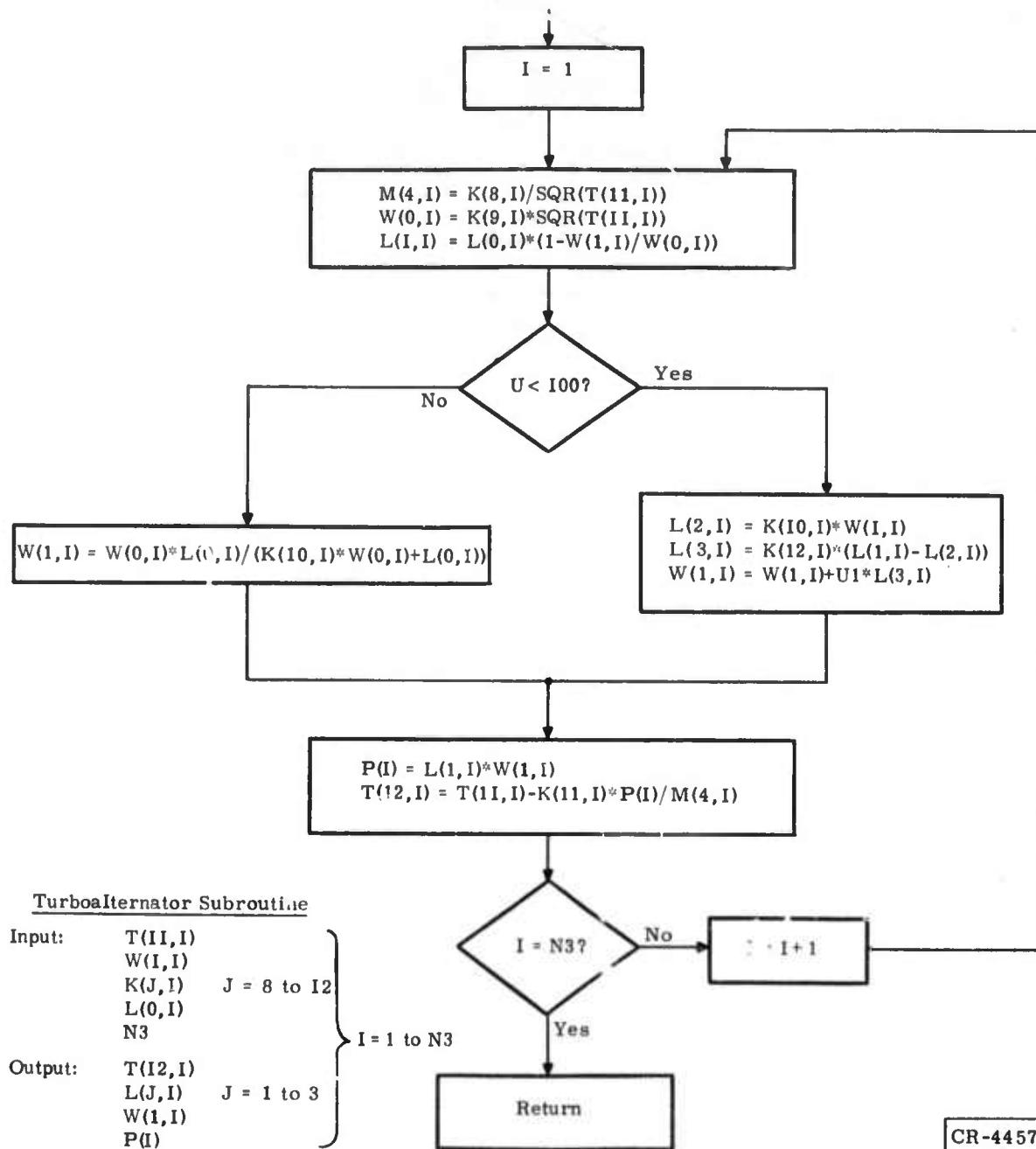


Figure 103. Flowchart of Thermal Load Subroutine



Turboalternator Subroutine

Input:	$T(11,I)$ $W(1,I)$ $K(J,I) \quad J = 8 \text{ to } 12$ $L(0,I)$ $N3$	$\left. \vphantom{\begin{matrix} T(11,I) \\ W(1,I) \\ K(J,I) \\ L(0,I) \\ N3 \end{matrix}} \right\} I = 1 \text{ to } N3$
Output:	$T(12,I)$ $L(J,I) \quad J = 1 \text{ to } 3$ $W(1,I)$ $P(I)$	

CR-4457

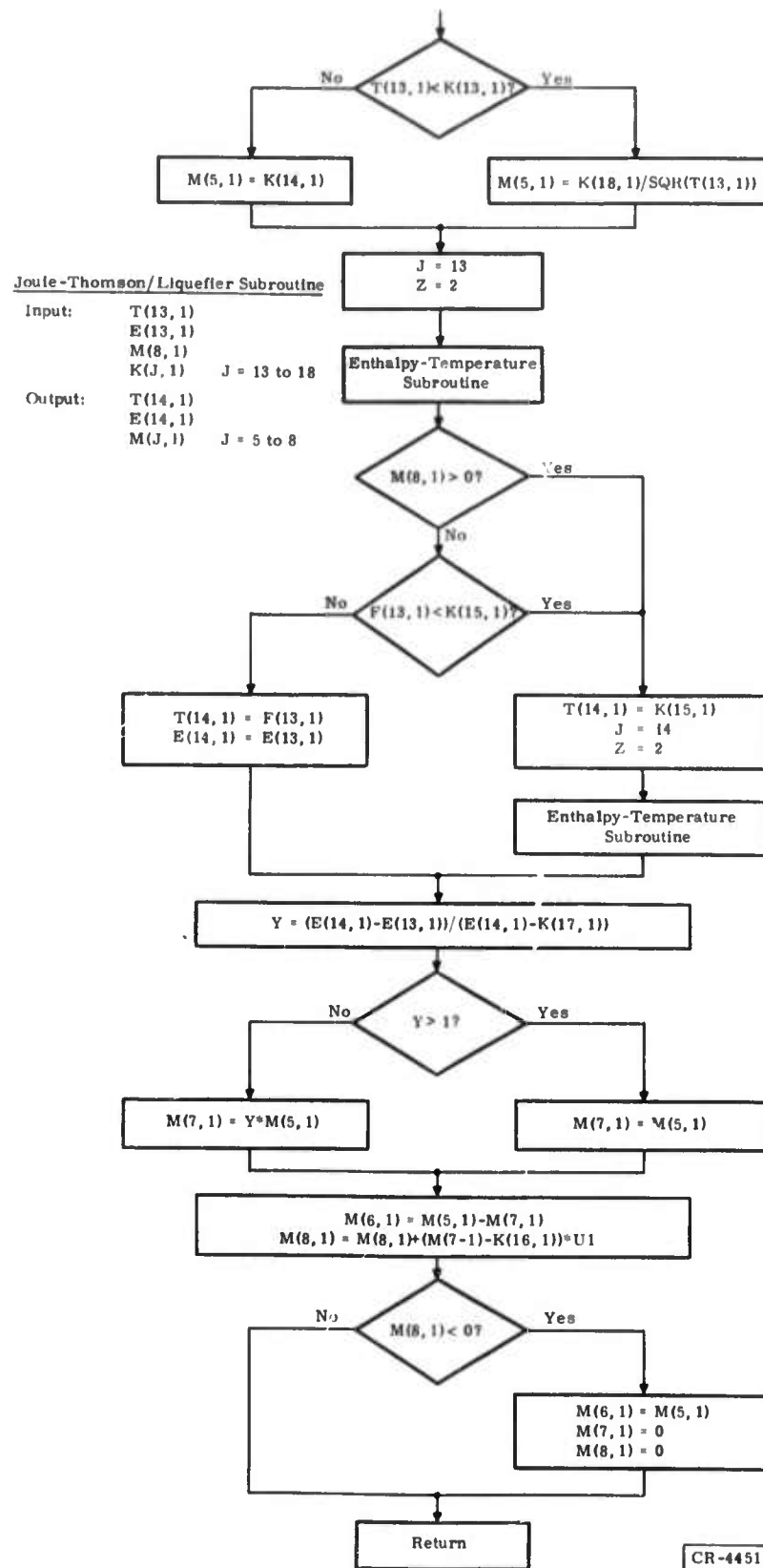
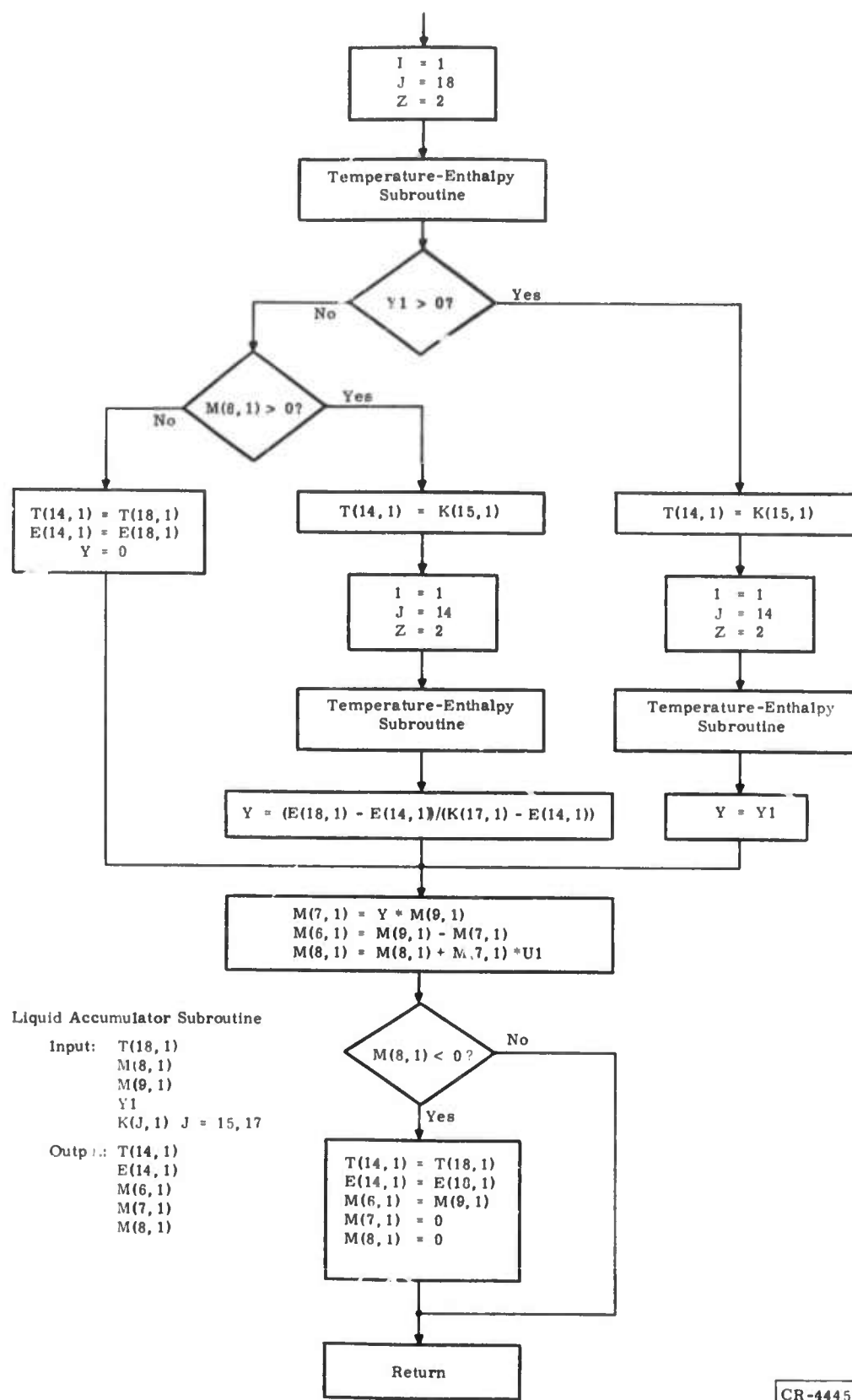


Figure 105. Flowchart of Joule-Thomson/Liquefier Subroutine

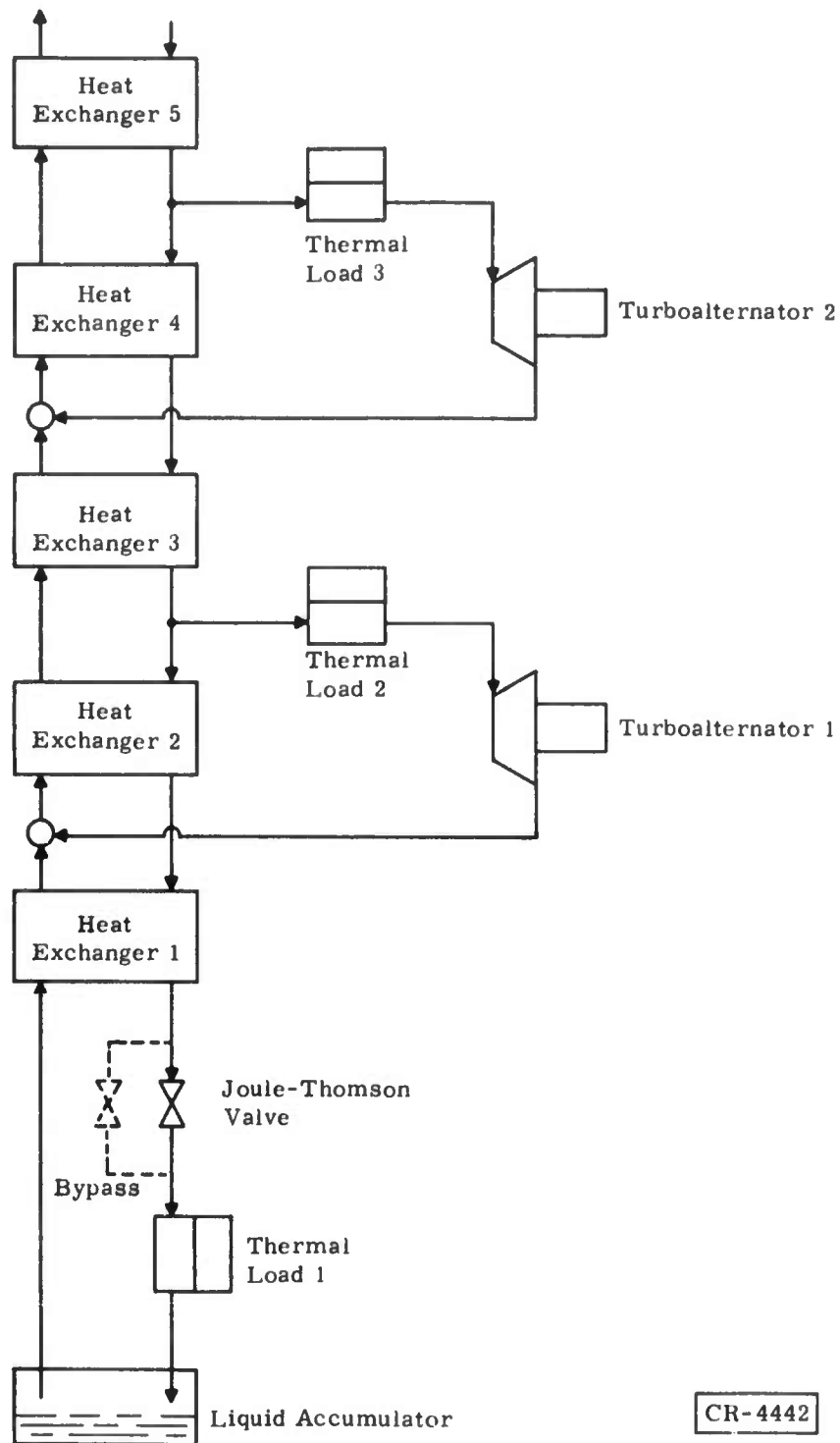


CR-4445

Figure 107. Flowchart of Liquid Accumulator Subroutine

NUMERICAL EXAMPLE

The specific configuration considered is shown in Figure 108. The steady-state design point is shown in Figure 109.



CR-4442

Figure 108. System Configuration

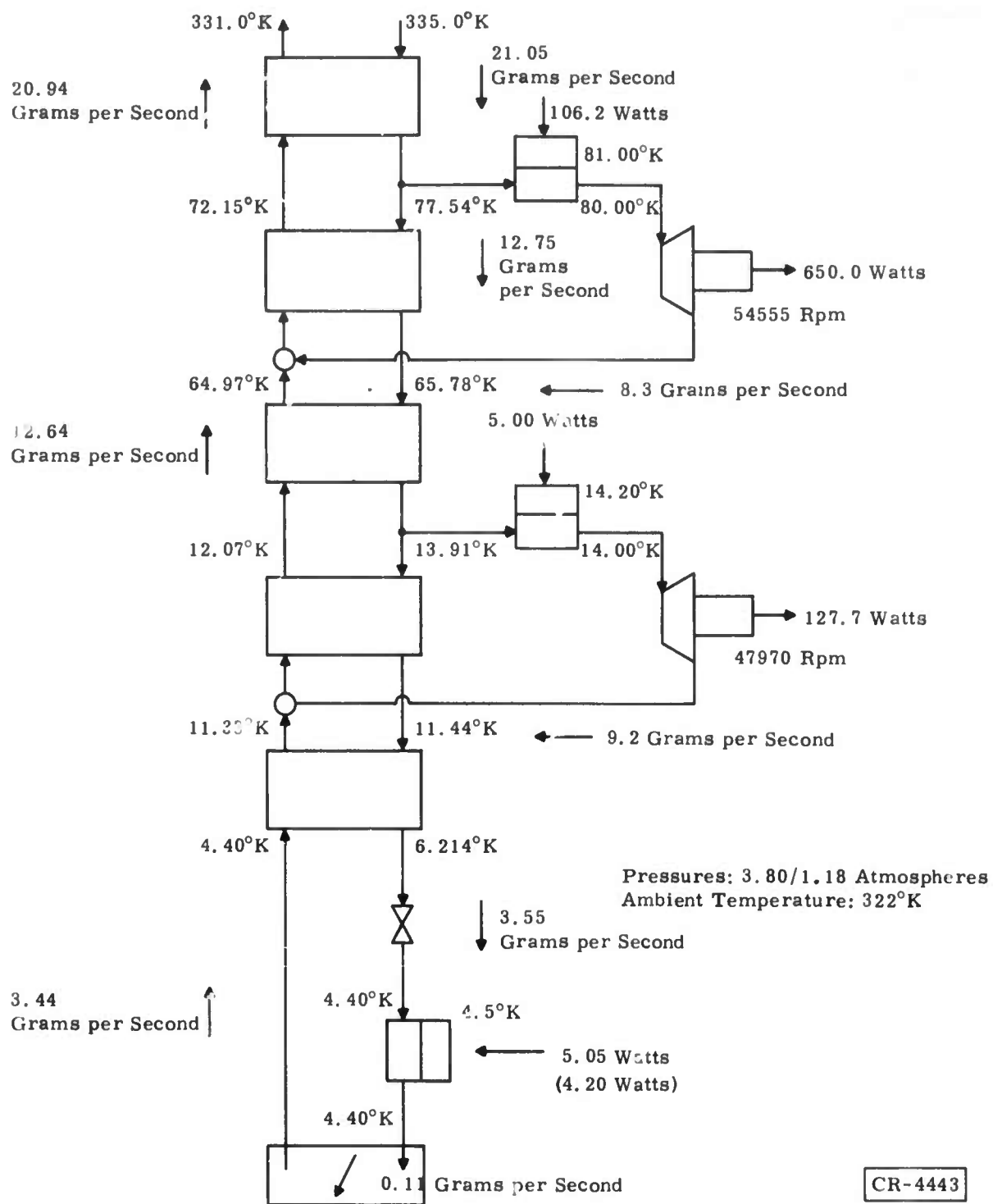


Figure 109. Steady-State Design Point

From these data, plus information regarding the thermal time constants of the various component devices, the specifying parameters for all devices (e.g., the $K(J, I)$) can be determined algebraically using Equations 1 through 86. The specific numerical values for this case are given in Figures 111 and 113.

In this experimental transient run, neither the true sequence and timing of the events nor the proper time step size for stability is initially known. For this reason two program variations were used. The first of these, designated ARPA1, contains ambient temperature initial conditions. The second, designated ARPA2, contains a set of arbitrary initial conditions. This second variation is used to restart the run at any point -- in particular, when a change in the step size is needed. At any such point, the new initial conditions are set to the last valid values of the system variables from the preceding portion of the transient run.

In this particular case, the step size was initially set at 1 second; it then was increased to 10 seconds and finally it was increased to 100 seconds at the beginning of the run. This permitted the turbines to accelerate to normal operating speed and allowed the system to settle into the steady cooldown mode in a stable manner.

Toward the end of the cooldown transient it was necessary to reduce the step size to 20 seconds, 10 seconds, 5 seconds, 1 second, and finally to 0.1 second, as the thermal time constants were reduced by the lowering temperatures.

To simulate the temperature rise at the input to the cryosection (compressor and intercooler), that input temperature was initially set at the ambient 322°K and was arbitrarily made to rise exponentially to the steady-state design value of 335°K with a time constant of 60 seconds.

As an experiment, the flow through the Joule-Thomson valve was arbitrarily programmed (simulating cooldown control) to permit 200 percent of the steady-state design flow initially and then 100 percent of the design flow below 50°K . Finally, at 6.25°K , control was removed. The purpose of this experiment was to aid cooldown of the massive thermal load (Thermal Load 1) at that point.

For the transient run, load Q_1 for Thermal Load 1 was set to be 4.20 watts at 4.5°K (a change from the steady-state design point of 5.05 watts at 4.5°K).

COMPONENT DEVICE TIME CONSTANTS

The estimated time constants for the various component devices at 350°K were:

<u>Component</u>	<u>Time Constant (seconds)</u>
Heat Exchanger 1	560
Heat Exchanger 2	158
Heat Exchanger 3	500
Heat Exchanger 4	5,870
Heat Exchanger 5	12,300
Thermal Load 1	5,670
Thermal Load 2	100
Thermal Load 3	8,004
Turboalternator 1	5
Turboalternator 2	5

The very great range among devices dictates the progress of the stepwise computation procedure. In particular, the short time constants for the cold-end heat exchangers require relatively short time steps, and the long time constants among the remaining devices determine a relative long total elapsed time for cooldown.

To aid in the computational procedure without significantly affecting the simulated system performance, the turboalternator time constants were simply eliminated algebraically after the turbines had completed their acceleration to normal speed (after 100 seconds).

The equations used for calculation of thermal load decrements were described above under "Thermal Load Model." The manner in which values for the heat exchanger time constants were calculated is outlined below.

The time constant for a counterflow heat exchanger was defined. It is assumed that, for the two streams in the counterflow, the products of the flow rate and the heat capacity (heat capacity flow rate) are the same. With the heat exchanger at a steady-state condition, and with one of the two inlet stream temperatures held fixed, the temperature of the other inlet stream is suddenly changed to a new constant value. The outlet temperature of that stream will gradually go through an excursion to a new steady-state value. The time constant is defined as the time required for that outlet temperature to go through a fraction $1-(1/e)$ of the total temperature excursion. This fraction is equal to 0.632.

A further definition needed is for thermal effectiveness. This parameter is defined as the ratio of the amount of heat actually transferred between streams to the maximum amount of heat that could theoretically be transferred in an infinitely large counterflow heat exchanger.

To calculate the heat exchanger time constants, the following assumptions were made:

- Heat capacity flow rates are the same for each stream.
- Heat exchanger thermal effectiveness is sufficiently high that the temperature difference between streams is small relative to the temperature difference along the length of the streams.
- Thermal wave propagates along the length of the exchanger without diffusion (a rectangular wavefront remains rectangular).
- Heat capacity of the gas within the exchanger at a given time is small relative to the heat capacity of the exchanger itself.

Reference 4 was used as the basis for derivation of the following equation:

$$\text{Time Constant} = 0.316 \frac{M_c C_c}{M C_p (1 - \epsilon)} \quad (87)$$

where:

M_c = Mass of heat exchanger core

C_c = Specific heat of heat exchanger core material

M = Mass flow rate for gas

C_p = Specific heat of gas

ϵ = Exchanger thermal effectiveness

For example, the time constant for the largest heat exchanger (Heat Exchanger 5) was calculated as follows:

$M_c = 70.2$ kilograms

$C_c = 0.91$ joules per gram $^{\circ}K$

$M = 21.0$ grams per second

$C_p = 5.2$ joules per gram $^{\circ}K$

$\epsilon = 0.985$

$$\begin{aligned} TC &= \frac{1}{K_{25}} = 0.316 \frac{70,200 \times 0.91}{21 \times 5.2 (1 - 0.985)} \\ &= 12,300 \text{ seconds} \end{aligned} \quad (88)$$

TEMPERATURE-ENTHALPY DATA

The sample points listed in Figure 110 are taken from the (continuous) empirically derived temperature-enthalpy functions used.

PRESSURE = 3.8

T	H
6.1	24.4307
6.214	27.9366
6.5	32.7544
7	38.414
8	46.9
9	54.0273
10	60.5477
11.44	69.3684
13.91	83.6812
20	117.177
40	222.93
65.78	357.473
77.54	418.056
100	535.433
200	1054.79
300	1573.91
322	1688.11
335	1755.58

PRESSURE = 1.18

T	H
4.3	27.7686
4.4	29.9474
5	36.0442
6	42.9076
8	54.5915
10	65.5578
11.33	72.704
12.07	76.6515
20	118.405
40	222.653
64.97	352.478
72.15	389.791
100	534.493
200	1053.96
300	1573.37
322	1687.64
331	1734.39

Figure 110. Temperature-Enthalpy Sample Points

SAMPLE PRINTOUT -- ARPA1

Figure 111 is a reproduction of the heading printout and sample data for the beginning of a transient run. The heading information includes parameter data for all component devices. The first data sheet defines and illustrates the normal data printout.

ARPA TRANSIENT REFRIGERATOR MODEL
 AMBIENT START (ARPA1)

HEAT EXCHANGERS -- 5
 THERMAL LOADS -- 3
 TURBO-ALTERNATORS -- 2
 J-T VALVE/LIQUEFIER

AMBIENT TEMPERATURE-- 322 DEG K
 INITIAL TIME STEP-- 1 SECONDS
 TIME STEP ADJUSTED BETWEEN 0.1 AND 100 SEC DURING RUN

HEAT EXCHANGER 1
 K1= 46.5251 K2= 1.66371 E-3

HEAT EXCHANGER 2
 K1= 15.9946 K2= 5.89669 E-3

HEAT EXCHANGER 3
 K1= 560.522 K2= 1.86335 E-3

HEAT EXCHANGER 4
 K1= 64.8278 K2= 1.58718 E-4

HEAT EXCHANGER 5
 K1= 1160.98 K2= 7.57461 E-5

THERMAL LOAD 1 TYPE 1
 K3= 50.5 X= 9.52652 E-6 K5= 5.19
 K6= 1.32283 E-2

THERMAL LOAD 2 TYPE 1
 K3= 20.9395 K4= 5.49081 E-4 K5= 5.19
 K6= 1.62449 E-2

THERMAL LOAD 3 TYPE 1
 K3= 53.5899 K4= 3.74264 E-6 K5= 5.19
 K6= 0.440665

TURBO-ALTERNATOR 1
 K8= 34.4306 K9= 25.6356 K10= 5.54947 E-2
 K11= 0.192789 K12= 0.900987

TURBO-ALTERNATOR 2
 K8= 74.2374 K9= 12.1989 K10= 0.218396
 K11= 0.190937 K12= 0.228942

J-T VALVE/LIQUEFIER
 K13= 50 K14= 7.1 K15= 4.4
 K16= 0 K17= 10.96 K18= 8.8494

CoolDOWN FROM AMBIENT TEMPERATURE
 CONSTANT PRESSURE 3.8/1.18 ATM
 WITH LIQUEFIER
 CONTROLLED J-T VALVE--M=7.10 FOR TEMP ABOVE 50
 --M=3.55 FOR 50 TO 6.25
 --NO CONTROL BELOW 6.25

Figure 111. Heading Printout and Sample Data for ARPA1

TIME--SECONDS
T=TEMPERATURE--DEG K
Q=HEAT FLOW--WATTS
M=MASS FLOW--GRAMS/SEC
W=SHAFT SPEED--RPM*1000
P=POWER--WATTS

TIME

H-E	T1	T2	T3	T4
T-L	T8	T9	T10	Q
T-A	T12	M4	W	P
J-T/LI0	T14	M5	M7	M8

TIME= 0

H-E 1	322	322	322	322
H-E 2	322	322	322	322
H-E 3	322	322	322	322
H-E 4	322	322	322	322
H-E 5	322	322	322	322
T-L 1	322	322	322	0
T-L 2	322	322	322	0
T-L 3	322	322	322	0
T-A 1	322	1.91874	0	0
T-A 2	322	4.13709	0	0
J-T/LI0	322	7.1	0	0

TIME= 10

H-E 1	321.914	322.	322.023	322.
H-E 2	322.	321.914	318.12	321.952
H-E 3	321.99	322.	321.952	322.
H-E 4	322	321.99	310.659	321.997
H-E 5	323.996	322	321.997	322.001
T-L 1	322.023	322.	322	-2.72495 E-6
T-L 2	322.	322.	322	4.33786 E-7
T-L 3	322.	322	322	0
T-A 1	303.762	1.91874	36.8207	181.515
T-A 2	285.935	4.13709	39.3955	781.423
J-T/LI0	322.023	7.1	0	0

TIME= 200

H-E 1	317.712	321.939	322.023	321.562
H-E 2	321.689	317.712	314.175	319.588
H-E 3	321.511	321.689	319.588	321.938
H-E 4	322.	321.511	305.152	321.828
H-E 5	334.536	322.	321.828	322.125
T-L 1	322.023	322.004	322	-5.59119 E-5
T-L 2	321.944	321.949	322	8.24565 E-4
T-L 3	322.	322	322	0
T-A 1	286.844	1.9188	79.3834	349.722
T-A 2	268.557	4.13709	72.8156	1157.96
J-T/LI0	322.023	7.1	0	0

Figure 111. Heading Printout and Sample Data for ARPA1 (Continued)

TIME= 1200

H-E 1	312.066	321.085	321.852	316.161
H-E 2	317.243	312.066	309.229	314.701
H-E 3	319.103	317.243	314.701	320.22
H-E 4	321.97	319.103	303.986	320.985
H-E 5	335.	321.97	320.985	323.051
T-L 1	321.82	321.952	322	6.28504 E-4
T-L 2	318.141	318.202	322	6.16998 E-2
T-L 3	321.997	321.999	322	2.72323 E-4
T-A 1	283.715	1.92895	79.311	349.066
T-A 2	268.556	4.1371	72.8155	1157.96
J-T/LIQ	321.852	7.1	0	0

TIME= 2200

H-E 1	307.482	320.183	321.465	311.712
H-E 2	312.572	307.482	304.781	310.068
H-E 3	316.833	312.572	310.068	317.937
H-E 4	321.883	316.833	302.434	320.189
H-E 5	335.	321.883	320.189	323.91
T-L 1	321.419	321.715	322	3.77279 E-3
T-L 2	313.461	313.522	322	0.137723
T-L 3	321.986	321.995	322	2.3181 E-3
T-A 1	279.386	1.94326	79.2092	348.169
T-A 2	268.547	4.13717	72.8151	1157.94
J-T/LIQ	321.465	7.1	0	0

TIME= 3200

H-E 1	303.245	319.211	320.941	307.764
H-E 2	308.068	303.245	300.715	305.687
H-E 3	314.665	308.068	305.687	315.681
H-E 4	321.745	314.665	300.897	319.422
H-E 5	335	321.745	319.422	324.703
T-L 1	320.881	321.318	322	9.02759 E-3
T-L 2	308.907	308.965	322	0.211757
T-L 3	321.964	321.983	322	0.007699
T-A 1	275.15	1.95758	79.1075	347.276
T-A 2	268.529	4.1373	72.8143	1157.92
J-T/LIQ	320.941	7.1	0	0

TIME= 4200

H-E 1	299.285	318.166	320.292	304.079
H-E 2	303.822	299.285	296.922	301.574
H-E 3	312.589	303.822	301.574	313.516
H-E 4	321.562	312.589	299.415	318.677
H-E 5	335	321.562	318.677	325.437
T-L 1	320.221	320.781	322	1.61262 E-2
T-L 2	304.603	304.658	322	0.281724
T-L 3	321.929	321.96	322	1.76758 E-2
T-A 1	271.145	1.97142	79.0095	346.416
T-A 2	268.5	4.13752	72.8131	1157.88
J-T/LIQ	320.292	7.1	0	0

Figure 111. Heading Printout and Sample Data for ARPA1 (Continued)

SAMPLE PRINTOUT -- ARPA2

Figure 112 is a reproduction of data taken near the end of the transient cooldown run.

At this point (Time = 314,710 seconds) the point of liquefaction is just being reached, and the Joule-Thomson valve flow control is at the point of switching to normal (uncontrolled flow). A time step of 0.1 second is being used, and printout occurs at intervals of 120 steps (12 seconds).

PROGRAM LISTINGS

ARPA1 PROGRAM

Figure 113 is a complete listing of the ARPA1 model program.

ARPA2 PROGRAM

Figure 114 contains a portion of the listing for the ARPA2 model program. This portion contains the specification of initial conditions. The remainder of the program is identical to the ARPA1 listing in Figure 113.

ARPA TRANSIENT REFRIGERATOR MODEL
ARBITRARY START (ARPA2)

TIME= 314710

H-E 1	13.8483	6.25855	4.41877	13.5984
H-E 2	16.9121	13.8483	13.7232	14.6882
H-E 3	108.541	16.9121	14.6882	106.913
H-E 4	125.214	108.541	106.46	119.162
H-E 5	335	125.214	119.162	331.757
T-L 1	4.41793	4.4943	322	4.20006
T-L 2	17.0205	17.2073	322	4.95133
T-L 3	129.49	130.597	322	84.3446
T-A 1	13.7763	8.3456	50.306	140.44
T-A 2	105.635	6.52385	61.0917	815.096
J-T/LIQ	4.41877	3.55	0	0

TIME= 314722

H-E 1	13.8465	6.24631	4.4	13.5959
H-E 2	16.9106	13.8465	13.7217	14.6864
H-E 3	108.535	16.9106	14.6864	106.907
H-E 4	125.207	108.535	106.454	119.156
H-E 5	335	125.207	119.156	331.757
T-L 1	4.4	4.49077	322	4.20011
T-L 2	17.019	17.206	322	4.95135
T-L 3	129.483	130.59	322	84.3476
T-A 1	13.775	8.34598	50.3049	140.434
T-A 2	105.628	6.52404	61.0909	815.076
J-T/LIQ	4.4	3.54078	2.49769 E-3	7.14274 E-4

TIME= 314733

H-E 1	13.8473	6.24704	4.4	13.5955
H-E 2	16.92	13.8473	13.726	14.6879
H-E 3	108.529	16.92	14.6879	106.903
H-E 4	125.201	108.529	106.449	119.149
H-E 5	335	125.201	119.149	331.756
T-L 1	4.4	4.48819	322	4.20014
T-L 2	17.0266	17.2107	322	4.95127
T-L 3	129.476	130.583	322	84.3507
T-A 1	13.7812	8.34413	50.3102	140.464
T-A 2	105.623	6.52421	61.0902	815.057
J-T/LIQ	4.4	3.5406	8.25501 E-3	8.74099 E-2

Figure 112. Transient Cooldown Sample Data for ARPA2

TIME= 314745

H-E 1	13.8519	6.24793	4.4	13.5966
H-E 2	16.9295	13.8519	13.7317	14.6935
H-E 3	108.523	16.9295	14.6735	106.899
H-E 4	125.194	108.523	106.445	119.143
H-E 5	335	125.194	119.143	331.756
T-L 1	4.4	4.48648	322	4.20016
T-L 2	17.036	17.2197	322	4.95113
T-L 3	129.469	130.576	322	84.3537
T-A 1	13.7888	8.34183	50.3168	140.5
T-A 2	105.617	6.52438	61.0895	815.038
J-T/LIQ	4.4	3.54035	9.36468 E-3	0.193739

TIME= 314757

H-E 1	13.8578	6.24854	4.4	13.5993
H-E 2	16.9389	13.8578	13.7378	14.7004
H-E 3	108.518	16.9389	14.7004	106.896
H-E 4	125.188	108.518	106.44	119.136
H-E 5	335	125.188	119.136	331.755
T-L 1	4.4	4.48535	322	4.20018
T-L 2	17.0454	17.2291	322	4.95097
T-L 3	129.462	130.57	322	84.3567
T-A 1	13.7965	8.33953	50.3234	140.537
T-A 2	105.611	6.52455	61.0888	815.019
J-T/LIQ	4.4	3.54017	1.00148 E-2	0.31042

TIME= 314769

H-E 1	13.8641	6.24897	4.4	13.6032
H-E 2	16.9478	13.8641	13.7442	14.7075
H-E 3	108.512	16.9478	14.7075	106.892
H-E 4	125.181	108.512	106.436	119.13
H-E 5	335	125.181	119.13	331.755
T-L 1	4.4	4.48461	322	4.20019
T-L 2	17.0545	17.2332	322	4.95082
T-L 3	129.456	130.563	322	84.3597
T-A 1	13.8039	8.33732	50.3297	140.573
T-A 2	105.606	6.52473	61.0881	815.
J-T/LIQ	4.4	3.54005	1.03591 E-2	0.432927

TIME= 314780

H-E 1	13.8704	6.24927	4.4	13.6079
H-E 2	16.9562	13.8704	13.7504	14.7147
H-E 3	108.506	16.9562	14.7147	106.888
H-E 4	125.175	108.506	106.431	119.124
H-E 5	335	125.175	119.124	331.754
T-L 1	4.4	4.46412	322	4.2002
T-L 2	17.063	17.2468	322	4.95068
T-L 3	129.449	130.556	322	84.3628
T-A 1	13.8108	8.33524	50.3357	140.606
T-A 2	105.6	6.5249	61.0874	814.981
J-T/LIQ	4.4	3.53997	1.05038 E-2	0.558272

Figure 112. Transient Cooldown Sample Data for ARPA2 (Continued)

TIME= 314792

H-E	1	13.8766	6.24949	4.4	13.613
H-E	2	16.9638	13.8766	13.7564	14.7215
H-E	3	108.5	16.9638	14.7215	106.885
H-E	4	125.168	108.5	106.427	119.117
H-E	5	335	125.168	119.117	331.754
T-L	1	4.4	4.48379	322	4.2002
T-L	2	17.0708	17.2548	322	4.95055
T-L	3	129.442	130.549	322	84.3658
T-A	1	13.8171	8.33334	50.3412	140.637
T-A	2	105.594	6.52507	61.0867	814.962
J-T/LIQ		4.4	3.5399	0.01052	0.684515

TIME= 314804

H-E	1	13.8824	6.24966	4.4	13.6184
H-E	2	16.9708	13.8824	13.7621	14.7279
H-E	3	108.494	16.9708	14.7279	106.881
H-E	4	125.162	108.494	106.422	119.111
H-E	5	335	125.162	119.111	331.753
T-L	1	4.4	4.48358	322	4.2002
T-L	2	17.0779	17.2622	322	4.95044
T-L	3	129.435	130.542	322	84.3688
T-A	1	13.8229	8.3316	50.3461	140.664
T-A	2	105.589	6.52524	61.0859	814.943
J-T/LIQ		4.4	3.53986	0.010456	0.810428

Figure 112. Transient Cooldown Sample Data for ARPA2 (continued)

```

00010 PRINT "ARPA TRANSIENT REFRIGERATOR MODEL"
00020 PRINT "AMBIENT START (ARPA1)"
00030 PRINT
00040 PRINT
00050 READ N1,N2,N3,N4
00060 READ T0,U1
00070 READ N5
00080 IF N5=0 THEN 190
00090 PRINT "HEAT EXCHANGERS --" N1
00100 PRINT "THERMAL LOADS --" N2
00110 PRINT "TURBO-ALTERNATORS --" N3
00120 IF N4=0 THEN 140
00130 PRINT "J-T VALVE/LIQUEFIER"
00140 PRINT
00150 PRINT "AMBIENT TEMPERATURE--"T0" DEG K"
00160 PRINT "INITIAL TIME STEP--"U1" SECONDS"
00170 PRINT "TIME STEP ADJUSTED BETWEEN 0.1 AND 100 SEC DURING RUN"
00180 PRINT
00190 FOR I=1 TO N1
00200 FOR J=1 TO 2
00210 READ K(J,I)
00220 NEXT J
00230 IF N5=0 THEN 270
00240 PRINT "HEAT EXCHANGER "I
00250 PRINT "K1="K(1,I),"K2="K(2,I)
00260 PRINT
00270 NEXT I
00280 FOR I=1 TO N2
00290 FOR J=3 TO 7
00300 READ K(J,I)
00310 NEXT J
00320 IF N5=0 THEN 370
00330 PRINT "THERMAL LOAD "I,"TYPE "K(7,I)
00340 PRINT "K3="K(3,I),"K4="K(4,I),"K5="K(5,I)
00350 PRINT "K6="K(6,I)
00360 PRINT
00370 NEXT I
00380 FOR I=1 TO N3
00390 FOR J=8 TO 12
00400 READ K(J,I)
00410 NEXT J
00420 IF N5=0 THEN 470
00430 PRINT "TURBO-ALTERNATOR "I
00440 PRINT "K8="K(8,I),"K9="K(9,I),"K10="K(10,I)
00450 PRINT "K11="K(11,I),"K12="K(12,I)
00460 PRINT
00470 NEXT I
00480 IF N4=0 THEN 560
00490 FOR J=13 TO 18
00500 READ K(J,I)
00510 NEXT J
00520 IF N5=0 THEN 570
00530 PRINT "J-T VALVE/LIQUEFIER"

```

Figure 113. Complete Listing of ARPA1 Program

```

00540 PRINT "K13="K(13,1),"K14="K(14,1),"K15="K(15,1)
00550 PRINT "K16="K(16,1),"K17="K(17,1),"K18="K(18,1)
00560 PRINT
00570 FOR Z=1 TO 2
00580 READ C(1,Z),C(2,Z),C(3,Z),C(4,Z),C(5,Z),C(6,Z),C(7,Z),C(8,Z)
00590 NEXT Z
00600 REM INITIAL CONDITIONS
00610 REM PRINT CONTROL
00620 LET I1=10
00630 REM INITIAL TIME
00640 LET U=0
00650 REM H-E TEMP
00660 FOR I=1 TO N1
00670 FOR J=1 TO 6
00680 LET T(J,I)=T0
00690 NEXT J
00700 NEXT I
00710 FOR I=1 TO N1
00720 FOR J=1 TO 2
00730 LET E(J,I)=1688.10
00740 NEXT J
00750 FOR J=3 TO 4
00760 LET E(J,I)=1687.64
00770 NEXT J
00780 NEXT I
00790 REM ADDITIONAL H-E IC
00800 REM ADDITIONAL H-E IC
00810 REM ADDITIONAL H-E IC
00820 REM ADDITIONAL H-E IC
00830 REM ADDITIONAL H-E IC
00840 REM ADDITIONAL H-E IC
00850 REM ADDITIONAL H-E IC
00860 REM ADDITIONAL H-E IC
00870 REM ADDITIONAL H-E IC
00880 REM ADDITIONAL H-E IC
00890 REM T-L TEMP & Q
00900 FOR I=1 TO N2
00910 FOR J=8 TO 10
00920 LET T(J,I)=T0
00930 NEXT J
00940 LET Q(I)=0
00950 NEXT I
00960 LET I=1
00970 FOR J=7 TO 8
00980 LET E(J,I)=1687.64
00990 NEXT J
01000 FOR I=2 TO N2
01010 FOR J=7 TO 8
01020 LET E(J,I)=1688.10
01030 NEXT J
01040 NEXT I
01050 REM ADDITIONAL T-L IC
01060 REM ADDITIONAL T-L IC

```

Figure 113. Complete Listing of ARPA1 Program (Continued)

```

01070 REM T-A TEMP, SPEED, POWER, TORQUE, MASS FLOW
01080 FOR I=1 TO N3
01090 FOR J=11 TO 12
01100 LET T(J,I)=T0
01110 NEXT J
01120 LET W(1,I)=0
01130 LET P(I)=0
01140 NEXT I
01150 LET L(0,1)=5.32416
01160 LET L(0,2)=23.8292
01170 LET M(4,1)=1.91874
01180 LET M(4,2)=4.13709
01190 REM ADDITIONAL T-A IC
01200 REM ADDITIONAL T-A IC
01210 REM J-T/LIQ TEMP, ENTHALPY, MASS FLOW
01220 LET T(14,1)=T0
01230 LET T(15,1)=T0
01240 LET M(5,1)=7.1
01250 LET M(6,1)=7.1
01260 LET M(7,1)=0
01270 LET M(8,1)=0
01280 LET E(2,1)=1688.10
01290 LET E(8,1)=1687.64
01300 LET Y0=0
01310 LET Y8=0
01320 REM ADDITIONAL J-T/LIQ IC
01330 REM ADDITIONAL J-T/LIQ IC
01340 REM CHECK FOR CONSISTENT INTERCONNECTIONS
01350 GOSUB 4610
01360 FOR J=1 TO 2
01370 FOR I=1 TO N1
01380 LET N(J,I)=M(J,I)
01390 NEXT I
01400 NEXT J
01410 REM SPECIFY RUN TYPE
01420 IF N5=0 THEN 1780
01430 PRINT "COLDOWN FROM AMBIENT TEMPERATURE"
01440 PRINT "CONSTANT PRESSURE 3.8/1.18 ATM"
01450 IF N4=0 THEN 1500
01460 PRINT "WITH LIQUEFIER"
01470 PRINT "CONTROLLED J-T VALVE--M=7.10 FOR TEMP ABOVE 50"
01480 PRINT "                                --M=3.55 FOR 50 TO 6.25"
01490 PRINT "                                --NO CONTROL BELOW 6.25"
01500 PRINT
01510 PRINT
01520 PRINT
01530 PRINT
01540 PRINT
01550 PRINT
01560 PRINT "TIME--SECONDS"
01570 PRINT "T=TEMPERATURE--DEG K"
01580 PRINT "Q=HEAT FLOW--WATTS"
01590 PRINT "M=MASS FLOW--GRAMS/SEC"

```

Figure 113. Complete Listing of ARPA1 Program (Continued)

```

01600 PRINT "W=SHAFT SPEED--RPM*1000"
01610 PRINT "P=POWER--WATTS"
01620 PRINT
01630 PRINT
01640 PRINT "TIME"
01650 PRINT
01660 PRINT "H-E","T1","T2","T3","T4"
01670 PRINT
01680 PRINT "T-L","T8","T9","T10","Q"
01690 PRINT
01700 PRINT "T-A","T12","M4","W","P"
01710 PRINT
01720 IF N4=0 THEN 1750
01730 PRINT "J-T/LIQ","T14","M5","M7","M8"
01740 PRINT
01750 PRINT
01760 PRINT
01770 PRINT
01780 IF I1<10 THEN 1980
01790 REM PRINT PRESENT STATE
01800 PRINT "TIME="U
01810 PRINT
01820 FOR I=1 TO N1
01830 PRINT "H-E "I,T(1,I),T(2,I),T(3,I),T(4,I)
01840 NEXT I
01850 PRINT
01860 FOR I=1 TO N2
01870 PRINT "T-L "I,T(8,I),T(9,I),T(10,I),Q(I)
01880 NEXT I
01890 PRINT
01900 FOR I=1 TO N3
01910 PRINT "T-A "I,T(12,I),M(4,I),W(1,I),P(I)
01920 NEXT I
01930 PRINT
01940 IF N4=0 THEN 1970
01950 PRINT "J-T/LIQ",T(14,I),M(5,I),M(7,I),M(8,I)
01960 PRINT
01970 LET I1=0
01980 REM HEAT EXCHANGER CALCULATION
01990 GOSUB 2140
02000 REM THERMAL LOAD CALCULATION
02010 GO SUB 2800
02020 REM TURBO-ALTERNATOR CALCULATION
02030 GOSUB 3470
02040 IF N4=0 THEN 2090
02050 REM J-T VALVE CALCULATION
02060 GOSUB 3620
02070 REM LIQUID ACCUMULATOR CALCULATION
02080 GOSUB 3900
02090 REM MISCELLANEOUS TIME FUNCTIONS
02100 GOSUB 4400
02110 REM INTERCONNECTIONS
02120 GOSUB 4610

```

Figure 113. Complete Listing of ARPA1 Program (Continued)

```

02130 GO TO 1780
02140 REM HEAT EXCHANGER SUBROUTINE
02150 FOR I=1 TO N1
02160 IF M(2,I)=0 THEN 2610
02170 FOR J=1 TO 2
02180 LET Z=1
02190 GOSUB 4250
02200 NEXT J
02210 FOR J=3 TO 4
02220 LET Z=2
02230 GOSUB 4250
02240 NEXT J
02250 IF ABS(T(1,I)-T(2,I))<.01 THEN 2280
02260 IF ABS(E(1,I)-E(2,I))<.01 THEN 2280
02270 LET N(1,I)=M(1,I)*((E(1,I)-E(2,I))/(T(1,I)-T(2,I)))/5.2
02280 IF ABS(T(4,I)-T(3,I))<.01 THEN 2310
02290 IF ABS(E(4,I)-E(3,I))<.01 THEN 2310
02300 LET N(2,I)=M(2,I)*((E(4,I)-E(3,I))/(T(4,I)-T(3,I)))/5.2
02310 IF ABS(N(2,I)-N(1,I))<.001 THEN 2430
02320 IF N(2,I)>N(1,I) THEN 2380
02330 LET A=K(1,I)*(1/N(2,I)-1/N(1,I))
02340 LET B=1-(N(2,I)/N(1,I))*EXP(-A)
02350 LET C=1+(N(2,I)/N(1,I))
02360 LET D=1-(N(2,I)/N(1,I))
02370 GO TO 2450
02380 LET A=K(1,I)*(1/N(2,I)-1/N(1,I))
02390 LET B=1-(N(1,I)/N(2,I))*EXP(A)
02400 LET C=1+(N(1,I)/N(2,I))
02410 LET D=1-(N(1,I)/N(2,I))
02420 GO TO 2500
02430 LET A=K(1,I)/N(1,I)
02440 GO TO 2550
02450 LET F(2,I)=(D*T(1,I)+(1-EXP(-A))*(C-1)*T(3,I))/B
02460 LET F(4,I)=((1-EXP(-A))*T(1,I)+D*EXP(-A)*T(3,I))/B
02470 LET F(5,I)=((1-.5*C*EXP(-A))*T(1,I)+.5*D*EXP(-A)*T(3,I))/B
02480 LET F(6,I)=(.5*D*T(1,I)+(.5*C-(C-1)*EXP(-A))*T(3,I))/B
02490 GO TO 2650
02500 LET F(2,I)=(D*EXP(A)*T(1,I)+(1-EXP(A))*T(3,I))/B
02510 LET F(4,I)=((1-EXP(A))*(C-1)*T(1,I)+D*T(3,I))/B
02520 LET F(5,I)=((.5*C-(C-1)*EXP(A))*T(1,I)+.5*D*T(3,I))/B
02530 LET F(6,I)=(.5*D*EXP(A)*T(1,I)+(1-.5*C*EXP(A))*T(3,I))/B
02540 GO TO 2650
02550 LET B=1+A
02560 LET F(2,I)=(T(1,I)+A*T(3,I))/B
02570 LET F(4,I)=(A*T(1,I)+T(3,I))/B
02580 LET F(5,I)=((.5+A)*T(1,I)+.5*T(3,I))/B
02590 LET F(6,I)=(.5*T(1,I)+(.5+A)*T(3,I))/B
02600 GO TO 2650
02610 FOR J=2 TO 6
02620 LET F(J,I)=T(1,I)
02630 NEXT J
02640 GO TO 2650
02650 LET F(1,I)=T(1,I)

```

Figure 113. Complete Listing of ARPA1 Program (Continued)


```

02660 LET F(3,I)=T(3,I)
02670 LET H(1,I)=0
02680 LET H(3,I)=0
02690 LET H(2,I)=K(2,I)*T0/T(6,I)
02700 LET H(4,I)=K(2,I)*T0/T(5,I)
02710 LET H(5,I)=H(4,I)
02720 LET H(6,I)=H(2,I)
02730 NEXT I
02740 FOR I=1 TO N1
02750 FOR J=1 TO 6
02760 LET T(J,I)=T(J,I)+U1*H(J,I)*(F(J,I)-T(J,I))
02770 NEXT J
02780 NEXT I
02790 RETURN
02800 REM THERMAL LOAD SUBROUTINE
02810 FOR I=1 TO N2
02820 IF I=1 THEN 2880
02830 FOR J=7 TO 8
02840 LET Z=1
02850 GOSUB 4250
02860 NEXT J
02870 GO TO 2920
02880 FOR J=7 TO 8
02890 LET Z=2
02900 GOSUB 4250
02910 NEXT J
02920 IF T(8,I)-T(7,I)<.01 THEN 2940
02930 LET K(5,I)=(E(8,I)-E(7,I))/(T(8,I)-T(7,I))
02940 IF T(7,I)>K(15,I) THEN 2960
02950 GO TO 3270
02960 LET A=K(3,I)/(M(3,I)*K(5,I))
02970 LET B=EXP(-A)
02980 LET C=1-B
02990 LET D=M(3,I)*K(5,I)*C
03000 LET E=K(6,I)/D
03010 IF K(7,I)=0 THEN 3210
03020 IF K(7,I)=1 THEN 3150
03030 LET E1=E*T(10,I)+4-E*F(9,I)+4+T(7,I)-F(9,I)
03040 LET E2=1+4+E*F(9,I)+3
03050 LET X=F(9,I)+E1/E2
03060 IF ABS(X-F(9,I))<1E-5 THEN 3090
03070 LET F(9,I)=X
03080 GO TO 3030
03090 LET F(9,I)=X
03100 LET H(9,I)=K(4,I)*D*T0/T(9,I)
03110 LET T(9,I)=T(9,I)+U1*H(9,I)*(F(9,I)-T(9,I))
03120 LET T(8,I)=T(7,I)*B+T(9,I)*C
03130 LET O(I)=K(6,I)*(T(10,I)+4-T(9,I)+4)
03140 GO TO 3450
03150 LET F(9,I)=(K(6,I)*T(10,I)+D*T(7,I))/(K(6,I)+D)
03160 LET H(9,I)=(K(6,I)+D)*K(4,I)*T0/T(9,I)
03170 LET T(9,I)=T(9,I)+U1*H(9,I)*(F(9,I)-T(9,I))
03180 LET T(8,I)=T(7,I)*B+T(9,I)*C

```

Figure 113. Complete Listing of ARPA1 Program (Continued)

```

03190 LET Q(I)=K(6,I)*(T(10,I)-T(9,I))
03200 GO TO 3450
03210 LET F(9,I)=T(7,I)+Q(I)/D
03220 LET H(9,I)=D*K(4,I)*T0/T(9,I)
03230 LET T(9,I)=T(9,I)+U1*H(9,I)*(F(9,I)-T(9,I))
03240 LET T(8,I)=T(7,I)*B+T(9,I)*C
03250 LET T(10,I)=T(9,I)+Q(I)/K(6,I)
03260 GO TO 3450
03270 LET Y8=Y7-K(3,I)*(T(9,I)-K(15,I))/(M(3,I)*(E(7,I)-K(17,I)))
03280 IF Y8<0 THEN 3300
03290 GO TO 3410
03300 LET Z1=M(3,I)*(E(7,I)-K(17,I))*Y7/(K(3,I)*(T(9,I)-K(15,I)))
03310 LET A=K(3,I)*(1-Z1)/(M(3,I)*K(5,I))
03320 LET B=EXP(-A)
03330 LET C=M(3,I)*K(5,I)*(T(9,I)-K(15,I))*(1-B)
03340 LET X=K(4,I)*(K(6,I)*(T(10,I)-T(9,I)))
03350 LET D=X-K(4,I)*(K(3,I)*Z1*(T(9,I)-K(15,I))+C)
03360 LET T(9,I)=T(9,I)+D*U1*T0/T(9,I)
03370 LET T(8,I)=T(9,I)-(T(9,I)-K(15,I))*B
03380 LET Q(I)=K(6,I)*(T(10,I)-T(9,I))
03390 LET Y8=0
03400 GO TO 3450
03410 LET A=K(4,I)*(K(6,I)*(T(10,I)-T(9,I))-K(3,I)*(T(9,I)-K(15,I)))
03420 LET T(9,I)=T(9,I)+A*U1*T0/T(9,I)
03430 LET T(8,I)=K(15,I)
03440 LET Q(I)=K(6,I)*(T(10,I)-T(9,I))
03450 NEXT I
03460 RETURN
03470 REM TURBO-ALTERNATOR SUBROUTINE
03480 FOR I=1 TO N3
03490 LET M(4,I)=K(8,I)/SQRT(T(11,I))
03500 LET W(0,I)=K(9,I)*SQRT(T(11,I))
03510 LET L(1,I)=L(0,I)*(1-W(1,I)/W(0,I))
03520 IF U<100 THEN 3550
03530 LET W(1,I)=W(0,I)*L(0,I)/(K(10,I)*W(0,I)+L(0,I))
03540 GO TO 3580
03550 LET L(2,I)=K(10,I)*W(1,I)
03560 LET L(3,I)=K(12,I)*(L(1,I)-L(2,I))
03570 LET W(1,I)=W(1,I)+U1*L(3,I)
03580 LET P(I)=L(1,I)*W(1,I)
03590 LET T(12,I)=T(11,I)-K(11,I)*P(I)/M(4,I)
03600 NEXT I
03610 RETURN
03620 REM J-T VALVE SUBROUTINE
03630 IF T(13,I)>6.25 THEN 3660
03640 LET M(5,I)=K(18,I)/SQRT(T(13,I))
03650 GO TO 3710
03660 IF T(13,I)<K(13,I) THEN 3700
03670 IF M(5,I)<K(14,I) THEN 3700
03680 LET M(5,I)=K(14,I)
03690 GO TO 3710
03700 LET M(5,I)=K(14,I)/2
03710 LET I=1

```

Figure 113. Complete Listing of ARPA1 Program (Continued)

```

03720 LET J=13
03730 LET Z=2
03740 GOSUB 4320
03750 IF F(13,1)>K(15,1) THEN 3860
03760 LET T(15,1)=K(15,1)
03770 LET I=1
03780 LET J=15
03790 LET Z=2
03800 GOSUB 4250
03810 LET Y0=(E(15,1)-E(13,1))/(E(15,1)-K(17,1))
03820 IF Y0>1 THEN 3840
03830 GO TO 3890
03840 LET Y0=1
03850 GO TO 3890
03860 LET T(15,1)=F(13,1)
03870 LET E(15,1)=E(13,1)
03880 LET Y0=0
03890 RETURN
03900 REM LIQUID ACCUMULATOR SUBROUTINE
03910 LET I=1
03920 LET J=18
03930 LET Z=2
03940 GOSUB 4250
03950 IF Y1>0 THEN 4080
03960 IF M(8,1)>0 THEN 4010
03970 LET T(14,1)=T(18,1)
03980 LET E(14,1)=E(18,1)
03990 LET Y=0
04000 GO TO 4140
04010 LET T(14,1)=K(15,1)
04020 LET I=1
04030 LET J=14
04040 LET Z=2
04050 GOSUB 4250
04060 LET Y=(E(18,1)-E(14,1))/(K(17,1)-E(14,1))
04070 GO TO 4140
04080 LET T(14,1)=K(15,1)
04090 LET I=1
04100 LET J=14
04110 LET Z=2
04120 GOSUB 4250
04130 LET Y=Y1
04140 LET M(7,1)=Y*M(9,1)
04150 LET M(6,1)=M(9,1)-M(7,1)
04160 LET M(8,1)=M(8,1)+M(7,1)*U1
04170 IF M(8,1)<0 THEN 4190
04180 GO TO 4240
04190 LET T(14,1)=T(18,1)
04200 LET E(14,1)=E(18,1)
04210 LET M(6,1)=M(9,1)
04220 LET M(7,1)=0
04230 LET M(8,1)=0
04240 RETURN

```

Figure 113. Complete Listing of ARPA1 Program (Continued)

```

04250 REM TEMP T0 ENTHALPY SUBROUTINE
04260 IF T(J,I)<C(5,Z) THEN 4300
04270 LET V=((C(4,Z)/C(3,Z))+2)*((T(J,I)-C(1,Z))+2)-C(4,Z)+2
04280 LET E(J,I)=C(2,Z)+C(8,Z)+SQR(V)
04290 GO TO 4310
04300 LET E(J,I)=C(7,Z)*(T(J,I)-C(6,Z))
04310 RETURN
04320 REM ENTHALPY T0 TEMP SUBROUTINE
04330 IF E(J,I)<C(7,Z)*(C(5,Z)-C(6,Z)) THEN 4380
04340 LET E3=E(J,I)-C(8,Z)
04350 LET V=C(3,Z)+2+((E3-C(2,Z))+2)/((C(4,Z)/C(3,Z))+2)
04360 LET F(J,I)=C(1,Z)+SQR(V)
04370 GO TO 4390
04380 LET F(J,I)=C(6,Z)+E(J,I)/C(7,Z)
04390 RETURN
04400 REM MISCELLANEOUS TIME FUNCTION SUBROUTINE
04410 LET U=U+U1
04420 LET I1=I1+1
04430 LET T(1,5)=T0+13*(1-EXP(-U/60))
04440 IF T(1,1)>15 THEN 4470
04450 LET U1=2
04460 GO TO 4600
04470 IF T(1,1)>60 THEN 4500
04480 LET U1=10
04490 GO TO 4600
04500 IF T(1,1)>120 THEN 4530
04510 LET U1=20
04520 GO TO 4600
04530 IF U<100 THEN 4560
04540 LET U1=100
04550 GO TO 4600
04560 IF U<10 THEN 4590
04570 LET U1=10
04580 GO TO 4600
04590 LET U1=1
04600 RETURN
04610 REM INTERCONNECTION SUBROUTINE
04620 REM MASS FLOW RELATIONS
04630 LET M(1,1)=M(5,1)
04640 LET M(1,2)=M(5,1)
04650 LET M(1,3)=M(5,1)+M(4,1)
04660 LET M(1,4)=M(5,1)+M(4,1)
04670 LET M(1,5)=M(5,1)+M(4,1)+M(4,2)
04680 LET M(2,1)=M(6,1)
04690 LET M(2,2)=M(6,1)+M(4,1)
04700 LET M(2,3)=M(6,1)+M(4,1)
04710 LET M(2,4)=M(6,1)+M(4,1)+M(4,2)
04720 LET M(2,5)=M(6,1)+M(4,1)+M(4,2)
04730 LET M(3,1)=M(5,1)
04740 LET M(3,2)=M(4,1)
04750 LET M(3,3)=M(4,2)
04760 LET M(9,1)=M(5,1)
04770 REM TEMPERATURE RELATIONS

```

Figure 113. Complete Listing of ARPA1 Program (Continued)

```

04780 LET T(1,1)=T(2,2)
04790 LET T(1,2)=T(2,3)
04800 LET T(1,3)=T(2,4)
04810 LET T(1,4)=T(2,5)
04820 LET T(3,1)=T(4,1)
04830 LET T(3,2)=(M(2,1)*T(4,1)+M(4,1)*T(12,1))/(M(2,1)+M(4,1))
04840 LET T(3,3)=T(4,2)
04850 LET T(3,4)=(M(2,3)*T(4,3)+M(4,2)*T(12,2))/(M(2,3)+M(4,2))
04860 LET T(3,5)=T(4,4)
04870 LET T(7,1)=T(15,1)
04880 LET T(7,2)=T(2,3)
04890 LET T(7,3)=T(2,5)
04900 LET T(11,1)=T(8,2)
04910 LET T(11,2)=T(8,3)
04920 LET T(13,1)=T(2,1)
04930 LET T(18,1)=T(8,1)
04940 REM ENTHALPY RELATIONS
04950 LET E(13,1)=E(2,1)
04960 LET E(18,1)=E(8,1)
04970 REM LIQUID FRACTION RELATIONS
04980 LET Y7=Y0
04990 LET Y1=Y8
05000 RETURN
05010 DIM K(20,10)
05020 DIM T(20,10)
05030 DIM E(20,10)
05040 DIM F(20,10)
05050 DIM H(20,10)
05060 REM NUMBER OF H-E,T-L,T-A,J-T/LI9
05070 DATA 5,3,2,1
05080 REM AMBIENT TEMP, TIME STEP
05090 DATA 323,1
05100 REM N5=1 FOR HEADINGS, =0 FOR DATA ONLY
05110 DATA 1
05120 REM K1,K2 FOR EACH HEAT EXCHANGER
05130 DATA 46.5251,.00166371
05140 DATA 15.9946,.00589669
05150 DATA 560.522,.00186335
05160 DATA 64.8278,.000158718
05170 DATA 1160.98,.0000757461
05180 REM K3,K4,K5,K6,K7 FOR EACH THERMAL LOAD
05190 DATA 50.5,.00000952672,5.19,.0132283,1
05200 DATA 20.9395,.000549081,5.19,.0162449,1
05210 DATA 53.5899,.00000374264,5.19,.440665,1
05220 REM K8,K9,K10,K11,K12 FOR EACH TURBO-ALTERNATOR
05230 DATA 34.4306,25.6356,0.0554947,.192789,.900987
05240 DATA 74.2374,12.1989,.218396,.190937,.228942
05250 REM K13,K14,K15,K16,K17,K18 FOR J-T VALVE/LIQUEFIER
05260 DATA 50,7.1,4.4,0,10.96,8.8494
05270 REM C1,C2,C3,C4,C5,C6,C7,C8 FOR EACH T-H FUNCTION
05280 DATA .8,4227,21.5304,5.22598,27.1228,6.1,5.49738,40.5405,0
05290 DATA 2.0853,18.9017,2.18996,11.3746,4.3,3.5202,35.6099,7.1523
05300 END

```

Figure 113. Complete Listing of ARPA1 Program (Continued)

```

00540 PRINT "K13="K(13,1),"K14="K(14,1),"K15="K(15,1)
00550 PRINT "K16="K(16,1),"K17="K(17,1),"K18="K(18,1)
00560 PRINT
00570 FOR Z=1 TO 2
00580 READ C(1,Z),C(2,Z),C(3,Z),C(4,Z),C(5,Z),C(6,Z),C(7,Z),C(8,Z)
00590 NEXT Z
00600 REM INITIAL CONDITIONS
00610 REM PRINT CONTROL
00620 LET I1=120
00630 REM INITIAL TIME
00640 LET U=314710
00650 REM H-E TEMP
00660 LET T(1,5)=335
00670 LET T(2,1)=6.25855
00680 LET T(2,2)=13.8483
00690 LET T(2,3)=16.9121
00700 LET T(2,4)=108.541
00710 LET T(2,5)=125.214
00720 LET T(4,1)=13.5984
00730 LET T(4,2)=14.6882
00740 LET T(4,3)=106.913
00750 LET T(4,4)=119.162
00760 LET T(4,5)=331.757
00770 LET T(5,1)=13.7234
00780 LET T(5,2)=15.8002
00790 LET T(5,3)=107.727
00800 LET T(5,4)=122.188
00810 LET T(5,5)=333.378
00820 LET T(6,1)=5.33866
00830 LET T(6,2)=13.7858
00840 LET T(6,3)=15.8002
00850 LET T(6,4)=107.500
00860 LET T(6,5)=122.188
00870 REM ADDITIONAL H-E IC
00880 REM ADDITIONAL H-E IC
00890 REM T-L TEMP & Q
00900 LET T(8,1)=4.41793
00910 LET T(8,2)=17.0205
00920 LET T(8,3)=129.490
00930 LET T(9,1)=4.49430
00940 LET T(9,2)=17.2073
00950 LET T(9,3)=130.597
00960 LET T(10,1)=322
00970 LET T(10,2)=322
00980 LET T(10,3)=322
00990 LET Q(1)=4.20006
01000 LET Q(2)=4.95133
01010 LET Q(3)=84.3446
01020 REM ADDITIONAL T-L IC
01030 REM ADDITIONAL T-L IC
01040 REM ADDITIONAL T-L IC
01050 REM ADDITIONAL T-L IC
01060 REM ADDITIONAL T-L IC

```

Figure 114. Partial Listing of ARPA2 Program

```

01070 REM T-A TEMP,SPEED,POWER,TORQUE,MASS FLOW
01080 LET T(12,1)=13.7763
01090 LET T(12,2)=105.635
01100 LET W(1,1)=50.3060
01110 LET W(1,2)=61.0917
01120 LET P(1)=140.440
01130 LET P(2)=815.096
01140 REM ADDITIONAL T-A IC
01150 LET L(0,1)=5.32416
01160 LET L(0,2)=23.8292
01170 LET M(4,1)=8.34560
01180 LET M(4,2)=6.52385
01190 REM ADDITIONAL T-A IC
01200 REM ADDITIONAL T-A IC
01210 REM J-T/LIQ TEMP,ENTHALPY,MASS FLOW
01220 LET T(14,1)=4.41877
01230 LET T(15,1)=4.34172
01240 LET M(5,1)=3.55
01250 LET M(6,1)=3.55
01260 LET M(7,1)=0
01270 LET M(8,1)=0
01280 LET E(2,1)=28.8775
01290 LET E(8,1)=30.2261
01300 LET Y0=0
01310 LET Y8=0
01320 REM ADDITIONAL J-T/LIQ IC
01330 REM ADDITIONAL J-T/LIQ IC
01340 REM CHECK FOR CONSISTENT INTERCONNECTIONS
01350 GOSUB 4610
01360 FOR J=1 TO 2
01370 FOR I=1 TO N1
01380 LET N(J,I)=M(J,I)
01390 NEXT I
01400 NEXT J
01410 REM SPECIFY RUN TYPE
01420 IF N5=0 THEN 1780
01430 PRINT "COOLDOWN FROM AMBIENT TEMPERATURE"
01440 PRINT "CONSTANT PRESSURE 3.8/1.18 ATM"
01450 IF N4=0 THEN 1500
01460 PRINT "WITH LIQUEFIER"
01470 PRINT "CONTROLLED J-T VALVE--M=7.10 FOR TEMP ABOVE 50"
01480 PRINT "                                --M=3.55 FOR 50 TO 6.25"
01490 PRINT "                                --NO CONTROL BELOW 6.25"
01500 PRINT
01510 PRINT
01520 PRINT
01530 PRINT
01540 PRINT
01550 PRINT
01560 PRINT "TIME--SECONDS"
01570 PRINT "T=TEMPERATURE--DEG K"
01580 PRINT "Q=HEAT FLOW--WATTS"
01590 PRINT "M=MASS FLOW--GRAMS/SEC"

```

Figure 114. Partial Listing of ARPA2 Program (Continued)

Section 4

POWER CONDITIONER FOR COMPRESSOR MOTORS

Each of the three cryogenic refrigeration systems considered in this study will require about 40 kilowatts at roughly 850 hertz and a power factor of 0.8. Shipboard auxiliary power is 60 hertz, so an interfacing power conditioner must produce 850 hertz for the compressor drive motors.

A practical choice of power conditioners is limited to two types: solid-state and dynamic. The strong points and weaknesses of each type of power conditioner are discussed below in a subjective manner, based largely on experience because no new investigation was conducted under this contract. A simplified approach would be to compare only cost and reliability factors. However, the implied assumption that one would be a direct replacement for the other is invalid; therefore, additional characteristics of potential importance are enumerated and briefly discussed in the following paragraphs.

Motor and generator technology of the type applicable to power conditioners is broad, having matured many years ago; even so, the technology by no means is stagnant. Solid-state technology is of recent origin. Changes and improvements are being vigorously pursued; progress is therefore current.

The attributes of solid-state technology center mainly on the ease of control and the absence of rotating parts, thereby implying no wearout mode. Starting, accelerating, and maintaining a motor speed or speed profile can be accomplished with ease, using integrated circuit control. Compressor speed is controlled simply by changing the frequency. The frequency may be made a function of a feedback error signal between a speed signal and a reference. Except for some transformer noise, there is very little acoustic noise. The inverter should weigh half as much as a motor-generator set, but would probably occupy the same floor space and volume.

Either type of power conditioner may be cooled with forced air and/or water. The solid-state type of conditioner will employ auxiliary fans and filters; therefore, some maintenance will be required. The same is true for bearing lubrication of the motor-generator set.

Acceleration of the compressors to operating speed may be of small consequence, because it will probably be accomplished at dockside, where ample power is available. If the compressors were restarted at sea, they could be a strain on the soft shipboard power system.

A dynamic power conditioner would probably have a two-winding drive motor. One winding would be for half-speed operation; the other winding would be for the rated speed. A reduced voltage acceleration would permit the compressor motors to track the generator frequency, enabling the whole

system to come up to speed together. A low-voltage start would be less demanding of the soft shipboard power system.

The more sophisticated solid-state power conditioner would bring the compressor motors up to speed with little or no noticeable effect on the power system. Frequency and slip are precisely controlled over the speed range, which is the inherent advantage of the solid-state system. At dockside, where plenty of power is available, this feature would be of less significance.

The inverter in a solid-state system would need adjustable direct current for acceleration and fixed direct current for steady-state operation. Rectifiers are notorious for creating difficulties with the power source, unless very complicated circuits (with many phases) are employed. The output waveshape of an inverter is typically full of time harmonics. These harmonics can be reduced best, in this case, with harmonic transformers and nonresonant filters. On the other hand, a motor-generator set is ideal for power conversion, because it automatically produces a sine wave output.

Reliability can be improved, for either type of power conditioner, to acceptable levels with suitable redundancy. In general, the dynamic type is significantly more reliable than the solid-state type. Considerably more expense in the way of quality control, burn-in, and testing is required for the solid-state type, to make their reliabilities comparable.

The dynamic power conditioner will operate longer without failure, will require less time to repair, will cost much less to repair, will require fewer spare parts to inventory, will use simpler robust tools, and will require repair crews with less training.

The solid-state power conditioner is more susceptible to shock and vibration and explosions under battle conditions than is the stronger motor-generator set. The solid-state type is more vulnerable to line transients and in its simpler versions passes on line voltage sag to the load motor.

Shortcomings of either type of power conditioner can be overcome at additional expense. The solid-state conditioner has further to go, so dynamic power conditioning appears to be the most cost effective method. However, this conclusion should not be made the only basis for selection; other criteria must be considered. Other pertinent features and characteristics are summarized in Table 13.

No documentary evidence is submitted to justify the individual items listed in Table 13. Instead, this summary merely reflects the experience of the author. Some of the assertions are contrary to popular belief and therefore will be debatable until resolved by considerable work.

Table 13
COMPARISON OF POWER CONDITIONER FEATURES
OR CHARACTERISTICS

Feature or Characteristic	Solid State	Dynamic
Technology base	Medium, recent, expanding	Broad, mature
Relative recurring cost	2	1
Relative development cost	3	1
Redundancy cost	Expensive	Inexpensive
Relative volume and space	1	1
Relative weight	1	2
Efficiency (percent)	≈85	≈85
Relative maintenance	1, (filters and fans)	2, (bearings and brushes)
Acoustic Noise	Little	Some
RF noise	Much	Little
Cooling	Air or water	Air or water
Speed (and frequency) control	Inherent	Added control
Compressor acceleration	No line surge (simultaneous start possible)	Some surge, reduced voltage (sequential start)
Effect on source	Degrades by chopping	None
Effect on motor load	Time harmonic losses	None
Shock and vibration tolerance	Expensively packaged	Inherent
Reliability		
Mean time between failures	Shorter	Longer
Relative mean time to repair	3	1
Availability	Less	Greater
Relative cost to repair	5	1
Inventory of spare parts	Many	Few
Wear-out mode	Abusive frequent repairs	Insulation age
Repair tools and instruments	Complex, costly, many are fragile	Simple, robust, few
Repair crew training	Long and expensive (experts only)	Short and simple (mechanics)
Emergency repair possibility	Improbable	Every service shop
Fault-produced toxic fumes	Potting compounds	Motor insulation
Susceptibility to line voltage transients	High	Low
Isolation from power source	Low	Very high

CR-4444

Section 5

LIQUID METAL CURRENT COLLECTOR TECHNOLOGY

PURPOSE

The purpose of these investigations in the area of liquid metal current collector technology is to identify potential problems pertaining to the use of liquid metals other than NaK for superconductive power applications. During the studies reported in the first semiannual technical report, it was concluded that only gallium (or gallium-indium) of the many potential metals and alloys considered offered any promise of providing a better solution to the problems of liquid metal current collection than that obtained using NaK as the liquid metal.

The advantages of gallium over NaK are confined primarily to the lower speeds of operation typical of motors (as contrasted to generators) in which I^2R losses or inefficiencies resulting from electromagnetically driven motion of the liquid metal are predominant over those resulting from centrifugal and viscous shearing forces in the liquid metal generated by high speeds. These functional advantages are of course independent of the problem areas involving material compatibilities.

Gallium has no significant chemical reaction with water, as does NaK. It is also nontoxic and thus is preferable to mercury. It does have chemical (amalgamation) reactions with many metals (e. g., iron, copper, and their alloys) that are satisfactory with NaK and that are electrically, magnetically, and structurally advantageous in the design of electrical machinery.

Therefore, much of the effort during this reporting period was devoted to the design and material and process selection and application in the preparation of test specimen equipment for use with gallium during the testing activities of Phase III.

GALLIUM COLLECTOR TESTS

The use of gallium as a collector fluid in place of NaK in a semiflooded system has the advantage of offering an inherent safety factor in the event of an accident. Due to the higher density and viscosity of gallium, one's first impression is that higher collector losses would occur. It can be shown, however, that in low-speed applications such as those typical of ship propulsion motors, the use of gallium results in lower viscous losses.

In Reference 5 (Equation 28), the average viscous loss in a radial collector gap is shown to be:

$$P_{av} = \frac{f\rho V_o^3}{8} [1 + 3\delta^2], \delta < 1 \quad (89)$$

$$P_{av} = \frac{f\rho V_o^3}{8} [2(1 + \delta)\sqrt{2\delta - 1}], \delta > 1 \quad (90)$$

where δ is a dimensionless ratio relating the electromagnetic forces acting on the fluid to the viscous forces, specifically:

$$\delta = \frac{2JBd}{f\rho V_o^2}$$

f = Fanning friction factor

V_o = Collector peripheral velocity

ρ = Collector fluid density

J = Current density in collector gap

B = Magnetic flux density

d = Collector radial gap

The effect of fluid properties on the loss is not immediately evident from the above loss expressions. For various machines considered earlier in the study, it has been found that the typical values of δ are well above 1.0 for motors and well below 1.0 for generators, when NaK is assumed as a collector fluid. It is therefore instructive to simplify Equations 89 and 90, assuming extreme values of the dimensionless ratio, δ :

$$P_{av} = \frac{f\rho V_o^3}{8}, \delta \ll 1 \quad (91)$$

$$P_{av} = \frac{(JBd)^{3/2}}{(f\rho)^{1/2}}, \delta \gg 1 \quad (92)$$

It is seen from the above equations that for low-speed machines ($\delta \gg 1$), the collector loss varies inversely with the fluid density, and thus the use of gallium can improve the efficiency. This is due to the fact that in this condition, the fluid velocity is much higher than the collector peripheral velocity, and it becomes the governing factor in the viscous loss. Increased density lowers this fluid velocity and hence lowers the losses. To give a concrete example, consider the propulsion motor presented in Table 43 of Reference 6, where:

- Power = 40,000 hp
- Inner collector radius = 12.13 inches
- Outer collector radius = 18.53 inches
- Magnetic flux density = 5.0 webers per square meter
- Design current = 150,000 amperes
- Speed = 200 rpm

At the inner and outer collectors, the dimensionless ratio, δ , has the following values when the collector fluid is NaK (density = 0.85×10^3 kilograms per cubic meter):

$$\delta_i = 22.9$$

$$\delta_o = 18.2$$

Assuming a radial clearance of 0.050 inch in both collectors, the inner and outer Reynolds numbers with NaK ($\mu = 4.7 \times 10^{-4}$ kilograms per millisecond) are:

$$(Re)_i = 29,600; \text{ therefore, } f_i = 0.0086$$

$$(Re)_o = 45,200; \text{ therefore, } f_o = 0.0035$$

where friction factors are obtained from Figure 8 of Reference 7.

If in this machine the NaK is replaced by gallium ($\rho = 6.0 \times 10^3$ kilograms per cubic meter, $\mu = 15 \times 10^{-4}$ kilograms per millisecond), the above parameters change to:

$$(Re)_i' = 65,400$$

$$(Re)_o' = 100,000$$

$$f_i' = 0.0084$$

$$f_o' = 0.0083$$

$$\delta_i' = 3.32$$

$$\delta_o' = 2.64$$

The ratio of NaK collector loss to gallium collector loss can be obtained from Equation 90:

$$\frac{\text{Gallium loss}}{\text{NaK loss}} = \frac{f_o' (1 + \delta') \sqrt{2\delta' - 1}}{f_o (1 + \delta) \sqrt{2\delta - 1}}$$

For the inner and outer collectors, these ratios become:

$$\left(\frac{\text{Gallium loss}}{\text{NaK loss}} \right)_i = 0.44$$

$$\left(\frac{\text{Gallium loss}}{\text{NaK loss}} \right)_o = 0.45$$

Thus, for this illustrative case, the collector losses can be halved by the substitution of gallium for NaK. Another advantage of gallium over NaK is its much greater compatibility with organic sealing and insulating materials.

The use of gallium in a dynamic current collection system has, however, acquired a very poor reputation, due to a phenomenon sometimes called "pasting." It has been found that liquid gallium, when exposed to air and agitated in a manner typical to that of a current collection system, in a period of time measured in minutes undergoes a thickening into a paste. Although this phenomenon defied rational explanation for some time, more recent experience has led to the conclusion that the paste formed is composed of microscopic spherules of liquid metal with an extremely thin skin of gallium oxide. The solution to the problem has been to protect the gallium from oxidation by the use of an inert cover gas having very low oxygen and water vapor content. Practical gallium collectors have been experimentally operated continuously for more than 500 hours, with no significant degradation of the liquid. It is felt that pasting can be postponed indefinitely in such a system with the addition of a bypass gallium purification loop consisting of either a filter or an electrolytic purifier.

Other distinct disadvantages, however, also result from the physical properties of gallium. The greater density of gallium causes an increase in liquid metal pressure generation in a flooded disk machine by a factor of seven over NaK. This increase may preclude the use of an uncirculated flooded collection system on a propulsion motor, as the resulting pressures may be impractically high from the standpoints of both sealing and rotor thrust and may dictate the necessity of fluid circulation or of unflooded collectors. Another shortcoming of gallium is its indicated incompatibility with metals having good electrical conductivities, such as aluminum, and its alloys, at room temperature and with copper and carbon steels at temperatures over 100°C.

Figure 115 shows the cross section of a collector device that has been fabricated to determine the problems in the design and operation of an inflooded gallium system. As the electromagnetic forces acting on the liquid of such a system, as applied to a marine propulsion motor, equal or exceed the dynamic forces, such a test device must include the current flow and the magnetic field. The present device is designed to duplicate conditions found in the collector region of a disk-type motor (the collector current being radial and the magnetic field axial). The magnetic field is obtained by placing the collector rig in the bore of an existing superconducting solenoid having a maximum central field flux density capability of 5.7 webers per square meter. This solenoid is fully described in Reference 5. The overall diameter of the test rig is thus restrained to a diameter of 8 inches, in order to fit the bore of the solenoid dewar.

The test rig consists of two collector sets of large and small diameter. The inner collectors (disks) are electrically connected at the hub to provide a continuous electrical circuit from the large diameter outer collector, through the paired inner collectors, to the small diameter outer collector. The two outer collector circuits are available to outside circuit connections through two concentric annular conductors that also form the outer housing of the test machine. Due to the difference in disk diameters, a net voltage will be generated, and current can be circulated through an external load resistor.

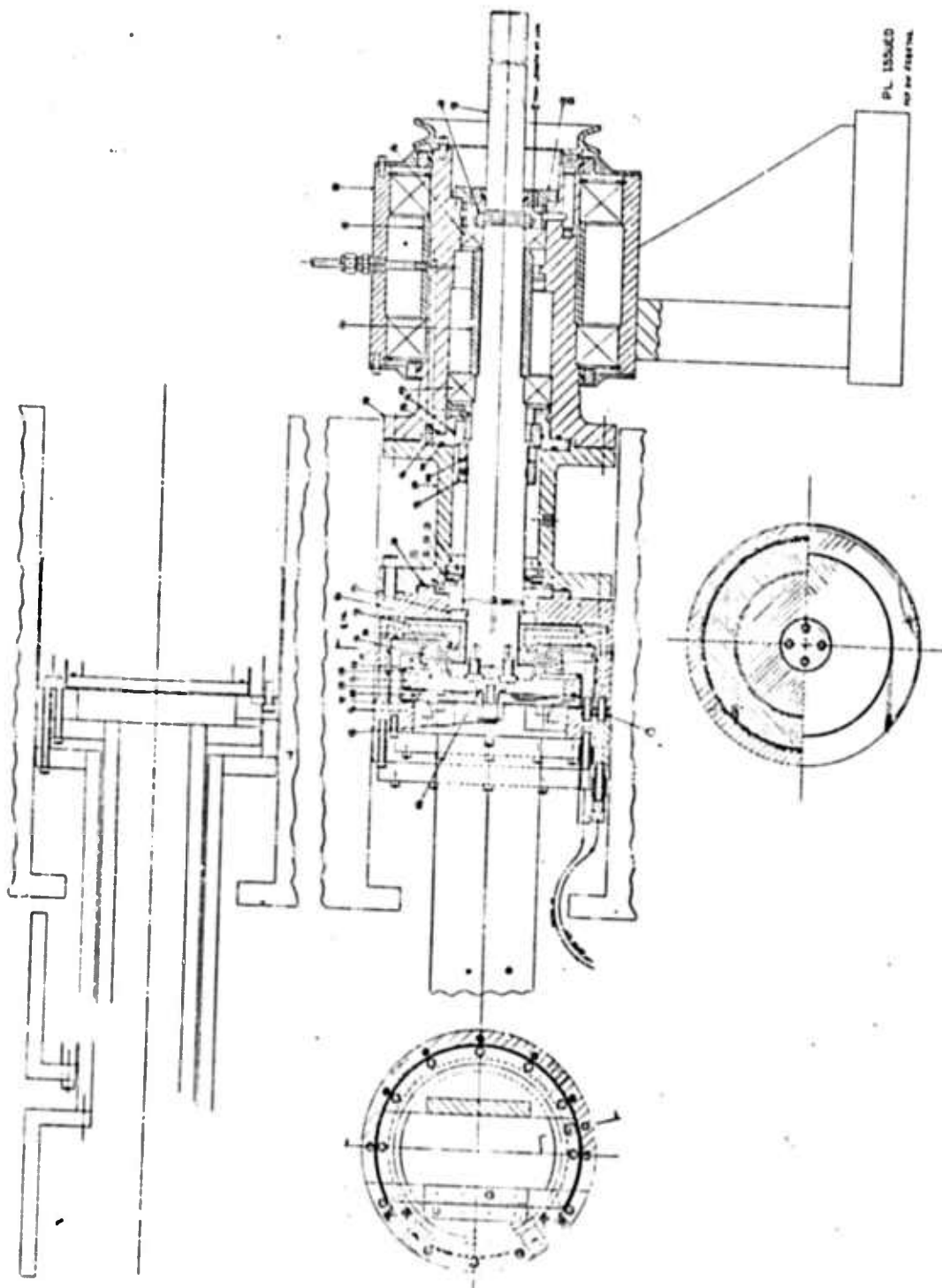


Figure :15. Semiflooded Collector Test Rig

A variable speed motor is the power source. Input torque and speed and electrical power output can be measured. An external current supply will be used to conduct motoring tests, particularly at the locked rotor condition at which time the liquid metal initially rests in a pool at the bottom of each collector. Visual observations can be made through the glass window at the undriven end and the transparent wall of the small diameter collector cup. The normal test mode will be with the outer housing stationary, but the rig can also be short-circuited or open-circuited in the contrarotating mode, the outer housing being driven by a V-belt. The baseplate can be tilted up to 30 degrees about the pitch axis, to simulate shipboard use. Pertinent specifications of the collector test rig are listed in Table 14.

Table 14
SPECIFICATIONS OF CURRENT COLLECTOR TEST RIG

Specification	Parameter
Speed	
Single rotation	0-4000 rpm
Contrarotating	0-1000 rpm
Drive motor	25 hp
Current	
Self-generating	10,000 amperes
External source	2,000 amperes
Generated voltage (3.0 watts per square meter, 2000 rpm)	0.68 volt
Central magnetic field (maximum)	5.7 watts per square meter
Collector diameter	
Inner	4.75 inches
Outer	6.00 inches
Maximum tilt angle (pitch axis)	30 degrees

The problem of material compatibility between the gallium and the test rig structure was first approached with the idea of a plated barrier of gallium resistant metal that would be applied thickly enough to resist penetration with normal care in handling. Electroless nickel plating (e.g., the Kanogen process) appeared to have the best potential, from several standpoints. Available data indicate that nickel was compatible with gallium. The electroless plating

process is capable of depositing heavy adherent coatings on a wide variety of metals, including iron, copper, and aluminum. Whereas electrolytic plating has difficulty with deposit thickness control on both sharp external corners and in cavities, the electroless process can deposit a uniform plating on either extreme. Durability of the resultant plating has been proven by many years of service as a corrosion barrier applied to the inside of steel railroad tank cars.

Plated samples of low-carbon steel, OFHC copper, and 6061 aluminum alloy were prepared and submerged in gallium. No attack was evident at room temperature, but after two weeks at 100°C, small crystalline growths were visible on the plated surfaces, indicating that an attack was taking place. Qualitative analysis indicated the crystals to be a gallium-nickel combination. No further investigation of plating was made, and the decision was made to construct the internal metal surfaces of the test rig of AISI-304 stainless steel, either solid, or as a cladding over copper in the current carrying parts.

Examination of Figure 115 will show that the two inner collector disks have cores of OFHC copper that limit the length of the current path in the stainless steel cladding to small distances. Similar copper inserts are visible in the outer collectors. A series of axial copper bars are placed in the axial portions of the outer collectors to conduct the load current to the terminal points. With this design approach, the total I^2R losses in the solid members were held to a calculated 350 watts for each collector at a load current of 10,000 amperes. This level is acceptable in view of the calculated losses of approximately 850 watts within the liquid-filled gap. These losses are removed by directing cooling with water on the outer collector copper inserts.

The copper inserts must be fully bonded to the stainless steel cladding, at least in the areas across which the load current passes. The initial concept was to cast the copper directly into cavities in the stainless steel. Test specimens were prepared by inserting machined slugs of OFHC copper into matching cavities in 304 stainless steel blocks, duplicating some of the governing dimensions in the outer collector piece. It was found that gross shrinkage cavities formed during solidification of the copper, to the extent that the results were not acceptable.

To preclude the possibility that the voids were caused by dissolved gases in the copper, picked up in the hydrogen furnace, new samples were melted in a vacuum furnace. Voids of substantially the same size and distribution were found when sectioning the pieces. Fusion of the copper was therefore not attempted on the actual piece; instead, the copper slugs were bonded to the stainless steel by brazing with Nicro alloy (Au 18Ni) in a hydrogen furnace. This particular braze alloy was chosen because its extremely good wetting qualities gave the best assurance of success on this one-of-a-kind assembly. After the copper slugs were brazed in place, the composite pieces were machined and fitted with stainless steel cover plates to complete the encasement of the copper. These covers were then electron-beam-welded to the steel cladding. No

bond was necessary between the copper and the cover plates, because these were not required to conduct either electrically or thermally.

Figure 116 is a view of the partially assembled test rig without the outer collectors. The two disks on the left are the copper/stainless steel composite inner collector disks (Parts 16 and 17 of Figure 115). The semifinished outer collectors (Parts 22 and 23 of Figure 115) are shown in Figure 117.

Austenitic stainless steel is not readily wetted by gallium, and if wetting is not achieved, high surface resistances will result; however, it has been found that a very tenacious coating of gallium can be achieved by electroplating. The plated gallium has been proven to maintain excellent electrical contact under operating conditions, without causing any apparent attack of the liquid on the underlying stainless steel substrate. Gallium will therefore be electroplated onto the conducting surfaces of the collectors, including the facing surfaces on the hubs of the two inner collector disks.

Surfaces requiring electrical insulation will be coated with flame-sprayed alumina. After impregnation with epoxy resin and surface grinding, an insulating surface results that has good insulating properties, is relatively durable (from the mechanical standpoint), and is smooth enough to form a hermetic seal against an O-ring. The smaller of the two outer collector rings in Figure 117 shows the flame-sprayed coating on its outside surface as applied, but before impregnating and grinding.

The gallium in the test rig will be protected from contact with oxygen and water vapor by minimizing the gas leakage through the enclosure walls and by supplying the interior with a slightly pressurized neutral cover gas of high purity. All static joints in the outer housing will be sealed with Viton O-rings, chosen to minimize the diffusion of atmospheric oxygen and water vapor. The dynamic seal where the shaft penetrates the housing is a carbon face seal operating against a titanium carbide ring. The floating face is sealed to the cartridge body with a metal bellows. Cooling and lubrication of the seal is furnished by an oil mist directed against the outside of the seal. The oil mist system also lubricates the bearings.

A carbon ring clearance seal is placed around the shaft between the current collector region and the carbon face seal. A constant purge flow of the neutral cover gas will be bled from the current collector region, past this clearance seal, into the region containing the face seal, and thence out through a restriction to the atmosphere. This purge bleed flow will have a relatively high velocity through the clearance of the ring seal and thus will minimize the diffusion of leakage and contaminants from the face seal into the gallium collector region.

The cover gas is nitrogen and is supplied to the collector region through a port in the observation window. The gas source is liquid nitrogen boil-off or high-purity cylinder gas, each having impurity levels of approximately

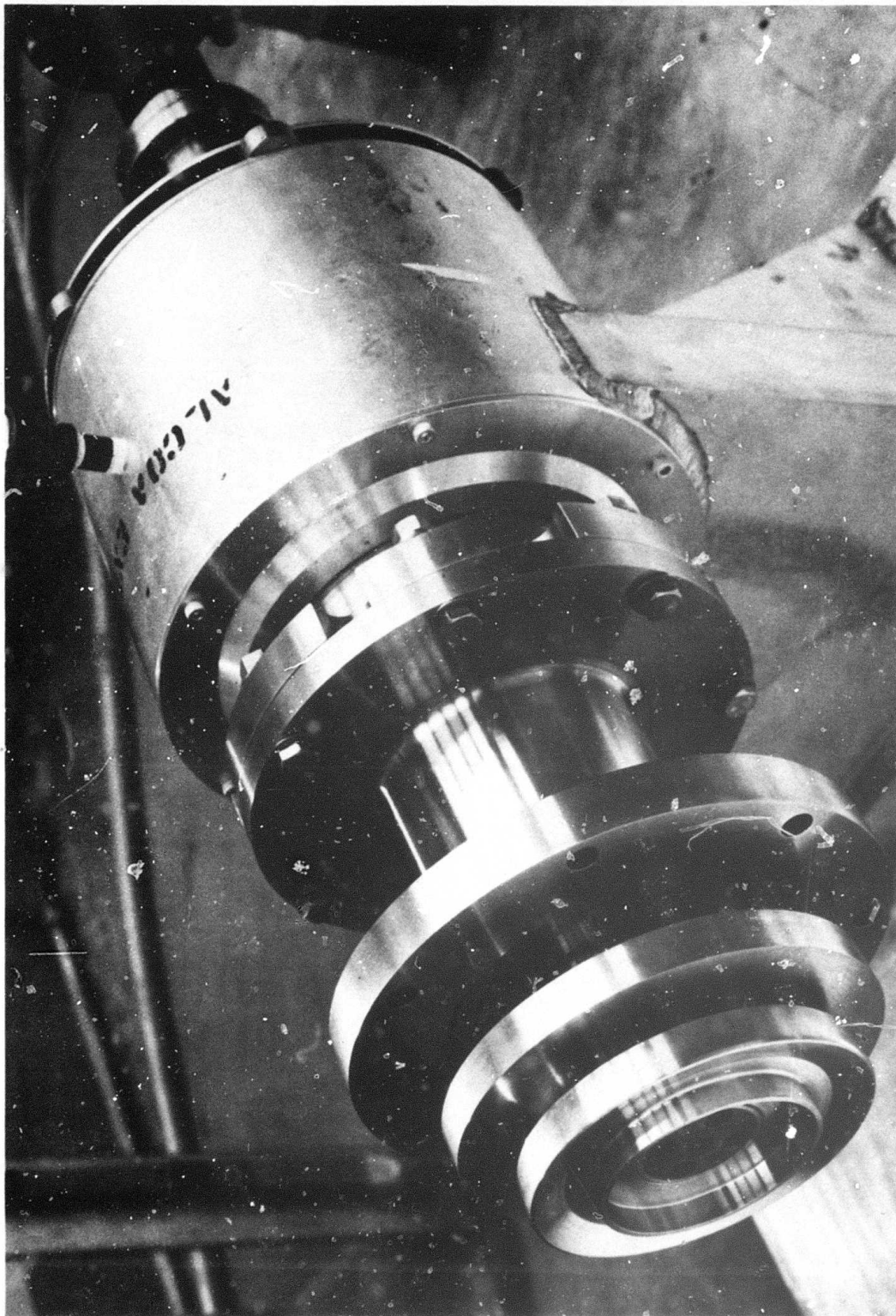


Figure 116. Partially Assembled Test Rig Without Outer Collectors

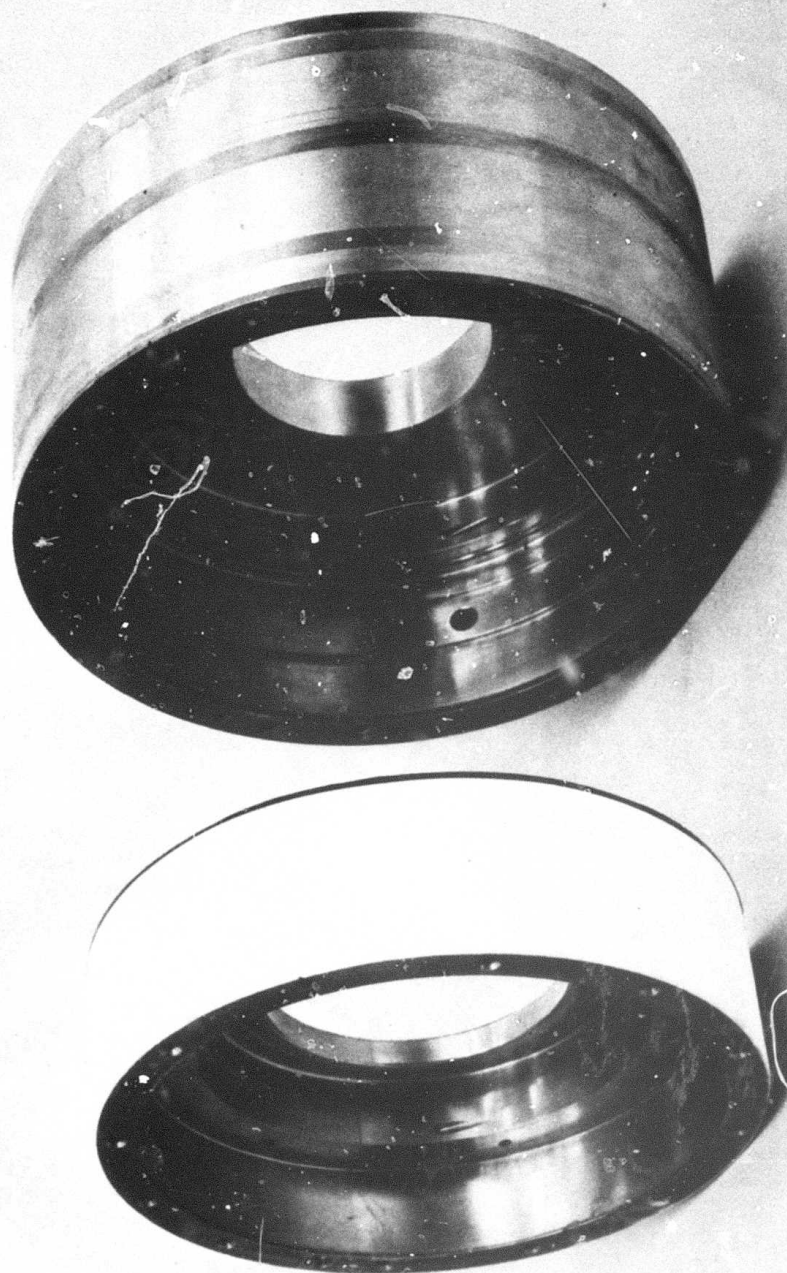


Figure 117. Semifinished Outer Collectors

10 ppm. Before injection into the test rig, the cover gas is bubbled through a column of NaK for final cleanup of the oxygen and the water vapor. The stream of extremely small diameter bubbles is produced by forcing the nitrogen through a fine glass frit having a pore size of 4 to 5.5 microns.

Liquid gallium is introduced into the collector cavities through a series of passages drilled in the outer collector pieces and terminating in the tangential ports in the inner walls of the outer collectors. These ports can be seen in both of the semifinished outer collector pieces shown in Figure 117. These tangential openings are also used as impact ports to collect the liquid metal during operation, developing sufficient pressure to circulate the gallium through a coarse (40 to 60 microns) glass frit.

The final auxiliary is the cooling system that will supply the cooling water, at a controlled inlet temperature, to the heat transfer surfaces in the outer collectors.

The detailed specifications of the various manufacturing processes and techniques developed to construct the liquid metal current collector test rig appear on the detailed parts drawings and will be released at the conclusion of the testing.

In accordance with the requirements of this program, all rotating tests of this test machine will be conducted in accordance with the statement of work and the program plan for Phase III.

The results of tests on these collector configurations may indicate that alternative configurations should also be evaluated. Such variations and supplemental tests may be conducted within the scope and schedule authorized under Phases II and III of the program. However, the specific objective of this portion of Phase III (evaluating gallium collectors in the patch roll and operational conditions of a superconductive power system applicable to Department of Defense requirements and experimentally evaluating the suitability of the control materials and processes related to such systems) will have been attained if satisfactory test results are obtained during Phase III.

Section 6

SUPERCONDUCTING COIL TECHNOLOGY

SUPERCONDUCTING COIL SHOCK AND VIBRATION TESTS

The purpose of this investigation is to evaluate the performance of superconducting coils in withstanding external environmental impact and vibratory forces and torques equal to or exceeding those that might be anticipated in naval service.

The specific objectives of this investigation are to:

- Evaluate various coil mountings and support structures for cylindrical superconducting coils of acyclic direct-current machines, which are energized at a flux density of 6 tesla.
- Investigate the extreme conditions of environmental shocks and/or vibrations that may be transmitted through the winding support structure and that could result in the quenching of the superconducting coils.

MODEL DESCRIPTION

The model setup for the shock experiments (Figures 118 through 120) consists of a frame made of structural U-channels, a dewar with its cover plate firmly supported by the frame, the superconducting coil and support structure (which is elastically suspended from the dewar cover plate by a flexible tube form mounting), and the falling weights that apply the linear and torsional shocks to the coil support structure.

The cylindrical superconducting coils (6-inch outside diameter by 3-inch by 2-1/2-inch length) are mounted on the lower end of the support structure in such a manner that their longitudinal axes can be either vertical or horizontal.

The coils will be spaced from each other and from the support plates by Textolite[®] disks that provide cooling and axial alignment for the coils (Figure 121). Circumferential and radial grooves will be machined at each face of the disk, to allow for direct cooling of the surfaces at contact.

The coil support structure consists of a thin 304L stainless steel tube with flange F welded at its upper end and square plate P welded at its lower end. The superconducting coils can be mounted on plate P in either of two arrangements:

- Vertical Coil Longitudinal Axis. The coils are held flat against support plate P by square aluminum plate A, which is bolted directly onto plate P (Figure 118).

[®]Registered trademark of the General Electric Company

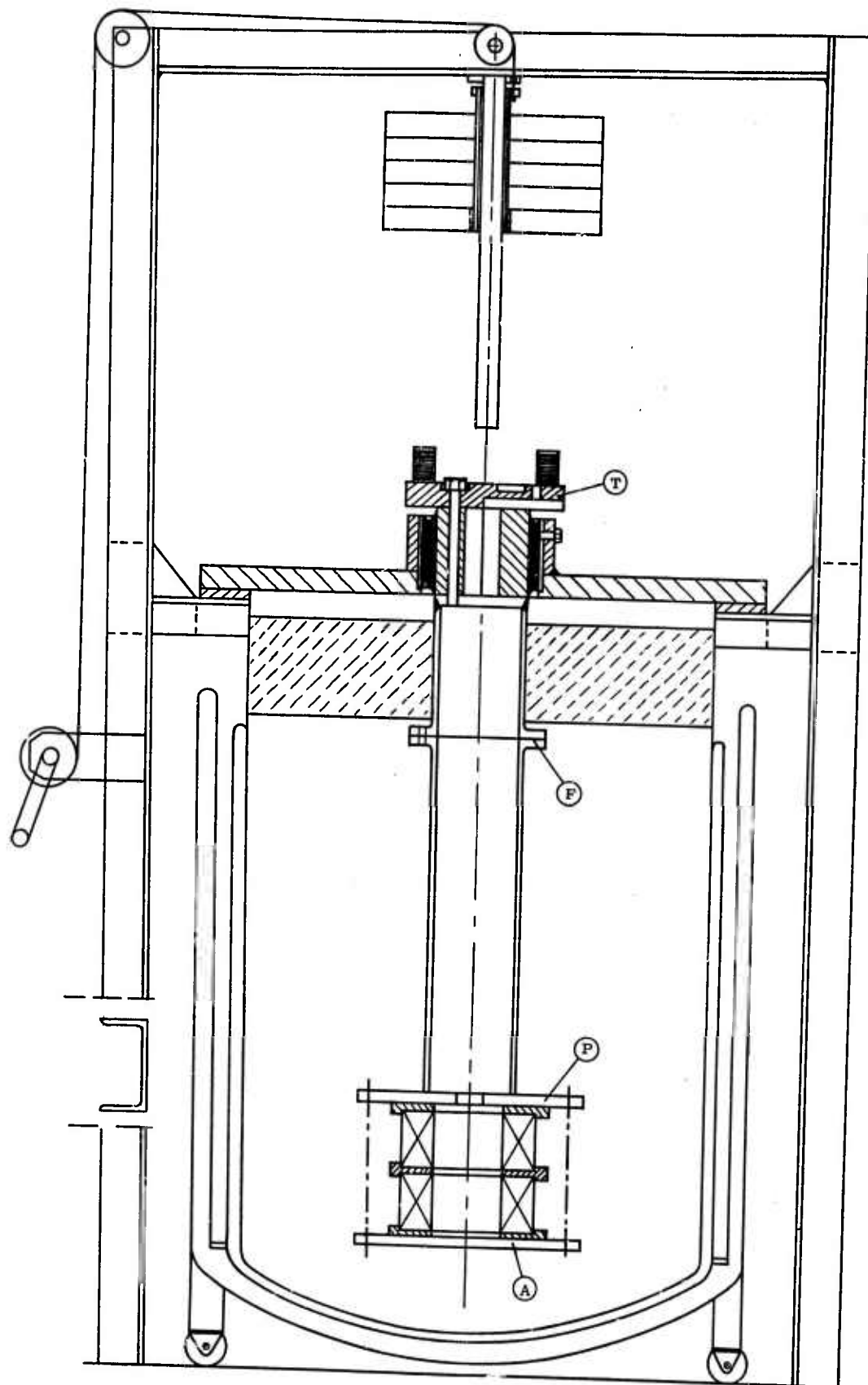


Figure 118. Model Setup for Linear Shock Test Applications

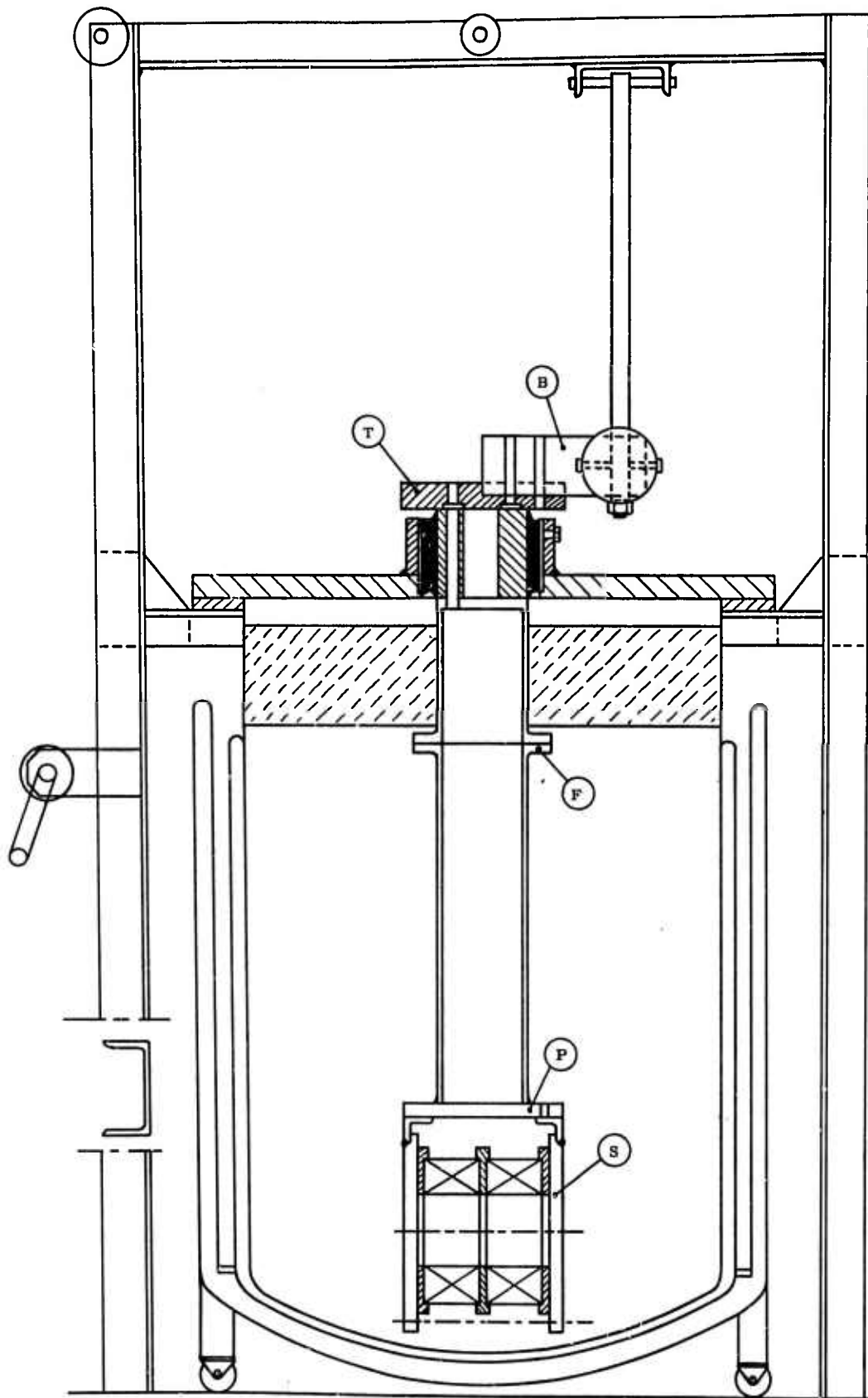


Figure 119. Model Setup for Torsional Shock Test Applications

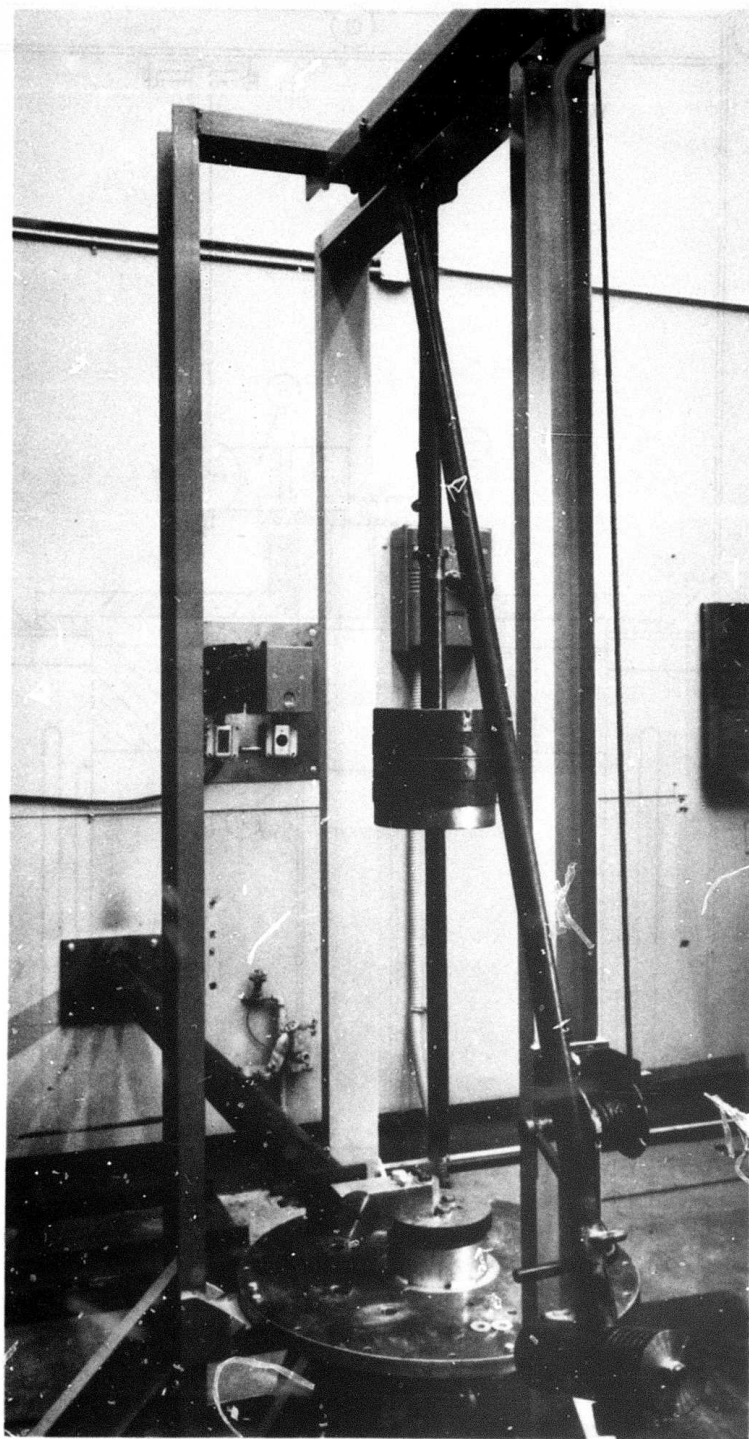


Figure 120. Shock Test Facility

- Horizontal Coil Longitudinal Axis. The coils are held flat against each other by two rectangular aluminum square plates, S, each of which has an aluminum structural angle welded on its top. The bolted assembly of coils and plates, S, can be fastened firmly against support plate P, as shown in Figure 119.

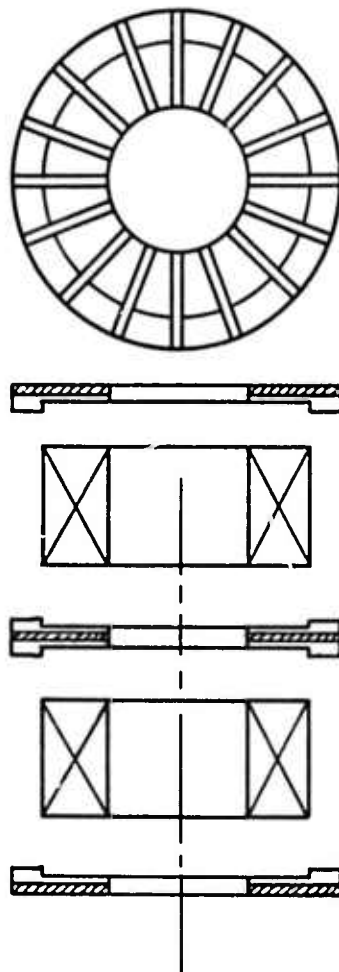


Figure 121. Textolite Disks for Superconducting Coil Alignment and Cooling

The shock and vibration that are applied to the superconducting coils and their support structure are elastically absorbed by a tube form rubber mounting (Figure 118). The outer shell of the rubber mounting is firmly fastened inside the aluminum tubular housing on the top of the dewar cover plate, while the inner hollow cylinder of the mounting is fastened to the coil support structure and is subjected to the applied shock and vibration.

The linear and torsional impact to the coil support structure is received by a thick plate, T, which is mounted on top of the inner cylinder of the rubber mounting. On one side of plate T, an annular groove is machined in such a way that the heads of the mounting bolts are recessed while, on the other side of the plate, a radial rectangular groove is machined to provide support for an aluminum bar with a square cross section. To receive the linear impact,

plate T is mounted so the mounting bolts are recessed and so a set of shock prisms of rectangular cross section are laid symmetrically on the flat surface of the plate, to absorb the impact through their plastic deformation. By varying the number of lead prisms laid on the plate, the impact force and the resulting acceleration can be varied.

To receive the torsional impact, an aluminum bar, B, with a square cross section, is mounted into the rectangular slot of plate T, and the assembled unit is then fastened to the inner cylinder of the rubber mounting (Figure 119).

The assembly of weights for applying the linear shock consists of a set of disks with a central bore and a tube bolted into one of them (the bottom one), to serve as a guide for assembling the stack. The assembled stack of weights slides about a vertical tube at the center of the top cross beam of the structural frame. Removal or addition of weights is performed by lifting the stack and disassembling the weight at the bottom.

The torsional impact is applied by an anvil hammer, of adjustable weight and height, to the projecting aluminum bar that is firmly attached to top plate T. The impact force is absorbed similarly by a circular plate of lead attached to the hammer. Varying the outside and inside diameters of the lead plate, the impact force and acceleration can be varied.

The model setup for exciting linear vibrations is similar to the setup for applying linear shocks, except the assembly of the weight stack is removed and the vibrator is instead mounted onto the dewar plate (Figure 121).

The vibrator exciter (Figures 122 and 123) consists of a direct-current, variable speed motor (1-1/2 hp, 3400 rpm), a shaft that is mounted on two pillow blocks, and a spherical roller bearing with an eccentric adapter sleeve mounted in the middle of the section of the shaft between the pillow block bearings. The amplitude of the vibration is determined by the eccentricity of the adapter sleeve of the spherical roller bearing, while the frequency of the vibration can vary by varying the speed of the motor.

To obtain a nearly uniform vibration frequency, the pulley driving the vibrator shaft is designed to also serve as a flywheel.

The position of the vibrator for exciting torsional vibrations is shown in Figure 124. The vibration force is applied at the end of aluminum bar B, and it is reacted by the force of the compressed coil spring at the opposite side of bar B. For assembly purposes, a shorter vibrator shaft is used with this configuration, while all the other components of the vibrator remain the same.

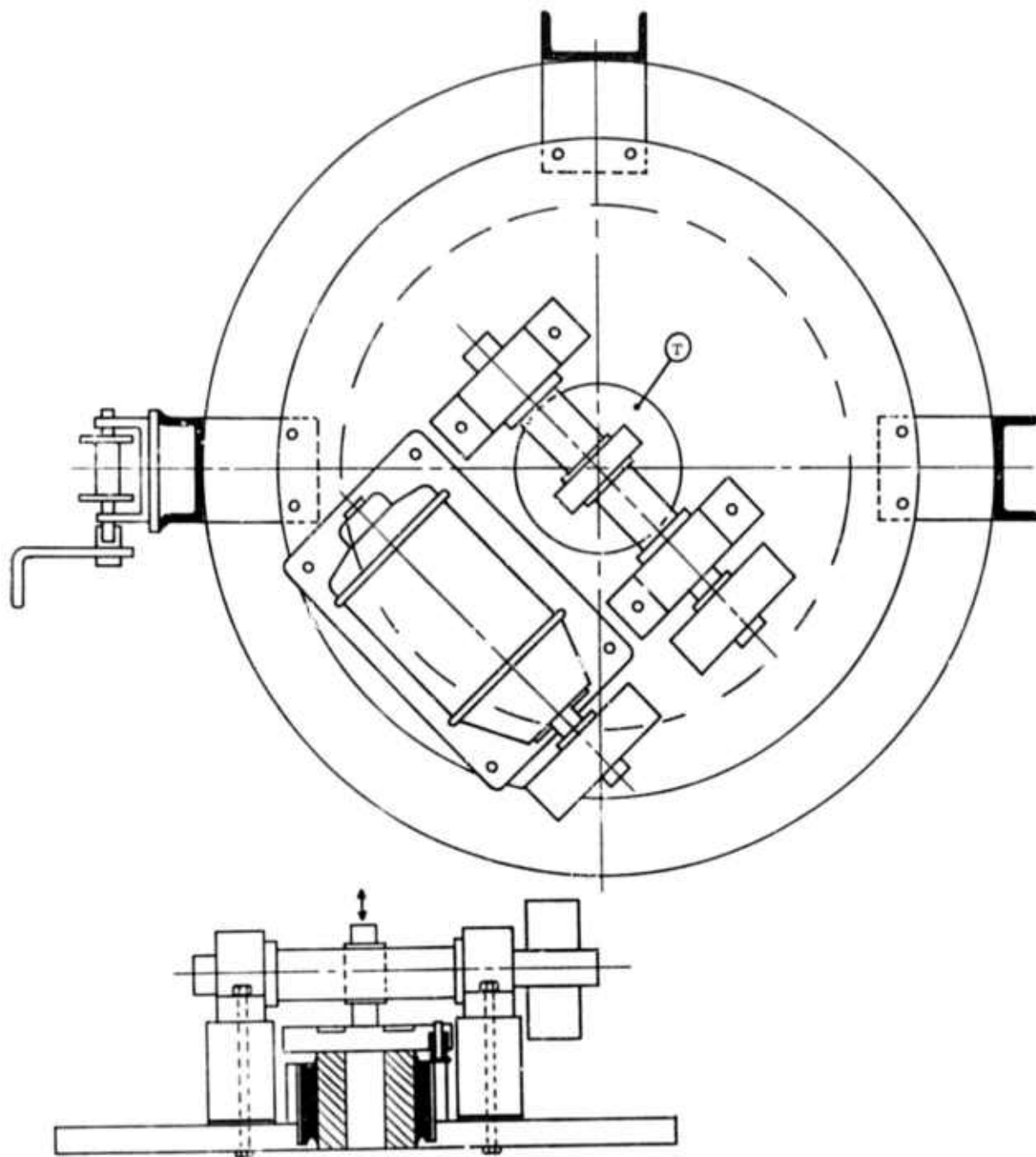


Figure 122. Vibrator Arrangement for Linear Vibration Tests

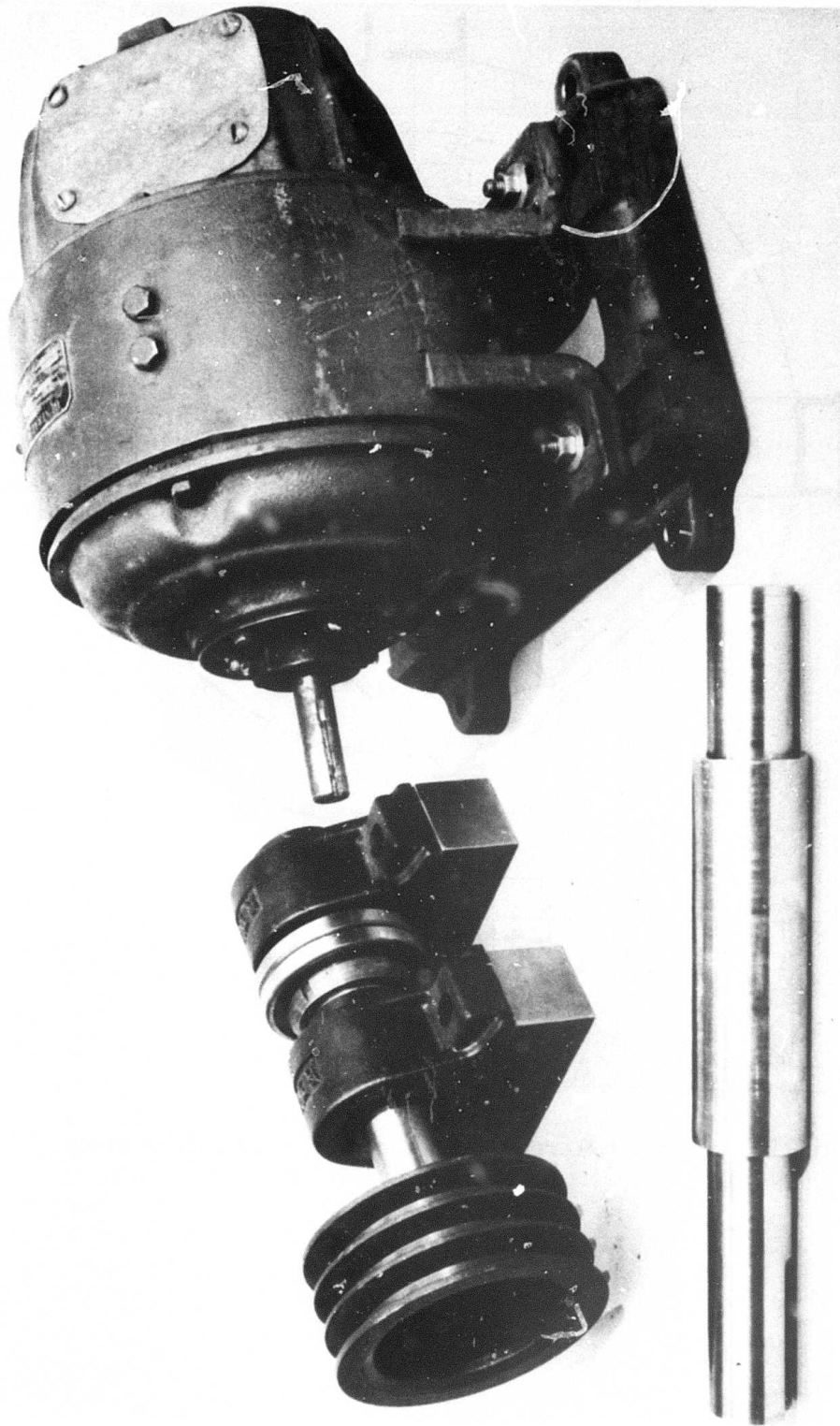


Figure 123. Vibrator Exciter

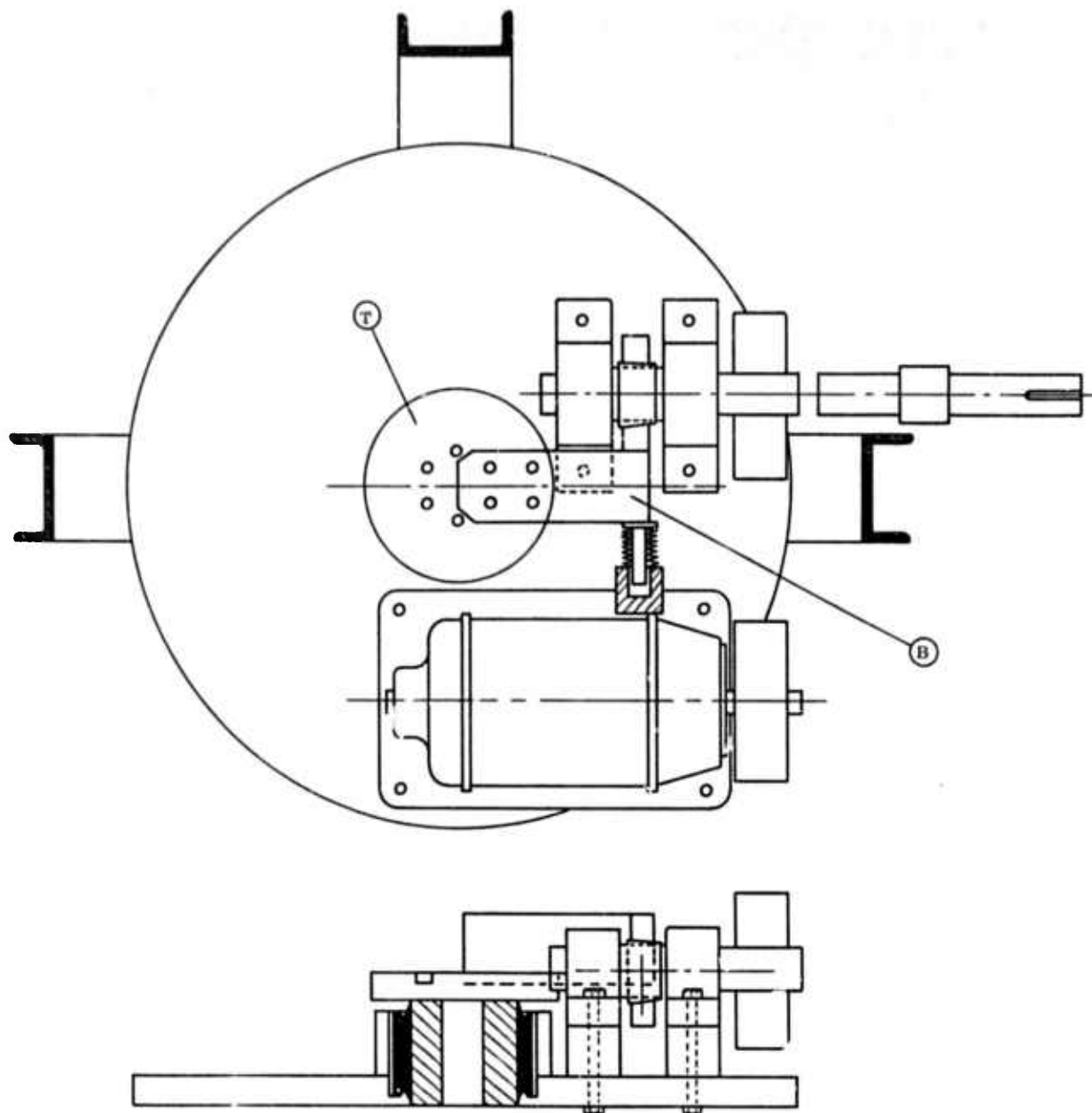


Figure 124. Vibrator Arrangement for Torsional Vibration Tests

SHOCK TESTS

REQUIREMENTS

In this experimental investigation, the following modes of environmental shocks will be investigated:

- Linear Shock Along the Longitudinal Axis. The coils will be mounted on the support structure, as shown in Figure 118, and the vertical stack of weights will be assembled on the frame.

- Linear Shock Normal to the Longitudinal Axis Through the Center. The coils will be mounted on the support structure, as shown in Figure 119, and the vertical stack of weights will be used to apply the shock.
- Torsional Shock Along the Longitudinal Axis. The coils will be mounted on their support, as shown in Figure 118, and the anvil hammer assembly will be mounted on the frame.
- Torsional Shock Normal to the Longitudinal Axis Through the Center. The coils will be mounted, as shown in Figure 119, and the shock will be applied by the anvil hammer assembly.

The applied impact forces and torques will subject the coils to the following conditions:

- Acceleration of the coils at linear impact, up to 300g, for a shock duration of up to 2 milliseconds
- Acceleration of the coils at torsional impact, up to 300g at the outside diameter of the coil, for a duration of shock of up to 2 milliseconds

SHOCK TEST PROCEDURE

Preliminary Tests

The purpose of these tests is to determine the yield strength of the lead prisms at high rates of deformations due to a shock.

The test setup (Figure 125) consists of a vertical tube mounted on a rigid metal foundation and a falling 24-pound weight, which is released around the tube from a predetermined height. The lead prisms (1 by 1 by 1.5 inches) are positioned symmetrically around the vertical tube.

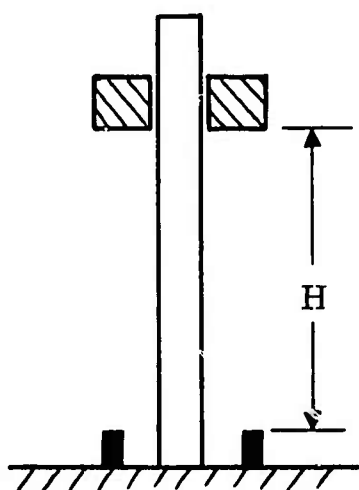


Figure 125. Test Setup to Determine Yield Strength of Lead

The average yield strength of lead was calculated from:

$$S = \frac{G \cdot H}{n \cdot A_{av} \cdot d}, \quad A_{av} = \frac{A_b + A_a}{2}$$

where:

G = Falling weight = 24 pounds

H = Distance weight falls before striking lead

A_{av} = Average cross section area of lead during deformation

A_b = Cross section area of lead before impact

A_a = Cross section area of lead after impact

n = Number of lead prisms

d = Plastic deformation of lead

Table 15 summarizes the results of these tests. Based on these results, the yield strength of lead is 4000 psi.

Table 15

RESULTS OF SHOCK TESTS TO DETERMINE YIELD STRENGTH OF LEAD

Test	Prism Dimensions				Average Cross Section A _{av} (square inches)	Plastic Deflection d (inch)	Load Stroke ii (inches)	Lead Prisms n	Yield Strength (psi)
	Before Shock		After Shock						
	A (square inches)	L (inches)	A (square inches)	L (inches)					
I	1	1.501	1.084	1.384	1.041	0.115	58.5	3	3900
II	1	1.500	1.050	1.416	1.030	0.084	38.5	3	3560
III	1	1.500	1.121	1.338	1.060	0.182	58.5	2	4088
IV	1.059	1.416	1.113	1.348	1.085	0.068	38.5	3	4174

Determination of Test Parameters

Given an impact acceleration, α , and a corresponding shock duration, δt , the following expressions can be applied to determine required test parameters A, m_2 , and H (see Appendix I, "Shock Parameters"). For linear shock:

$$\text{Area of lead } A = \frac{\alpha \cdot m_1}{S}$$

$$\text{Shock duration } \delta t = \frac{\sqrt{2gH m_1}}{(m_1 + m_2)\alpha}$$

(93)

For torsional shock:

$$\text{Area of lead } A = \frac{I \cdot \alpha}{r \cdot S \cdot R} = \frac{I \cdot \dot{\omega}}{R \cdot S} \quad (94)$$

$$\text{Shock duration } \delta t = \frac{m_2 \cdot R \cdot r \cdot \sqrt{2gH}}{(I + m_2 R^2) \alpha}$$

where:

- A = Average area of lead during deformation
- g = Standard gravity
- H = Vertical distance that weights fall before striking
- I = Polar moment of inertia of superconducting coil and support
- m₁ = Mass of superconducting coil and support
- m₂ = Mass of falling weights
- R = Radius at point of torsional impact
- r = Radius at point of linear acceleration α
- S = Average yield strength of lead during deformation
- δt = Shock duration
- α = Linear acceleration at point of interest
- $\dot{\omega}$ = Angular acceleration of superconducting coil at impact

The mass, m₁, and the polar moment of inertia, I, of the superconducting coil assemblies and their support structure are summarized in Table 16.

Table 16

MASS AND POLAR MOMENT OF INERTIA OF SUPERCONDUCTING COILS AND THEIR SUPPORT STRUCTURE

Item	Designation	Mass (pound _m)		Inertia (pound _m -square inch)	
		I*	II**	I	II
1	Superconductor coil and copper coil	26	26	265.6	149.5
2	304 stainless steel support tube, 3-1/2-inch SCH5	13.02	13.0	50	50
3	304 stainless steel support plate, 7 x 7 x 3/8 inches	5.25	5.25	42.9	42.9
4	304 stainless steel disk	1.25	1.25	2.3	2.3
5	Aluminum support plate 7 x 7 x 1/2 inches	240	--	10.6	--
6	Two aluminum support plates 7 x 6 x 1/2 inches	--	7.10	--	116
7	304 stainless steel flange	3.41	3.41	22.2	22.2
8	Steel disk for impact	0.0	0.0	60.3	60.3
9	Inner cylinder of rubber mounting	12.47	12.47	26.6	26.6
10	Three textolite spacer disks for coils	2.0	2.0	12.2	18.0
11	Fastening bolts for coils	2.0	2.0	30.2	15.0
12	Aluminum square bar, 2-1/2 x 2-1/2 x 7 inches	--	--	71.5	71.5
13	Steel disk for impact	--	--	26.5	26.5
14	Assembly for linear shock test	76.8	81.5	--	--
15	Assembly for torsional shock test	--	--	632.1	602.6

*I = Assembly, where axis of SC is vertical

**II = Assembly, where axis of SC is horizontal

Instrumentation Test Procedure

The acceleration and shock duration will be measured using an accelerometer that will be mounted on top plate T of the coil support structure. The impact force will then be calculated from $P = m_1 \alpha$.

The test will be carried out as follows:

1. Set the test parameters (area of lead A, weight m_2 , and striking height H) so the desired acceleration and shock duration are obtained from Equations 93 and 94.
2. Perform the trial shock test in air or liquid nitrogen, to measure impact acceleration α and shock duration δt , using the readings of the accelerometer. Modify the test parameters as required to obtain the acceleration and shock duration that were specified.
3. Cool the superconducting coil assembly to 4.2°K, energize the superconducting coil to a flux density of 6 tesla, and perform the shock tests described above.

VIBRATION TESTS

REQUIREMENTS

The coil configurations and modes of vibration that will be investigated are:

- Linear Vibration Along Longitudinal Axis of Coils. The coils are assembled so their longitudinal axis is vertical (Figure 118). The vibrator exciter is mounted on the top of the dewar cover plate, as shown in Figure 122.
- Linear Vibration Normal to Longitudinal Axis of Coils. The coil assembly is as shown in Figure 119, while the vibrator exciter is mounted as shown in Figure 122.
- Torsional Vibration Along Longitudinal Axis of Coils. The coils are arranged as shown in Figure 118, aluminum bar B is mounted on plate T and the vibrator is assembled as shown in Figure 124.
- Torsional Vibration Normal to Longitudinal Axis of Coils. The coil configuration of Figure 119 is used with the vibrator assembled as shown in Figure 124.

The vibration tests will run between 5- and 50-hertz frequencies in discrete intervals of 1 hertz at 15 seconds per interval. Discrete vibration table excursions of 0.020, 0.040, and 0.060 inch will be applied throughout the above frequency range.

VIBRATION TEST PROCEDURE

Preliminary Tests

The purpose of these tests is to determine the vibration characteristics of the coil and their support structure in air and liquid nitrogen (see Appendix II, "Vibration Characteristics"):

- Initial preload of the rubber mounting required to prevent separation of the exciter cam from plate T
- Vibrator frequency nonuniformity
- Resonance frequencies, if any

Instrumentation Test Procedure

The vibrator frequency will be determined by using either a mechanical tachometer for approximate readings or a stroboscope for more accurate measurements. The vibration acceleration will be measured using an accelerometer that is to be mounted on plate T.

The test will be carried out as follows:

1. Set the vibration amplitude mechanically by assembling a bearing adapter sleeve of known eccentricity.
2. Set the initial preload of the rubber mounting and perform a trial vibration test in air to assure that no separation of the exciter cam from plate T occurs while the frequency nonuniformity is acceptable.
3. Cool the superconductive coil assembly to 4.2°K, energize the coil to a flux density of 6 tesla, and perform the above vibration test.

Section 7

REFERENCES

1. P.A. Rios et al., Investigation of Complementary Equipments (ICE) (U), Report No. SRD-73-071, U.S. Army Safeguard Systems Command Contract No. DAHC60-73-C-0001, General Electric Company, Schenectady, N.Y., May 1973.
2. Materials Handbook, Small Aircraft Engine Department, General Electric Company, Lynn, Mass.
3. D.B. Colyer and W.R. Oney, High-Speed Cryogenic Alternator Development, Vol. I, U.S. Army Mobility Equipment Research and Development Center Contract No. DAAK02-68-C-0320, General Electric Company, Schenectady, N.Y., July 1970.
4. A.L. London, D.F. Sampsell, and J.D. McGowan, "The Transient Response of Gas Turbine Plant Heat Exchangers -- Additional Solutions for Regenerators of the Periodic-Flow and Direct-Transfer Types," Transactions of the ASME, Journal of Engineering for Power, Los Angeles, Cal., March 3-7, 1963, Vol. 86, American Society of Mechanical Engineers, Easton, Pa., April 1964, p. 130.
5. R.L. Rhodenizer, Development of Solid and/or Liquid Metal Collectors for Acyclic Machines (Tasks 1 through 3), Report No. S-70-1032, Naval Ship Systems Command Contract No. N-00024-68-C-5415, General Electric Company, Schenectady, N.Y., 27 February 1970.
6. B.D. Hatch et al., Cryogenic Systems and Superconductive Power, First Semiannual Technical Report, Report No. SRD-73-022, Advanced Research Projects Agency Contract No. DAHC-15-73-C-0235, General Electric Company, Schenectady, N.Y., 20 December 1972.
7. R.L. Rhodenizer, Development of Solid and/or Liquid Metal Collectors for Acyclic Machines (Tasks 4 and 5), Report No. S-71-1110, Naval Ship Systems Command Contract No. N-00025-68-C-5415, General Electric Company, Schenectady, N.Y., 30 September 1971.

Appendix I

SHOCK PARAMETERS

LINEAR IMPACT

Assuming that masses m_1 and m_2 are moving at velocities v_1 and v_2 , respectively, just prior to an impact, that e is the coefficient of impact, and that u_1 and u_2 are the velocities just after the collision, then, by the definition of the coefficient of impact:

$$u_1 - u_2 = -e(v_1 - v_2)$$

and the momentum balance equation is:

$$m_1(u_1 - v_1) + m_2(u_2 - v_2) = 0$$

Velocities u_1 and u_2 just after the collision can then be determined:

$$u_1 = v_1 - \frac{(v_1 - v_2)(1 + e)}{1 + \frac{m_1}{m_2}} \quad (95)$$

$$u_2 = v_2 + \frac{(v_1 - v_2)(1 + e)}{1 + \frac{m_2}{m_1}}$$

The loss of kinetic energy due to the impact is then:

$$\begin{aligned} \Delta K &= \frac{1}{2} m_1 v_1^2 + \frac{1}{2} m_2 v_2^2 - \frac{1}{2} m_1 u_1^2 - \frac{1}{2} m_2 u_2^2 \\ &= \frac{1}{2} \frac{m_1 m_2}{m_1 + m_2} (v_1 - v_2)^2 (1 - e^2) \end{aligned} \quad (96)$$

When mass m_2 is at a standstill prior to the collision ($v_2 = 0$) and when the impact is ideally plastic (coefficient of impact $e = 0$), then Equations 95 and 96 yield:

$$u = u_1 = u_2 = v_1 \frac{m_1}{m_1 + m_2} \quad (97)$$

$$\Delta K = \frac{1}{2} \frac{m_1 m_2}{m_1 + m_2} v_1^2$$

If mass m_1 develops its velocity, v_1 , by falling from a standstill from height H relative to the collision point, then its velocity prior to collision is:

$$v_1 = \sqrt{2gH} \quad (98)$$

Further, if the acceleration of mass m_2 just after the collision and during the duration of the impact is constant, then:

$$u = \alpha_2 \delta t = \frac{P}{m_2} \delta t = v_1 \frac{m_1}{m_1 + m_2} = \sqrt{2gH} \frac{m_1}{m_1 + m_2}$$

and the duration of the shock is:

$$\begin{aligned} \delta t &= \sqrt{2gH} \frac{m_1}{(m_1 + m_2)} \times \frac{1}{\alpha_2} \\ &= \sqrt{2gH} \frac{m_1 m_2}{(m_1 + m_2)} \frac{1}{P} \end{aligned} \quad (99)$$

where P is the internal impact force.

Equation 99 could also have been derived by considering the constant deceleration of mass m_1 :

$$\begin{aligned} \delta t &= \frac{v_1 - u_1}{\alpha_1} = \left[v_1 - v_1 \frac{m_1}{m_1 + m_2} \right] \frac{1}{\alpha_1} = \frac{m_2 v_1}{(m_1 + m_2) \alpha_1} \\ &= \sqrt{2gH} \frac{m_1 m_2}{(m_1 + m_2)} \frac{1}{P} \end{aligned}$$

Making use of the principle that the loss of kinetic energy must be equal to the work of the internal stresses, the following expression results for an ideally plastic impact:

$$\Delta K = \frac{1}{2} \frac{m_1 m_2}{m_1 + m_2} v_1^2 = P \delta \quad (100)$$

where:

P = Impact force that is assumed to be constant during deformation

δ = Plastic deformation

TORSIONAL IMPACT

The following discussion considers the plastic collision of mass m_2 moving on a vertical plane about the center of rotation O_2 with mass m_1 , which is at standstill and has only one rotational degree of freedom on the horizontal plane, about the axis of rotation Z (Figure 126).

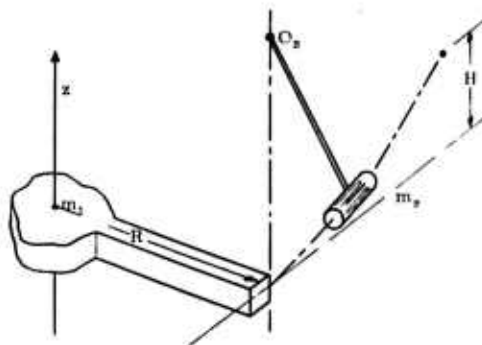


Figure 126. Torsional Impact of Mass m_2 with Mass m_1

Let:

I = Polar moment of inertia of mass m_1 about vertical axis of rotation Z

R = Radius at point of impact from axis of rotation Z

w = Angular velocity of masses m_1 and m_2 after impact

$v = \sqrt{2gH}$ velocity of mass m_2 just prior to collision

The rate of change of the angular momentum before and after the impact will be equal to the torque of external forces with respect to the axis of rotation Z , because the only external forces are the reactions through the axis of rotation Z :

$$\Delta\theta = (Iw + m_2 w R^2) - m_2 v R = 0 \quad (101)$$

Equation 101 can be solved for the angular velocity, w :

$$w = \frac{m_2 v R}{I + m_2 R^2} \quad (102)$$

The loss of kinetic energy due to the impact would be equal to the work of the internal stresses, and for an ideally plastic impact:

$$\Delta K = \frac{1}{2} m_2 v^2 - \frac{1}{2} (I + m_2 R^2) w^2 = P \times \delta \quad (103)$$

where:

P = Impact force (constant)

δ = Plastic deformation

Substituting, in Equation 103, the expression for w given by Equation 102 yields:

$$\frac{1}{2} m_2 v^2 - \frac{(m_2 v R)^2}{I + m_2 R^2} = P \times \delta \quad (104)$$

To determine the shock duration, constant angular acceleration \dot{w} of mass m_1 during the impact can be considered:

$$\delta t = \frac{w}{\dot{w}} = \frac{m_2 v R}{(I + m_2 R^2)} \times \frac{1}{\dot{w}} \quad (105)$$

Angular acceleration \dot{w} is calculated from:

$$I \dot{w} = P \times R$$

where P is the average impact force during the collision.

The linear acceleration at a given point of mass m_1 can be found from angular acceleration \dot{w} as follows:

$$\alpha = \dot{w} r = \frac{P \cdot R \cdot r}{I} \quad (106)$$

The impact is absorbed entirely by the plastic deformation of m_2 . If A and S are the average area of deformation and the yield strength, respectively, then:

$$P = A \cdot S \quad (107)$$

and Equations 105 through 107 can be combined to give:

$$\alpha = \frac{A \cdot S \cdot R \cdot r}{I}$$

$$\delta t = \frac{m_2 \cdot v \cdot R \cdot r}{(I + m_2 R^2) \alpha} \quad (108)$$

$$v = \sqrt{2gH}$$

Appendix II

VIBRATION CHARACTERISTICS

If the linear vibration of the coils and their support are nearly sinusoidal (that is, if vibration displacement X were defined as follows:

$$X = X_o \sin(\omega t) \quad (109)$$

for this case), then the governing differential equation of the forced vibration would be:

$$m_1 \frac{d^2 X}{dt^2} + KX = F \quad (110)$$

where:

m_1 = Mass of coils and support structure

K = Spring constant of rubber mounting

F = Exciting force

Substituting for X , in Equation 110, the expression from Equation 109 yields:

$$F = X_o \left[1 - \frac{\omega^2}{P^2} \right] K \sin(\omega t) = F_o \sin(\omega t) \quad (111)$$

$$P^2 = \frac{K}{m_1}$$

$$F_o = X_o \left[1 - \frac{\omega^2}{P^2} \right] K$$

If F_i is the initial compression force of the rubber mounting, then the total applied force would be:

$$F = F_i + F_o \sin(\omega t) \quad (112)$$

To prevent separation between the vibrator cam and the vibrating structure, the total applied force, given in Equation 112 should always be positive. This requirement is fulfilled when the initial compression force, F_i , is:

$$F_i > F_o = X_o \left[1 - \frac{\omega^2}{P^2} \right] K \quad (113)$$

The instantaneous power requirement of the vibration is calculated from:

$$N = F \frac{dX}{dt} = [F_i + F_o \sin(\omega t)] X_o \omega \cos(\omega t) \quad (114)$$

To meet this variable instant power requirement at a fairly uniform frequency, the inertia of the vibrator shaft must be increased by the addition of

a flywheel. The differential equation that governs the frequency fluctuation due to the power variation is:

$$I \frac{dw}{dt} = (F_i + F_o \sin wt) X_o w \cos(wt) \quad (115)$$

Integrating Equation 115 over half a period $(-\pi/2w, \pi/2w)$ yields:

$$\frac{I}{2} (w_2^2 - w_1^2) = 2 F_i X_o \quad (116)$$

Introducing the coefficient of frequency nonuniformity:

$$c = \frac{w_2 - w_1}{w_2 + w_1} = 2 \frac{(w_2 - w_1)}{w_m}$$

then Equation 116 yields the required flywheel inertia:

$$I = \frac{2 F_i X_o}{w_m^2 c} \quad (117)$$